Spring 1990

ENDOR and ESEEM studies of a cyanide adduct of transferrin

Penny Ann Snetsinger
University of New Hampshire, Durham

Order Number 9027438

ENDOR and ESEEM studies of a cyanide adduct of transferrin

Snetsinger, Penny Ann, Ph.D.

University of New Hampshire, 1990

U·M·I
300 N. Zeeb Rd.
Ann Arbor, MI 48106

ENDOR AND ESEEM STUDIES OF A CYANIDE ADDUCT OF TRANSFERRIN

BY

PENNY A. SNETSINGER
A.B., Brandeis University, 1981
M.S., University of Illinois, 1986

DISSERTATION

Submitted to the University of New Hampshire
in Partial Fulfillment of
the Requirements for the Degree of

Doctor of Philosophy

in

Chemistry

May, 1990

This dissertation has been examined and approved.

N. Dennis Chasteen

Dissertation director, N. Dennis Chasteen
Professor of Chemistry

Richard L. Kaufmann, Professor of Physics

Frank L. Pilar, Professor of Chemistry

W. Rudolf Seitz, Professor of Chemistry

Edward H. Wong

Edward Hou S. Wong, Professor of Chemistry

May 10, 1990
Date

ACKNOWLEDGEMENTS

I am deeply indebted to Dr. Chasteen for his support, patience, and ideas (except for the dipole calculation). The past few years have been both rewarding and challenging which is as much as one can ask for in a graduate career. Thanks to Phillip Hanna who listened patiently to the step by step development of much of this work and probably learned more about ESEEM and ENDOR than he ever wanted to. John Grady was particularly helpful in dealing with the trials and tribulations of life with computers and, no doubt, many of his pens donated their lives to this dissertation. I also want to thank the rest of the Chasteen group for their interest. I appreciate the ENDOR spectra provided by Dr. Hans VanWilligen and the help of Dr. John McCracken and Jeff Cornelius in obtaining the ESEEM data. Drs. Belford and Clarkson were responsible for my comprehensive introduction to ESE and ENDOR at the University of Illinois which was instrumental to my success here. The Belford gang at Illinois, Harry, Karen, Dave, and Kurt provided long distance moral support, obscure references from obscure journals, and a constant infusion of BITNET mail. I especially want to thank Jeff Cornelius who served as major resource of information and expertise and who provided the support that only one who has dealt with it all first-hand could offer (too bad you weren't around to help with the figures, though). Finally, I undoubtedly owe Peter for life since he put up with me during all this. I would list everything you did, but that would take another two hundred pages. I appreciate it all more than you can imagine.

TABLE OF CONTENTS

LIST OF TABLES

LIST OF FIGURES

LIST OF SYMBOLS

A_{aniso}	total anisotropic hyperfine coupling
A_d	anisotropic hyperfine coupling due to dipole-dipole interaction
A_{iso}	isotropic hyperfine coupling
A_n	total hyperfine coupling (sum of anisotropic and isotropic terms)
A_p	anisotropic coupling due to electron spin density in carbon p-orbitals
$\overleftrightarrow{A}$	tensor of hyperfine coupling values
β_e	Bohr magneton
β_n	nuclear magneton
f_π	electron spin density on carbon π-bonding orbitals
f_σ	electron spin density on carbon σ-bonding orbital
γ_e	electron magnetogyric ratio
g_e	g value for a free electron
g_n	g value for nucleus, n
$\overleftrightarrow{g}$	tensor of electron g-values
$\hat{\mathcal{H}}$	effective spin Hamiltonian
H_0	constant magnetic field
H_1	magnetic field of the microwave pulse
H_2	rf field

$\vec{H}$	external magnetic field described as a vector in g-coordinate system
$\hat{\vec{I}}$	nuclear spin operator
M_0	net magnetic moment due to paramagnetic sample in an external magnetic field
ν_n	free precessional frequency of a nucleus (in MHz) at a given magnetic field
$\hat{\vec{S}}$	electron spin operator
T_1	spin-lattice relaxation time
T_2	spin-spin relaxation time
T_m	phase memory time of spin packets
t_p	time of duration of the microwave pulse
ω_I	free precessional frequency of a nucleus, I, at the applied magnetic field

ABSTRACT

ENDOR AND ESEEM STUDIES OF A CYANIDE ADDUCT OF TRANSFERRIN

by

Penny A. Snetsinger
University of New Hampshire, May, 1990

Information about the ligand environment of the iron binding sites in a cyanide adduct of transferrin was obtained by an analysis of powder-type ENDOR and ESEEM spectra. The low-spin cyanide adduct of transferrin is formed only in the C-terminal site of the protein and is characterized by a rhombic EPR spectrum. Earlier work demonstrated that three cyanide groups are necessary to form the adduct, but it wasn't clear whether these groups were coordinated directly to the metal or to cationic sites on the protein. The ENDOR spectra of the ^{13}CN adduct showed one set of ^{13}C ENDOR resonances which probably corresponds to only one or two of the CN groups, the other(s) being ENDOR silent. Simulations of the ENDOR line positions indicate a substantial isotropic coupling and smaller dipolar couplings. From an analysis of the orientation dependent dipolar term it is concluded that the carbon giving rise to the ENDOR signals lies along the g_{xx} axis of the g-tensor. The iron-carbon distance was calculated based on a point dipole model and a model in which the ground state metal-based d_{xy} orbital of the electron was considered explicitly. ESEEM studies with $C^{15}N$ indicated that there are at least two equivalent CN groups coordinated to the iron center. The maximum hyperfine coupling for the nitrogen was observed near g_{xx} which is consistent with the ENDOR results which placed the carbon of the

cyanide group on the g_{xx} axis. There is a substantial hyperfine contribution along g_{zz} which indicates that the CN bond is not aligned along the g_{xx} axis. The lack of resolved couplings in the spectrum along g_{yy} makes it impossible to determine the nitrogen position exactly. The ESEEM spectra of the $C^{14}N$ adduct were complicated, presumably because the Zeeman and hyperfine terms did not cancel at the spectrometer frequencies used. The ESEEM and ENDOR spectra of the D_2O solvent exchanged adduct demonstrated that water does not coordinate directly to the iron. The ESEEM of the g'=4.3 signal which arises from the high-spin N-terminal site was also studied and the observed ESEEM resonances were attributed to histidine nitrogen.

CHAPTER 1

ESEEM AND ENDOR SPECTROSCOPY

Introduction

Electron paramagnetic resonance (EPR) spectroscopy has typically been the method of choice with which to study paramagnetic centers of biochemical systems. Since the EPR spectrum is determined by the number and nature of ligating atoms and the geometry of the ligand field, precise information about the geometric and electronic environment of a paramagnetic center can be obtained by analyzing its EPR spectrum. However, in rigid media the EPR lines are inhomogeneously broadened by the large number of nuclei which interact with the unpaired electron. Consequently, ligand hyperfine couplings are often not resolved in the EPR display. Metalloproteins are usually studied as solids (i.e., frozen solutions, glasses, or single crystals) so ligand interactions in these systems are frequently obscured within the inhomogeneously broadened EPR line.

Electron spin echo (ESE), specifically electron spin echo envelope modulation (ESEEM), and electron nuclear double resonance (ENDOR) have proven to be powerful methods in resolving hyperfine and quadrupole interactions not observable with conventional EPR spectroscopy [1,2]. There is enormous potential in employing these methods to probe the coordination sphere of metal ions in biological systems. Both ESEEM and ENDOR are techniques which observe the same transition, a nuclear spin flip transition (the "NMR" transition) within an electron spin manifold. However, the experimental

methods by which this transition is observed differ considerably. Consequently, ESEEM and ENDOR often provide complementary information about the paramagnetic center. By using both techniques to study the same system one can obtain a more complete picture of the metalloprotein than would be possible with EPR spectroscopy alone.

ESE Spectroscopy

Introduction

Hahn first observed NMR spin echoes in 1950 [3]. Although the EPR equivalent, electron spin echoes, were described in 1965 [4], it has only been recently that ESE spectroscopy has been used by more than a few labs. Currently, there is considerable interest in the technique and its application to biochemical systems.

All spin echo experiments, whether in NMR or EPR, require the use of a pulse. Pulse techniques have essentially replaced continuous wave experiments in NMR; however, the development of pulsed EPR experiments has been much slower. The main difference between pulsed EPR and pulsed NMR experiments is the time scale. For instance, the free induction decay signal for a typical EPR line of 1 Gauss would completely disappear in less than 100 nanoseconds [5]. Recent improvements in microwave pulse technology and high speed detectors have aided the development of ESE spectroscopy and consequently, pulsed EPR is becoming more available, although it is still by no means common. Commercially built pulsed EPR spectrometers have only been produced in the past few years.

In general, there are two pulse sequences used in ESE experiments. The sophisticated pulse sequences which are standard

in pulsed NMR are still rarely applied in ESE. There have been a few recent discussions of the potential of some complicated sequences in ESE, but these sequences are still considered novel and have only been applied experimentally to model systems [6,7]. The two sequences standardly used are the two-pulse or Hahn sequence and the three-pulse or stimulated echo sequence.

Two-pulse Sequence

In the two pulse experiment a paramagnetic spin system in a constant magnetic field H_0 is acted on by a series of two microwave pulses of a magnetic field H_1 which is perpendicular to H_0. One studies the spontaneous emission of the system, its echo signal. A pictorial description of the ESE experiment is provided by analyzing the motion of the sample magnetization vector under the action of the magnetic field pulse.

As pictured in Figure 1.1 b) in an external magnetic field H_0 a sample with paramagnetic particles acquires a magnetic moment M_0 which is parallel to H_0 under thermal equilibrium. It is convenient to analyze the evolution of this spin system in a coordinate system rotating about H_0 with a frequency ν_0, the frequency of the field oscillation. In the field H_1, the magnetization M_0 rotates about the x' axis in the y'z plane and turns through the angle

$$\theta = \gamma_e H_1 t_p \qquad (1.1)$$

within the time of the microwave pulse duration t_p. Pulse sequences are typically described in terms of degrees, referring to the number of degrees the sample magnetization vector is tipped by the

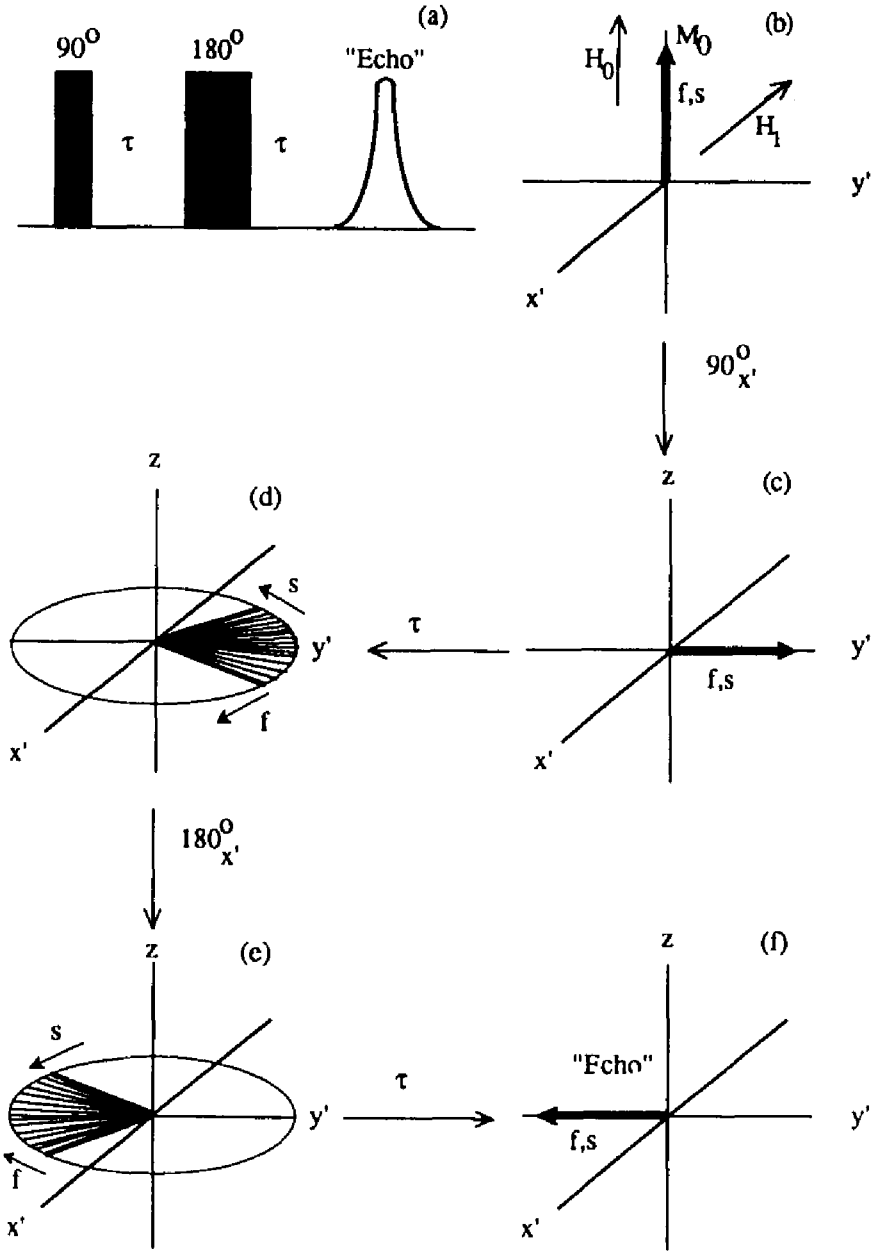

Figure 1.1 Vector diagram of the formation of a spin echo by the Hahn (90^0, 180^0) pulse sequence. (a) the pulse sequence (b) At t=0, the sample magnetization, M_0, is aligned with the magnetic field H_0 along the + z axis. (c) The magnetization immediately after the 90^0 pulse is aligned along the y' axis (d) The individual spin packets spread out after a time τ. (e) The magnetization after the 180^0 pulse. (f) After time τ, the magnetization vectors have refocussed along the y' axis to form the echo.

application of the strong microwave pulse. The field pulse is a 90 degree pulse if $\theta=\pi/2$. It is evident from Equation 1.1 that the angle of the pulse can be controlled by either the field H_1 or the time of the pulse t_p. For experimental reasons, it is usually the duration of the pulse which is varied in order to change the angle.

Under the action of a 90 degree pulse the magnetization becomes directed along y' axis as shown in Figure 1.1 c). Since the EPR line is inhomogeneously broadened by various magnetic interactions, individual spin packets within this bulk magnetization vector experience slightly different environments and consequently precess at different frequencies relative to the frequency of the rotating frame axis. This effect causes a "fanning out" of the magnetization after time τ as shown in Figure 1.1 d), with some spin packets moving slower (s) and others moving faster (f) relative to the rotating axis system. The resulting signal decay is the free-induction decay (FID) signal.

A second pulse of 180 degrees rotates every magnetization vector through 180 degrees about the x' axis. The "fan" of magnetization is still in the x'y' plane, but now the magnetization due to spins packets traveling faster than the rotating frame recombines with that due to magnetization vectors traveling more slowly, thus forming the echo and the return of a detectable signal after a time τ (Figure 1.1 f)).

In an ESE experiment this series of pulses is repeated with different times τ between the first and second pulse, allowing the magnetization vectors to fan out for different periods of time. The echo is detected and recorded for each time τ. Figure 1.2 shows the

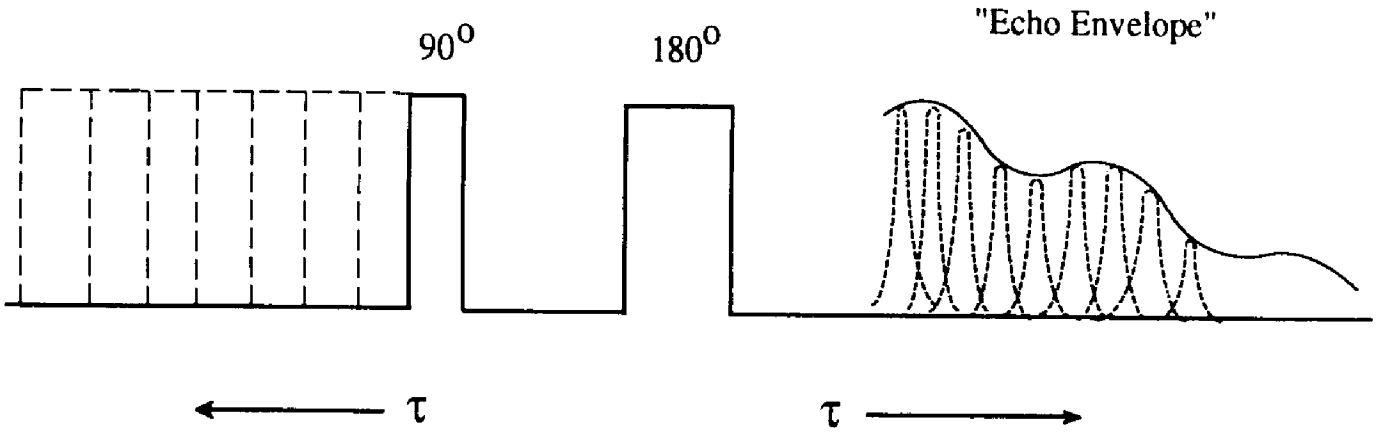

Figure 1.2 The echo envelope as a result of the two pulse spin echo experiment as the time between the first and second pulse, τ, is varied.

resultant echo envelope of an ESE experiment as τ is varied. The time over which this experiment can be performed is limited by the "phase memory time", T_m of a system [8]. This time is exactly analogous to T_2 (the spin-spin relaxation time) in NMR. At times τ longer than T_m no echo will be observed. Although the two pulse experiment has been described in terms of a 90 and 180 degree pulse, it is important to note that any combination of two pulses will create an echo. For instance, Hahn saw his original spin echoes with two approximately 90 degree pulses [3].

Three-pulse Sequence

The other commonly used pulse sequence is the three pulse or stimulated echo sequence. This sequence consists of three pulses of 90 degrees. The first pulse brings the bulk magnetization, M_0, down to y' axis where the spin packets dephase for a time τ as in the two pulse experiment. The second 90 degree pulse brings the "fan" of magnetization down to the -z axis (in a direction opposite the field H_0) where it remains for a time T. Finally, the third pulse brings the spins up to the x'y' plane again and as in two pulse after time tau the echo is observed. As the spin echo experiment is repeated, the time between the second and third pulses, T, is stepped. Figure 1.3 illustrates the resulting envelope as T is varied.

An important difference between the two and three pulse experiments is the time over which a signal can be detected. The three pulse experiment takes place over a longer time scale than the two pulse experiment since it is limited by an electron relaxation time T_{1e} which is analoguous to T_1, the spin lattice relaxation in NMR. This

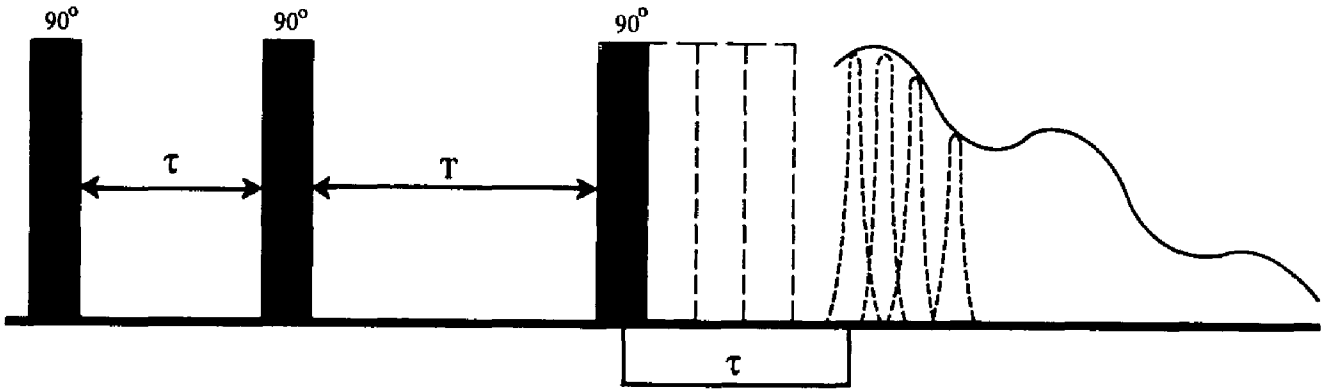

Figure 1.3 The echo envelope of a three pulse stimulated echo experiment. The time, τ, between the first and second pulse is held constant as the time, T, between the second and third pulse is varied.

time is longer than or equal to the phase memory time T_2 which limits a two-pulse experiment.

Modulation

Along with the discovery of the spin-echo phenomenon in NMR, Hahn observed that in certain cases a periodic oscillating component is superimposed upon the decay of the echo amplitude with increasing pulse separation [3]. This so-called echo envelope modulation was attributed to coupling to other non-resonant nuclear spins. The effect can, in principle, be used to obtain information about the non-resonant nuclei, but in practice the amplitude of the modulation tends to be small in NMR.

However, in the equivalent EPR experiment, any nucleus having sufficiently strong hyperfine coupling to the paramagnetic centers can cause the effect. Thus, contrary to the situation in NMR, modulation of the echo envelope in pulsed EPR is almost always observed and is often significant. The result of this effect is shown in the echo envelopes in Figures 1.2 and 1.3 where the decay is not monotonic, but modulated with a clearly defined periodicity.

A qualitative explanation of the modulation effect can be provided by considering a nucleus near the paramagnetic center. The Hamiltonian describing such a system is:

$$\hat{\mathcal{H}}=\beta_e\vec{\mathbf{H}}\cdot\overleftrightarrow{g}\cdot\hat{\vec{\mathbf{S}}}+g_N\beta_N\vec{\mathbf{H}}\cdot\hat{\vec{\mathbf{I}}}+\hat{\vec{\mathbf{S}}}\cdot\overleftrightarrow{A}\cdot\hat{\vec{\mathbf{I}}} \qquad (1.2)$$

The largest term is listed first. This is the electronic Zeeman term describing the interaction of the unpaired electron spin, **S**, with the magnetic field, **H**. The second term describes the nuclear Zeeman

term which is the analogous interaction of the nuclear spin with the magnetic field. The final term is the electron-nuclear hyperfine interaction and describes the coupling between the electron and nuclear spin. If one considers a simple case in which an unpaired electron (S=1/2) with an isotropic g-factor interacts with a nucleus of I=1/2 with isotropic coupling then the resultant energy diagram is shown in Figure 1.4.

Between the upper and lower electron spin manifolds there may occur four EPR transitions induced by microwave pulses at a resonance frequency. The probability of a transition occurring is determined by the values of the corresponding matrix elements. Two of these transitions, the solid bold lines in Figure 1.4, occur without changing the nuclear spin and are allowed EPR transitions. The two transitions shown with dashed lines are accompanied by a change in the nuclear spin and are thus forbidden transitions. In solids, anisotropic interactions result in off diagonal elements of the hyperfine tensor and these transitions become semi-allowed. For instance, the energy difference between the allowed transition from level 1 to 3 and the "forbidden" transition from level 2 to 3 is given by

$$g_N\beta_N\mathbf{H} + hA/2 \qquad (1.3)$$

and is equal to the energy of the NMR transition. If the microwave pulse has sufficient width such that it causes both allowed and "forbidden" transitions, then the two excited transitions will contain frequencies differing by the NMR frequency given in Equation 1.3. The resulting interference pattern manifests itself as a variation in the

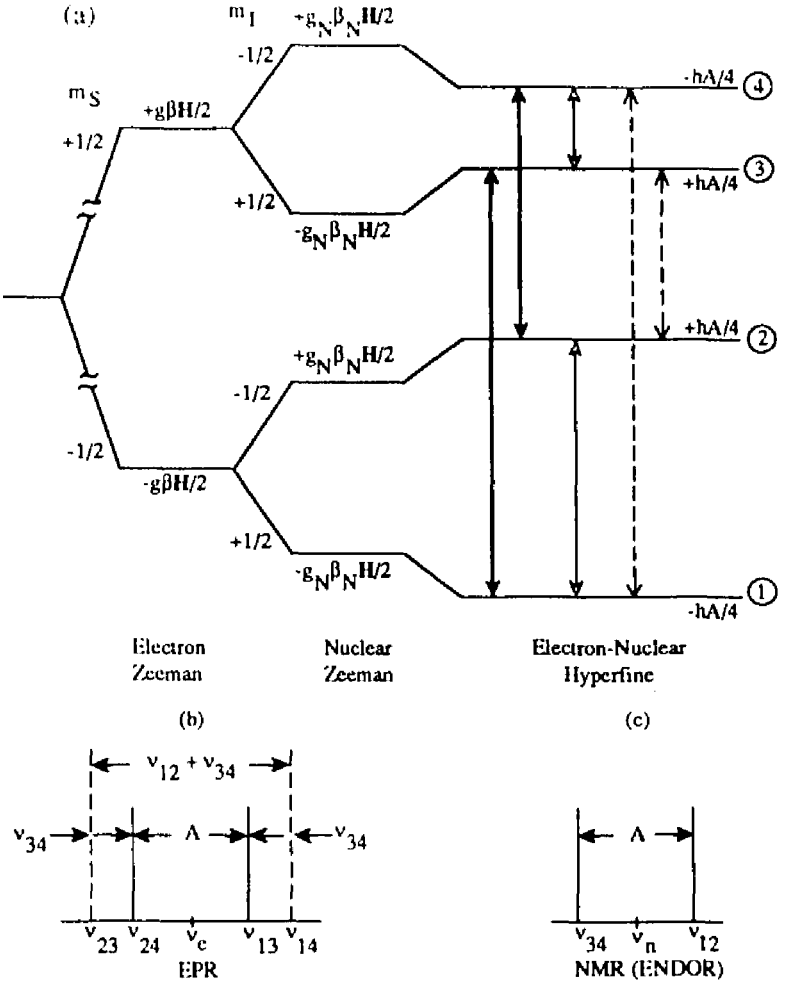

Figure 1.4 The energy level diagram for an S=1/2, I=1/2 system as described by the Hamiltonian given in Equation 1.2. The g-value and hyperfine coupling are assumed to be isotropic. The bold lines show the allowed EPR transition, the solid lines show the NMR (ENDOR, ESEEM) transitions, and the dashed lines show the EPR "forbidden" transitions. (b) The EPR spectrum that would be observed from this energy diagram. (c) the ENDOR (NMR) spectrum observed for this case.

echo amplitude, and thus causes the observed modulation pattern in the echo envelope. Although this description is useful for understanding the cause of the modulation effect, it is insufficient for a detailed analysis of experimental data.

The rigorous quantum mechanical model of the echo signal and its modulation was developed by Mims [9,10]. The detailed analysis involves a density matrix calculation. This calculation and the results are discussed in detail in several places and so only the results are briefly summarized here [11,12]. For the simplest case, an electron and proton (S=1/2, I=1/2), which is an axial system, the modulation for the Hahn echo sequence is [9]:

$$V_{mod}(2\tau, I=1/2) = 1 - 2k \sin^2(\omega_a \tau/2) \sin^2(\omega_b \tau/2) \qquad (1.4)$$

where $k = (\omega_I B/\omega_a\omega_b)^2$,

$\omega_a = [(A/2 + \omega_I)^2 + (B/2)^2]^{1/2}$

$\omega_b = [(A/2 - \omega_I)^2 + (B/2)^2]^{1/2}$

$A = F(3\cos^2\theta - 1) + 2\pi a$

$B = F(3\cos\theta \sin\theta)$

$F = g_e g_n \beta_e \beta_n / r^3 h$

ω_I is the free precessional frequency for the nucleus at the applied magnetic field. θ is the angle between the magnetic field and the electron-nuclear axis. ω_a and ω_b are the nuclear transition frequencies in the upper and lower electron manifolds. The modulation can also be written in an equivalent form:

$$V_{mod}(2\tau, I=1/2) = 1 - 1/4\ k\ [2 - 2\cos(\omega_a\tau) - 2\cos(\omega_b\tau) + \cos(\omega_a-\omega_b)\tau + \cos(\omega_a+\omega_b)\tau] \quad (1.5)$$

which clearly shows that in addition to the nuclear frequencies ω_a and ω_b, the two pulse modulation pattern includes the sum and difference of these frequencies.

The parameter, k, determines the depth of the modulation and is proportional to the square of the magnitude of B. B is the anisotropic term of the dipolar coupling. This is important in that ESEEM can only be observed with an anisotropic hyperfine interaction between an electron and a nucleus. This means the system must be studied as a solid and must have appreciable anisotropy before modulation will be observed.

Using the same situation (S=1/2,I=1/2) as described for the two pulse case, the equation for stimulated echo modulation can be written as [9]:

$$V_{mod}(2\tau+T,I=1/2) = 1- k[\sin^2(\omega_a\tau/2)\ \sin^2(\omega_b\ (\tau+T)/2) + \sin^2(\omega_b\tau/2)\ \sin^2(\omega_a\ (\tau+T)/2)] \quad (1.6)$$

This reduces to the equation for the two-pulse modulation if T=0. In contrast with the equation for the two-pulse modulation (1.5), this one contains only the nuclear frequencies ω_a and ω_b, not the sums and differences.

A number of assumptions were made in the derivation of these equations. It was assumed that the electron spin was quantized along

the magnetic field direction, thus allowing the S_x and S_y terms to be dropped from the Hamiltonian. The equations are written assuming an isotropic g-value. Considerations necessary for systems with an anisotropic g-tensor will be discussed in Chapter 2. The expressions for the dipolar part of the anisotropic hyperfine coupling (terms A and B in (Equation 1.5)) are based on a point dipole approximation. The validity of this approximation for the particular case studied here will be addressed later.

An important assumption is that H_1, the microwave magnetic field amplitude, is much larger than the nuclear Zeeman and hyperfine interactions and is large enough to excite both the allowed as well as the forbidden EPR transitions. This so called "branching" or simultaneous excitation is essential and requires that all the transitions are bracketed by the microwave magnetic field H_1 [11]. In other words, the frequency spread of H_1 must be as large as the largest splitting between the m_I energy levels in an m_S manifold or

$$\gamma_e H_1/2\pi \geq \Delta\nu \qquad (1.7)$$

where γ_e is the magnetogyric ratio for the electron and $\Delta\nu$ is the frequency spread of the hyperfine splitting levels. Experimental confirmation of this requirement has been obtained [13].

ESEEM is a time domain experiment. As is apparent from Equations (1.5) and (1.6), the Fourier transform of the time series data should give the nuclear frequencies, and their sums and differences in the case of the Hahn echo experiment. Due to experimental complications, routine Fourier transform of the echo envelope is rarely

possible. The problems with transforming time domain ESE data into a frequency spectrum will be discussed in Chapter 2.

Two-pulse Versus Three-pulse

Although both pulse sequences described above ostensibly give the same information, i.e. the NMR frequencies ω_a and ω_b, there are distinctions between the two experiments. As can be seen from equation (1.5), the modulation from a two pulse experiment, in addition to the nuclear frequencies, also involves the sums and differences. This is rarely a complication when the type of nucleus giving rise to the modulation is known, but can become a problem when dealing with an unknown nucleus or with several nuclei which will often have overlapping sums and differences that complicate the appearance of the spectrum.

As mentioned before, any combination of two pulses gives an echo. This result can complicate a three pulse modulation envelope. In Figure 1.5 all the echoes created in a three pulse experiment are illustrated. In addition to the stimulated echo at time τ after the third pulse, echoes are created by the combination of pulse one and three (the echo at time $T + \tau$), pulse two and three (the echo at time T), and the two pulse echo at time τ which acts as in combination with the third pulse giving rise to the echo at $T - \tau$. Overlap of these echoes with the stimulated echo occurs when $T=\tau$ and $T=2\tau$ and these two-pulse signals may be superimposed on the three-pulse modulation pattern.

For a particular frequency to be detected several periods of modulation must be observed in the signal. Since the phase memory time of biological samples is very short, on the order of 0.1-2 μs,

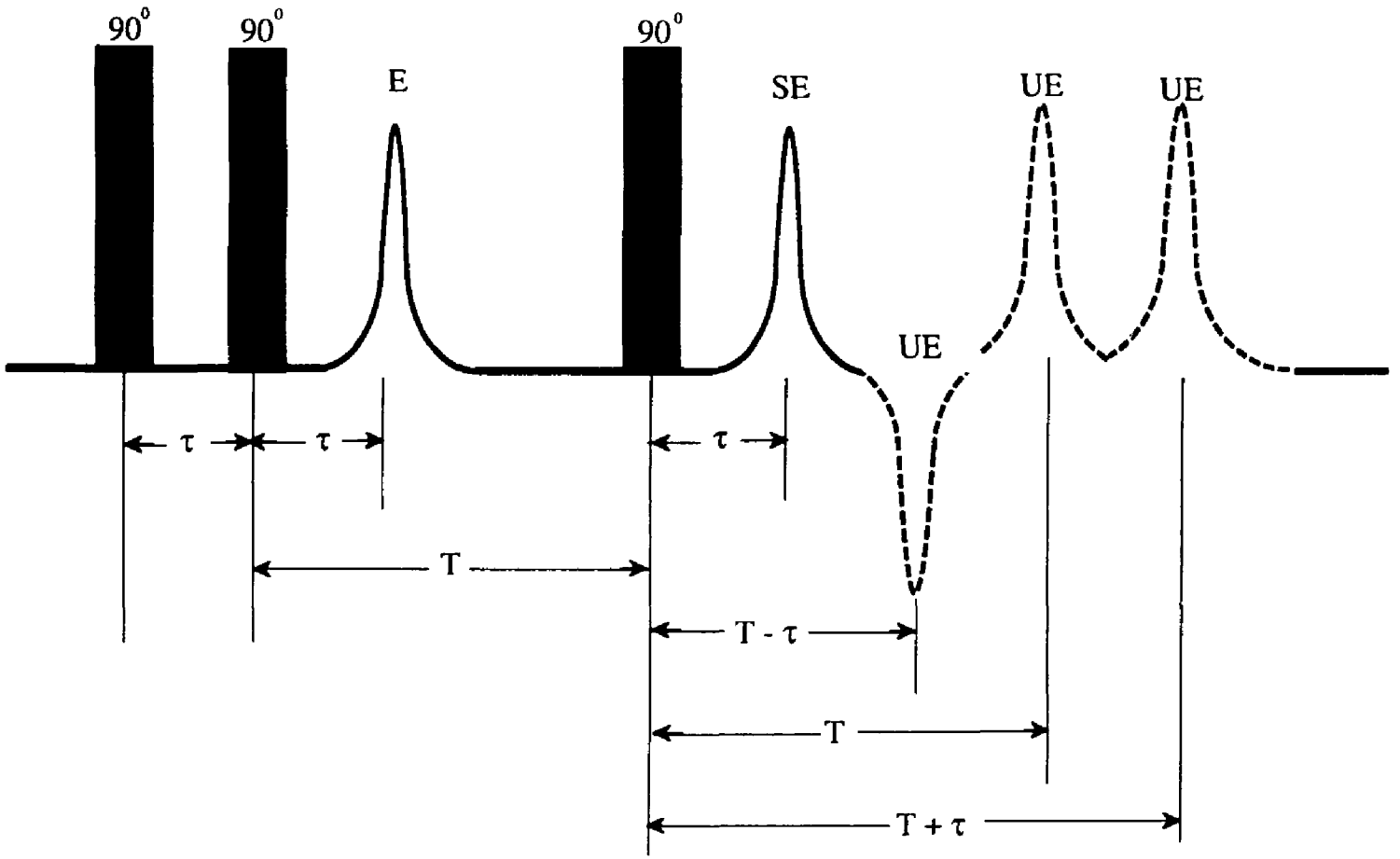

Figure 1.5 Detailed picture of a three pulse experiment showing all two pulse echoes.

ESEEM is usually run at liquid helium temperatures. The time limiting a three pulse experiment is usually longer than the phase memory time limiting the observation of a two pulse echo so a three pulse experiment has the advantage of a longer data acquisition time. Consequently, weaker interactions which die off slowly in the modulation pattern are best studied with a three pulse experiment. In contrast, the two pulse sequence is better for studying short range strongly coupled interactions which tend to decay quickly in the modulation pattern.

It is apparent from equation (1.6) for the three pulse experiment that if τ is set equal to an appropriate number of cycles of the frequency ω_a, then the $\sin^2(\omega_a\tau/2)$ term will equal zero and equation (1.6) will reduce to:

$$V_{mod}(2\tau+T,I=1/2) = 1- k[\sin^2(\omega_b\tau/2)\ \sin^2(\omega_a\ (\tau+T)/2)] \qquad (1.8)$$

Since T is the experimental time variable, only the ω_a modulation will appear in the envelope. Although equation (1.6) was developed for a particularly simple case and is rarely strictly true, this "tau suppression" effect is usually observed to some degree [14]. This can be experimentally useful in eliminating modulations due to nuclei such as protons which are numerous and may mask modulations due to other nuclei. Tau suppression can, in some cases, actually complicate a frequency spectrum since it may cause one broad line to appear as two distinct lines if a frequency in the middle is suppressed [15]. In general the choice of a two or three pulse experiment is governed by the particular system being studied and the specific information which

is sought. Ideally, one uses both pulse sequences to obtain information about both weakly and more strongly coupled nuclei. Any information which is duplicated by the two experiments is useful in verifying an analysis.

ENDOR Spectroscopy

In contrast with ESEEM, ENDOR spectroscopy is a well established technique; consequently, there are detailed discussions of the theory and instrument available so only a brief summary is included here [16,17]. The enormous potential of ENDOR as a structural probe in metalloproteins was first demonstrated in heme proteins by Feher and coworkers in the early 1970s [18,19]. The results have contributed to an enhanced understanding of metal coordination in proteins and have frequently clarified the nature of the ligands.

The main impact of ENDOR spectroscopy as compared to conventional EPR comes from the enhanced spectral resolution obtainable. ENDOR essentially has the linewidth of the homogeneous spin packets and can reduce orientation broadening. This increase in resolution is of the order of a thousand or more [16]. An additional enhancement of resolution come from the decrease in spectral density by hyperfine coupling of equivalent nuclei which is additive in ENDOR but increases the number of lines multiplicatively in EPR [20]. This is due to the different selection rules which govern the two spectroscopies. For allowed transitions in EPR, $\Delta m_S=1$, $\Delta m_I=0$ while for ENDOR $\Delta m_S=0$, $\Delta m_I= 1$. Other advantages of ENDOR come from the possibility of direct determination of the interacting nucleus via the nuclear g-factor, first-order contribution of nuclear quadrupole

interaction to the spectra which allows for analysis of quadrupole splitting, and the possibility of evaluation of the relative signs of hyperfine and quadrupolar interaction. ENDOR thus provides for a detailed analysis of spin density distribution in the transition metal-ligand complex.

The information obtained with ENDOR can frequently extend beyond the directly coordinated ligands by analysis of purely dipolar interactions of nuclei in the immediate environment of the complex. This coordination sphere can have a radius of 4-6 Å with a spatial resolution of about 0.5 Å [21]. ENDOR spectroscopy has the potential of being a very powerful structural probe of metal coordination in metalloproteins.

Like ESEEM, ENDOR observes a nuclear spin flip transition within an electron spin manifold; however, it is achieved in a very different manner. Consider the energy diagram of an S=1/2, I=1/2 system as discussed for the ESEEM. This was illustrated in Figure 1.4. In the permanent magnetic field there is a small spin population difference between levels 2 and 4 since the lower manifold represents a less energetic state. If the EPR transition is then saturated with a microwave frequency, the spin populations of the two states are equalized. One observes an EPR absorption signal only until the spin populations are equalized. While maintaining this saturation, in an ENDOR experiment, a second frequency (rf) is swept. When this frequency matches that of the NMR transition between levels 3 and 4, the populations of levels 2 and 4 are no longer equal and the net result is to produce an inequality in the spin populations of the two energy levels corresponding to the EPR transition. Consequently, one

observes an EPR absorption again. Thus ENDOR is really an EPR detected NMR experiment. The ENDOR lineshape and amplitude is affected by complicated relaxation mechanisms. For complex systems such as proteins knowledge of these mechanisms is at best empirical and, consequently, the principal information obtained from such an experiment is in the ENDOR frequencies, not in lineshape or amplitude.

As described above ENDOR requires saturation of both the NMR and EPR lines. The requirements for saturation are [22]:

$$\gamma_e{}^2H_1{}^2T_{1e}T_{2e} \geq 1 \qquad (1.9)$$

$$\gamma_n{}^2H_2{}^2T_{1n}T_{2n} \geq 1 \qquad (1.10)$$

where H_1 is the microwave magnetic field and H_2 is the rf field. T_1 and T_2 are the spin-lattice and spin-spin relaxation times and γ is the gyromagnetic ratio. Both sets of parameters are strongly temperature dependent. In transition metal complexes the relaxation times are very short at room temperature so the ENDOR is typically run below 30 K in order to see a signal. For nuclei of low magnetic moment (e.g. ^{13}C, ^{2}D, ^{14}N) the condition described in equation 1.10 is hard to achieve. However, the effective rf field at the nucleus is often enchanced significantly for nuclei which are strongly coupled to the electron spin [22]. Consequently, ENDOR spectra of nuclei with low magnetic moments can frequently be obtained.

There are several advantages of ENDOR over EPR. As mentioned, in EPR the number of lines increase multiplicatively with non-equivalent nuclei. This relationship is only additive in ENDOR.

Also in EPR quadrupole transitions are second order and are consequently hard to observe. Information on nuclear quadrupole interactions is normally obtained from NQR spectroscopy. In paramagnetic compounds however, this spectroscopy suffers from the short relaxation times and from poor sensitivity [23]. Thus ENDOR represents an alternative and very sensitive method to study quadrupole coupling of ligands in paramagnetic transition metal complexes.

The Limiting Cases

The first order equations for ENDOR (and ESEEM) spectra are typically given for two limiting cases, one in which $\nu_n > A/2$, the other $\nu_n < A/2$. In the first case, the spectrum observed is two lines separated by A and centered around ν_n. This situation is that typically observed for nuclei such as protons and others with weak hyperfine couplings and large nuclear precessional frequencies. The ENDOR spectrum for the second case is pictured in Figure 1.6 c). The two lines appear at $A/2 \pm \nu_n$. Nuclei that often fall in this category are ^{13}C and ^{15}N. Most ENDOR experiments have been performed at X-band (9.5 GHz) and these two cases are usually sufficient to describe them. If one considers a hypothetical experiment in which A/2 is made larger and larger then one would observe a two line spectrum in which the lower frequency line moves closer and closer to zero frequency. Eventually A/2 would become equal to ν_n. This is known as "exact cancellation" [24] and would result in the energy diagram shown in Figure 1.7 b) with the corresponding single line spectrum as shown in Figure 1.6 b). If one considers making A/2 still larger, a two peak spectrum centered around ν_n would result with the low frequency ν_n-

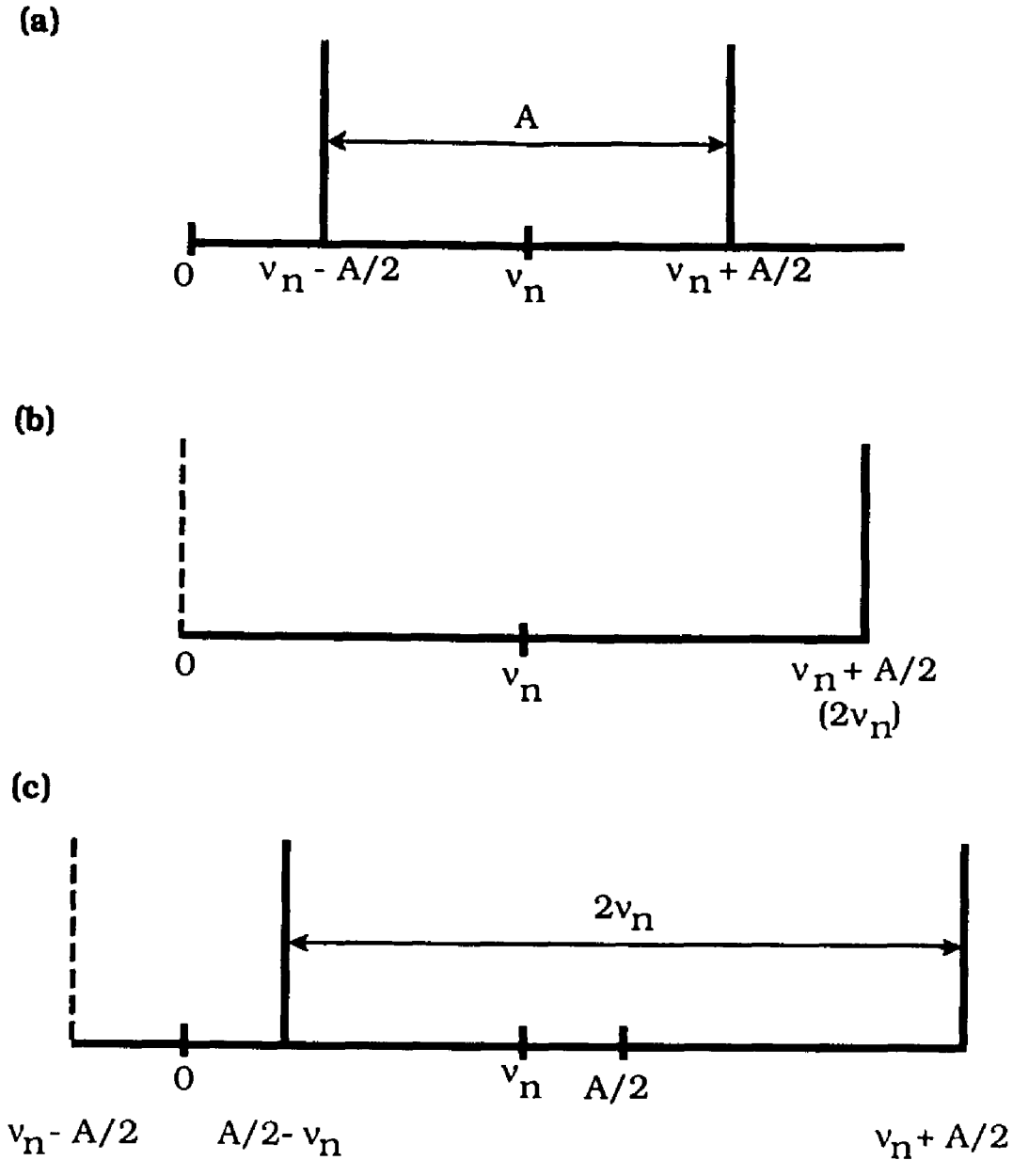

Figure 1.6 The three ENDOR (ESEEM) frequency spectra for the energy diagrams in Figure 1.7.

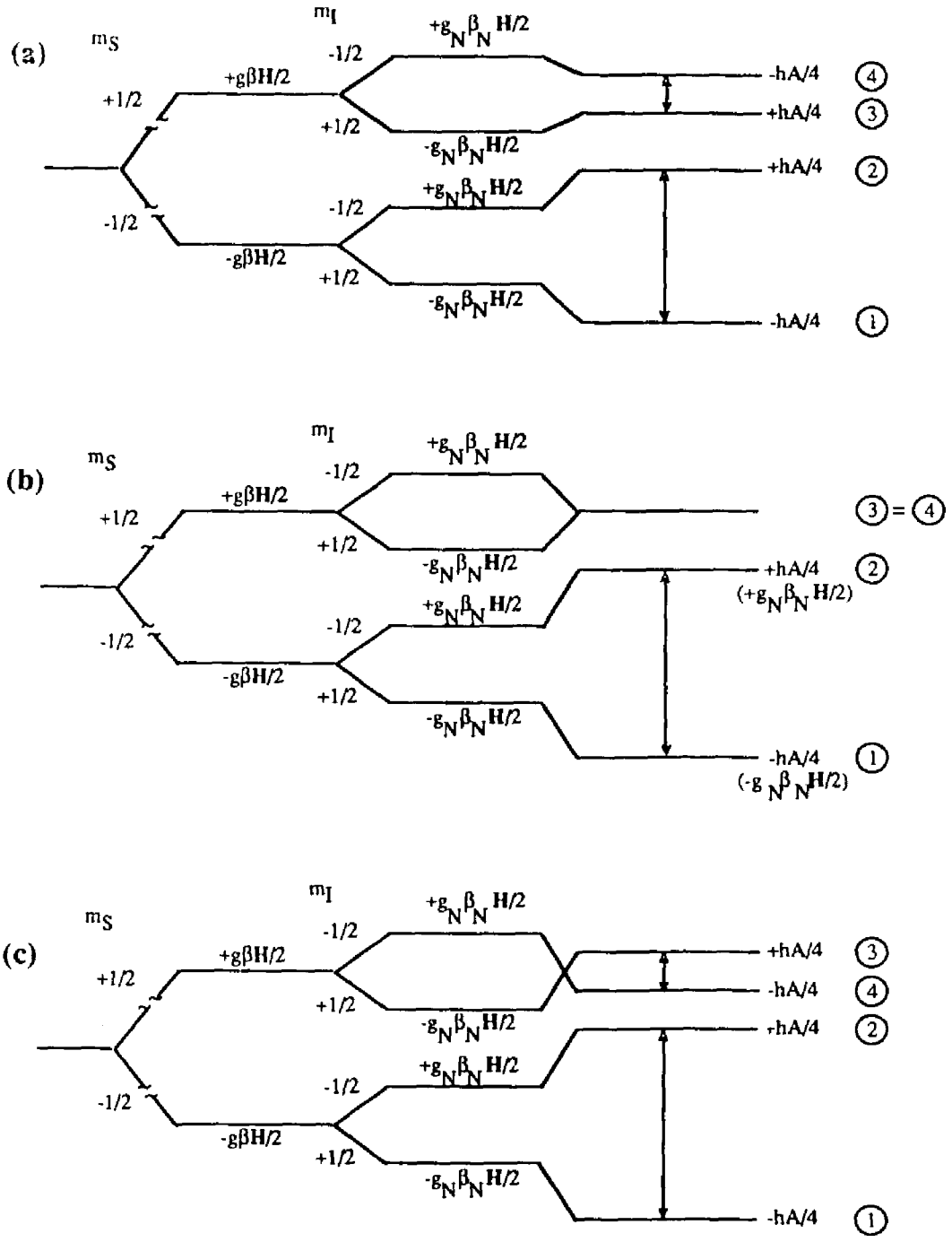

Figure 1.7 The energy diagrams for the cases (a) $A/2 < \nu_n$ (b) $A/2 = \nu_n$ (c) $A/2 > \nu_n$.

A/2 peak at some negative frequency as shown as a dotted line in Figure 1.6 c). The position of this "negative" peak is A/2 - ν_n. By looking at the energy diagram in Figure 1.7 c) one can see that at this point the energy levels corresponding to level 3 and 4 have crossed, thus the "negative" frequency peak is actually observed at the positive frequency A/2 - ν_n. The high frequency peak will continue to appear at A/2 + ν_n. This situation corresponds to the other limiting case of ν_n<A/2 with the two lines separated by twice the nuclear frequency and centered around A/2. The understanding of cases not falling within one of the two traditional limits is becoming increasingly important with the advent of ESE and ENDOR spectrometers operating at frequencies other than X-band. Since ν_n is dependent on spectrometer frequency, by varying frequency one can essentially choose the case, ν_n>A/2, ν_n<A/2, or exact cancellation, under which the system will be studied. This discussion has been limited to the very simple case of an isotropic system with one nucleus of I=1/2. In more complicated situations which result in multiple lines, the choice of spectrometer frequency can be exploited to cause exact cancellation of certain lines.

ESEEM Versus ENDOR

Although from the discussion so far there appears to be little difference in the information obtained from ESEEM and ENDOR the experimental differences give rise to distinctions. Occasionally information is duplicated, but usually the two techniques are complementary. ENDOR is better suited for studying proton interactions. As described in the section on ESEEM, observation of modulation depends on the ability to excite both allowed and

"forbidden" transitions with the pulse. Since the nuclear precessional frequency is large for a proton it is not often possible to cause this simultaneous excitation in ESE and consequently resolved proton interactions in ESE are rarely observed. Likewise, in a complex with large hyperfine coupling, the energy levels are far apart and simultaneous excitation is difficult. ENDOR is better suited for studying large hyperfine interactions.

ESEEM is the better technique at low frequencies and with weaker couplings since the saturation requirement of ENDOR is difficult to meet under such circumstances. As will be explained in the next chapter, in theory, ESEEM can be used to obtain quantitative information about the number of nuclei contributing to a signal for while ENDOR, due to the complex relaxation mechanisms controlling lineshape and intensity, can not. Additionally, ESEEM can provide information about the angular distribution of nuclei. By using a combination of two and three pulse ESEEM in conjunction with ENDOR one obtains a detailed picture of the coordination environment of the paramagnetic center.

Quadrupole

The discussion of ENDOR and ESEEM above was limited to the simple case of S=1/2, I=1/2. This describes nuclei such as ^{15}N, ^{1}H, ^{31}P and ^{13}C, but not others. A more complete Hamiltonian is necessary to describe a nucleus with $I \geq 1$ which has a quadrupole interaction. In addition to the terms in equation 1.2 this Hamiltonian for an axial case includes the term:

$$h\mathcal{Q}'(\hat{\vec{I}}_z - \hat{\vec{I}}/3) \qquad (1.11)$$

where $\mathcal{Q}' = e^2qQ/(4I(2I-1))$.

The parameter e represents the electronic charge, eq is the electric field gradient at the nucleus ($eq= V_{zz} =\delta^2V/\delta z^2$, where V is the electrostatic potential), and eQ is the nuclear quadrupole moment. The energy level diagram for this Hamiltonian is shown in Figure 1.8. The allowed transitions are shown as the bold solid lines. The forbidden transitions are shown as dotted lines. One would expect to observe four lines in the ESEEM or ENDOR of such as system. These would occur at

$$\nu=A/2 + \nu_n \pm \mathcal{Q}' \text{ and} \qquad (1.12)$$
$$\nu=A/2 - \nu_n \pm \mathcal{Q}'.$$

These four lines are often not observed experimentally. A detailed discussion of the effect of quadrupole on ESEEM spectra will be left until Chapter 4.

Transferrin

The system studied here by ESEEM and ENDOR is a cyanide adduct of transferrin. Transferrin is an iron protein of approximately 80,000 molecular weight which reversibly binds iron in the +3 oxidation state [25]. Serum transferrin is essential in the transport of iron from sites of storage and absorption in vertebrates while other transferrins serve a function in the defense against systemic infection by making it difficult for microorganisms to obtain iron.

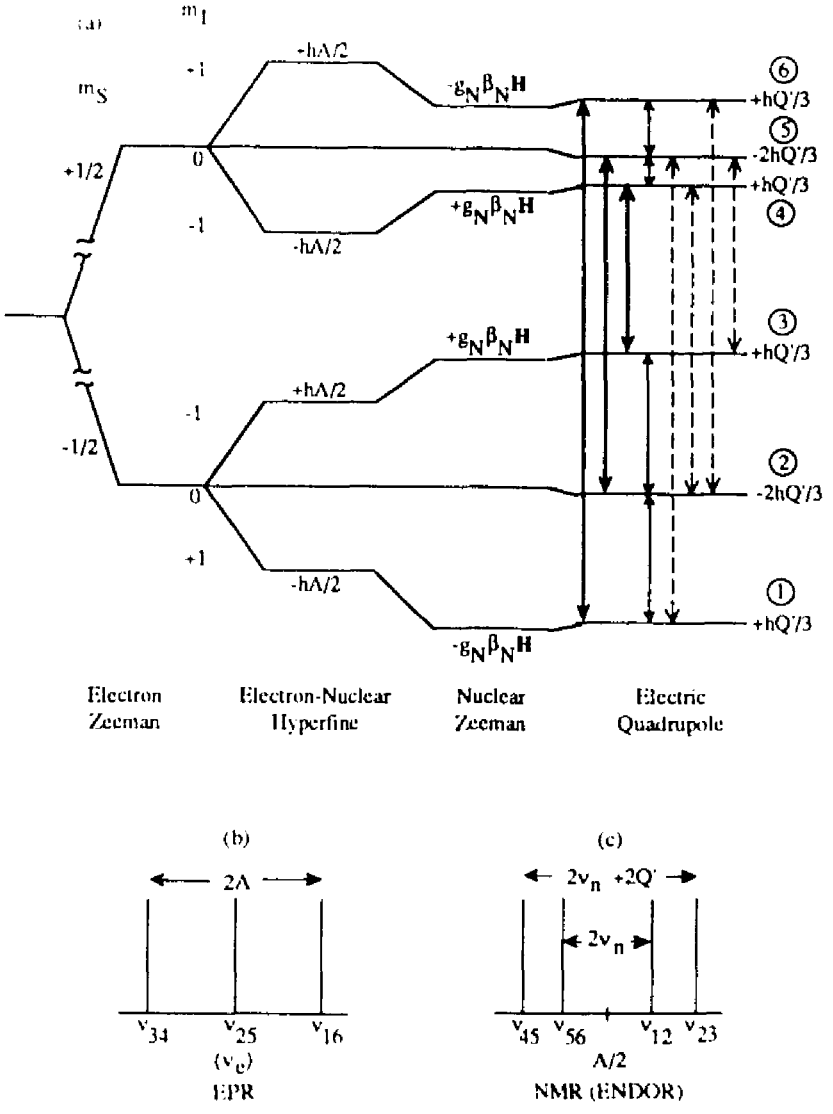

Figure 1.8 The energy diagram for I=1 nucleus. (a) Allowed EPR transitions are indicated by bold lines, NMR (ENDOR, ESEEM) lines by the solid lines, and EPR "forbidden" transitions by the dashed lines. (b) The corresponding EPR spectrum (c) The corresponding NMR (ENDOR, ESEEM) spectrum.

Transferrin consists of two lobes, N-terminal and C-terminal, which are essentially independent in nature. Each lobe contains one site which binds iron or other metals. Iron(III) binds to transferrin with an approximately octahedral crystal field of six coordinating ligands. The x-ray structure of lactoferrin has recently been published and the ligands are known to be two tyrosines, one histidine, and one aspartate [26,27]. The remaining two positions are filled by (bi)carbonate. Transferrin displays an EPR signal at g'=4.3 which is characteristic of high spin Fe(III) in a ligand environment of low symmetry.

Although the iron exchange mechanism of serum transferrin is not well understood, the role of anions is important. For instance, (bi)carbonate is required for metal binding [28]. Other anions such as chloride and perchlorate are known to affect the kinetics of iron exchange as well as the thermodynamic stability of the protein [29,30,31,32]. There are questions about the accessibility of exogenous anions to the metal center.

Since cyanide anion is kinetically inert and produces spectroscopically distinct low-spin complexes upon interaction with the high spin metal centers, it is a particularly useful probe of the accessibility to exogenous ligands of the coordination sites in metal-protein complexes. Its small size, the fact that it is a good ligand for iron(III), and the possibility of isotopic substitution of ^{13}CN and $C^{15}N$ for magnetic resonance studies are also advantages.

Although such low-spin cyanide complexes have been extensively investigated with hemoglobins and ferrihemes [33,34], it is only recently that a number of low-spin adducts of non-heme iron proteins

have been studied. In addition to the transferrin-cyanide adduct, protocatechuate 3,4 dioxygenase [35,36] and a number of model compounds which mimic the specific iron binding site of transferrin have been shown to form low-spin cyano complexes [37,38,39]. These complexes all display distinctive low-spin rhombic EPR spectra in the g=2 region. In transferrin, the binding of cyanide forms a low-spin adduct at only the C-terminal iron binding site. The characteristic g'=4.3 EPR signal is converted to a low-spin rhombic spectrum. Although the N-terminal site does not convert to low-spin, there are indications that this center is perturbed by the presence of cyanide as well [40]. The earlier work found that the reaction for the formation of the cyanide adduct in the C-terminal site is:

$$\text{Fe-Tf-}CO_3^{z} + 3CN^{-} \text{ ----------> Fe-Tf-}(CN)_3^{z-1} + CO_3^{=}$$

where the (bi)carbonate is displaced from the first coordination sphere of the Fe(III) by cyanide. Thus three cyanides are necessary to form the stable low-spin adduct. The structure shown in Figure 1.9 was proposed for the cyanide adduct although conclusive determination of the structure was not possible. Here the cyanide adduct of serum transferrin was investigated by ENDOR and ESEEM spectroscopy to obtain additional information about the ligand environment of iron.

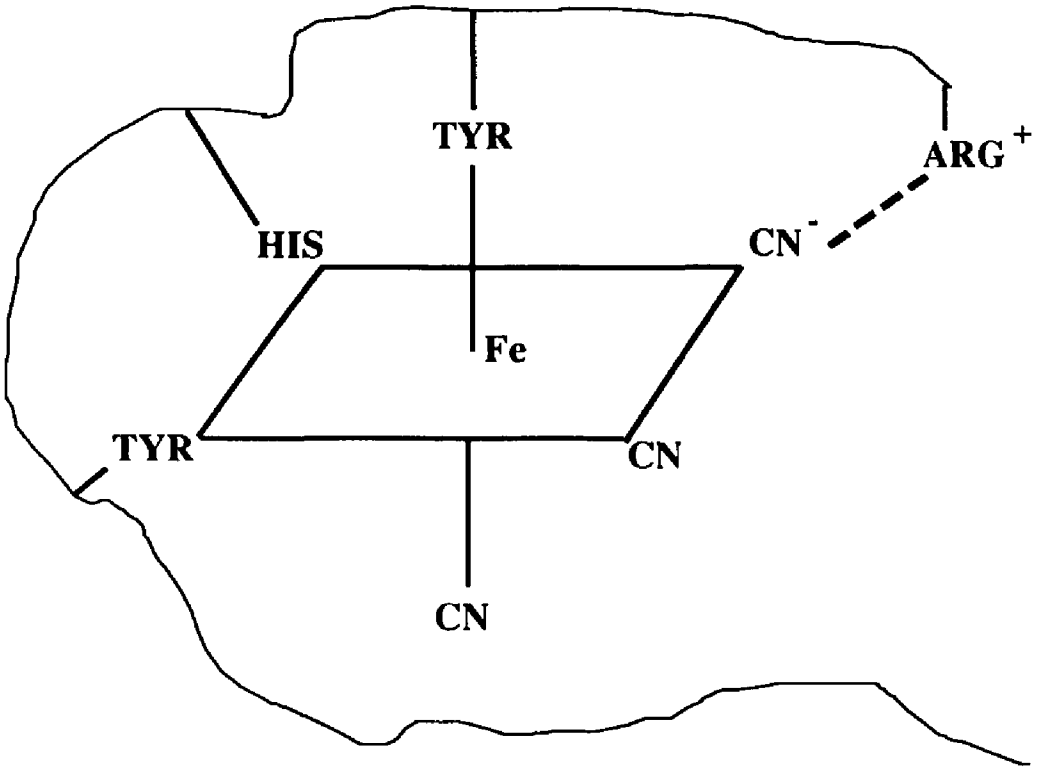

Figure 1.9 The structure proposed for the cyanide transferrin adduct [40].

CHAPTER 2

COMPUTER ANALYSIS AND SIMULATION

Introduction

One is rarely able to analyze an ESEEM or ENDOR spectrum with the first order equations given in Chapter 1. Computer simulation using either higher order perturbation equations or a full matrix calculation is usually a necessary step in understanding the spectrum and eliciting structural information. The general procedure is to analyze the data in terms of a geometric model with the ligand nuclei positioned at a specific locations relative to the unpaired electron. Overlap of the electron wavefunction with these nuclei produces an isotropic hyperfine coupling. A computer simulation is obtained by substituting the geometric and coupling parameters into the appropriate equations. The primary data for ESEEM is in the time domain and simulations can be calculated either in the time domain or in the frequency domain. Each has distinct advantages, as well as disadvantages, so it is useful to make use of both frequency and time simulations whenever possible.

ESEEM Analysis

Background Decay

The background in an ESEEM spectrum is the exponentially decaying envelope on which the modulation pattern is superimposed. Usually one is interested only in the modulation pattern. Background removal techniques are necessary since the decay, in general, is

complex and unknown [41, 42]. The time dependence of the echo sequence can be written as a combination of the signal decay and the modulation resulting from magnetic interactions [41]:

$$V_{echo}(t) = V_{decay}(t) \cdot V_{mod}(t) \qquad (2.1)$$

In the absence of interaction between unpaired electrons and neighboring nuclei with magnetic moments, the variation of the echo amplitude V_{decay} is expected from the Bloch equations to be a simple exponential decay

$$V_{decay}(t) = V_0 \exp(-t/T_m) \qquad (2.2)$$

where T_m is the phase memory time [41]. More than one exponential frequency component is usually required to simulate the decay function since the ring-down of the pulse in the cavity and other effects contribute to the background decay. Because of this fact, in most cases, one chooses not to simulate the decay signal explicitly, but instead to treat it as an empirical background. The assumption that all of the relaxation effects are found in V_{decay} is used in all simulations described in this work. Therefore any apparent decay in V_{mod} is assumed to result from destructive interference between the modulations produced by individual single crystal orientations. Most of the effort in ESEEM simulation has been focussed on the modulation function.

The program PREPARE is designed to remove the background decay from a data set. It uses a least squares procedure to fit a

polynomial of arbitrary order (specified by user) to the data points as shown by the line in Figure 2.1. The experimental data are then divided by the resulting background curve leaving just the modulation pattern (Figure 2.1 (b)). Selected frequencies within this pattern can be isolated by averaging points as shown in Figure 2.1 (c). The lower curve show the result of a ten point moving average. The higher frequency proton modulation has been removed by this procedure. If, on the other hand, the proton modulation is the modulation of interest, then the top curve can be divided by the bottom one, leaving just the proton modulation. This averaging procedure works well when the modulation pattern is comprised of several frequencies which are many megahertz apart.

Lin et al. proposed using the tau suppression effect to create a three pulse sequence spectrum where the envelope is not modulated [43]. By dividing the modulated envelope by the unmodulated one, the modulation pattern can then be isolated. The main drawback with this technique is that "tau suppression" only suppresses a single frequency. In some cases a single nucleus may give rise to several frequencies and in spectra where the modulation is due to more than one nucleus there are usually many frequencies. In these cases it is impossible to choose a tau that will suppress all the frequencies simultaneously. Consequently, this approach has found only limited application, mainly in studies of weakly coupled "matrix" nuclei.

Multiple Nuclei

If the modulation function is due to coupling with n nuclei, then

$$V_{mod} = (V_{mod1})\ (V_{mod2})\ (V_{mod3}) \ldots (V_{modn}), \qquad (2.3)$$

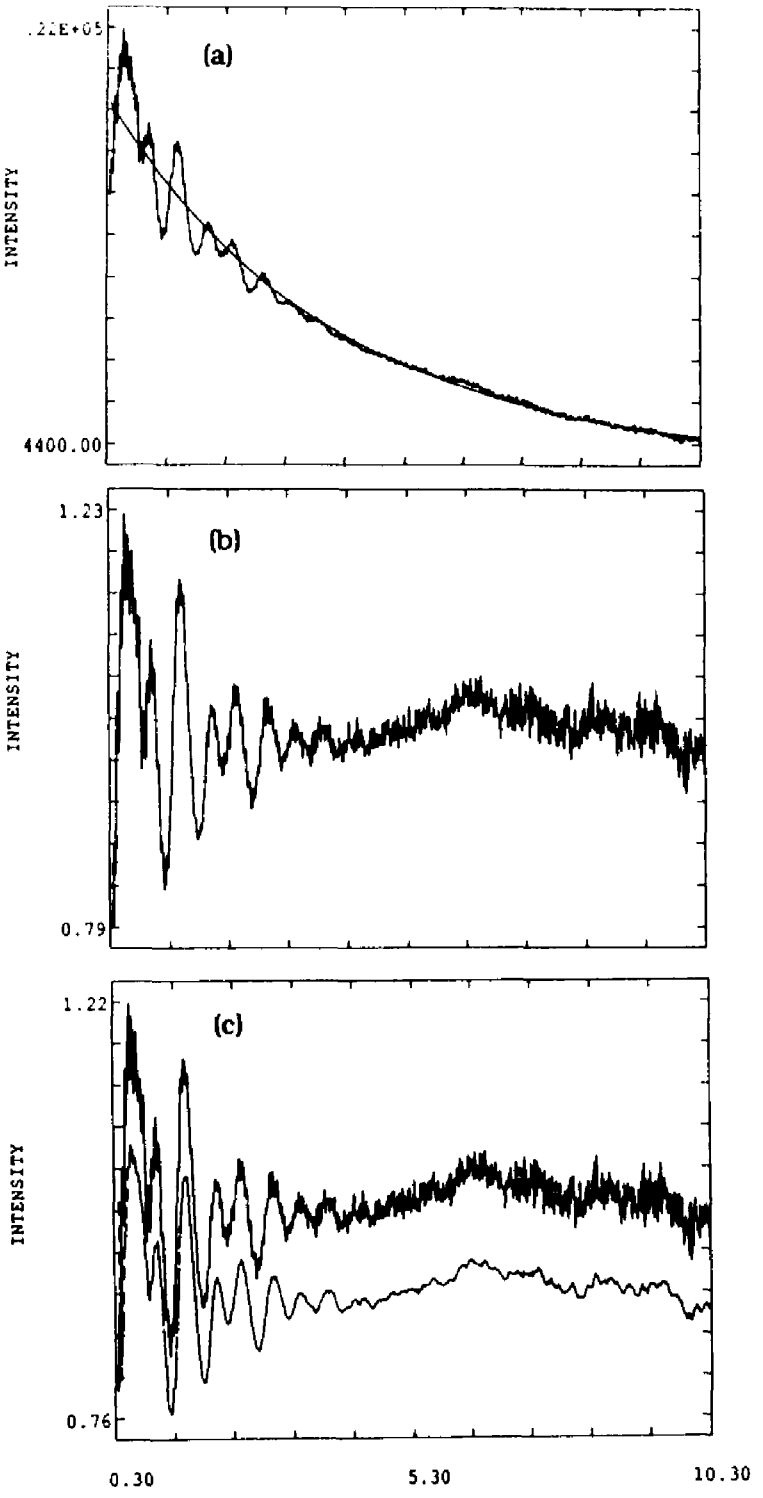

Figure 2.1 Illustration of the program PREPARE. (a) A polynomial is fitted by least squares to the data decay. (b) Division of data by polynomial leaves just the modulation pattern. (c) Frequencies can be isolated by averaging points. Data file SE4727.nip.

i.e. the overall modulation function is the product of the modulation functions for each nucleus considered separately [9]. The averaged ESEEM pattern from a polycrystalline or glassy sample is given by the angular integration of this modulation function with respect to the external magnetic field

$$\langle V(t)\rangle = \int\int (\Pi\, V_{mod,I}(\theta,\phi))\, \sin\theta\, d\theta\, d\phi \qquad (2.4)$$

where theta and phi are the polar and azimuthal angles describing the orientation of the external magnetic field with respect to the molecular coordinate system and $(\Pi\, V_{mod,I}(\theta,\phi))$ is the product of the individual modulation functions as in Equations 1.4 and 1.6 [41]. Mims [9], Kevan [41,44], and others have justified an approximation to Equation 2.4 which essentially reverses the order of the integration and product operations. In the approximation one first integrates over the magnetic field for each individual modulation function $V_{mod,I}(\theta,\phi)$ and then takes the product of the averaged modulation pattern for all the nuclei. This model is known as the spherical approximation and works reasonably well in cases where the electron-nuclear distance is greater than 4 Å. From this model it is possible to calculate an effective interaction distance for the closest shell of nuclei. The programs which perform this kind of calculation are ANDYI for nuclei of I=1/2, ANDYI1 for nuclei with I=1 and TPANDYI which calculates a two pulse modulation function [45]. All versions employ the spherical approximation and assume isotropic g-values. ESEEM spectroscopy typically observes weakly interacting nuclei so the spherical approximation is often valid. The spherical approximation has been

used extensively and successfully in estimating numbers of weakly interacting matrix nuclei [46-50], but cannot be applied in cases where the interaction distance is less than 4 Å [51]. To perform the integration in cases with a small interaction distance it is necessary to transform the local coordinate frame for each nucleus into a common laboratory axis system before calculating the modulation functions and taking their product .

Fourier Transformation of the Incomplete Time Waveform

From the form of the theoretical expressions for ESEEM modulation (Equations 1.4 and 1.6) it would appear that the ENDOR frequencies might be obtained straightforwardly by making a Fourier transform of the time series data. Some minor problems could arise at very low frequency on account of the phase memory decay, but these could be dealt with easily by removing the low frequency components before the data are transformed. The main difficulty however, is that the time waveform is incomplete at the low time end. After switching off the exciting pulse in a real spectrometer, the cavity ringing is usually so great that the receiver is overloaded for a certain period of time and cannot detect the weak echo signal. The cavity Q must be kept small enough for individual microwave pulses to decay before the electron echo has completely decayed, but this must be balanced against the need to maximize the signal-to-noise ratio which is best when Q is maximized. In the two pulse case, the missing portion of the data corresponds to the time during which the microwave transmitter signal after the second pulse decays to the noise level. This so-called "dead time" of the spectrometer can amount to 100-200 nsec which is substantial in a typical modulation spectrum lasting

only a few μsec. In the stimulated echo case the problem is worse since T, the time between the second and third pulse, cannot be less than zero [52]. Pulses two and three must be far enough apart so that they are discerned by the electron spin packets as two separate pulses. Thus the dead time of the three pulse sequence includes the entire time between the second pulse and observation of the echo (T + τ).

There are several possible approaches to the problem of transforming the incomplete time waveform. Since, by the nature of the Fourier transform, any point in the time domain affects all frequencies, any missing time data points will necessarily contaminate the transform. One could simply choose to ignore the missing points and Fourier transform the data without any preliminary processing. Unfortunately, the exponential decay results in a large peak with side lobes near zero frequency. The amplitudes of this peak and the side lobes usually exceed that of the resonance lines and consequently may hide lines with real ESEEM frequencies and small amplitudes. In addition, this method underestimates the amplitude of the ESEEM peaks which makes it inadequate for quantitative work. One way to lessen these problems is to smooth over the discontinuity at the start of the data by means of a function and another is to attempt to reconstruct the missing portion of the data. There is much to be gained by reconstructing the waveform in the dead time interval, provided that this can be done without generating spectral artifacts worse than those generated by using alternative procedures.

Questions as to whether all of the spectral features appearing in the transform of the reconstructed curve are implicit in the data or

whether certain of them have been introduced by the reconstruction procedure need to be considered carefully. Mims [53] developed an algorithm for a reconstruction procedure which has been written into the program FTBILL [54]. One initially creates a smoothing function for the missing data as shown in Figure 2.2 a) and then this function and the data are transformed. Although there are still some artifacts as shown in Figure 2.2 b) distinct frequencies are evident. These frequencies are used to recreate the missing portion of the modulation function as shown in Figure 2.2 c) and then this piece in combination with the data are transformed back to the frequency domain. The final result in shown in Figure 2.2 d). Unfortunately, it is possible to "create" peaks merely by the addition of this preliminary function. One must be very careful to check that the frequencies are really present in the data and have not been created by the choice of frequencies in the reconstructed dead time. There are several ways to do this. One can take a few points off the beginning of the time spectrum and repeat the transformation or one can choose a different smoothing function and compare the results. The best check, although it is the hardest to implement, is a comparison of the time domain simulation with the experimental data.

Recently there has been considerable interest in several least squares methods for analyzing ESEEM data. They are grouped under the general term LP (linear prediction) methods although several different algorithms have been used to solve the general problem (SVD-singular value determination [55,56,57], QRD- Householder triangulation decomposition [58,59]). Both SVD and QRD techniques use a least squares procedure to obtain estimates of the frequencies,

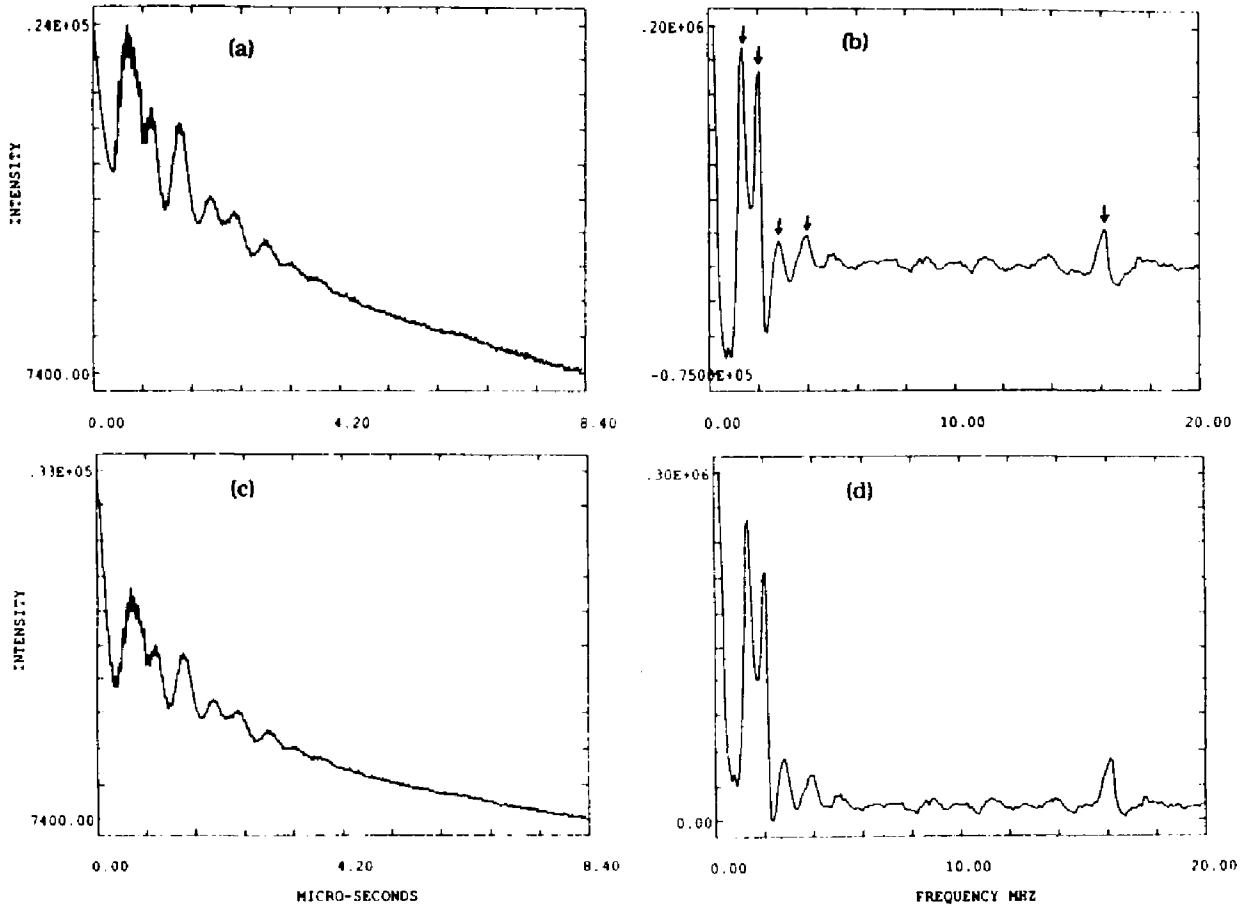

Figure 2.2 Illustration of the program FTBILL. (a) Data is extended to zero time by means of an exponential function. (b) Fourier transform of (a) with ESEEM frequencies marked with arrows. (c) Frequencies determined from (b) are used to recreate dead time modulation pattern. (d) Fourier transform of (c). Data file SE4727.nip.

decay rates, amplitudes, and phases of damped sinusoidal signals. The user does not have to make initial trial estimates of any sort or worry about removing the decay envelope which appears naturally as one or more zero-frequency exponential decays. If the frequency lines are Lorentzian then these techniques are insensitive to truncation at the beginning or end of the signal. The basic assumption of these techniques is that the time data can be described adequately by the sum of a series of exponentially damped sinusoids If this is true, then each point can be expressed as a linear combination of all previous points. These methods have a number of advantages including direct determination of phase, frequency, damping, and amplitudes and complete reconstruction of the missing time data since the equation which describes the data can be solved back to zero time. From a practical standpoint, these methods are particularly good at discerning low-amplitude frequencies and separating individual peaks with broad linewidths which may overlap.

However, there are also a number of disadvantages. The above methods are computationally slow and require much more computer memory than FFT. A very big drawback is the assumption that each point can be described as a linear combination of all previous points which is strictly true only for Lorentzian lines [60]. In the case of non-Lorentzian lines, just one peak may give rise to several frequencies with varying phases. In general, these methods are much too slow (QRD is somewhat faster than SVD, but still very slow compared with FFT) for analyzing more than a few spectra and are unreliable when samples have non-Lorentzian lines.

Quantitative Measurements Using ESEEM

An important advantage of ESE is that it can be used for quantitative measurements of the line intensities in the spectrum because the depth of modulation is exactly calculable from the spin Hamiltonian parameters and is independent of the apparatus settings (as long as H_1 is large enough). The main practical problem is that the echo envelope function cannot be recorded in its entirety due to the observational dead time following the microwave pulses. This gives rise to some uncertainty in the peak amplitudes.

Another problem is partial excitation [61]. If H_1 is not large enough to completely excite the observed transition then the intensity of the peaks is not described by the equations. Because the onset of partial excitation is subtle and modulations are still observed even when the transition is only partially excited, this problem is difficult to assess. Tau suppression can also distort line intensity although one can usually avoid this to some degree by taking three pulse data at several tau values. With detailed knowledge of the system, exact quantitative analysis is possible [62], but in the most general case ESEEM can only be used to estimate the number of nuclei. However, this is still an advantage over ENDOR which cannot be used for quantitative information at all.

Angle Selection

Introduction

The maximum possible spectroscopic information in ENDOR and ESEEM (as well as in continuous wave EPR) is obtained when it is possible to study the paramagnetic species in all orientations with respect to the applied magnetic field H_0. This is usually accomplished

by examining a sample which is magnetically diluted by introducing the paramagnetic molecule into a single-crystal host matrix. The problem of finding a suitable host and growing large crystals is often impossible with biochemical systems such as proteins. These systems are typically studied as magnetically dilute frozen solutions. Angle selection is a promising new way of obtaining single-crystal type spectra from a disordered frozen solution or powdered sample.

Rist and Hyde were the first to see the potential in powder pattern ENDOR [63,64]. They realized that the so-called "turning points" of an EPR spectrum corresponded to single molecular orientations. By taking ENDOR at these points one could obtain ENDOR due to pure "single crystal" orientations. There are a number of cases in which angle selection can be exploited [63]. These are:

1) One element of the hyperfine coupling tensor is large compared to the others and there is no g-anisotropy. Such cases include nitroxide radicals.

2) Anisotropy of the electron spin-spin interactions is large. This results in a triplet state spectrum dominated by the zero-field splitting. Examples of such cases include Mn^{2+} complexes and aromatic compounds in the triplet state.

3) Hyperfine and g-tensor interactions are of the same magnitude, but coincident. Examples of this include many copper and cobalt compounds [65].

4) Anisotropy of the g-tensor dominates. This is the case for the transferrin cyanide adduct.

The theory of angle selection will only be discussed in the context of case 4) although much of the development is similar for the other cases.

Orientation Selection

For randomly oriented samples, such as powders or frozen solutions, the continuous wave EPR spectrum consists of contributions from all possible individual single crystal molecular orientations with respect to the laboratory magnetic field direction. For anisotropic systems only specific orientations contribute to the intensity at a given magnetic field strength. Because the ENDOR or ESEEM experiment is performed at a fixed magnetic field within the continous wave EPR absorption spectrum, only a select group of orientations is observed during a particular measurement. The initial calculation for angle selection is to determine the molecular orientations that contribute to the EPR spectrum at a given field [66]. The spin Hamiltonian used to determine orientations is

$$\hat{\mathcal{H}} = \beta_e \vec{\mathbf{H}} \cdot \overleftrightarrow{\mathbf{g}} \cdot \hat{\mathbf{S}} + \hat{\mathbf{S}} \cdot \overleftrightarrow{\mathbf{A}} \cdot \hat{\mathbf{I}} \qquad (2.5)$$

where the parameters were defined in Chapter 1. Ligand hyperfine and quadrupole interactions are assumed not to contribute significantly to the overall angular dependence of the EPR powder pattern. The electron Zeeman interaction is the dominant energy term so it is convenient to use the coordinate system where the g-tensor is diagonal as a frame of reference. The applied magnetic field is considered a vector which assumes some specific orientation in the

g-axis system. Thus the projection of the magnetic field with respect to the g-axis system is

$$\vec{\mathbf{H}} = [\ \cos\phi\sin\theta \quad \sin\phi\sin\theta \quad \cos\theta\ ]\ H_0 \qquad (2.6)$$
$$= [\ h_x \quad h_y \quad h_z\ ]\ H_0$$

where ϕ and θ are defined in the g-axis system as shown in Figure 2.3. The Hamiltonian given in equation 2.5 thus becomes

$$\hat{\mathcal{H}} = \beta_e H_0\ (\hat{\mathbf{S}}_x g_x h_x + \hat{\mathbf{S}}_y g_y h_y + \hat{\mathbf{S}}_z g_z h_z) + \hat{\vec{\mathbf{S}}} \bullet \overleftrightarrow{\mathbf{A}} \bullet \hat{\vec{\mathbf{I}}} \qquad (2.7)$$

To sufficient accuracy for our purposes, the contributing orientations are those which satisfy the first-order resonance condition

$$H_r = [\ h\nu - M_I A(\phi,\theta)\ ] \ /\ \beta_e\ g(\phi,\theta) \qquad (2.8)$$

where

$$g(\theta,\phi) = [\ (g_{xx}\sin\theta\cos\phi)^2 + (g_{yy}\sin\theta\sin\phi)^2 + (g_{zz}\cos\theta)^2\ ]^{1/2} \qquad (2.9)$$

and

$$A(\theta,\phi) = [\ (A_{xx}g_xh_x + A_{yx}g_yh_y + A_{zx}g_zh_z)^2 + (A_{xy}g_xh_x + A_{yy}g_yh_y + A_{zy}g_zh_z)^2 + (A_{xz}g_xh_x + A_{yz}g_yh_y + A_{zz}g_zh_z)^2\ ]^{1/2} / g(\theta,\phi) \qquad (2.10)$$

Thus a specific magnetic field, $\vec{\mathbf{H}}$, within the EPR spectrum, will give a set of θs and ϕs for which Equation 2.8 is satisfied. The set of θs

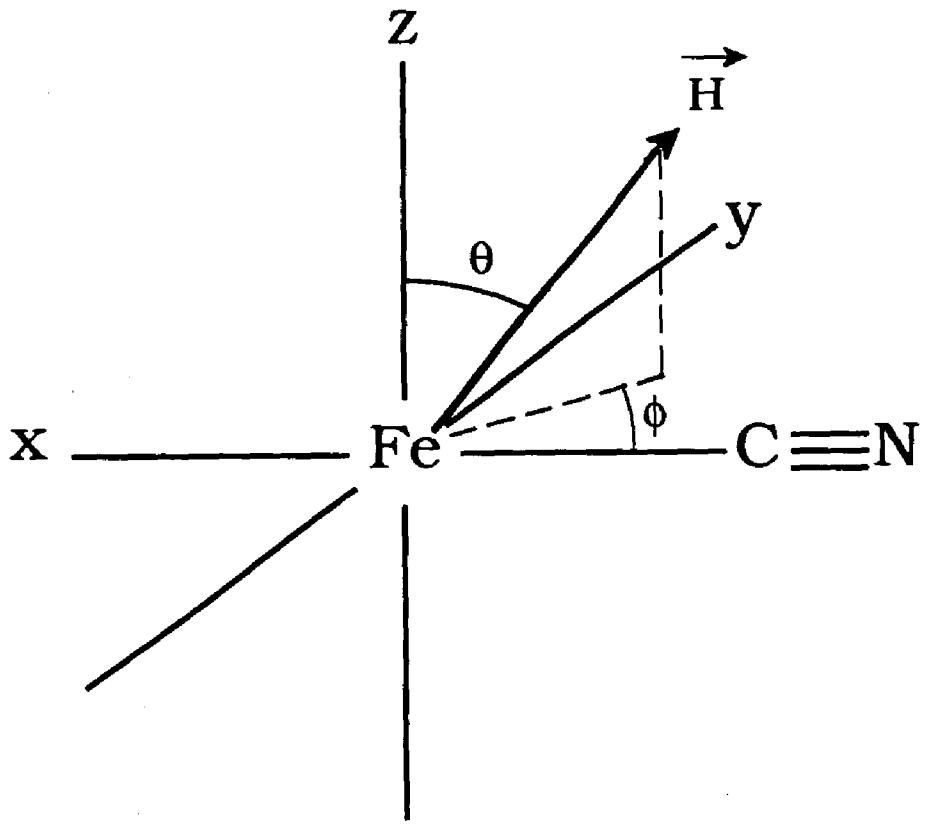

Figure 2.3 Definition of coordinates used in the derivation of angle selection equations.

and ϕs represents all orientations giving rise to the same g-value. The orientations determined from this calculation are then used to calculate the modulation function for ESEEM or frequency spectrum for ENDOR.

Since the iron nucleus in the transferrin cyanide adduct has I=0, there is no metal hyperfine interaction and the orientation selection is strictly due to the g-anisotropy. Equation 2.8 thus reduces to

$$H_r = [h\nu]/ \beta_e g(\phi,\theta). \qquad (2.11)$$

H_r and ν are determined from the experimental conditions, so for a specific experiment the values for phi and theta can be obtained from Equation 2.11. Figure 2.5 shows the phi and theta solutions to Equation 2.11 for the transferrin cyanide adduct at several magnetic fields which are labelled on the EPR spectrum in Figure 2.4. At fields close to g_x there is only a narrow range of theta and phi which cause resonance, along g_y a wide range of phis and thetas satisfy the equation, and along g_z there is only a small variation in the theta values for the entire phi range. These same results are shown on a unit sphere (only top half is shown) in Figure 2.6 where the allowed orientations for specific g-values are shown with curves (or pairs of curves for the case of A and B) of constant g. Each line represents all sets of theta and phi which satisfy Equation 2.11 for a particular g-value.

ENDOR and ESEEM Simulation

As described above, the magnetic field "selects" orientations. One must now figure out what the corresponding ENDOR (or ESEEM)

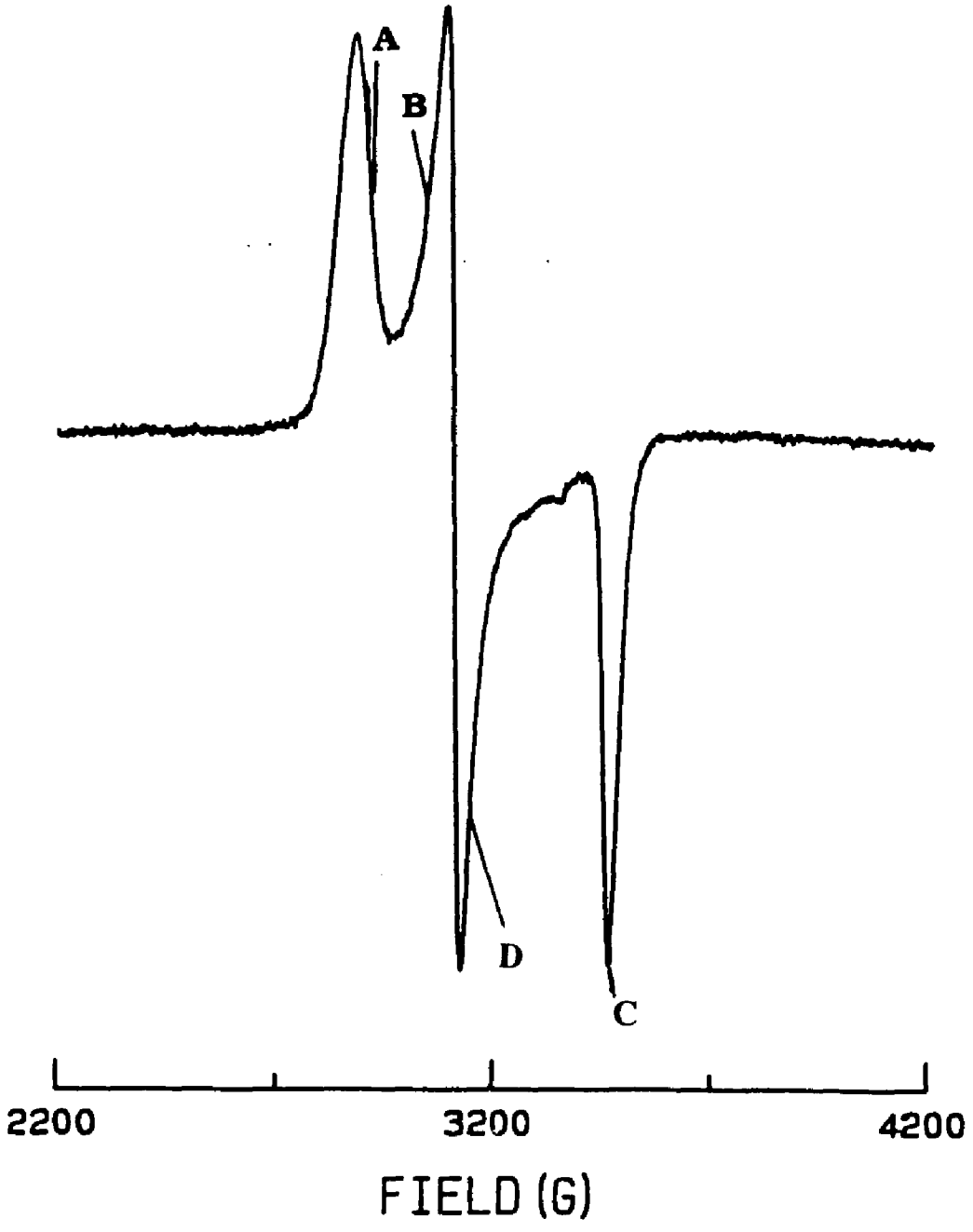

Figure 2.4 The X-band EPR spectrum of the g=2 region of the cyanide-transferrin adduct [39]. Experimental conditions: temperature 77 K, .58 mM protein, time constant 1 s., modulation amplitude 1.25 G, power 20 mW, frequency 9.36 GHz.

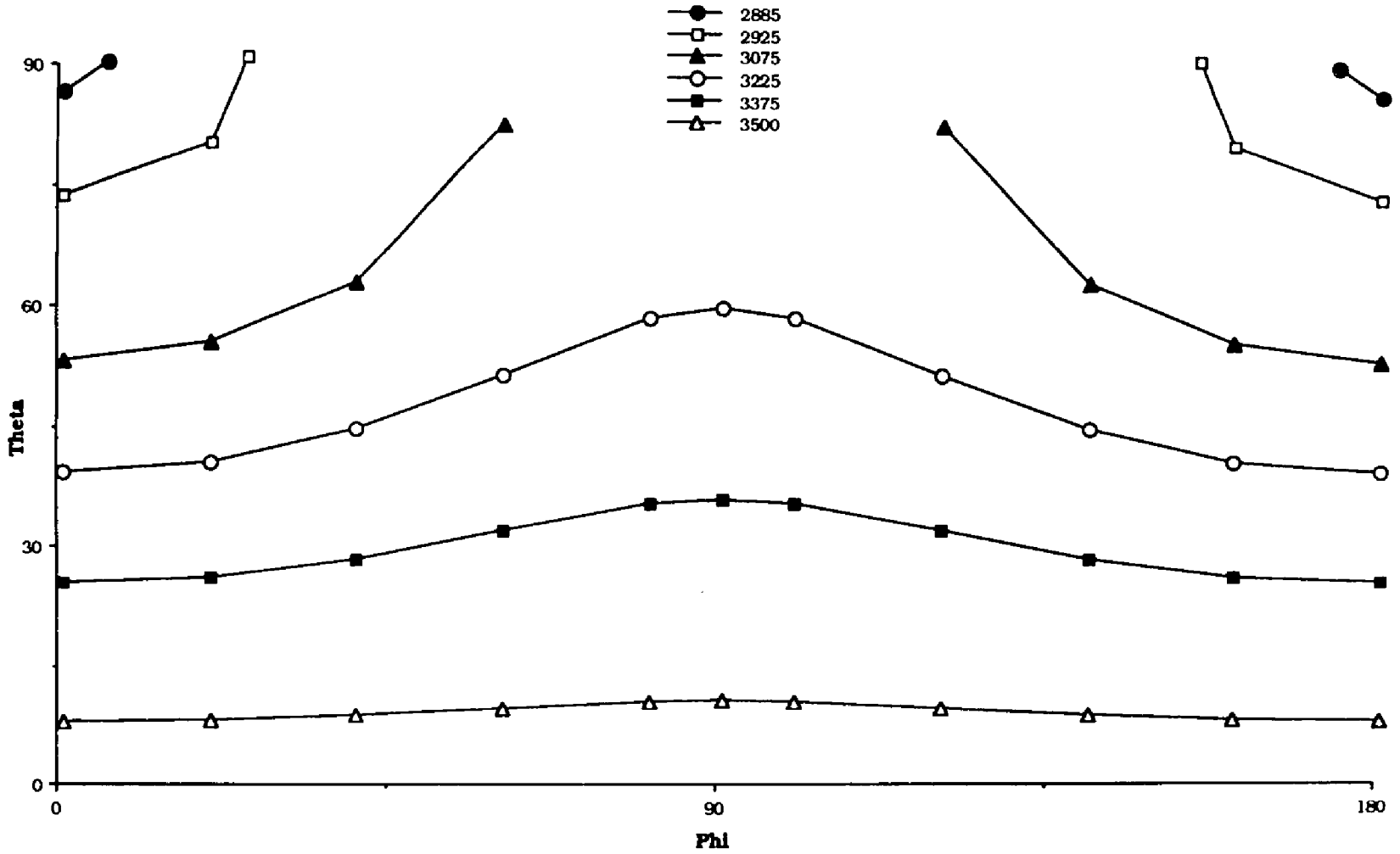

Figure 2.5 Solutions of equation 2.11 shown for various magnetic fields ranging from approximately g_x (2885 G) to approximately g_z (3500 G). Microwave frequency is 9.44 GHz.

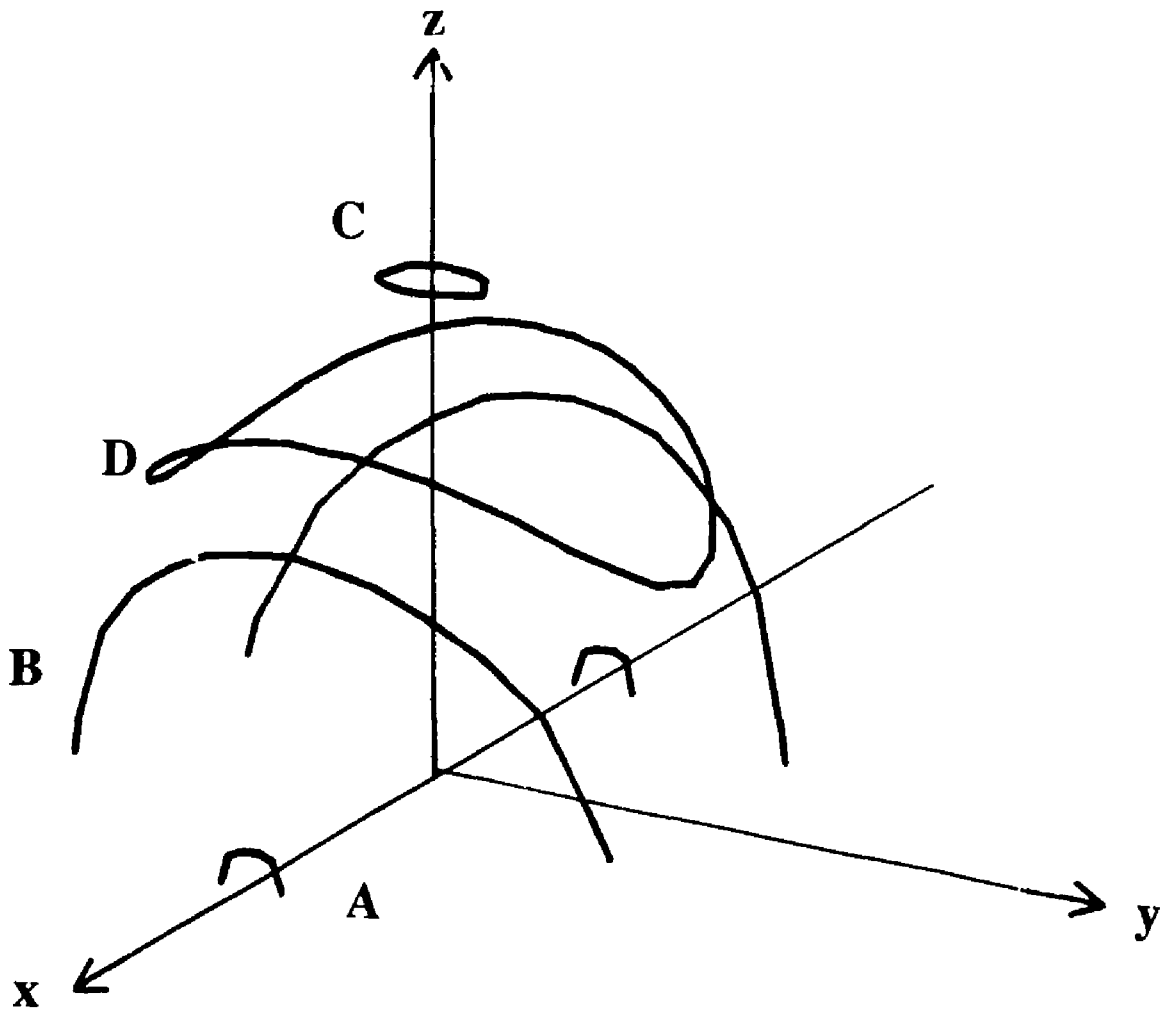

Figure 2.6 Unit sphere (only top half is shown) with curves (or pairs of curves for the case of A and B) of constant g. Each line represents all sets of theta and phi which satisfy equation 2.11. Field is 2925 G for A, 3075 G for B, 3500 G for C and 3225 G for D as indicated in Figure 2.4. Microwave frequency is 9.44 GHz.

transition frequency is from these orientations. Since ENDOR is essentially a nuclear resonance spectrum, one must determine the total field at a given nucleus in order to calculate the transition frequency. The Hamiltonian:

$$\hat{\mathcal{H}} = \hat{\vec{S}} \cdot \overleftrightarrow{A} \cdot \hat{\vec{I}} - g_n\beta_n\vec{H} \cdot \hat{\vec{I}} \qquad (2.12)$$

describes the spin 1/2 ligand nuclear energies in an S=1/2 metal complex. The problem is to describe the system with two independent axis systems so that the Hamiltonian is diagonalized. $\hat{\vec{S}} \cdot \overleftrightarrow{A}$ is a vector, so $\hat{\vec{S}} \cdot \overleftrightarrow{A} \cdot \hat{\vec{I}}$ can be rewritten as an inner product of the vector $\hat{\vec{S}} \cdot \overleftrightarrow{A}$ with the vector $\hat{\vec{I}}$ [67] and Equation 2.12 becomes

$$\hat{\mathcal{H}} = (\hat{\vec{S}} \cdot \overleftrightarrow{A})_x\hat{I}_x + (\hat{\vec{S}} \cdot \overleftrightarrow{A})_y\hat{I}_y + (\hat{\vec{S}} \cdot \overleftrightarrow{A})_z\hat{I}_z - g_n\beta_nH_0h_x\hat{I}_x$$
$$\hat{\mathcal{H}} = (\hat{\vec{S}} \cdot \overleftrightarrow{A})_x\hat{I}_x + (\hat{\vec{S}} \cdot \overleftrightarrow{A})_y\hat{I}_y + (\hat{\vec{S}} \cdot \overleftrightarrow{A})_z\hat{I}_z - g_n\beta_nH_0h_x\hat{I}_x$$
$$- g_n\beta_nH_0h_y\hat{I}_y - g_n\beta_nH_0h_z\hat{I}_z \qquad (2.13)$$

where $\vec{H}$ was defined in equation 2.6. The notation x,y,z refers to the axes in the diagonal electron g tensor axis system. Equation 2.13 can be rewritten as

$$= [\,(\hat{\vec{S}} \cdot \overleftrightarrow{A})_x - g_n\beta_nH_0h_x\,]\,\hat{I}_x + [\,(\hat{\vec{S}} \cdot \overleftrightarrow{A})_y - g_n\beta_nH_0h_y\,]\,\hat{I}_y$$
$$+ [\,(\hat{\vec{S}} \cdot \overleftrightarrow{A})_z - g_n\beta_nH_0h_z\,]\,\hat{I}_z. \qquad (2.14)$$

In some other coordinate system (x', y', z'), the mathematical description of the nuclear spin energy levels is a scalar expression

$$K(m_S)I_{z'} = K(m_S)\, M_I$$

where:

$$K(m_S)= [\, [\, (\hat{\vec{S}} \bullet \overleftrightarrow{A})_x - g_n\beta_n H_0 h_x \,]^2 + [\, (\hat{\vec{S}} \bullet \overleftrightarrow{A})_y - g_n\beta_n H_0 h_y \,]^2 +$$

$$[\, (\hat{\vec{S}} \bullet \overleftrightarrow{A})_z - g_n\beta_n H_0 h_z \,]^2 \,]^{1/2} \qquad (2.15)$$

The electron spin vector $\vec{S}$ is dependent on the g tensor and the field direction and is not necessarily aligned with the magnetic field. The expression for the electron spin is

$$\vec{S} = m_S/g(\theta,\phi)\, [\, g_x\cos\phi\sin\theta \quad g_y\sin\phi\sin\theta \quad g_z\cos\theta \,]. \qquad (2.16)$$

The matrix $\overleftrightarrow{A}$ is the sum of a dipolar term and the isotropic hyperfine interaction. Since most of the unpaired electron spin density is on the metal, the Fermi contact term is small. The electron is assumed to be a point dipole on the metal atom in the g-coordinate system. The Hamiltonian describing the dipole-dipole interaction of an electron and a nucleus is given by

$$\hat{\mathcal{H}}_d = -\beta_e\beta_n g_n/r^3 \;\; \hat{\vec{S}} \bullet \overleftrightarrow{g}(3\vec{r}\bullet\hat{\vec{I}} \bullet\vec{r} - \hat{\vec{I}})$$

$$= -\beta_e\beta_n g_n/r^3 \;\; \hat{\vec{S}} \bullet\overleftrightarrow{g}\bullet\overleftrightarrow{A}_d \qquad (2.17)$$

where r is the distance from the electron to the nucleus, $\vec{r}$ is a unit vector pointing in the direction of the vector from the electron to the nucleus. When $\vec{r}$ is expressed in the g diagonal reference frame and the nuclear coordinates are expressed in terms of θ_N and ϕ_N as shown in Figure 2.3 then $\overleftrightarrow{A}_d$ is given by

$$\frac{-\beta_e\beta_n g_n}{hr^3}\begin{pmatrix} g_{xx}((3\cos\phi_N\sin\theta_N)^2-1) & 3g_{xx}\cos\phi_N\sin^2\theta_N\sin\phi_N & 3g_{xx}\cos\phi_N\sin\phi_N\cos\theta_N \\ 3g_{yy}\cos\phi_N\sin^2\theta_N\sin\phi_N & g_{yy}((3\sin\phi_N\sin\theta_N)^2-1) & 3g_{yy}\sin\phi_N\sin\theta_N\cos\theta_N \\ 3g_{zz}\cos\phi_N\sin\phi_N\cos\theta_N & 3g_{zz}\sin\phi_N\sin\theta_N\cos\theta_N & g_{zz}((3\cos\theta_N)^2-1) \end{pmatrix} \tag{2.18}$$

Using these expressions and converting from energy to frequency units yields a final expression for the frequency of the ENDOR transitions.

$$\begin{aligned} \nu_{endor} = [\ & (m_S/g(\theta,\phi)((A_{xx}+A_{iso})g_xh_x + A_{yx}g_yh_y + A_{zx}g_zh_z) - h_x\nu_0)^2 + \\ & (m_S/g(\theta,\phi)(A_{xy}g_xh_x + (A_{yy}+A_{iso})g_yh_y + A_{zy}g_zh_z) - h_y\nu_0)^2 + \\ & (m_S/g(\theta,\phi)(A_{xz}g_xh_x + A_{yz}g_yh_y + (A_{zz}+A_{iso})g_zh_z) - h_z\nu_0)^2\ ]^{1/2} \end{aligned} \tag{2.19}$$

where $\nu_0 = g_N\beta_N H_0/h$ and the A_{ij} (i,j=x,y,z) are the elements of the dipole tensor in Equation 2.18. If one considers the specific case in which $\hat{S}$ is quantized along the field direction (which is assigned to the z-axis). then Equation 2.12 becomes

$$\hat{\mathcal{H}} = \hat{\vec{S}}_z (A_{zx}\hat{I}_x + A_{yz}\hat{I}_y + (A_{zz}+A_{iso})\hat{I}_z) - g_n\beta_n\vec{H} \bullet \hat{\vec{I}} . \quad (2.20)$$

where the elements of A are those assigned above in Equation 2.18. If the nucleus is also quantized in the same direction then Equation 2.20 is simplified to

$$\hat{\mathcal{H}} = \hat{\vec{S}}_z (A_{zz}+A_{iso})\hat{I}_z - g_n\beta_n H_0 \hat{I}_z \quad (2.21)$$

From Equation 2.18, A_{zz} is

$$\frac{-\beta e\beta n g n g_{zz}}{hr^3} ((3\cos\theta)^2 - 1) \quad (2.22)$$

where θ is angle between the magnetic field (which is also the $\hat{\vec{S}}$ and $\hat{\vec{I}}$ quantization axis) and the vector from the electron to the nucleus. This simplifies the equation for the ENDOR transitions to the often used formula

$$\nu_{endor} = m_s \left[\left(\frac{-\beta e\beta n g n g_{zz}}{hr^3} ((3\cos\theta)^2 - 1) \right) + A_{iso} \right] - \nu_0 . \quad (2.23)$$

This formula is accurate only when $\hat{\vec{S}}$ and $\hat{\vec{I}}$ are both quantized along the magnetic field which is generally not strictly true.

The Simulation Program

The program ANGSEL [68] has been written as an ENDOR and ESEEM simulation program employing angle selection. The adjustable parameters are A_{iso}, the distance r, and the angles which specify the the coordinates of the ligand nucleus in the principal axis system of the g-matrix. For cases in which there is metal nuclear hyperfine coupling the program iteratively searches through theta and phi by use of a parabolic search algorithm [66]. Otherwise, it steps through phi solving for theta values which satisfy Equation 2.11. To reduce calculation time, weaker interaction such as those due to metal quadrupole and ligand hyperfine interactions, are treated by applying a lineshape function to the ESE modulation pattern or ENDOR spectrum rather than including them specifically in the orientation selection process. The number of orientations is chosen to minimize calculation time without introducing distortions. The ENDOR frequencies for each theta-phi orientation are then calculated as described above. For an ENDOR simulation these calculated frequencies can be directly converted to an ENDOR spectrum by the means of the program ENCOUNT. For the ESEEM time domain, the modulation functions are obtained through the density matrix formalism developed by Mims [9,10] and applied by Reijerse and Keijzers [68,69] to give equations written as functions of the ENDOR frequencies.

CHAPTER 3

ENDOR SPECTROSCOPY OF THE TRANSFERRIN-CYANIDE ADDUCT

Introduction

The general theory of setting the external field $\vec{H}$ within the EPR envelope of a polycrystalline sample to obtain ENDOR spectra corresponding to particular orientations has been discussed extensively in Chapter 2. The samples employed in this study are frozen solutions and thus contain a random distribution of all protein orientations. Since rf irradiation at any field within the EPR spectrum allows one to select a distinct group of limited molecular orientations, the anisotropy in the EPR spectrum can be exploited to obtain a series of ENDOR spectra, each representing a different subset of molecular orientations. With the exception of the recent pioneering work by Hoffman and coworkers, applications of angle selected ENDOR to proteins have been limited and have not generally made full use of the angular selection information available in an anisotropic EPR spectrum [71,72]. Here the use of such information is illustrated by preforming a detailed analysis of "off axis" powder type ENDOR spectra of the cyanide adduct to obtain structural information about the iron center in transferrin.

Experimental

The details of the preparation of the cyanide adduct of transferrin are given elsewhere [40]. Isotopes were obtained from Icon Services, the ^{13}C isotope as $Na^{13}CN$ in 91.5% purity and the ^{15}N isotope as $NaC^{15}N$ in 99.0% purity. The protein concentration was 1

mM with a cyanide concentration of 0.5 M. Samples were run in 4 mm OD, 3 mm ID quartz tubes.

ENDOR spectra were recorded by Dr. Hans van Willigen at the University of Massachusetts at Boston on a Varian E-9 X-band spectrometer equipped with a home-built ENDOR accessory [73,74]. Temperatures from 6-8 K were obtained with an Oxford instruments ESR9 helium cryostat. Typical spectra were recorded at 6K, using 2 mW microwave power, approximately 200 W rf power, and frequency modulation of 10 KHz. A frequency counter was used to measure the EPR spectrometer frequency and the free precessional frequency of protons from the matrix proton ENDOR signal was used to calibrate the magnetic field.

Nitrogen and Iron ENDOR

There are several nitrogen nuclei which could contribute to the ENDOR signal. In addition to the signals from cyanide nitrogen(s), nitrogen ENDOR signals are possible from both the directly coordinated imidazole nitrogen and the remote δ-nitrogen of histidine if histidine remains bound in the low-spin complex. Although the resonances were very weak, an ^{15}N coupling of 5.25 MHz was resolved in a study of C^{15}N adducts of hemoproteins [75]. A coupling of similar magnitude would be expected for the transferrin-cyanide adduct since the cyanide is also bonded through carbon in this case. Since the free precessional frequency for ^{15}N is 0.95 MHz at the electron g-value for the spectra in Figure 3.1, a coupling of approximately 5 MHz would would result in ^{15}N peaks around 1.6 and 3.5 MHz, separated by twice the free precessional frequency (the case illustrated in Figure 1.6 (c)). As can be seen from Figure 3.1 there is little difference between the

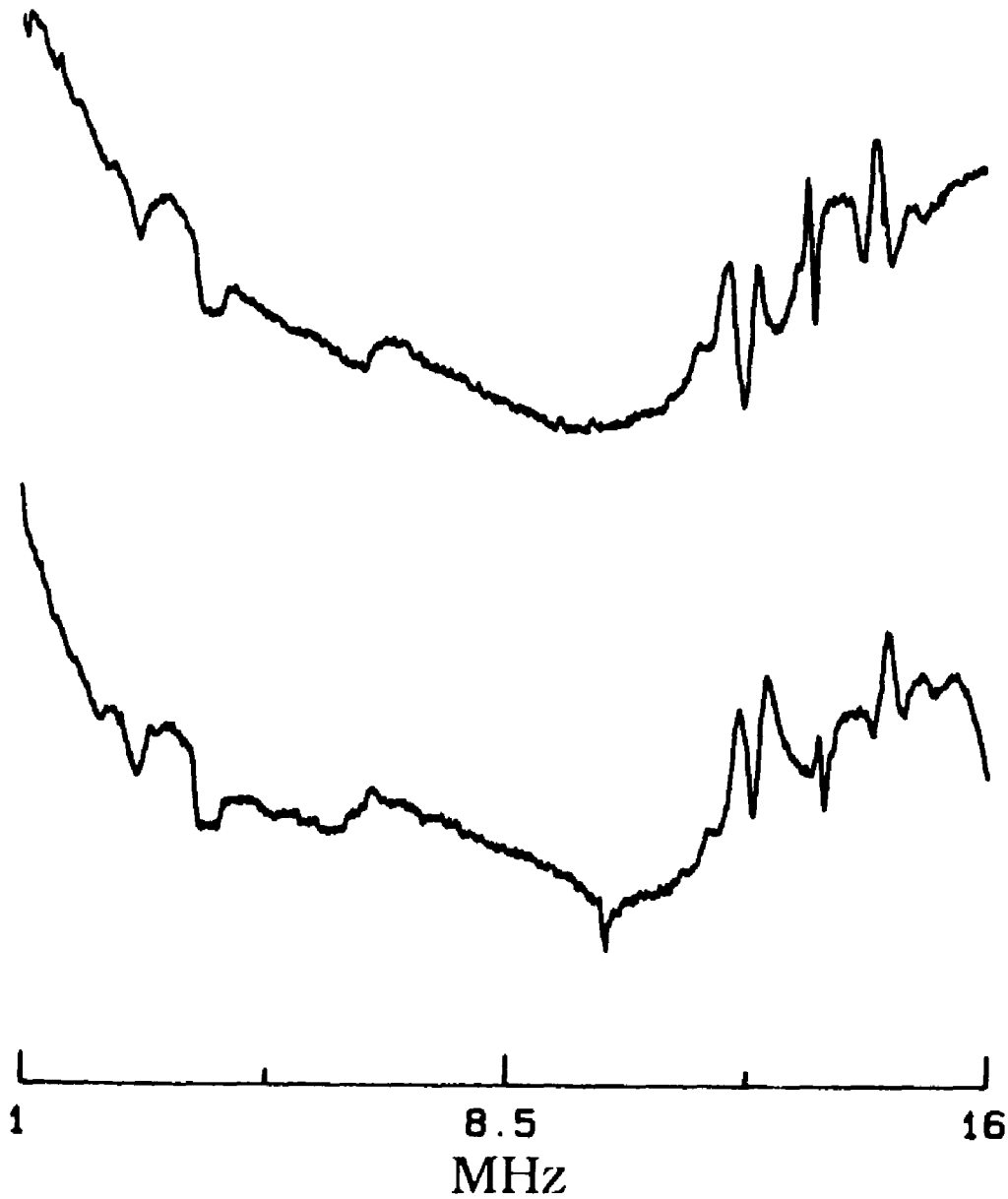

Figure 3.1 (a) ENDOR of isotopically substituted $C^{15}N$ transferrin adduct. (b) ENDOR with ^{14}N. Temperature 8 K, center rf frequency 18 MHz, sweep width 15 MHz, microwave frequency 9.44 GHz, microwave power 2 mW, rf power 200 W., and frequency of 10 KHz.

spectrum with $C^{14}N^-$ and the ^{15}N substituted isotope. Thus there is no firm evidence of ^{15}N signals from the CN^- anion. There are weak signals present in the 1-5 MHz range which are probably due to nitrogen, but these are hard to interpret because of poor signal to noise and rf interference. Since both ^{14}N and ^{15}N have small Zeeman frequencies at the magnetic fields studied, nitrogen signals in this region would correspond to small hyperfine couplings. ^{14}N couplings due to the metal coordinated imidazole nitrogen in histidine are typically quite large and are sometimes even resolved in the EPR spectrum [76]. There is no evidence in these ENDOR spectra of a large ^{14}N coupling. However, the experimental spectra in Figure 3.1 are rather noisy, and, since complicated relaxation mechanisms control line intensity in ENDOR, the lack of a given set of ENDOR peaks can not be considered proof of the absence of a particular ligand.

There was no evidence of ^{57}Fe signals in the frequency range from 1-37 MHz. However, it is possible that the hyperfine tensor is very anisotropic which would cause very broad signals that are hard to detect. ^{57}Fe ENDOR signals have been observed in only a few iron proteins [77-79].

Proton ENDOR

ENDOR resonances are observed from both matrix and weakly coupled protons. Figure 3.2 shows the proton region in spectra taken at the three principal g-values. The proton nuclear Zeeman frequency is large compared to the hyperfine coupling so the coupling can be analyzed by the equation:

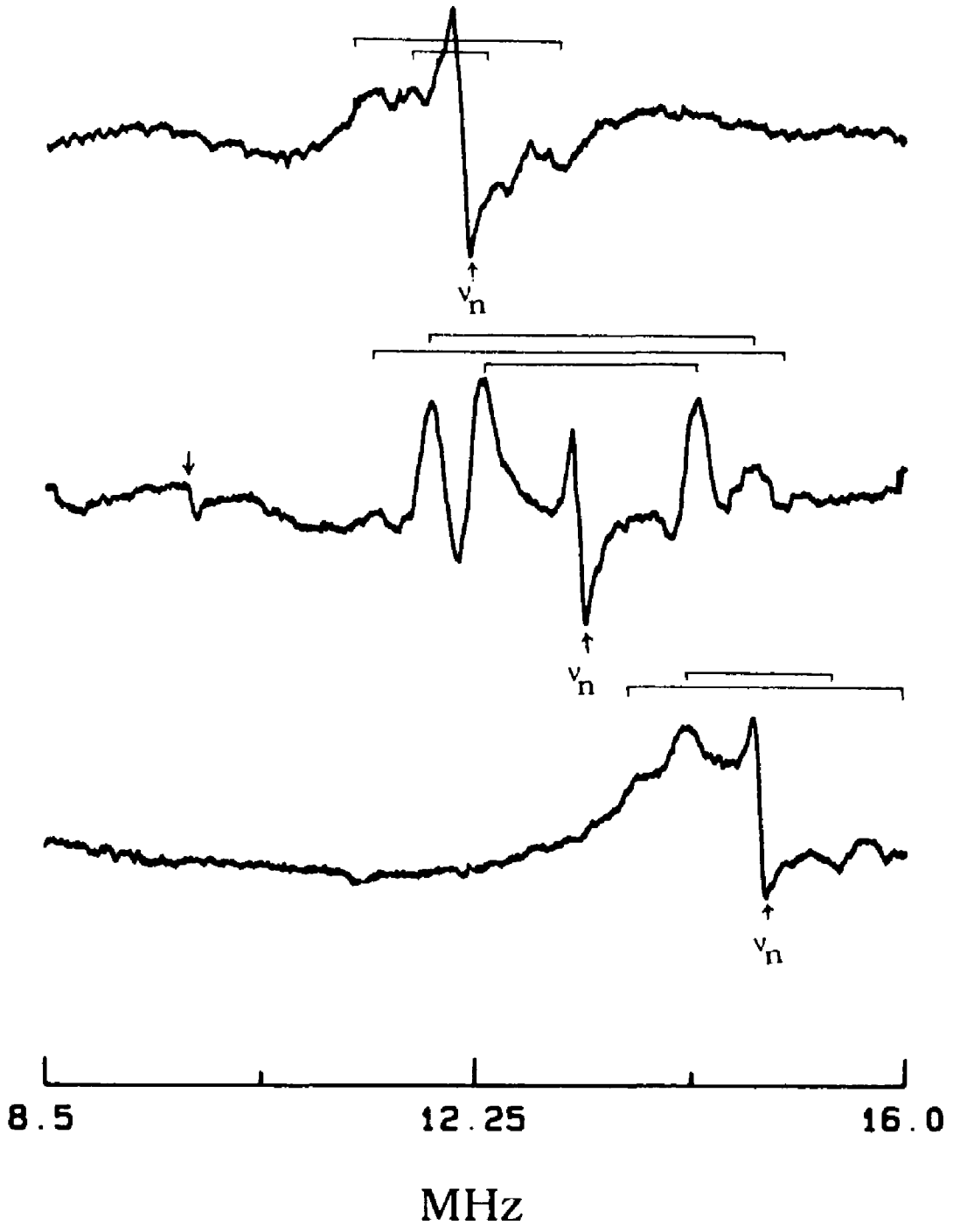

Figure 3.2 Proton region at (a) g_{xx} (b) g_{yy} (c) g_{zz}. Spectra of ^{13}CN adduct. Experimental conditions are the same as Figure 3.1 except with a field sweep of 10 MHz.

$$\nu_{endor} = \nu_n \pm |A_n| /2 \qquad (3.1)$$

where A_n (= A_{iso} + A_{aniso}) is the sum of the proton isotropic coupling (A_{iso}) and anisotropic (A_{aniso}) hyperfine coupling and $\nu_n = g_n\beta_n H/h$ is the free precessional frequency of the proton in a magnetic field of strength H. There are at least 3 distinct sets of proton resonances which are evenly split about the nuclear Zeeman frequency. These are most clearly resolved in the spectrum along g_{yy} (Figure 3.1 (b)). The resolved proton hyperfine couplings at all three of the principal g-values are given in Table 3.1. These couplings are small relative to the H-atom coupling of 1420 MHz [80] which indicates that little of the unpaired electron wavefunction extends to the protons. Localization of the electron spin at a distance from the protons means that a large fraction of the proton hyperfine coupling should be due the the anisotropic dipolar term (A_d). The dipolar nature of the coupling is clearly indicated by the variations in couplings over the range of g-values. The interaction between an electron spin and a proton several angstroms away can often be estimated by the first-order dipolar interaction given by:

$$A_d = g_e \beta_e g_n \beta_n (3\cos^2\theta - 1)/r^3 \qquad (3.2)$$

where r is the distance between the iron and the proton and θ is the angle between the direction of the applied magnetic field and the vector from the iron to the proton. Although this equation is strictly accurate only in the limit of negligible isotropic coupling and long

	Proton ENDOR Peak Position (MHz)	Coupling (MHz)	Distance (Å)
g_{xx}	11.87 12.55	.68	
	11.55 12.87	1.32	
	(10.94) 13.49	2.56	3.96
g_{yy}	12.31 13.36	1.05	
	11.77 14.01	2.24	4.13
	11.24 14.53	3.29	3.63
g_{zz}	14.23 15.24	1.01	
	13.78 15.73	1.95	

Table 3.1 Proton couplings from ENDOR spectra at the three g-values. Distances are calculated assuming a purely dipolar interaction (equation 3.5). The angle θ is assumed to be 0 when the coupling is a maximum.

distances between the electron and nucleus, it can be used to obtain an estimate of the distance of the protons from iron. Solving for r based on this equation one obtains the approximate distances listed in Table 3.1. These distances are calculated based on the assumption that each set of lines is due to a single proton or set of protons. Due to anisotropy, a single proton or set of protons could give rise to more than one set of peaks in a spectrum .

It is unusual that the splittings are most clearly resolved along g_{yy} since many orientations contribute to the signal at this field value. The maximum proton coupling is 3.26 MHz and is observed along g_{yy}. The proposed structure of the transferrin cyanide adduct has two proton containing ligands in the xy plane. Both histidine and tyrosine contain protons which would be close to the iron center and could give rise to this signal. In hemoprotein cyanides the largest proton hyperfine coupling constant of 4 MHz was tentatively assigned to the near-CH protons of the proximal histidine [75]. The results of a simulation in which two protons are placed at plus and minus thirty degrees off the g_{yy} axis, as would typically be expected for either a tyrosine or histidine bonded along the g_{yy} axis, are shown in Figure 3.3. The anisotropic effects are clearly evident. Although the analysis can hardly be considered conclusive, the the peak positions of the simulated spectra are at least consistent with some of the experimentally observed peaks. With histidine and tyrosine ligands there is likely to be some delocalization of the electron onto the protons which would cause an isotropic contribution and would lessen the anisotropic component thus increasing the distance, r, calculated from Equation 3.2.

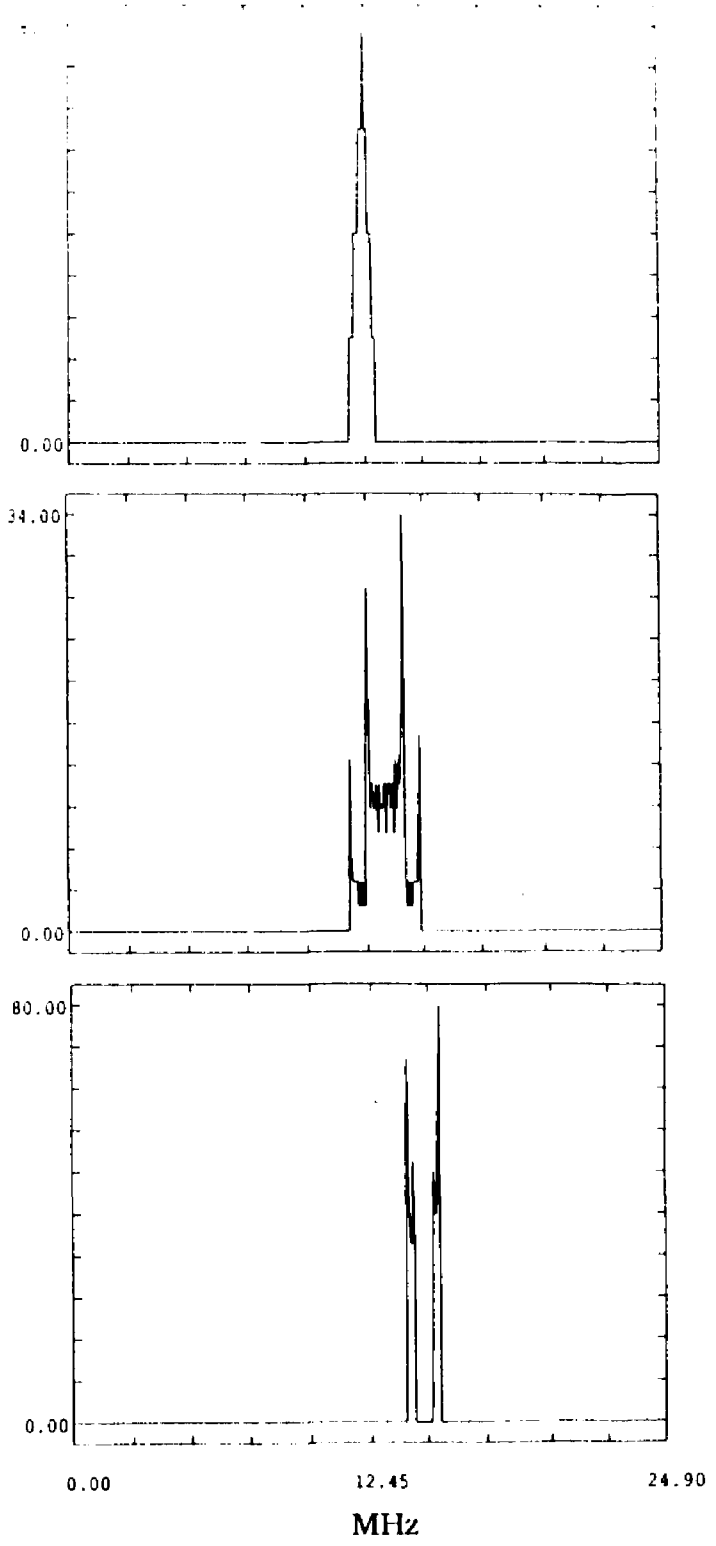

Figure 3.3 Simulation with two protons 3.75 A from the iron center at +30 and -30 degrees off g_y-axis. (a) simulation for g_x (1.92) (b)simulation for g_y (2.15) (c) simulation for g_z (2.34).

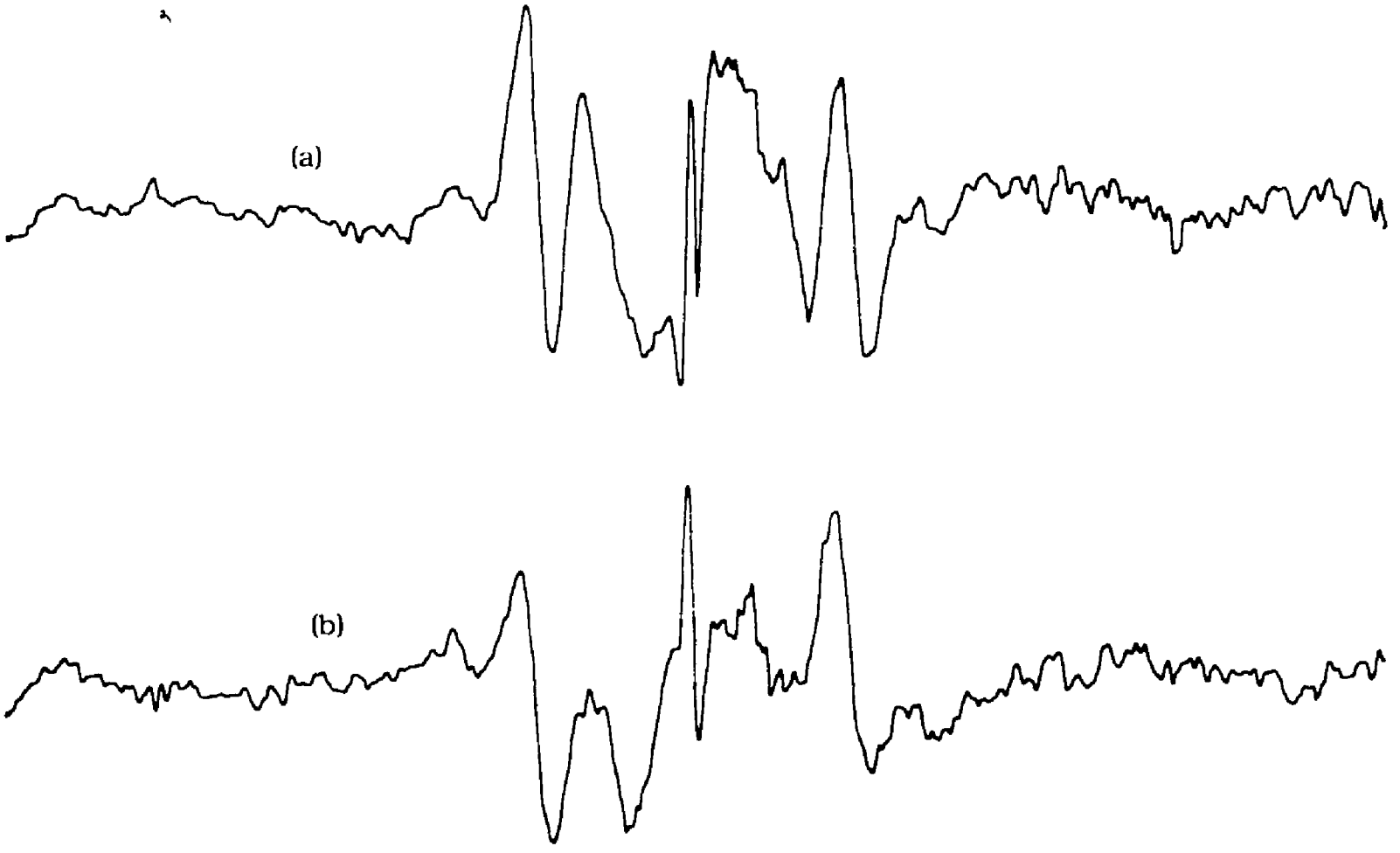

Figure 3.4 ENDOR of (a) transferrin adduct in H_20 (b) in D_20. Field sweep 10 MHz. Center Field 12.860 MHz. Magnetic field 3020 G.

As shown in Figure 3.4, the H_2O and D_2O spectra show very minor differences at frequencies close to the proton free precessional frequency. Matrix or distant proton ENDOR responses would contribute to this spectral region and the small effect from solvent exchange suggests that the metal center is relatively isolated from bulk solvent. Most of the resolved proton peaks are not affected by solvent deuteration which indicates that they are associated with ligand protons of the protein.

^{13}C ENDOR

The ENDOR Spectrum

The addition of cyanide to transferrin results in a low-spin rhombic EPR spectrum at the C-terminal site with g factors g_{xx} =2.34, g_{yy} =2.15, and g_{zz}=1.92 [40] as shown in the inset to Figure 3.5. The ^{13}C hyperfine coupling is not resolved in the EPR spectrum nor is any discernable broadening of the EPR line observed when ^{12}C cyanide is replaced with ^{13}C cyanide.

^{13}C has a nuclear spin of I=1/2 and consequently gives rise to a two line ENDOR pattern. In this case the electron nuclear hyperfine interaction is greater than the nuclear Zeeman term so, to first order, the frequencies of the ENDOR lines are given by:

$$\nu_{endor} = |A_n| /2 \pm \nu_n \qquad (3.3)$$

where A_n (= A_{iso} + A_{anisio}) is the sum of the ^{13}C isotropic coupling (A_{iso}) and anisotropic (A_{aniso}) hyperfine coupling and $\nu_n = g_n\beta_n H/h$ is the free precessional frequency of the ^{13}C nucleus in a magnetic field

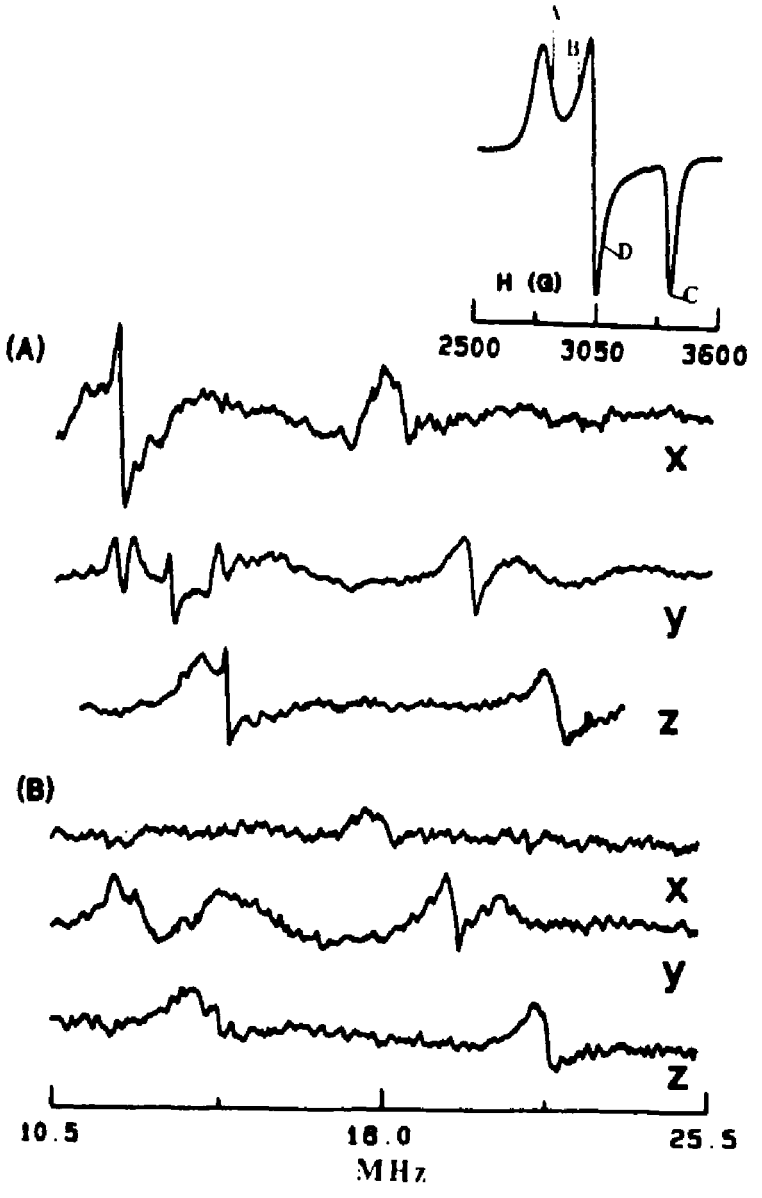

Figure 3.5 (a) ENDOR spectra of ^{13}CN-transferin adduct at g_{xx} (H_0=2870 G), g_{yy} (H_0=3113), and g_{zz} (H_0=3458 G) (b) Same spectra as in (a) after subtraction of ^{12}CN-transferrin spectra from those of the ^{13}CN enriched sample, thus removing all interactions due to nuclei other than ^{13}C. Experimental conditions: same as for Figure 3.1. Inset: X-band EPR spectrum showing g=2 region with ENDOR fields A, B, C, and D indicated. Experimental conditions are the same as for Figure 2.4.

of strength H. Thus one expects a pair of lines separated by $2\nu_n$ and centered at $|A_n|/2$.

Figure 3.5 shows the spectrum of the transferrin-CN adduct at three different fields when prepared with isotopically enriched ^{13}CN. As expected a two line spectrum is observed with a splitting twice the appropriate Zeeman frequency for ^{13}C. The lower frequency peak tends to be obscured by lines due to weakly coupled protons in the 12-14 MHz region. The proton interactions were removed by subtracting the spectrum of a transferrin-cyanide adduct prepared with ^{12}CN. Since ^{12}C has a nuclear spin of zero it does not contribute to the ENDOR spectrum; however, the interactions of all other nuclei, including protons, will be identical. This subtraction effectively removes all peaks due to nuclei other than ^{13}C.

To locate the CN position within the coordinate system of the g-tensor, ENDOR spectra were taken every 50G in the range 2850 G to 3500 G (g_{xx} to g_{zz}). Since the proton ENDOR lines overlap with the lower frequency ^{13}C line at all fields, only the position of the higher frequency peak was accurately measured and fitted in subsequent full-matrix calculations.

The position of the higher frequency ^{13}C peak increases almost linearly with increasing magnetic field. Figure 3.6 shows the change in both the free precessional frequency and the observed peak as a function of magnetic field. It is apparent that only some of the increase in the peak position is due to the increase in the free precessional frequency of the nucleus with field. The small change in $|A_n|$ from a minimum of 30.53 MHz at g_{xx} to a maximum of 37.17 MHz at g_{zz} indicates that the coupling is primarily isotropic with a

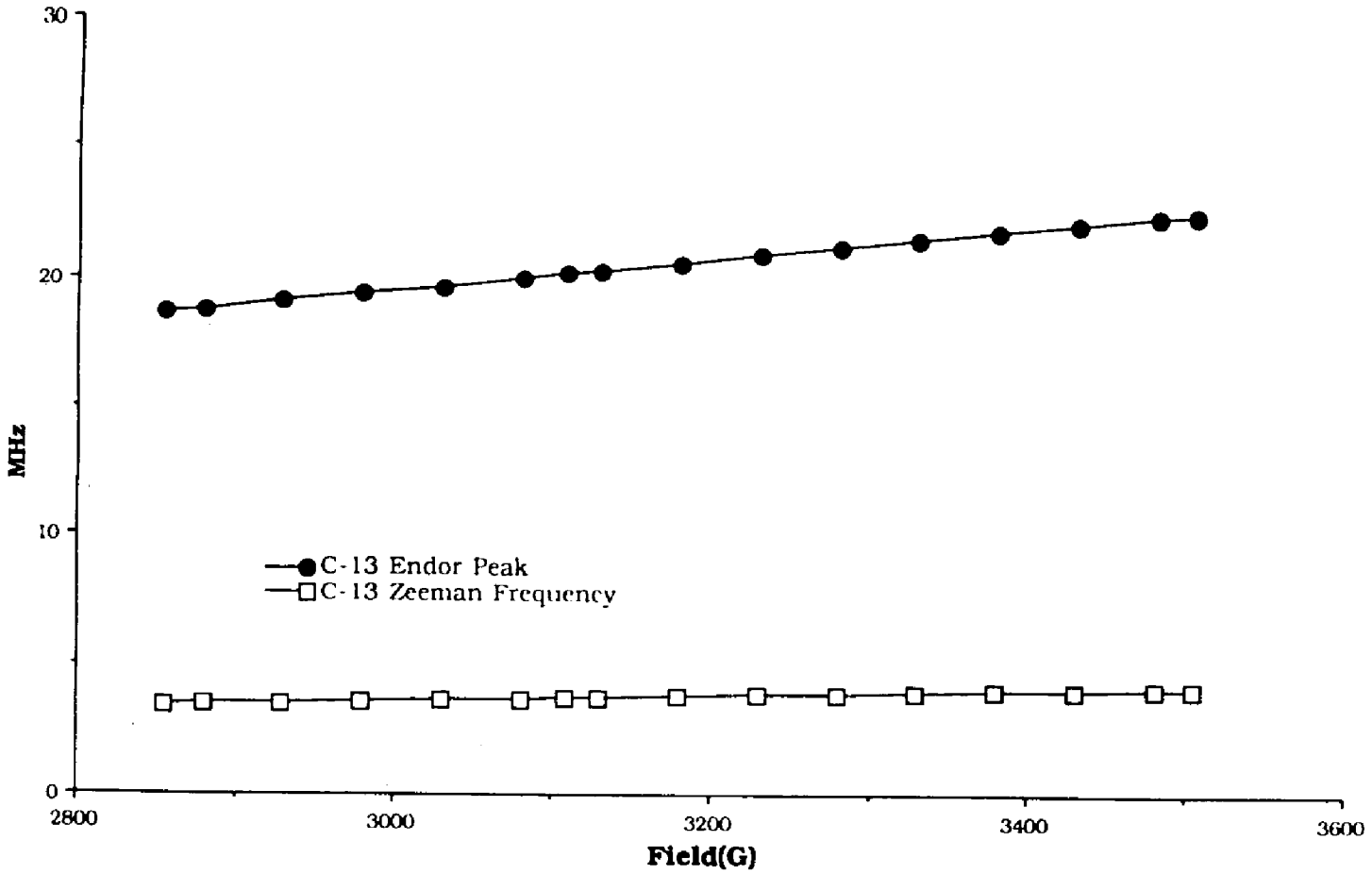

Figure 3.6 Location of high frequency ^{13}C ENDOR line and free precessional frequency of ^{13}C for magnetic fields from 2885 G to 3500 G. Same experimental conditions as for Figure 3.1.

small anisotropic component which varies according to the molecular orientations selected by the field position in the EPR spectrum. For strictly isotropic coupling, there would be no change in the value of $|A_n|$ with field.

Isotropic Coupling

The considerable isotropic component arises from s-orbital electron spin density on the carbon. Direct coordination of ^{13}C to the Fe(III) site is indicated by the magnitude of the coupling. Couplings with similar magnitudes (28.64 MHz and 27.33 MHz) have been reported in studies of ^{13}CN heme complexes [75]. Analysis of the g-factors of the transferrin adduct indicates that the unpaired electron is in an orbital which is mainly d_{xy} in character in the coordinate system of the g-tensor [40]. Since the carbon s-orbital has the wrong symmetry to bond directly to the d_{xy} orbital, the isotropic coupling cannot be due to the traditional Fermi contact term. A large contact interaction of negative sign (approximately -30 MHz) which is observed with metal cyanide complexes has been attributed to an exchange polarization mechanism between an unpaired electron in the metal d-orbital and paired electrons in a cyanide sigma orbital [81]. NMR work has confirmed the sign of this coupling for aqueous $K_3Fe(CN)_6$ and $K_4Fe(CN)_6$ [82]. The magnitude of the isotropic hyperfine coupling for the cyanide adduct of transferrin($|A_{iso}| = 35.5$ MHz) is in substantial agreement with hyperfine couplings for other transition metal cyanide complexes. These couplings are largely isotropic and of negative sign [82,83]. Therefore, we assume that the sign of the isotropic coupling in transferrin is likewise negative.

The sign of the dipolar hyperfine coupling for different magnetic fields is dependent on the location of the CN group in the axis system of the g tensor. The minimum apparent coupling $|A_n|$ is along g_{xx}, and the maximum along g_{zz}. This is consistent with the CN group being located on the x axis. For the magnetic field aligned along g_{xx}, a maximum positive dipolar coupling is expected which when added to the negative isotropic coupling results in a total coupling of less magnitude than the isotropic coupling alone. Along g_{zz} the maximum negative dipolar coupling adds to the negative isotropic coupling resulting in a maximum magnitude of the total coupling. Full matrix calculations show that moving the CN group only a few degrees off the x axis changes the dipolar coupling sufficiently that the variation in the ^{13}C hyperfine coupling across the EPR spectrum no longer matches that of the data (vide infra). Thus, the location of the ^{13}C on the x axis or within ± 5 degrees of it is firmly established. As is illustrated below, the small but readily measured dipolar component contains useful information.

Simulations

Simulations of the ENDOR spectra [68] were based on the approach by Hurst et al. [66]. The general method of simulation is to determine the molecular orientations which will contribute to the ENDOR at a given field value H in the EPR. The EPR spectrum is first simulated to determine allowed transitions at that field. Thus a distinct set of molecular orientations giving rise to transitions within the EPR at a given field value is obtained. In effect the external field "selects" certain molecular orientations according to g-anisotropy in the spectrum. Because the spectrum of transferrin is dominated by g-

anisotropy, i.e. the electron-ligand nuclei couplings are small and the metal nuclear spin is zero, the appropriate spin Hamiltonian for the EPR experiment is given by:

$$\hat{\mathcal{H}}=\beta_e \vec{\mathbf{H}} \cdot \overleftrightarrow{g} \cdot \hat{\vec{\mathbf{S}}} \tag{3.4}$$

where the required resonance condition is:

$$H_r= h\nu/g(\theta,\phi)\,\beta_e \tag{3.5}$$

where

$$g(\theta,\phi) = [(g_{xx}\sin\theta\cos\phi)^2 + (g_{yy}\sin\theta\sin\phi)^2 + (g_{zz}\cos\theta)^2]^{1/2} .$$

Thus a specific magnetic field, $\vec{\mathbf{H}}$, within the EPR spectrum, will give a set of θs and φs for which Equation 3.5 is satisfied. The set of θs and φs will represent all orientations giving rise to the same g-value. However, each theta-phi combination will give different ENDOR resonances since the dipolar interactions with ligand nuclei change with each theta-phi combination. Thus the ENDOR spectrum reflects the angular dependence of hyperfine energies of the ligand nuclei. Figure 3.7 shows the results of calculations illustrating this effect on the ENDOR spectrum. Here the ^{13}C nucleus is placed on the molecular g_{xx} axis. At the edges of the EPR spectrum, near g_{xx} and g_{zz} (peaks A and C in Figure 3.7), there are only a narrow range of ENDOR frequencies. At intermediate field values between g_{xx} and g_{zz}

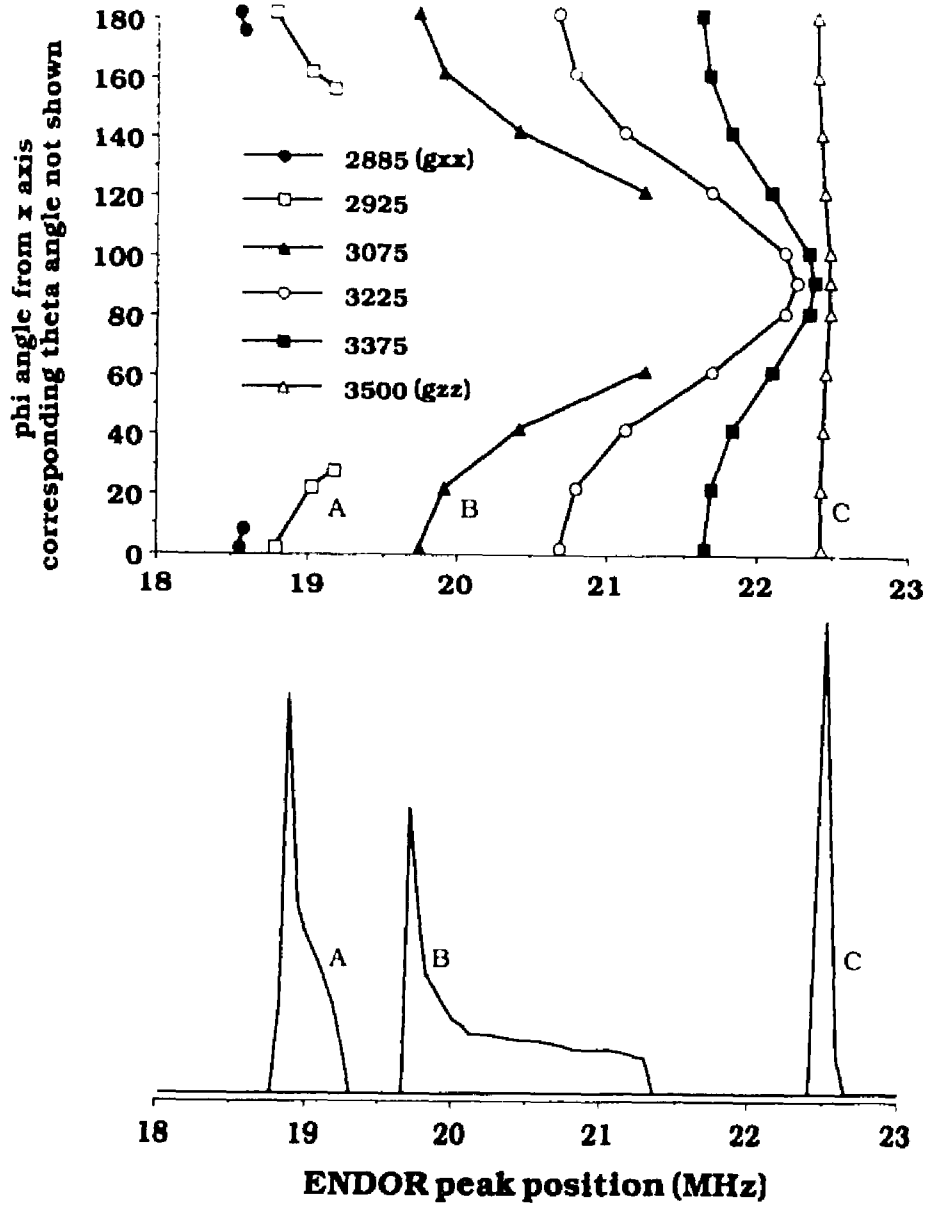

Figure 3.7 Simulations showing the dependence of the ENDOR absorption frequency (in MHz) for magnetic fields ranging from approximately g_{xx} to g_{zz} in the EPR spectrum. Phi is the angle used in Equation 3.5 for orientations from 0 to 180 degrees. Only the higher frequency peak of the ENDOR pair of lines is shown. Simulation assumes ^{13}C nucleus along g_{xx} axis with a point dipole interaction. A, B, and C correspond to the field positions indicated in the Figure 3.5 inset.

(Figure 3.7-peak B) a wider range of frequencies become possible giving rise to partial "powder" patterns in the ENDOR.

ENDOR spectra observed along the two edges of the EPR absorption spectrum, (i.e. along g_{xx} and g_{zz}) give true "single-crystal" like spectra, representing pure orientations [63, 84]. Since, between these two extremes a variety of orientations contribute to the ENDOR spectrum, two turning points or edges in the ENDOR "powder" pattern are observed and broadening of the observed ENDOR peaks is expected. The range of ^{13}C frequencies contributing to the ENDOR peak at a given field is determined by the g-tensor. In the case of transferrin, the largest difference between the high and low edges of the simulated peak is 1.7 MHz. Figure 3.8 shows that including a linewidth similar to that observed experimentally results in a derivative crossing point corresponding closely to the most intense absorption side of the simulated ENDOR peak. Consequently, we have chosen to match the higher intensity turning point of the simulated peak with the experimental peak location. Since our interest was in the position of the ^{13}C peak, no attempt was made to match either the ENDOR lineshape or its intensity. Figure 3.9 shows the results of the simulated ENDOR peak position as a function of EPR field compared with the experimental values. The position of both the high and low edges of the ENDOR peak are shown. Excellent agreement between the low frequency (higher intensity) edge and the experimental data is obtained.

Analysis of Anisotropic Coupling

The anisotropic electron-nuclear hyperfine coupling tensor used in the simulations has elements:

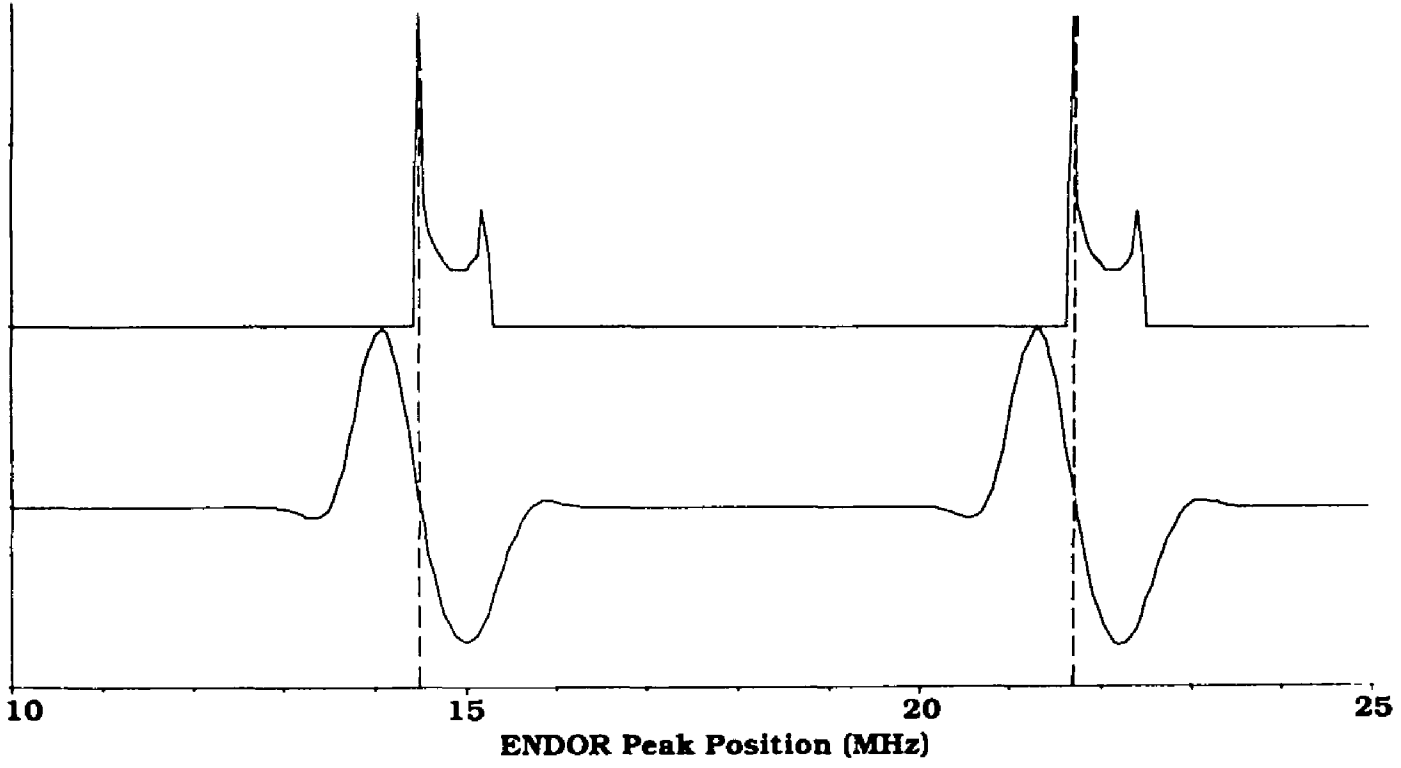

Figure 3.8 Simulation of ENDOR peaks at g=2.17 (H_0=3075). Top shows the simulated ENDOR "powder" pattern obtained from the subset of molecular orientations corresponding to g=217. Bottom is the derivative of this same simulation after including a linewdith of .94 MHZ similar to those observed experimentally. The derivative crossing point corresponds to the high intensity side of the simulated peak.

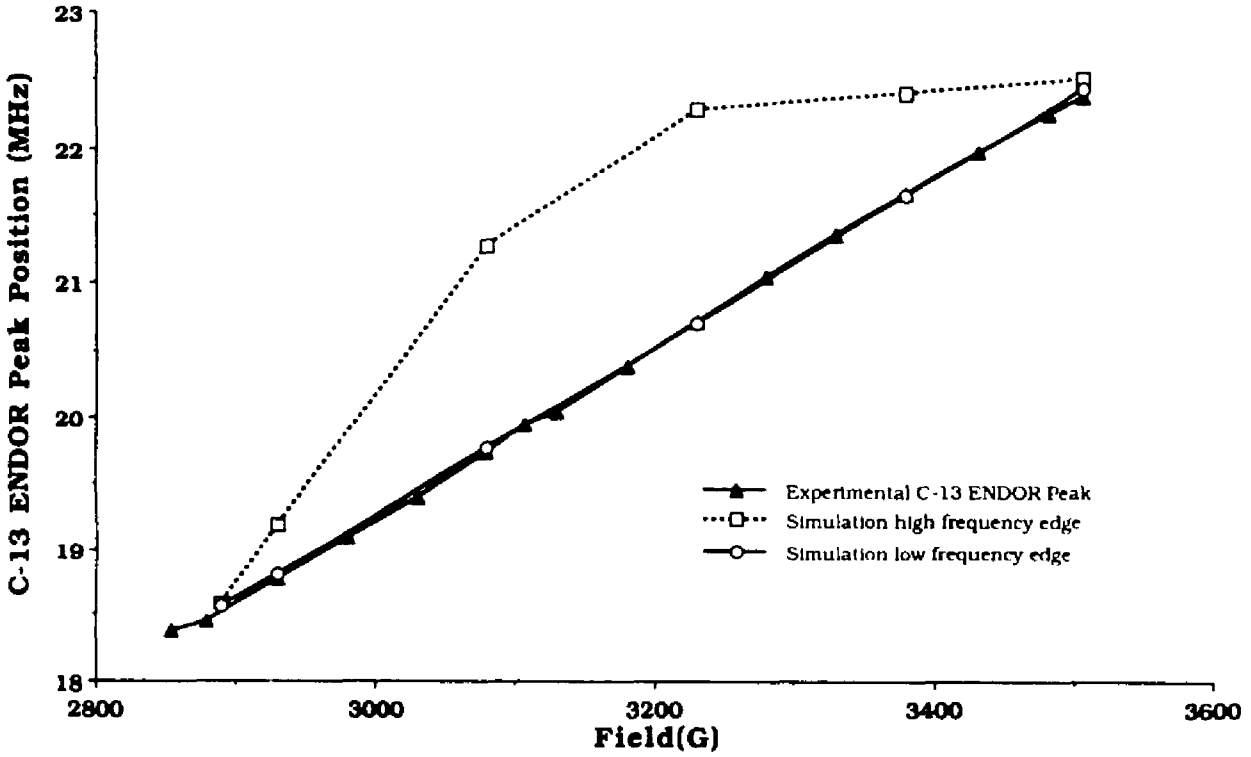

Figure 3.9 Comparison of ENDOR simulation (higher frequency peak of the ENDOR pair only) with experimental results. Both the high and low frequency edges of the simulated peak are shown. The calculation assumes the ^{13}C nucleus is located on the g_{xx} axis at a distance of 2.15 A with an isotropic coupling of -35.50 MHz and a point dipole interaction for the anisotropic coupling.

$$A_{aniso,xx} = 4.472 \text{ MHz} \qquad (3.6)$$
$$A_{aniso,yy} = -2.350 \text{ MHz}$$
$$A_{aniso,zz} = -2.122 \text{ MHz}$$

The Fe-^{13}C distance can be estimated from the anisotropic coupling A_{ansio} by assuming that this coupling is solely due to the through space dipolar interaction, A_d. The tensor elements of this dipole-dipole interaction are given by [68]:

$$\overleftrightarrow{A} = \frac{-\beta_e\beta_n g_n}{hr^3}\begin{pmatrix} g_{xx}((3\cos\phi_N\sin\theta_N)^2-1) & 3g_{xx}\cos\phi_N\sin^2\theta_N\sin\phi_N & 3g_{xx}\cos\phi_N\sin\phi_N\cos\theta_N \\ 3g_{yy}\cos\phi_N\sin^2\theta_N\sin\phi_N & g_{yy}((3\sin\phi_N\sin\theta_N)^2-1) & 3g_{yy}\sin\phi_N\sin\theta_N\cos\theta_N \\ 3g_{zz}\cos\phi_N\sin\phi_N\cos\theta_N & 3g_{zz}\sin\phi_N\sin\theta_N\cos\theta_N & g_{zz}((3\cos\theta_N)^2-1) \end{pmatrix} \qquad (3.7)$$

where r is the distance between the ^{13}C and the iron, g_n is the nuclear g-factor for ^{13}C, β_e and β_n are the Bohr and nuclear magnetons respectively, and θ_N and ϕ_N are the polar angles of the nucleus relative to the principal axis system for the g-tensor.

Figures 3.10 and 3.11 show the sensitivity of the simulated ENDOR peak position to changes in the variable simulation parameters. Since the position of the ^{13}C peak is established along the x-axis, the variable parameters are A_{iso} and the distance, r, which controls the dipolar contribution to A_n. As is readily apparent, the distance, r, determines the slope of the line of peak position as a function of magnetic field and the coupling, A_{iso}, controls the y-axis intercept. Although the simulations are obviously very sensitive to

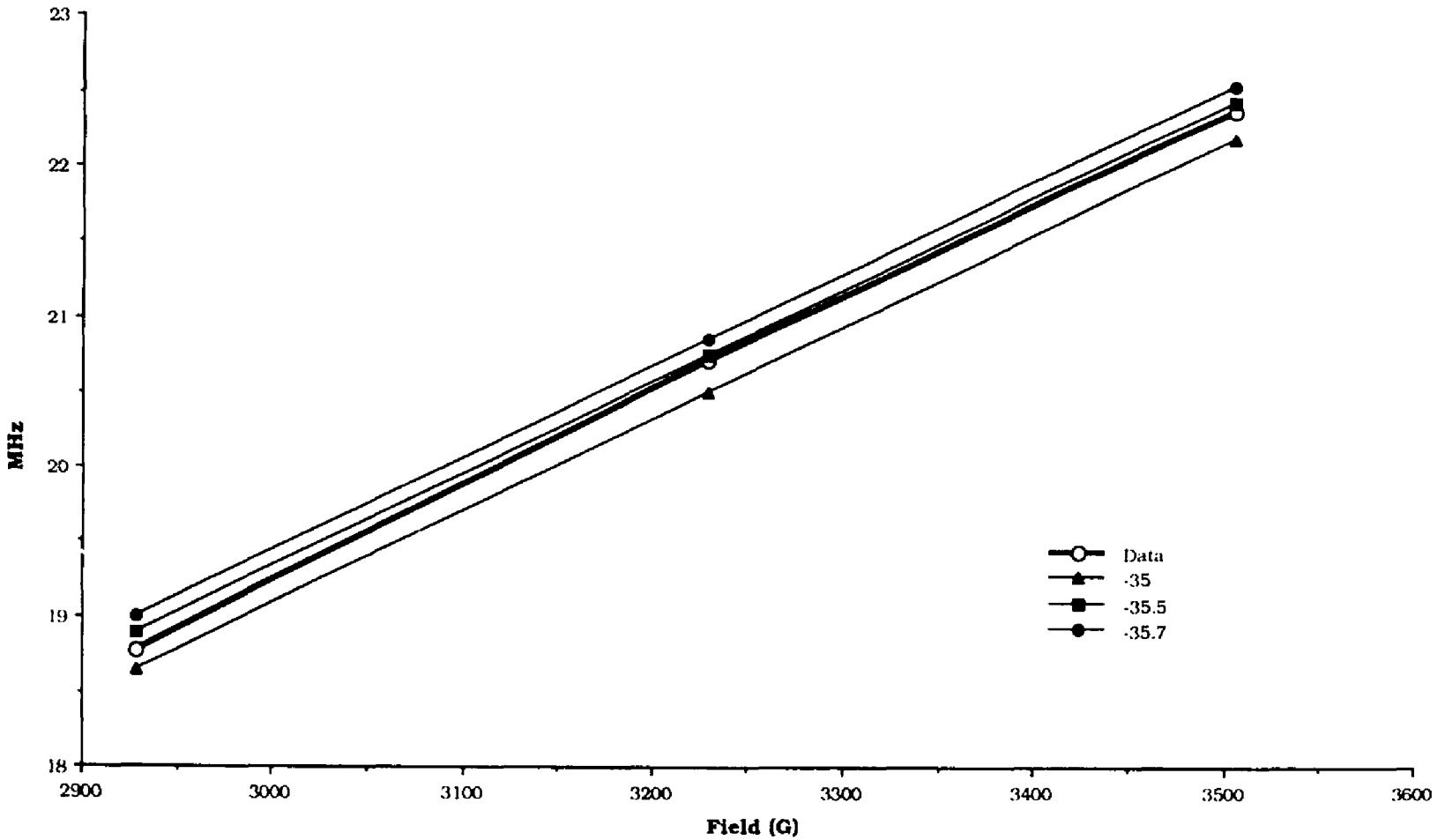

Figure 3.10 Simulated high frequency ^{13}C ENDOR peak as a function of magnetic field with different isotropic couplings (in MHz) used in the simulation.

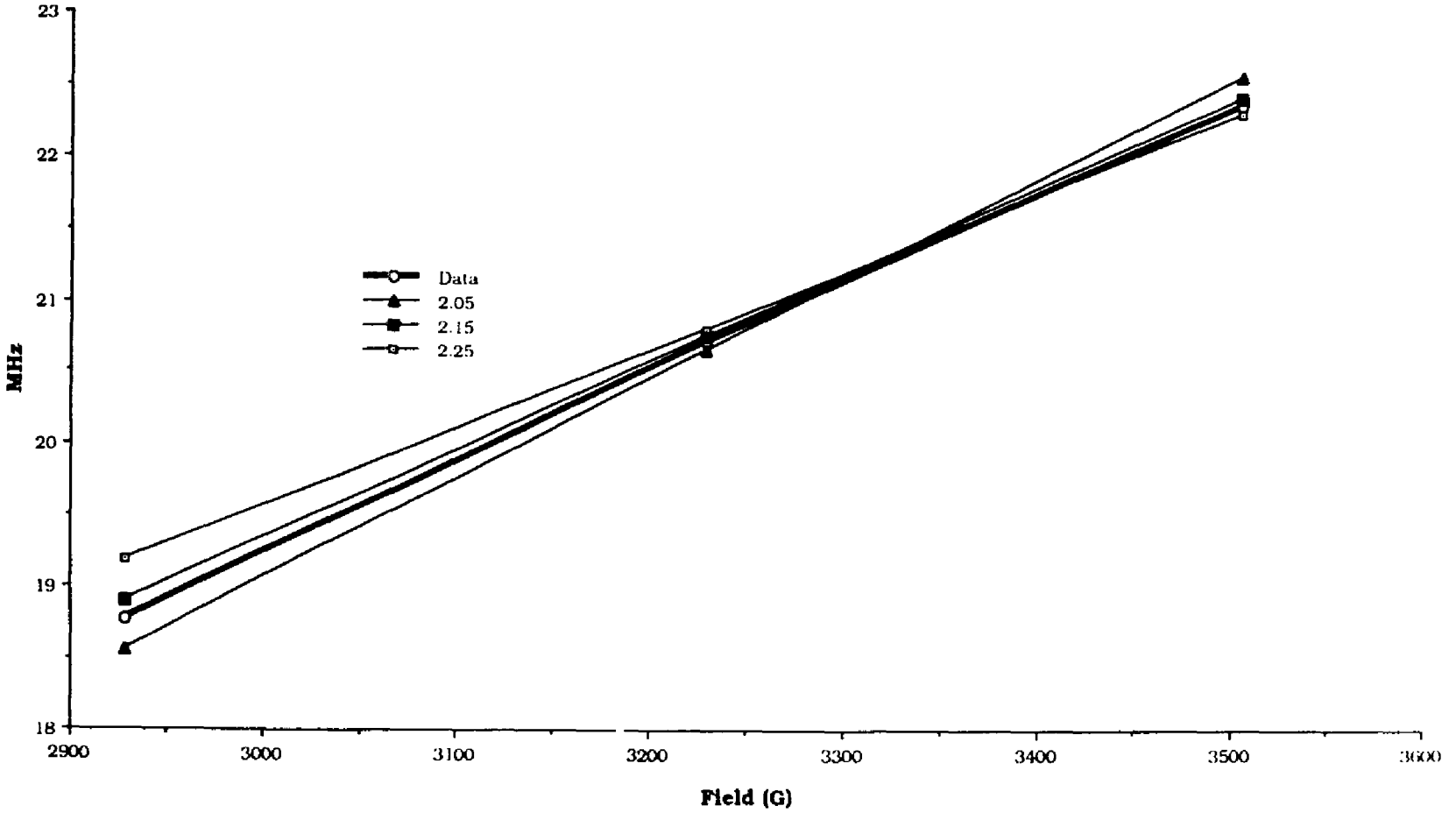

Figure 3.11 Simulated high frequency ^{13}C ENDOR peak as a function of magnetic field with different distances (in Å) used in the simulation.

small changes in those parameters, in reality some ambiguity is introduced by considering anisotropic effects which result in broad simulated ENDOR lines. However, the "pure orientations" along g_{xx} and g_{zz} do not have such broadening so it is important that the simulation parameters give results which match the experimental data closely at these points.

The point dipole approximation is generally considered valid for distances on the order of 2.5 Å or greater, with weak contact interaction [85]. Although that is obviously not the case here, a simple dipole calculation nevertheless gives an Fe-^{13}C distance of 2.15 Å, a result in reasonable agreement with the bond distances of 1.8-1.9 Å typically found for metal cyanide complexes [86,87,88].

To obtain a better estimate of the iron carbon distance, the dipole interaction was calculated explicitly using the ground state d_{xy} orbital for the unpaired electron. The details of the lengthy calculation are given in Appendix A. The use of the equations 1A, 2A, and 3A instead of the point dipole approximation (Equation 3.7) changes the distance only slightly from 2.15 Å to 2.09 Å. Thus it is evident that the point dipole approximation is reasonably good for estimating distances even at bond lengths approaching 2 Å. This result appears to be due largely to the contracted nature of the transition metal based d-orbital.

In addition to the dipolar interaction of the carbon nucleus with the d_{xy} electron on the iron, there are other contributions to the observed anisotropic coupling. The coupling A_p is due to the electron-nuclear interaction from unpaired electron density in the ^{13}C p-orbitals and its magnitude depends on the amount of electron spin

density in the various p-orbitals. The sigma coupling is due to electron density in the p_x carbon orbital and there are two pi-type interactions, one due to electron density in the p_y orbital ($\pi 1$), and the other due to density in the p_z orbital ($\pi 2$). Thus the total anisotropic coupling (A_{aniso}) is given by:

$$A_{ansio,xx} = 2A_d + 2f_\sigma A_p - f_{\pi 1}A_p - f_{\pi 2}A_p \qquad (3.8)$$
$$A_{ansio,yy} = -A_d - f_\sigma A_p + 2f_{\pi 1}A_p - f_{\pi 2}A_p$$
$$A_{ansio,zz} = -A_d - f_\sigma A_p - f_{\pi 1}A_p + 2f_{\pi 2}A_p$$

where f_σ and f_π are the spin densities on the carbon p-orbitals giving rise to sigma-bonding and pi-bonding respectively.

The isotropic coupling of -35.5 MHz corresponds to a spin density of 1.14% in the carbon s-orbital (unit spin density giving a coupling of 3110 MHz for ^{13}C [80]; 35.5/3110 x 100 = 1.14%). A similar spin density is anticipated for the carbon p-orbital since the sigma bond between carbon and iron to the first approximation involves a carbon sp-hybrid orbital. Thus the anisotropic coupling contribution for the case of an sp-bond would be 1.04 MHz, 1.14% of 90.8 MHz (unit spin density in a carbon p-orbital gives a dipolar coupling of 90.8 MHz for ^{13}C). As described for the isotropic coupling, this spin density arises from a spin-polarization mechanism and, consequently, f_σ should be negative. The anisotropic components due to the dipolar interaction from the metal alone would thus be increased from those given in Equation 3.6 to:

$$A_{d,xx} = 6.90 \text{ MHz} \qquad (3.9)$$
$$A_{d,yy} = -3.47 \text{ MHz}$$
$$A_{d,zz} = -3.12 \text{ MHz}.$$

These larger couplings lead to a decrease in the calculated distance between the iron and ^{13}C from 2.15 Å to 1.86 Å [89] using the point dipole approximation.

The 1.86 Å bond length is very close to those obtained from x-ray studies of metal cyanide complexes. However, there are several other interactions that have not yet been considered which would also change the magnitude of the orientation dependent coupling and thus the calculated distance. In addition to the unpaired spin density on carbon due to the Fe-CN sigma bond, there are interactions ($f_{\pi 1}A_p$ and $f_{\pi 2}A_p$) due to the spin density from the back-bonding contribution from the d_{xz} and d_{xy} orbitals to the cyanide pi-orbital. It is apparent from Equation 3.8 that if the spin densities $f_{\pi 1}$ and/or $f_{\pi 2}$ are substantial, the calculated distance would be in error. The delocalization of the electron spin density in the d_{xy} orbital onto other ligands would also change the calculated distance. Although the distance of 1.86 Å, calculated using an sp-hybrid orbital to obtain an estimate of f_σ while assuming $f_{\pi 1}$ and $f_{\pi 2}$ to be negligible, apparently gives the best agreement with the x-ray metal cyanide distances, this result may simply be due to the fortuitous cancellation of the various anistropic components, such as found for $Cr(CN)_6^{3-}$ [81].

Conclusion

The structure originally proposed for the cyanide adduct of transferrin includes three cyanides coordinated to the iron center in the C-terminal domain [40]. However, only one pair of ^{13}C lines were clearly observed in the current ENDOR study. There are a number of situations that could give rise to the single set of ^{13}C peaks:

(1) While three cyanides are involved in the conversion of the iron(III) to low-spin, only one cyanide may actually be bound to the metal center. The possibility that some of the CN^- groups bind to cationic sites on the protein causing a conformational change leading to a low-spin complex was suggested in the previous study [40]. The binding of simple inorganic anions such as chloride and perchlorate to transferrin causing a change in the spectral, kinetic, and thermodynamic properties of the iron, particularly in the C-terminal site, is well known [90,91,31,32].

(2) The set of peaks may represent two coordinating cyanide groups trans to one another with the same ^{13}C couplings. Trans complexes are known [92]. ENDOR cannot be used quantitatively to determine the number of ^{13}C nuclei since the intensity of the peaks is influenced by complicated and unknown relaxation mechanisms. From the structure of the metal site in transferrin [93,94,95], we would expect trans coordination of two cyanides to result in the displacement of a protein ligand. The third cyanide could be on the z-axis where the ^{13}C coupling with the unpaired electron in the d_{xy} orbital may be too small to be observed.

(3) There may be three cyanides bound to the iron with only one of them being ENDOR visible. The relaxation mechanisms which

influence the ability to see an ENDOR spectrum may be very different for the three groups. ESEEM spectroscopy, which is also sensitive to such relaxation mechanisms, and ENDOR spectroscopy were unable to observe isotopically substituted ^{13}C carbonate in studies of copper transferrin [96,97] even though the carbonate is coordinated to the metal [95].

Although there is only one clearly defined set of peaks that can be attributed to ^{13}C, there is an additional peak at 9.98 MHz observed only along g_{yy}. This small peak can be seen in Figure 3.1 (b) and Figure 3.2 (b) and was observed in several spectra of isotopically substituted ^{13}CN under different experimental conditions and was never observed with ^{12}CN. However, the peak is small and subtraction of a ^{12}CN spectrum does not reveal the partner peak. Consequently, if this peak is due to ^{13}C, then it could be either the $|A_n|/2 - \nu_n$ peak or the $|A_n|/2 + \nu_n$ peak. This would correspond to a coupling of 13.3 MHz in the former case or 26.6 MHz in the latter. If indeed this is a ^{13}C peak, then it is likely that the peak is due to a cyanide group along the g_{yy} axis since it is only observed at this orientation. The lack of the partner peak and the lack of observation of the peak at additional fields makes it difficult to analyze or even to attribute it conclusively to ^{13}C. Any further analysis would require careful study and tracking of this peak with different magnetic fields near g_{yy} .

Although the ENDOR study of the cyanide adduct of transferrin does not provide additional information about the number of cyanides bonded to the metal center, it does definitively locate at least one of the three cyanide groups of the adduct. Analysis of the orientation dependence of the dipole interaction places this CN^- along the g_{xx}

axis at a distance consistent with the x-ray bond lengths for other metal cyanide complexes. The detailed analysis reported here illustrates the application of ENDOR of "powdered" samples to studies of cyanide adducts of metalloproteins. This technique should be applicable to studies of the structure and bonding of small mixed-ligand Fe(III) cyano complexes in frozen solution as well.

CHAPTER 4

ESEEM OF TRANSFERRIN CYANIDE ADDUCT

Introduction

ENDOR spectroscopy was successfully used in investigating the proton and ^{13}C nuclei interactions of the transferrin cyanide adduct. However, there were additional low frequency signals which were too weak to analyze in the ENDOR spectra. Electron spin echo envelope modulation is particularly well-suited to the study of weak hyperfine interactions of low Zeeman frequency nuclei and often proves successful in studying the 0-5 MHz frequency region which is problematic in ENDOR. The complementary nature of the two spectroscopies makes it advantageous to use both methods to study the transferrin-cyanide adduct.

Experimental

The samples were prepared as described for the ENDOR experiments. ESEEM spectra were taken on the ESE spectrometer at the Albert Einstein College of Medicine with the assistance of Dr. Jeff Cornelius and Dr. John McCracken. The spectrometer is described in detail elsewhere [98]. Spectra were taken at liquid helium temperatures using a folded stripline reflection cavity [98]. Electron spin echo envelopes were obtained using both two pulse and three pulse sequences. The time domain data were transformed to frequency by use of the program FTBILL as described in Chapter 2. Three-pulse echo envelopes were generally recorded with a range of times (tau) between the first and second pulses in order to prevent

accidental suppression of frequencies. Spectra were taken at two spectrometer frequencies, 8.8 GHz and 10.5 GHz.

ESEEM of ^{13}C

Although three cyanide groups are involved in forming the transferrin cyanide adduct, ENDOR spectroscopy was only able to locate definitively one pair of ^{13}C resonance lines when isotopically enriched ^{13}C cyanide was used. Since ENDOR cannot be used quantitatively and since the quality of the low-frequency ends of the spectra was poor, ESEEM was used to see if additional interactions from other ^{13}C cyanide ligands could be observed. The time domain spectra for the adduct with and without ^{13}C are shown in Figures 4.1, 4.2, and 4.3 for g_{xx}, g_{yy}, and g_{zz} respectively. There is no obvious difference between the time domain spectra (a and b) which indicates that ^{13}C coupling is not observed. Since the contributions of different nuclei to the ESEEM modulation are multiplicative, the modulation induced by ^{13}C nuclei may be derived by dividing the envelope of (a) by that of (b). The ratios of the two time domain spectra for ^{12}C and ^{13}C cyanide are shown in part (c) of Figures 4.1, 4.2, and 4.3. At fields corresponding to g_{xx} (Figure 4.1) and g_{zz} (Figure 4.3) the ratios have no modulation indicating that there is no interaction due to ^{13}C. Figure 4.2 (c) shows some evidence of a low frequency modulation below 4 μsecs. The Fourier transform of Figure 4.2 (c) is shown in Figure 4.4. There are several peaks in the 3 MHz region which is near the free precessional frequency of ^{13}C (3.17 MHz) at that field. At g_{yy} the ratios of ^{12}C and ^{13}C three pulse spectra taken at several different tau values as well as the ratios of two pulse data all have similar, albeit weak and short-lived, modulation patterns corresponding

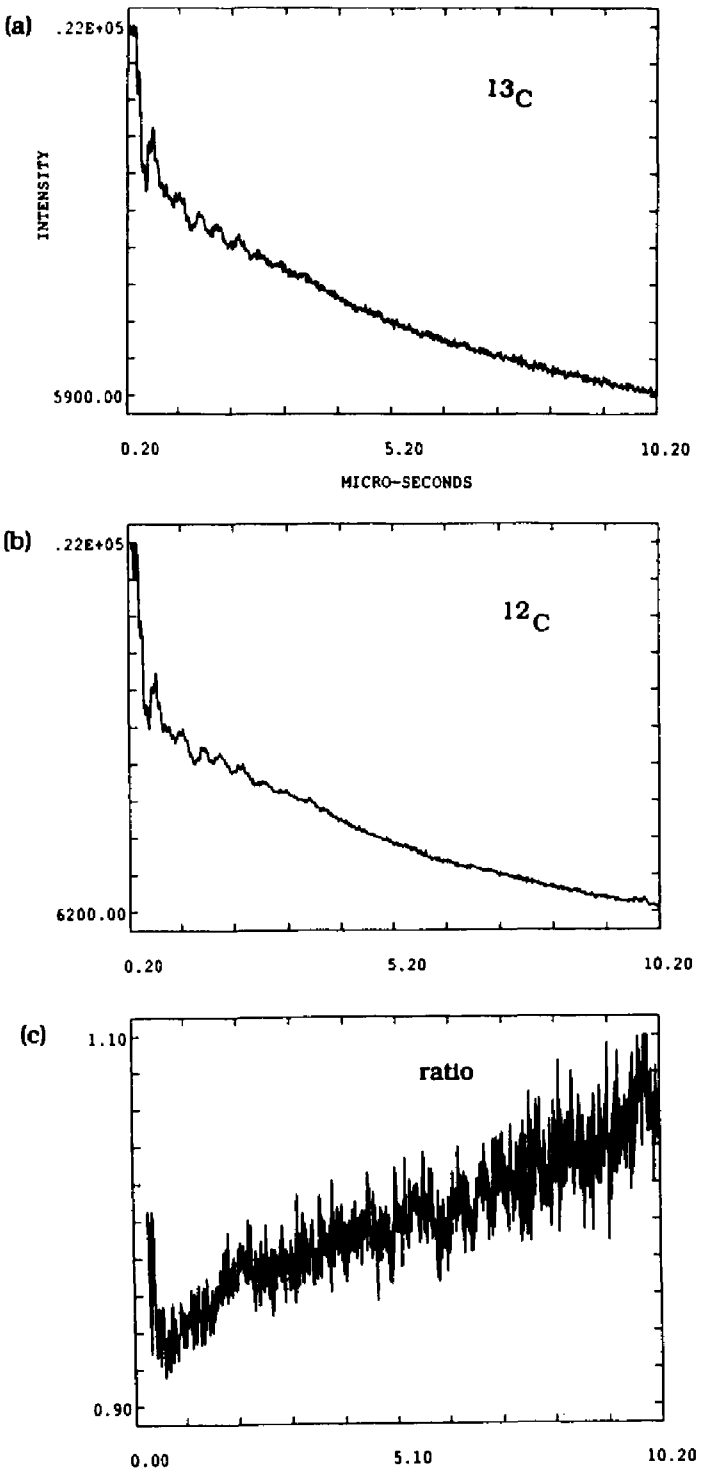

Figure 4.1 (a) Three-pulse ESEEM of ^{13}CN adduct of transferrin at g_{xx}. Data file SE2912.NIP. Frequency-8.866 GHz, Field-2702 G., tau-174 nsec. (b) Three-pulse ESEEM of CN adduct. Data file SE2876.NIP with same parameters as (a). (c) The ratio of (a) with (b).

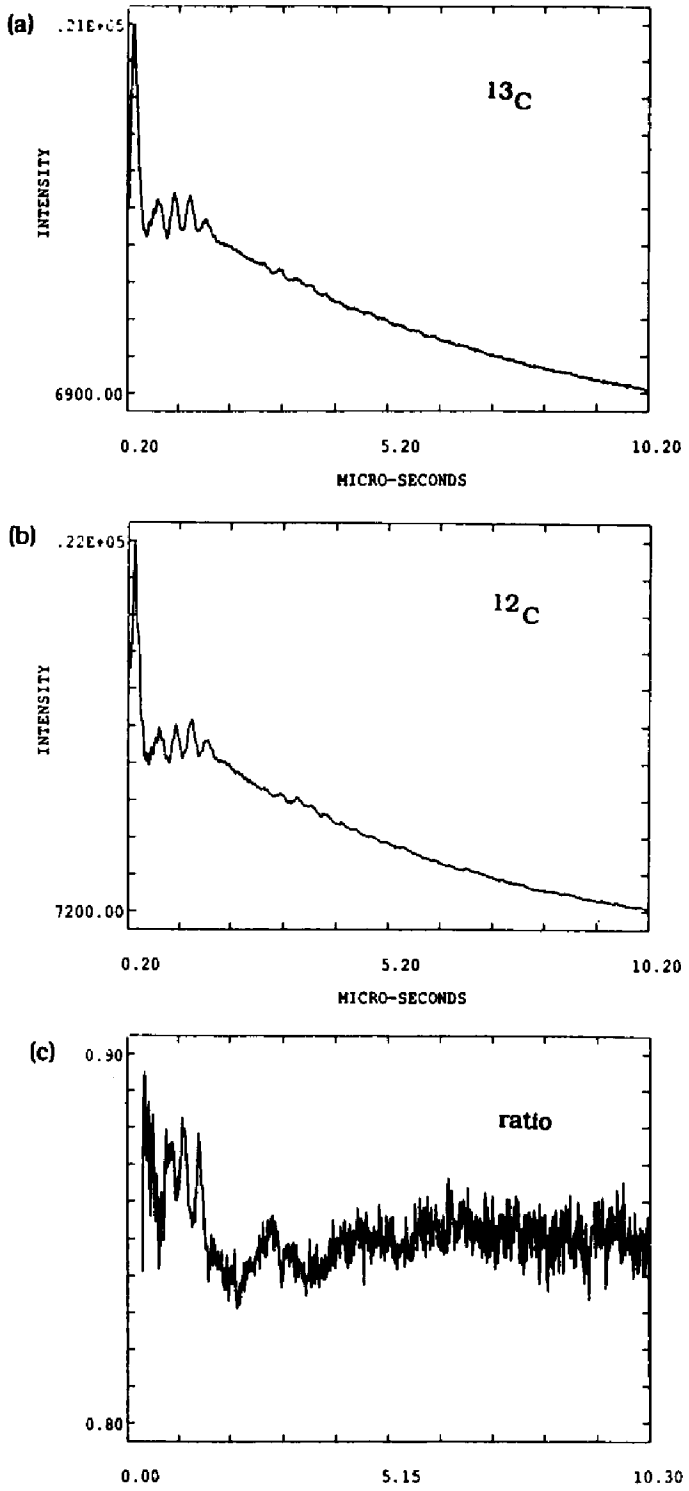

Figure 4.2 (a) Three-pulse ESEEM of ^{13}CN adduct of transferrin at g_{yy}. Data file SE2908.NIP. Frequency-8.866 GHz, Field-2595 G., tau-148 nsec. (b) Three-pulse ESEEM of CN adduct. Data file SE2873.NIP with same parameters as (a). (c) The ratio of (a) with (b).

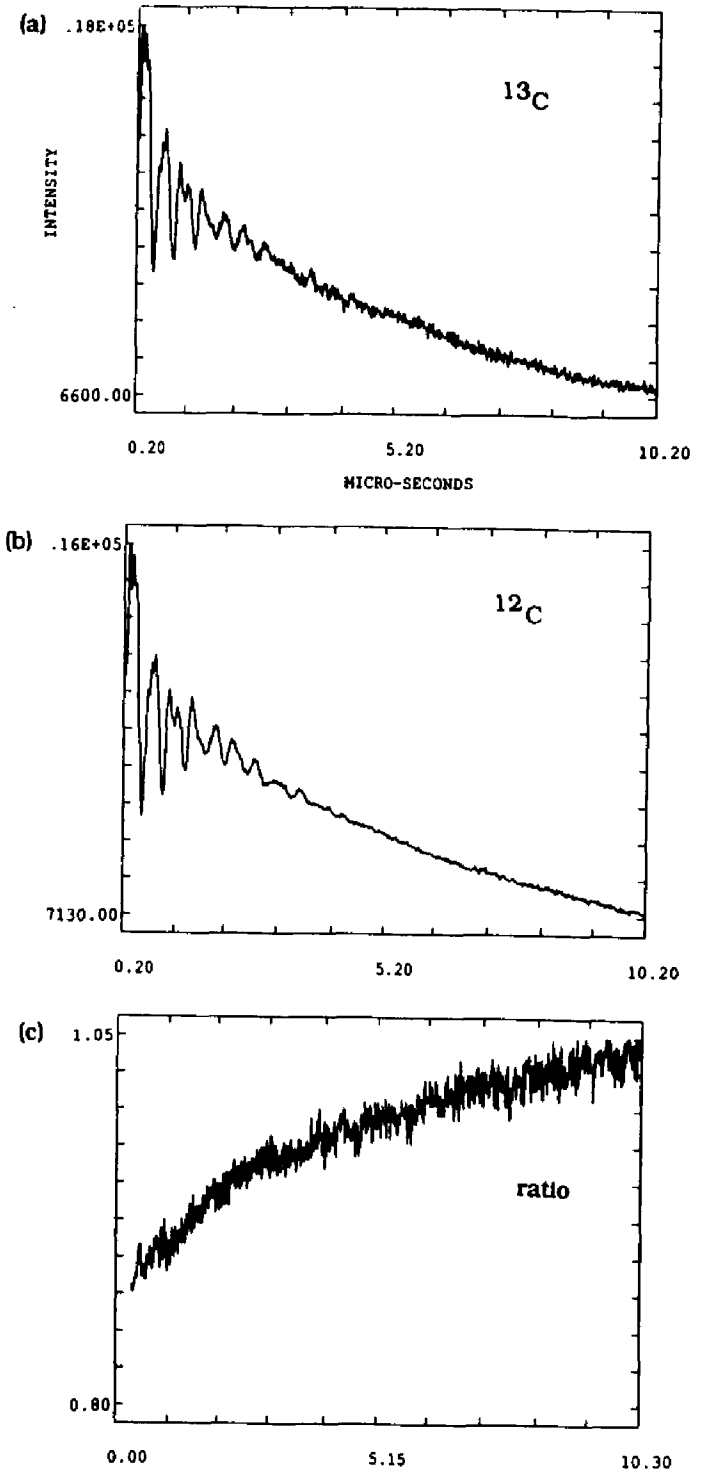

Figure 4.3 (a) Three-pulse ESEEM of ^{13}CN adduct of transferrin at g_{zz} Data file SE2915.NIP. Frequency-8.866 GHz, Field-3256 G., tau-144 nsec. (b) Three-pulse ESEEM of CN adduct. Data file SE2879.NIP with same parameters as (a). (c) The ratio of (a) with (b).

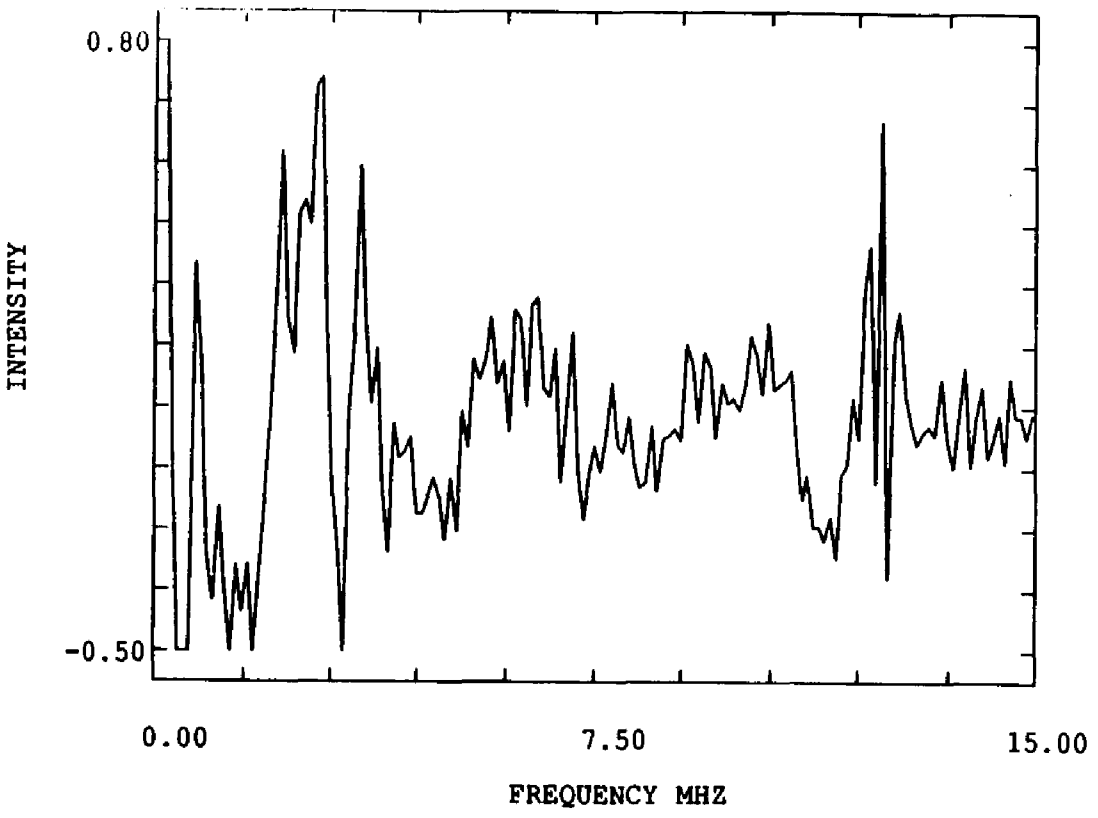

Figure 4.4 Frequency spectrum of Figure 4.2 (c).

approximately to the free precessional frequency of ^{13}C. The consistency of this modulation despite the different experimental conditions for the spectra would seem to indicate that a weakly interacting ^{13}C nucleus is observed at this g-value. The ^{13}C nucleus observed with ENDOR was relatively strongly coupled so the ^{13}C signal observed here would have to correspond to a CN group other than that which gives rise to the ENDOR signal. The ESEEM observed ^{13}C nucleus probably lies along or nearly along the g_{yy} axis which is perpendicular to the orbital containing the unpaired electron. Thus, the coupling to this nucleus is expected to be small. Given the poor signal to noise of the spectra, the few observed periods of modulation, and the number of molecular orientations contributing to the signal at this field, a more comprehensive analysis of this modulation pattern is unrealistic.

The lack of resolved ^{13}C couplings in the ESEEM spectra is not unexpected. The hyperfine couplings of the observed ^{13}C in the ENDOR study were quite large, on the order of 30 MHz. As mentioned in Chapter 1, due to experimental limitations, couplings of these magnitudes are are not observed with X-band ESEEM spectroscopy. An ESEEM study of copper transferrin was also unable to observe ^{13}C modulation due to a carbonate ligand although ^{13}C oxalate did cause modulation[96,97].

Deuterium ESEEM

The effect of solvent exchange was observed by using D_2O as a solvent. The quotient of the envelope of the sample containing D_2O with that of H_2O has the modulation from deuterium nuclei divided by the modulation from substituted protons. The resulting ESEEM

quotient curves have a characteristic modulation frequency and are shown in Figure 4.5 (a),(b), and (c) for g_{xx}, g_{yy}, and g_{zz} respectively. This frequency is coincident with the Zeeman frequency of deuterium and increases with the external field. This result proves the presence of deuterium near the iron nuclei in the protein which means the iron center is accessible to solvent. The frequency spectra of the quotient modulation spectra at the three g-values are shown in Figure 4.6. All of the spectra show a large peak at the free resonance frequency for deuterium. Since no coupling is observed, this spectral line belongs to the deuterium nuclei of ambient water molecules which are not directly coordinated to the iron and to exchangeable deuterons on the protein in the vicinity of the paramagnetic center.

Since the free precessional frequency of deuterium is low, coupled deuterium should be resolved in ESEEM. Resolved deuterium couplings of .8 MHz and 2-4 MHz were observed in metmyoglobin and uteroferrin respectively [99,100]. The lack of resolved couplings in the transferrin adduct proves the absence of any appreciable electron spin density at the surrounding deuterium nuclei and hence a weak coupling and a large Fe-^{2}H distance. These results are consistent with those observed using ENDOR. The ENDOR spectra in Figure 3.4 showed little difference in the proton couplings upon solvent exchange indicating that these couplings were due to ligand protons of the protein and not exchangeable solvent.

Nitrogen ESEEM

Introduction

There were weak ENDOR signals present in the 1-5 MHz range which were probably due to nitrogen, but these were hard to interpret

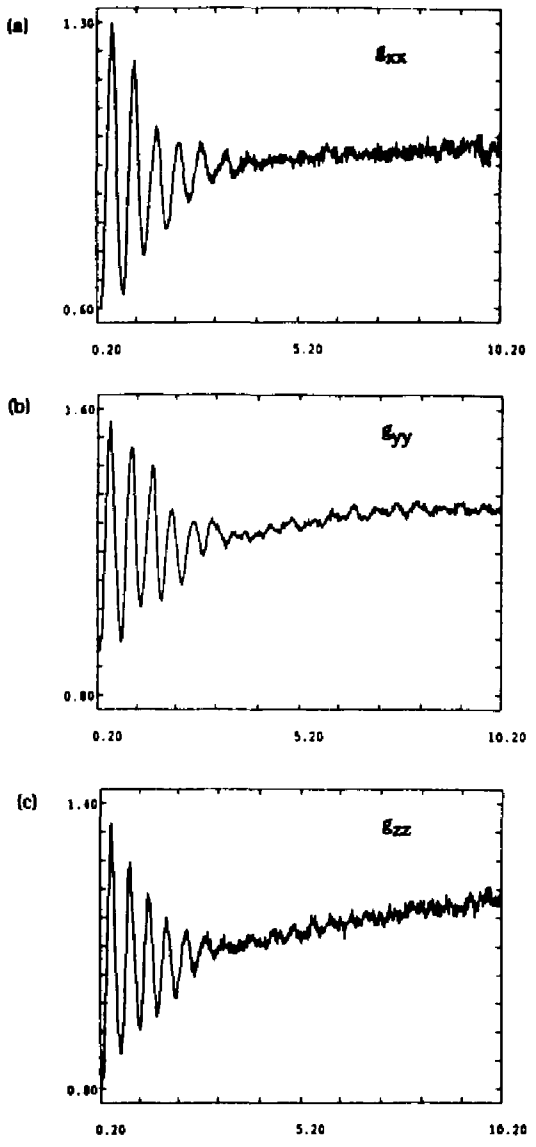

Figure 4.5 (a) Three pulse ESEEM spectrum of D_2O/H_2O at g_{xx}. D_2O data file-SE2900.NIP. Frequency-8.65 GHz, Field-2677 G., tau-175 nsec. H_2O data file-SE2876.NIP. Frequency-8.78 GHz, Field-2677 G., tau-175 nsec. (b) Three pulse ESEEM spectrum of D_2O/H_2O at g_{yy}. D_2O data file-SE2897.NIP. Frequency-8.65 GHz, Field-2906 G., tau-162 nsec. H_2O data file-SE2873.NIP. Frequency-8.78 GHz, Field-2906 G., tau-162 nsec. (c) Three pulse ESEEM spectrum of D_2O/H_2O at g_{zz}. D_2O data file-SE2903.NIP. Frequency-8.65 GHz, Field-3210 G., tau-142 nsec. H_2O data file-SE2879.NIP. Frequency-8.78 GHz, Field-3226 G., tau-145 nsec.

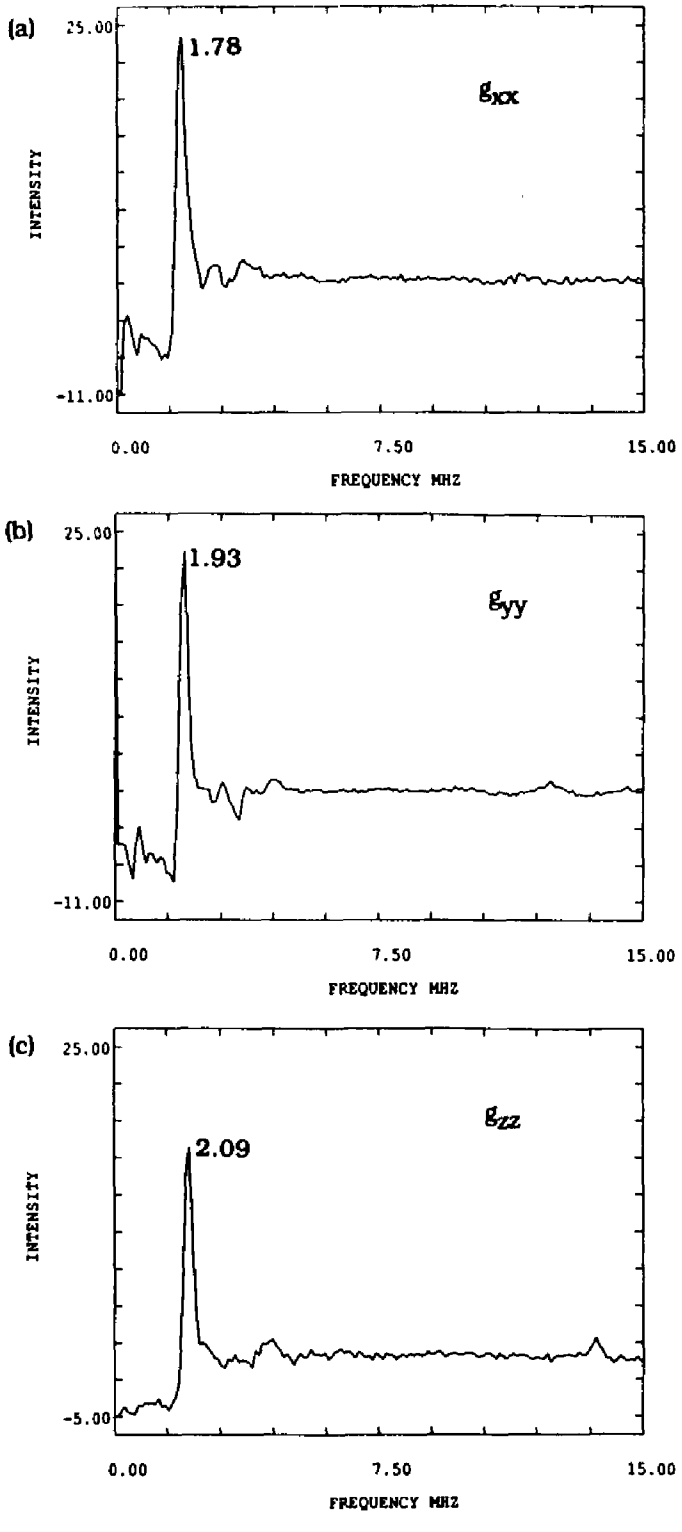

Figure 4.6 Frequency spectra of Figure 4.5.

because of poor signal to noise and rf interference. The weakly coupled low frequency peaks expected for nitrogen interaction are ideal for ESEEM analysis. One would expect modulation from the interaction of electron spins only with nitrogen nuclei with a weak coupling. In cases where the hyperfine coupling is large compared to the Zeeman interaction the microwave pulses are not able to cause modulation since this effect depends on interference between allowed and partially forbidden transitions both originating from the same level. However, as compared to ENDOR spectroscopy, ESEEM makes it possible to study the range of low frequencies expected for more weakly interacting nitrogen nuclei.

ESEEM of ^{15}N

Since ^{15}N has a nuclear spin of 1/2, ESEEM spectra of the $C^{15}N$ adduct were obtained as an aid to determining the hyperfine coupling parameters for the natural abundance nitrogen $C^{14}N$ which has a more complicated spectrum due to quadrupolar interactions. The time domain spectra of the $C^{14}N$ and $C^{15}N$ adducts as shown in Figures 4.7, 4.8 and 4.9 for the g_{xx}, g_{yy}, and g_{zz} fields are distinctly different. With $C^{15}N$ the spectra at the three g-values show modulation frequencies not observed with $C^{14}N$. The frequency spectra of the time domain modulation for $C^{15}N$ are shown in Figures 4.10, 4.11, and 4.12. At the field corresponding to g_{xx} (Figure 4.10) two narrow intense peaks at .59 and 1.59 MHz are centered around the free precessional frequency of 1.15 for ^{15}N. Likewise, along g_{zz} (Figure 4.12) there are two sharp peaks centered about the Zeeman frequency of 1.39 MHz at 1.11 and 1.76 MHz. There are also broader and less intense peaks at 2.70 and 3.53 MHz. At the field corresponding to g_{yy} (Figure 4.11) an intense

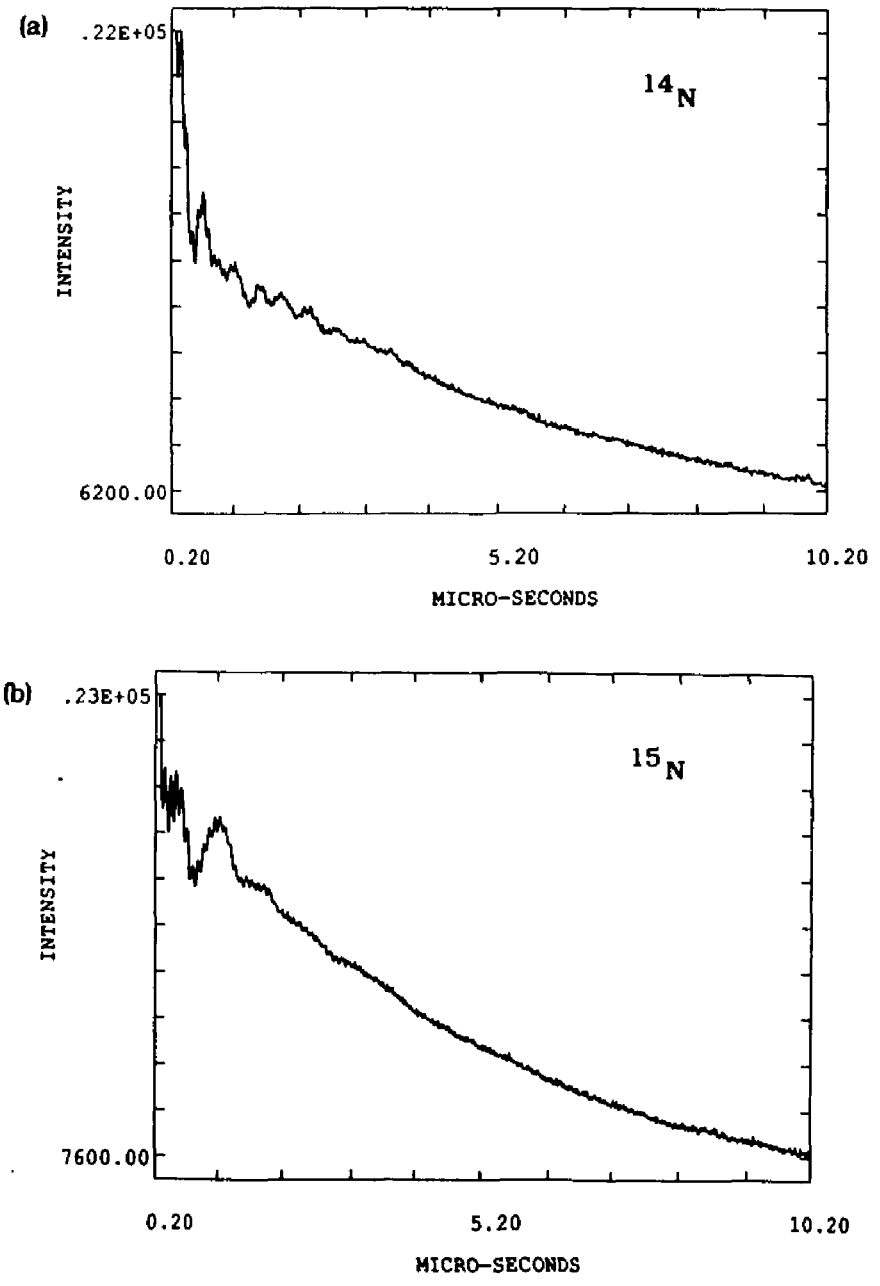

Figure 4.7 (a) Three pulse ESEEM spectrum of $C^{14}N$ adduct along g_{xx}. Data file SE2876.NIP. Frequency-8.78 GHz, Field-2677 G., tau-175 nsec. (b) $C^{15}N$ spectrum. Data file SE2887.NIP. Frequency-8.76 GHz, Field-2677 G., tau-175 nsec.

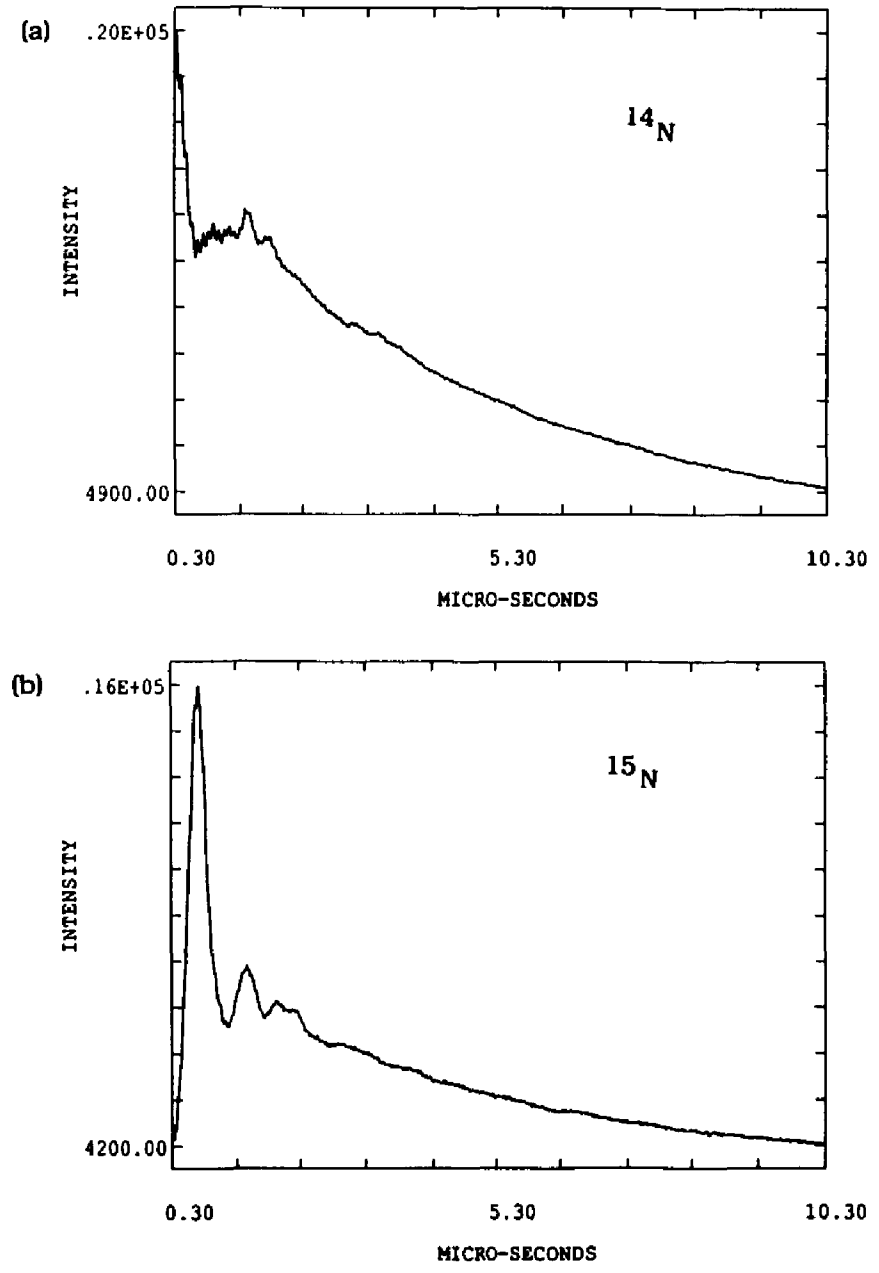

Figure 4.8 (a) Three pulse ESEEM spectrum of $C^{14}N$ adduct along g_{yy}. Data file SE2875.NIP. Frequency-8.78 GHz, Field-2906 G., tau-242 nsec. (b) $C^{15}N$ spectrum. Data file SE2886.NIP. Frequency-8.76 GHz, Field-2906 G., tau-323 nsec.

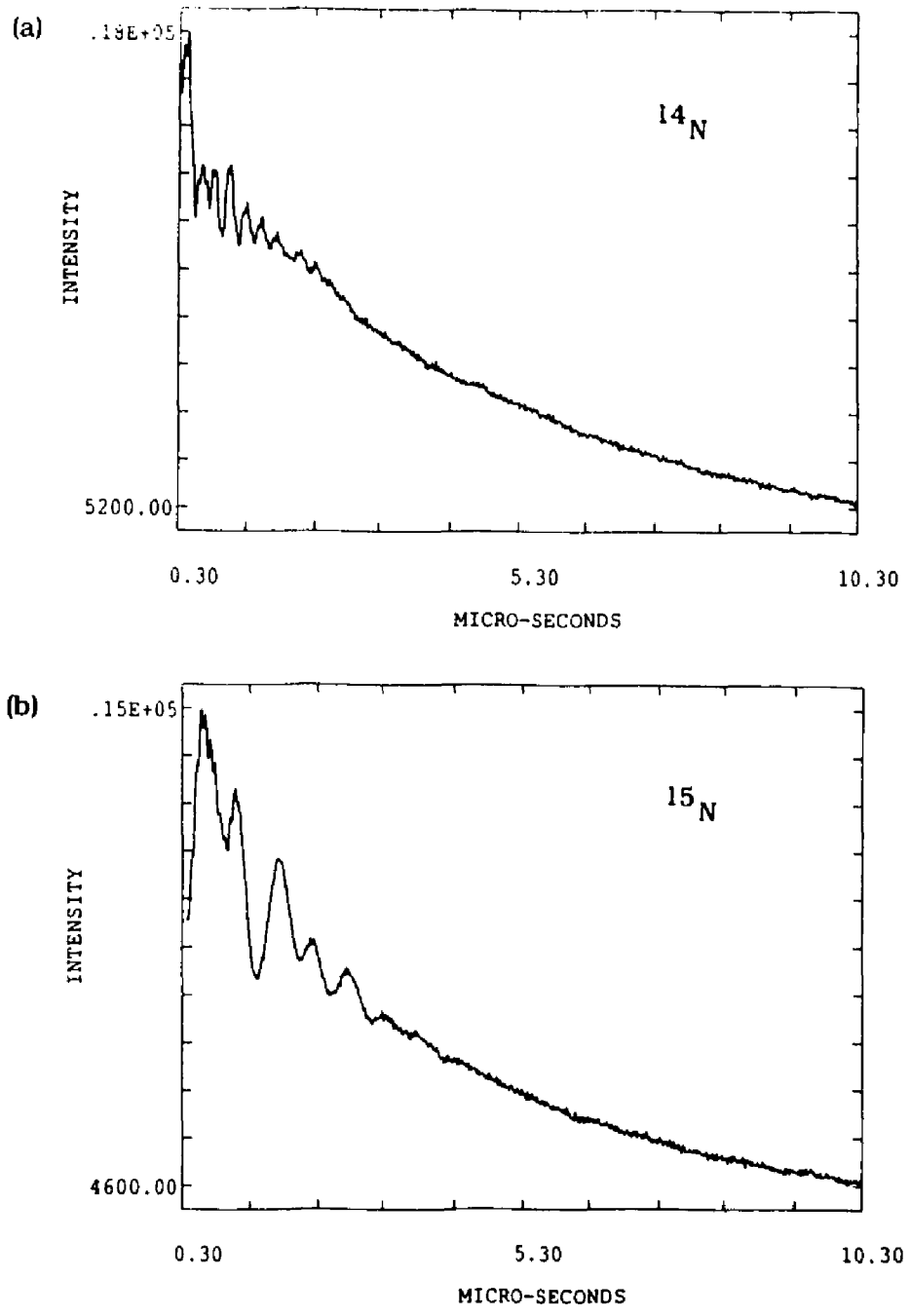

Figure 4.9 (a) Three pulse ESEEM spectrum of $C^{14}N$ adduct along g_{zz}. Data file SE2881.NIP. Frequency-8.78 GHz, Field-3226 G., tau-290 nsec. (b) $C^{15}N$ spectrum. Data file SE2892.NIP. Frequency-8.76 GHz, Field-3226 G., tau-290 nsec.

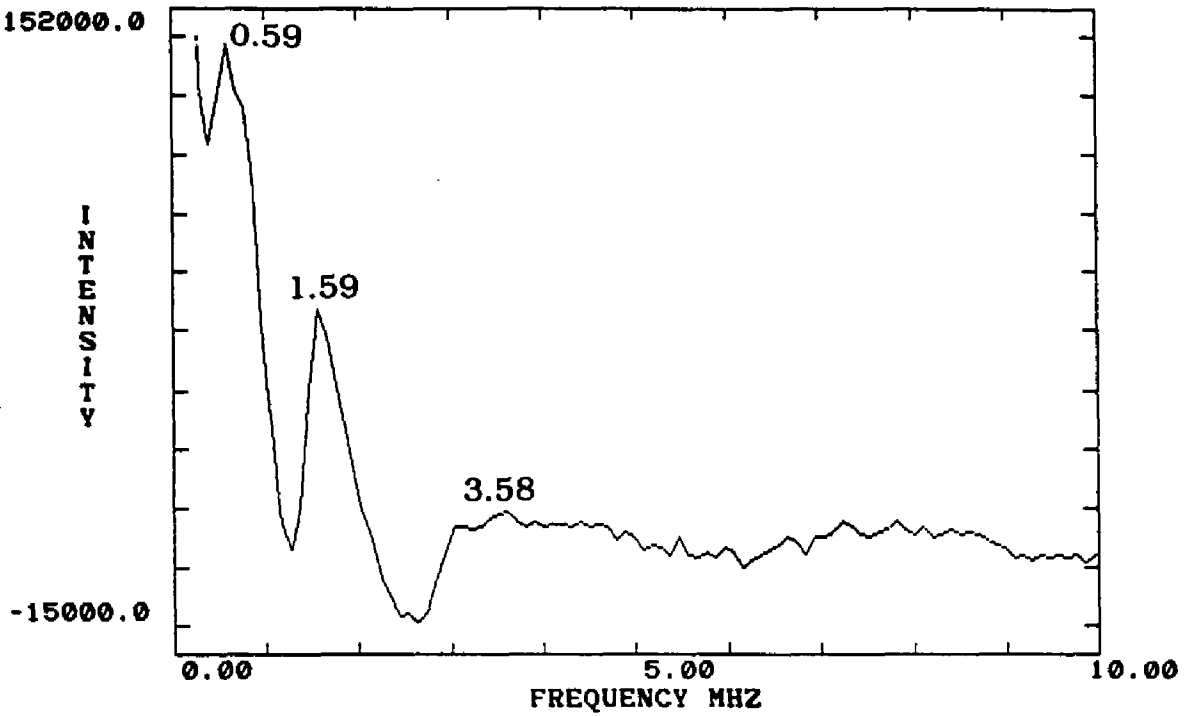

Figure 4.10 Frequency spectrum of Figure 4.7 (b).

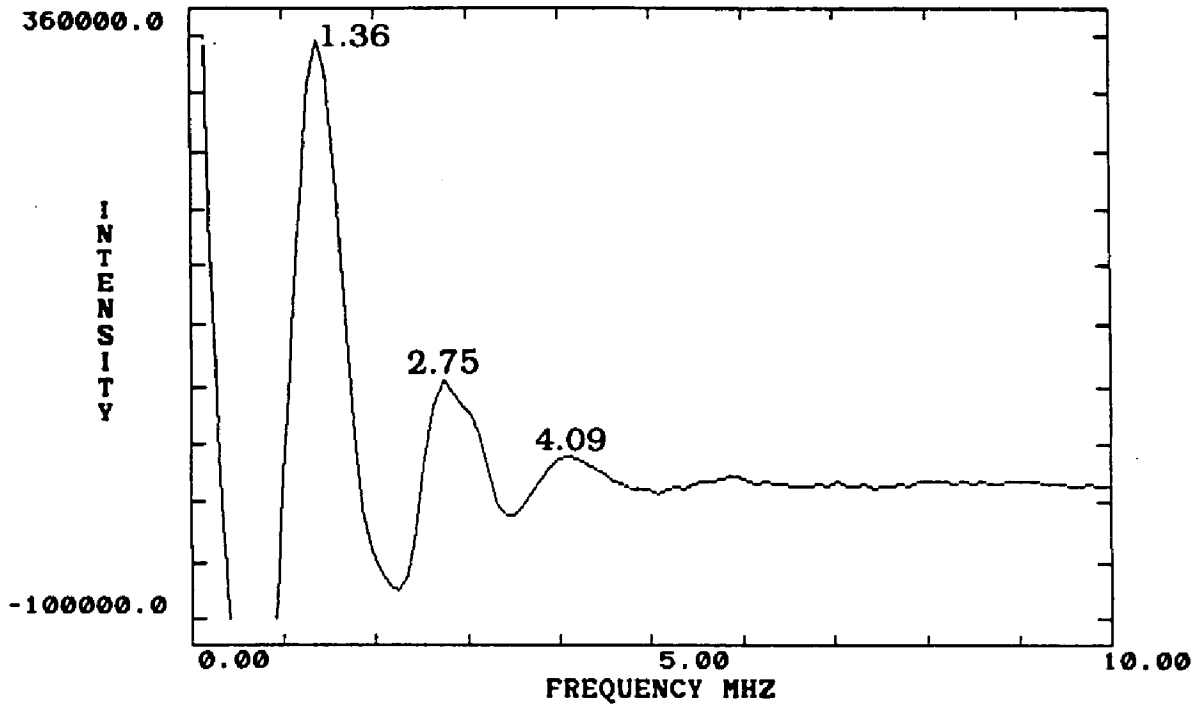

Figure 4.11 Frequency spectrum of Figure 4.8 (b).

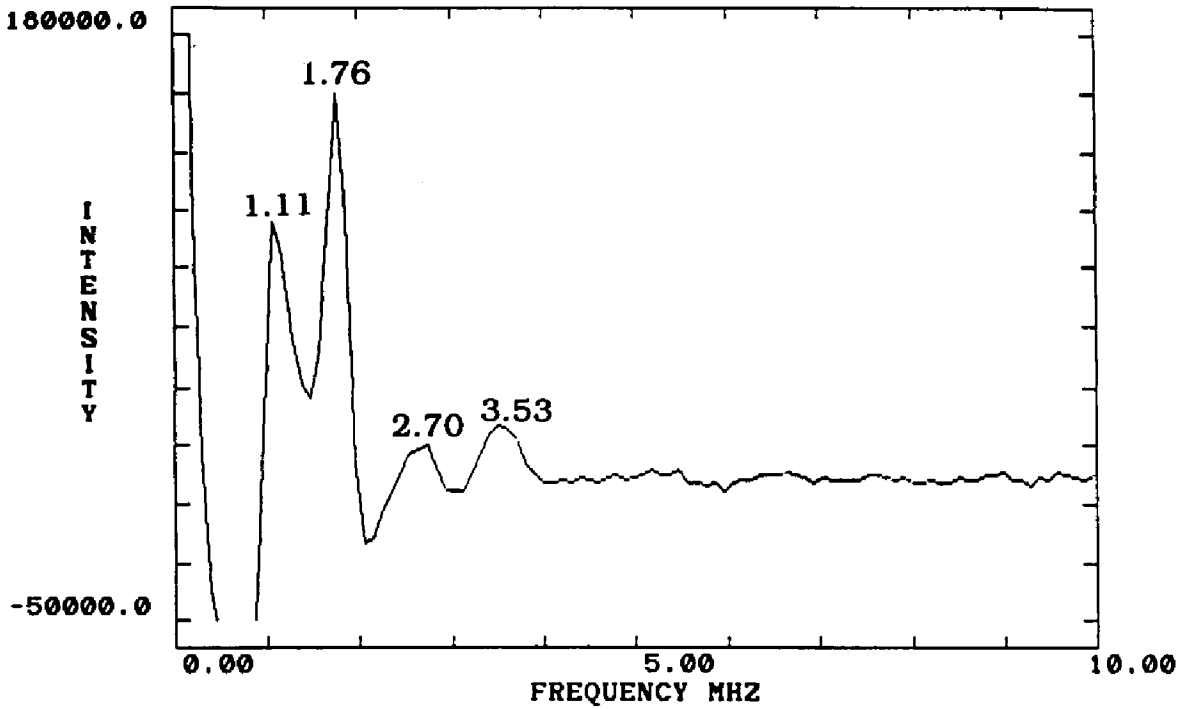

Figure 4.12 Frequency spectrum of Figure 4.7 (b).

peak at 1.36 MHz is observed with less intense peaks at 2.75 and 4.09 MHz. A single sharp peak at the proton Zeeman frequency is observed in all spectra, but is not shown in the figures.

Low amplitude components at twice the frequency of intense fundamentals are evident in many of the two- and three-pulse ESEEM patterns. The appearance of such combination frequencies indicates that more than a single nucleus contributes to the echo modulation. In principle, the number of equivalent nuclei can be deduced from the ESEEM pattern, but a variety of factors complicate such an analysis. One can rule out a single nucleus causing modulation, but cannot determine a definitive number.

When two or more nuclei are coupled to the same electron spin, the resultant modulation pattern is the product of patterns due to nuclei considered singly. Thus if the envelope for one ^{15}N contains the terms $\sin\omega_a(\tau +T)$, $\sin\omega_b(\tau +T)$ (as in Equation 1.6) then the envelope for two will contain terms $\sin2\omega_a(\tau +T)$, $\sin2\omega_b(\tau +T)$ and combination terms $\sin(\omega_a + \omega_b)(\tau +T)$. Likewise, the modulation pattern for three equivalent nuclei will contain harmonics at three times the frequency. Contributions due to these harmonics and combinations are relatively weak, but where they are observed they prove the existence of two or more nuclei.

Such harmonics and combinations are observed in the ^{15}N ESEEM spectra. At g_{yy} there appears to be a very weak peak at 4.09 MHz which is approximately three times the most intense peak at 1.36 MHz (Figure 4.11(c)). A harmonic such as this would indicate the possible presence of three CN groups. However, this frequency is not persistent since the Fourier transform of the same data after removing

ten initial points as shown in Figure 4.13 does not have this peak. This observation indicates that the frequency at 4.09 MHz is probably due to an artifact in the Fourier transform process and is not from a true modulation. In any case, the presence of the combination and harmonic peaks makes it apparent that there are at least two equivalent CN groups coordinated to the iron center.

Although there have been reports of ESE at frequencies from 1 to 34.2 GHz [101-104], typically ESE has been done at 9.5 GHz, X-band. The importance and advantages of taking data at several spectrometer frequencies has only recently been recognized. To facilitate analysis of the nitrogen interaction, modulation envelopes were taken at two frequencies. Sample frequency domain spectra at the three g-values at the second spectrometer frequency, approximately 10.5 GHz, are shown in Figures 4.14, 4.15, and 4.16. The two-pulse data at the same frequency is shown in Figures 4.17, 4.18, and 4.19.

With data at more than one frequency, the isotropic and anisotropic hyperfine couplings can be determined [105]. The observed ESEEM frequency, ν_{obs} is:

$$(\nu_{obs})^2 = (\nu_n + \xi m_s A)^2 + m_s^2 B^2 \qquad (4.1)$$

where ν_n is the free precessional frequency of ^{15}N, ξ is the sign of the hyperfine coupling (i.e. $\xi = \pm 1$) and A and B are the isotropic and anisotropic parts of the hyperfine coupling respectively. Multiplying out the equation and separating the terms which are frequency independent from those that are dependent gives:

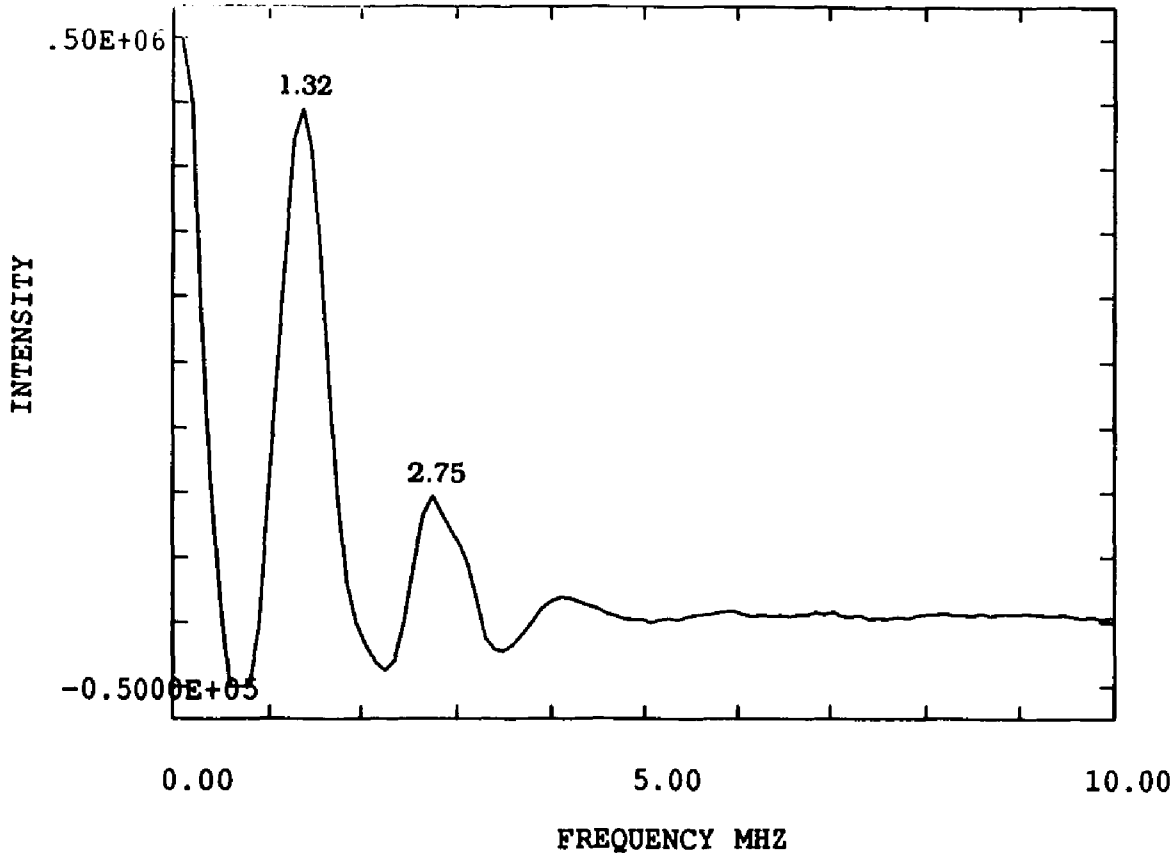

Figure 4.13 Frequency spectrum of Figure 4.8 (b) when 10 initial points are deleted from the time spectrum.

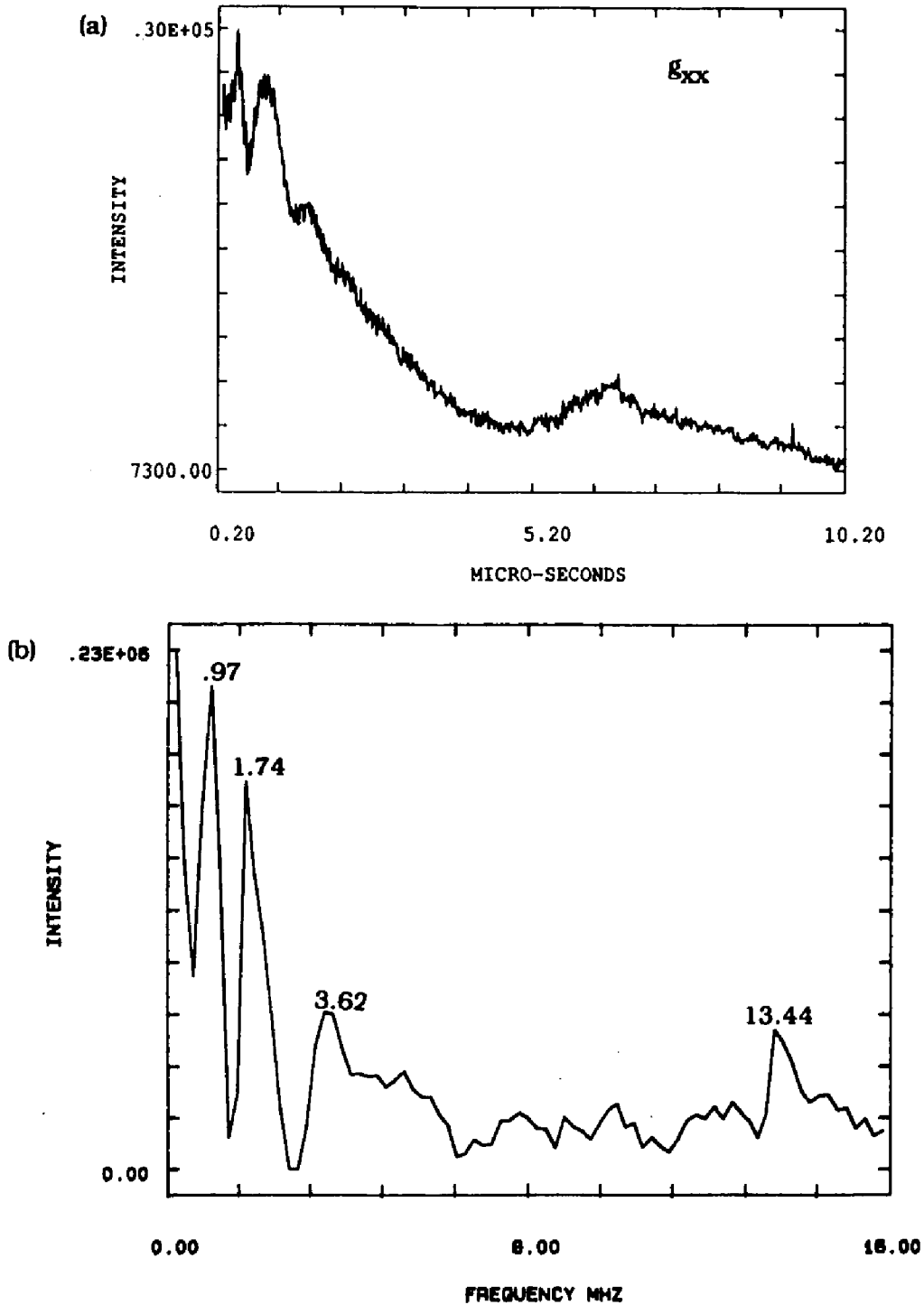

Figure 4.14 (a) Three pulse ESEEM spectrum of $C^{15}N$ adduct along g_{xx}. Data file SE4724.NIP. Frequency-10.34 GHz, Field-3175 G., tau-207 nsec. (b) Fourier transform of (a).

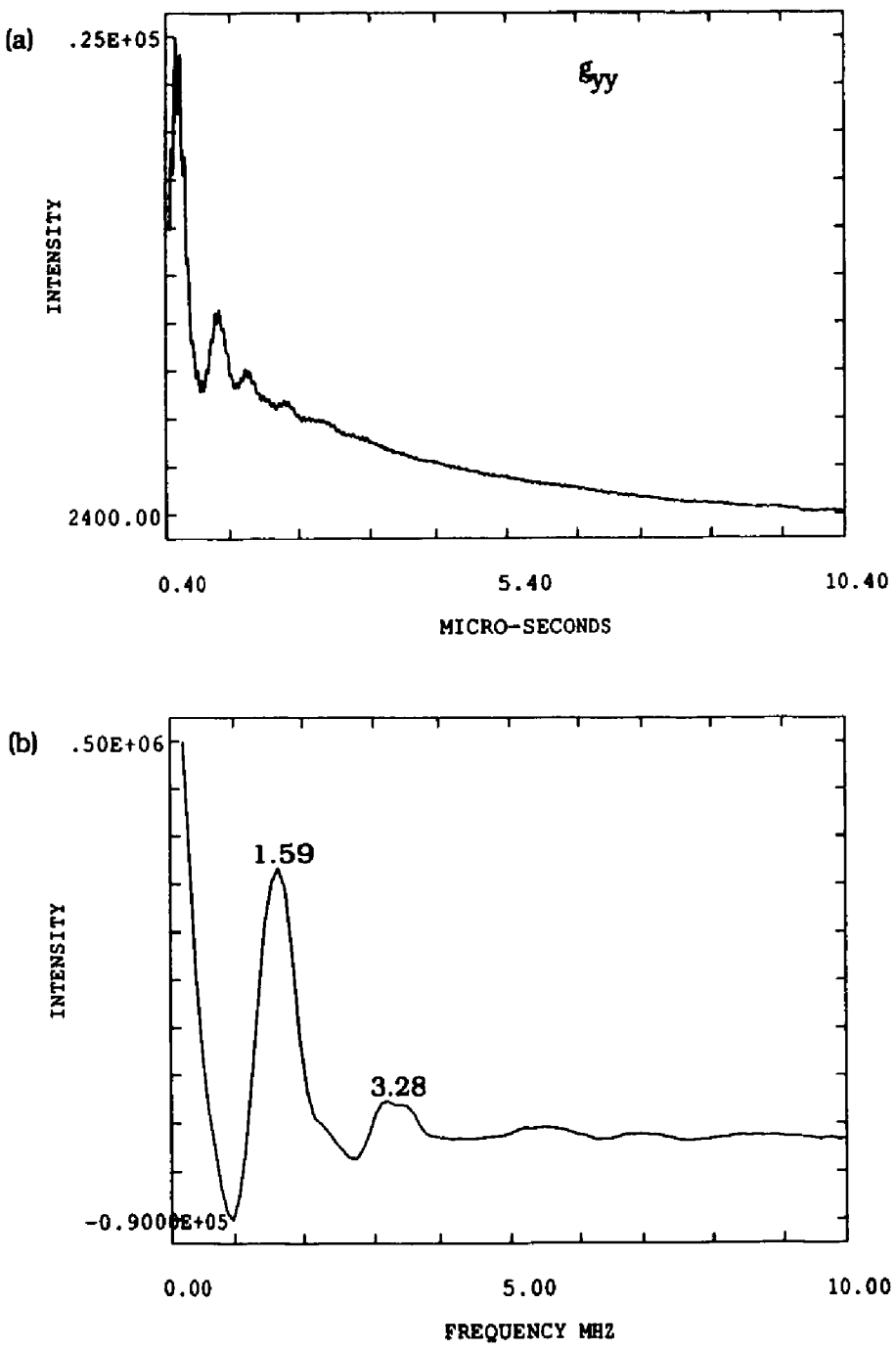

Figure 4.15 (a) Three pulse ESEEM spectrum of $C^{15}N$ adduct along g_{yy}. Data file SE4726.NIP. Frequency-10.32 GHz, Field-3430 G., tau-381 nsec. (b) Fourier transform of (a).

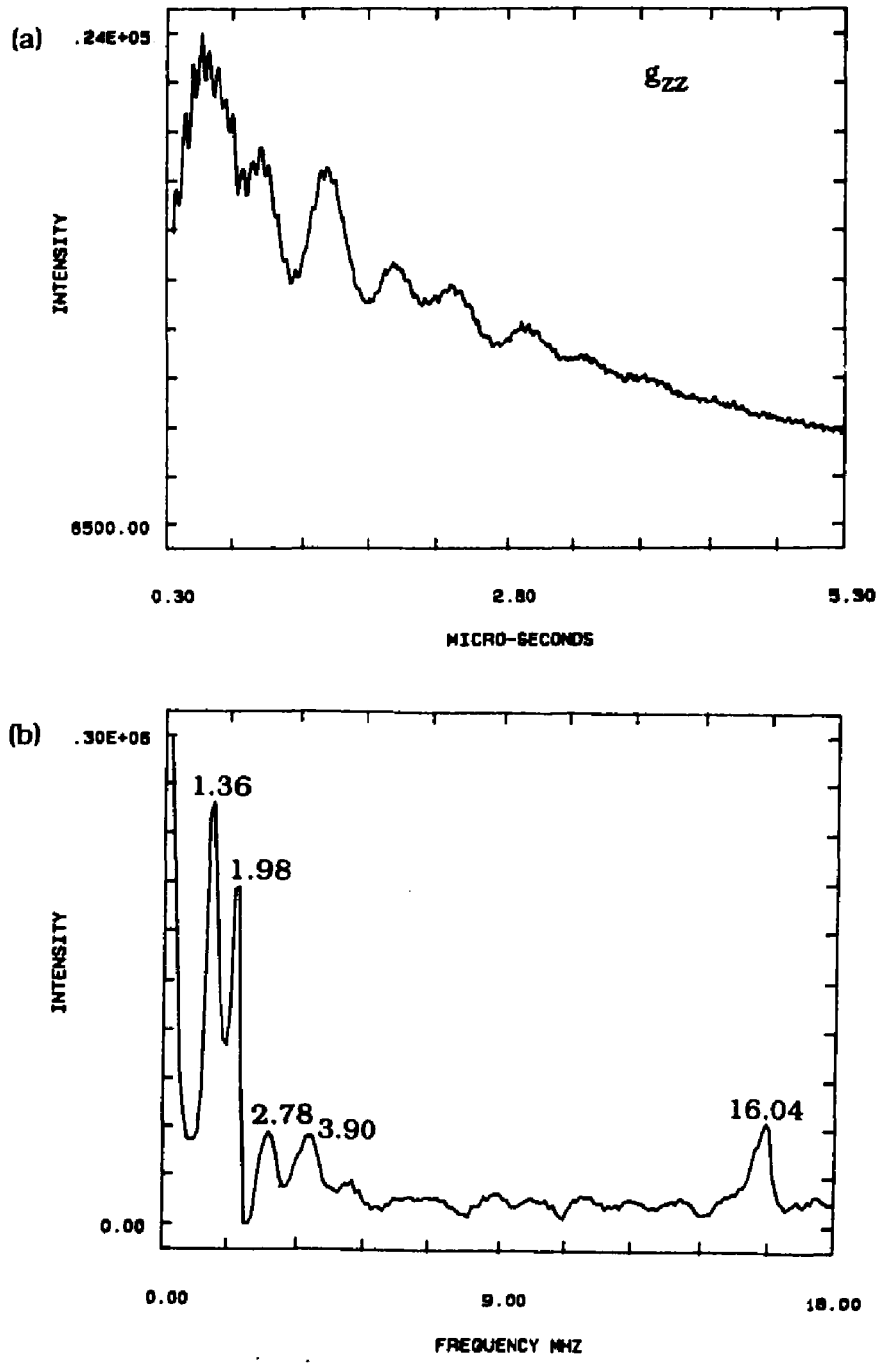

Figure 4.16 (a) Three pulse ESEEM spectrum of $C^{15}N$ adduct along g_{zz}. Data file SE4727.NIP. Frequency-10.32 GHz, Field-3807 G., tau-257 nsec. (b) Fourier transform of (a).

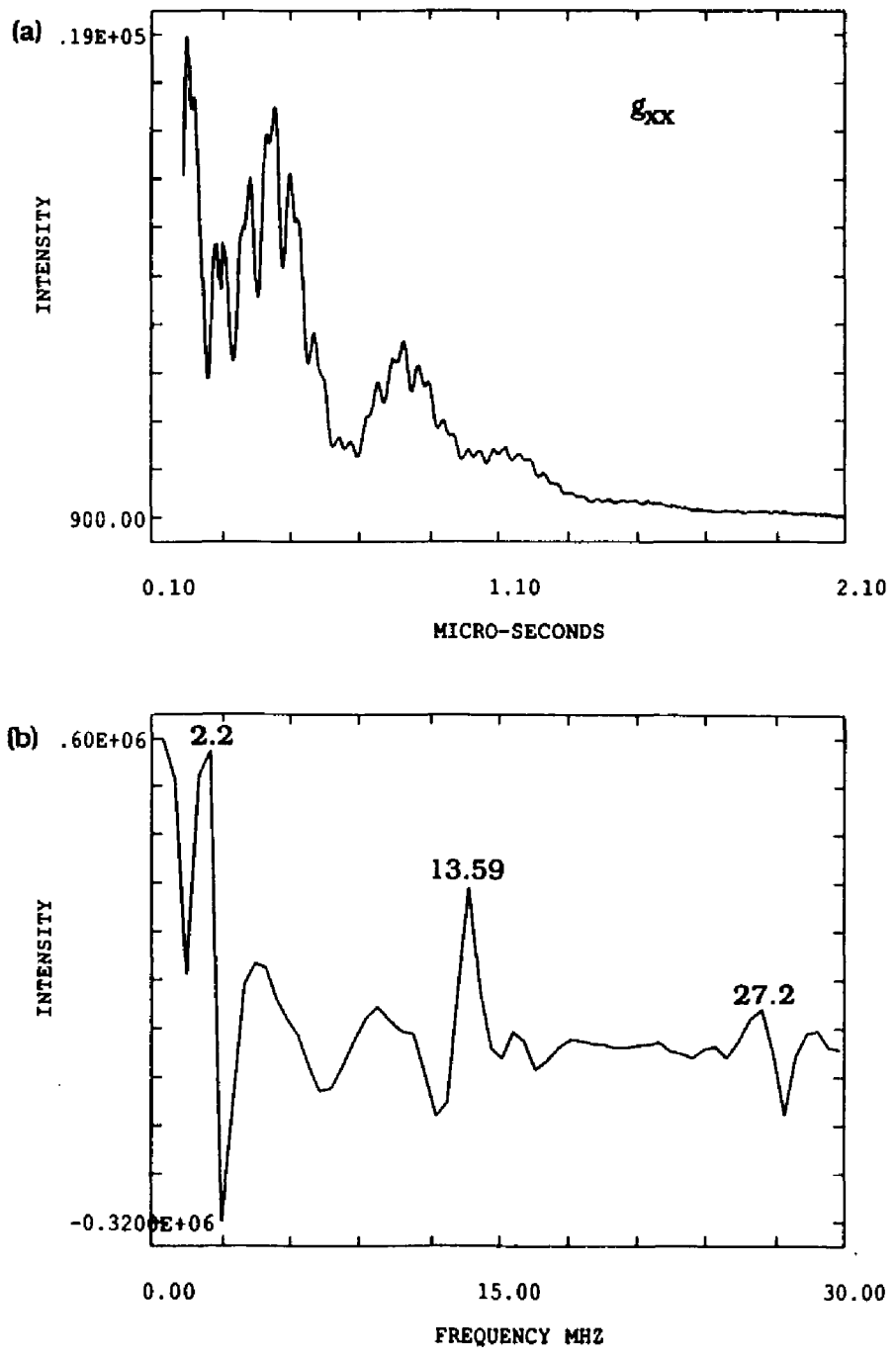

Figure 4.17 (a) Two pulse ESEEM spectrum of $C^{15}N$ adduct along g_{xx}. Data file TP1438.NIP. Frequency-10.34 GHz, Field-3175 G. (b) Fourier transform of (a).

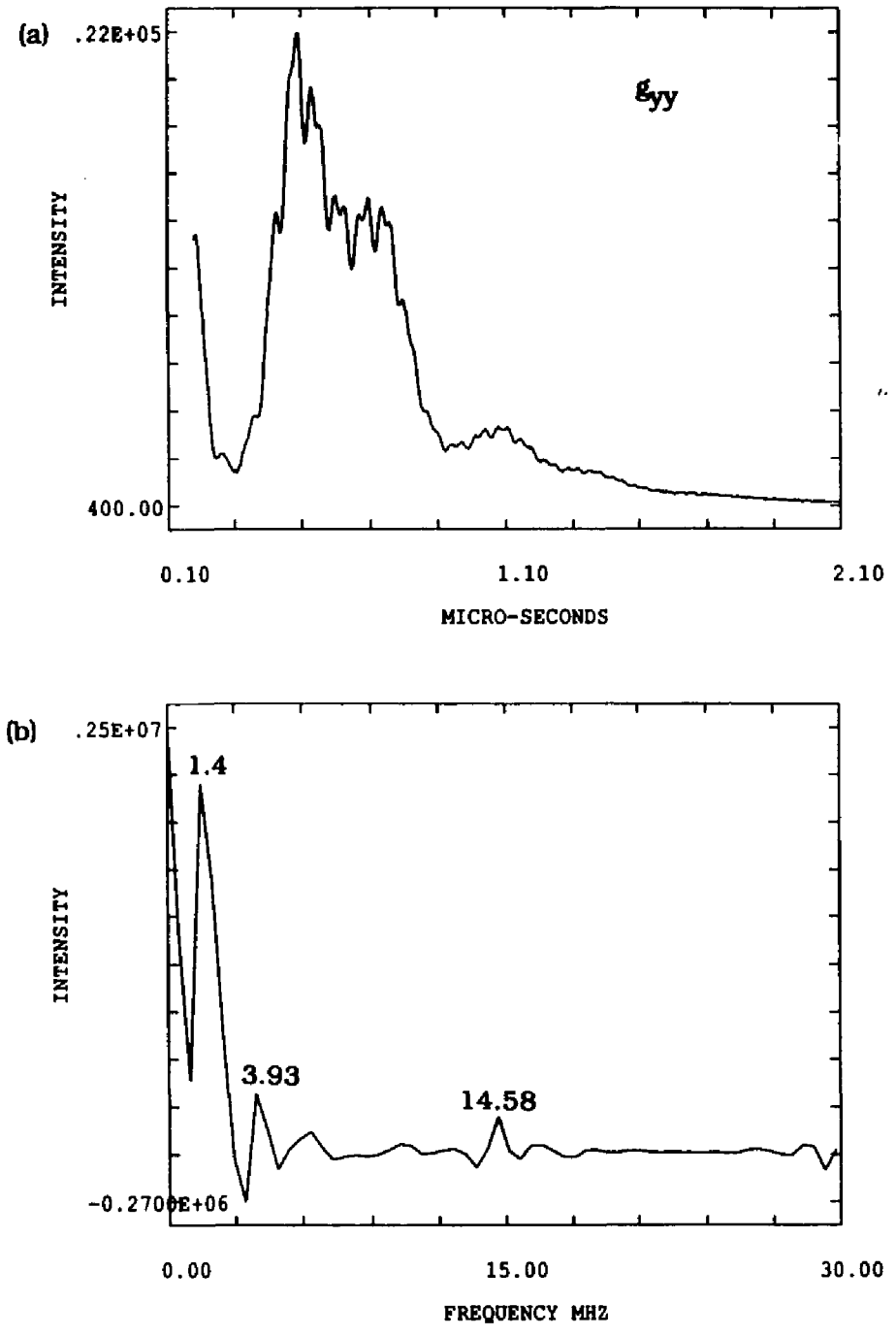

Figure 4.18 (a) Two pulse ESEEM spectrum of $C^{15}N$ adduct along g_{yy}. Data file TP1439.NIP. Frequency-10.32 GHz, Field-3430 G. (b) Fourier transform of (a).

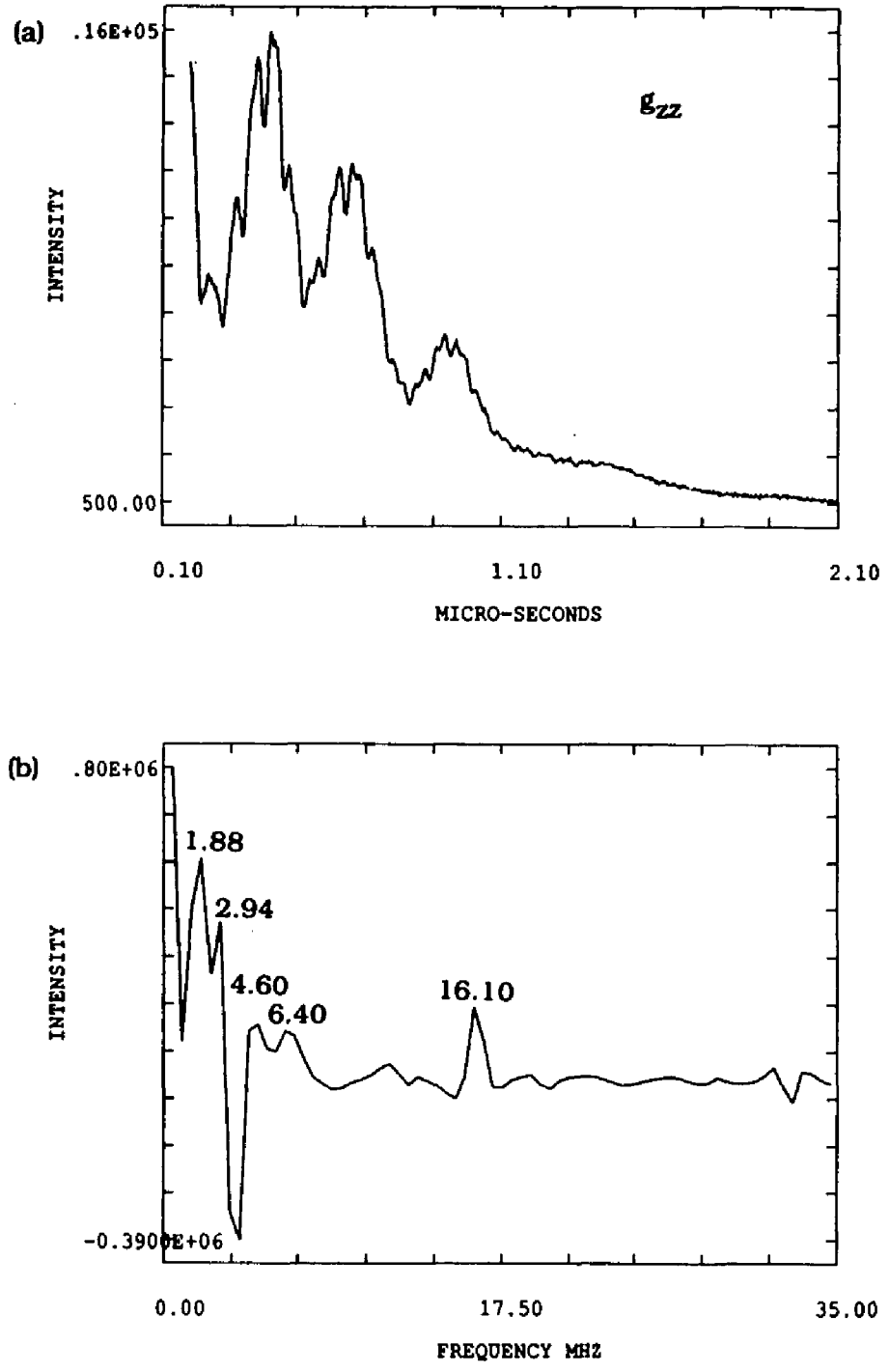

Figure 4.19 (a) Two pulse ESEEM spectrum of $C^{15}N$ adduct along g_{zz}. Data file TP1440.NIP. Frequency-10.32 GHz, Field-3807 G. (b) Fourier transform of (a).

$$\nu_{obs}^2=\nu_n^2 + 2m_s\xi\nu_nA + \xi^2m_s^2A^2 +m_s^2B^2$$

$$\nu_{obs}^2 - \nu_n^2 = \xi A\nu_n +1/4\ (A^2 +B^2)$$

$$4(\nu_{obs}^2- \nu_n^2) = 4\xi A\nu_n + (A^2 +B^2) \qquad (4.2)$$

Thus a graph of $4(\nu_{obs}^2- \nu_n^2)$ versus ν_n for the different spectrometer frequencies will result in a line with slope $4\xi A$ and intercept of $(A^2 + B^2)$. Note that the intercept cannot be less than zero. Figures 4.20 and 4.21 show these graphs for the g_{xx} and g_{zz} data. There is some uncertainty in peak position since different values of tau cause the frequency peak to shift position slightly. The peak positions for ^{15}N at all tau values are listed in Table 4.1. The error bars in Figure 4.20 are based on the variations in the peak positions for different tau values. From these graphs the values for the field set at g_{xx} are A= 0.80 ± 0.07 and B=0.23 ± 0.23 MHz and at g_{zz} are A=0.65 and B=0.65 MHz. This indicates a weak isotropic coupling as would be expected for a cyanide nitrogen which is several bond lengths from the unpaired electron spin. The anisotropic contribution to the coupling, B, should be predominantly dipolar at this distance. Although the error in the value for B along g_{xx} is large, it does indicate that the nitrogen is not directly along the g_{xx} axis. Since the ENDOR analysis placed the carbon along the g_{xx} this means that the carbon-nitrogen bond must not be aligned with the g_{xx} axis. As noted, spectra along g_{yy} (Figures 4.11 and 4.15) have only a single frequency peak with harmonics and cannot be analyzed similarly. Analysis at this particular g-value is complicated since many orientations are being observed with the field along g_{yy}. The fact that the single peak at g_{yy} shows up at the Zeeman

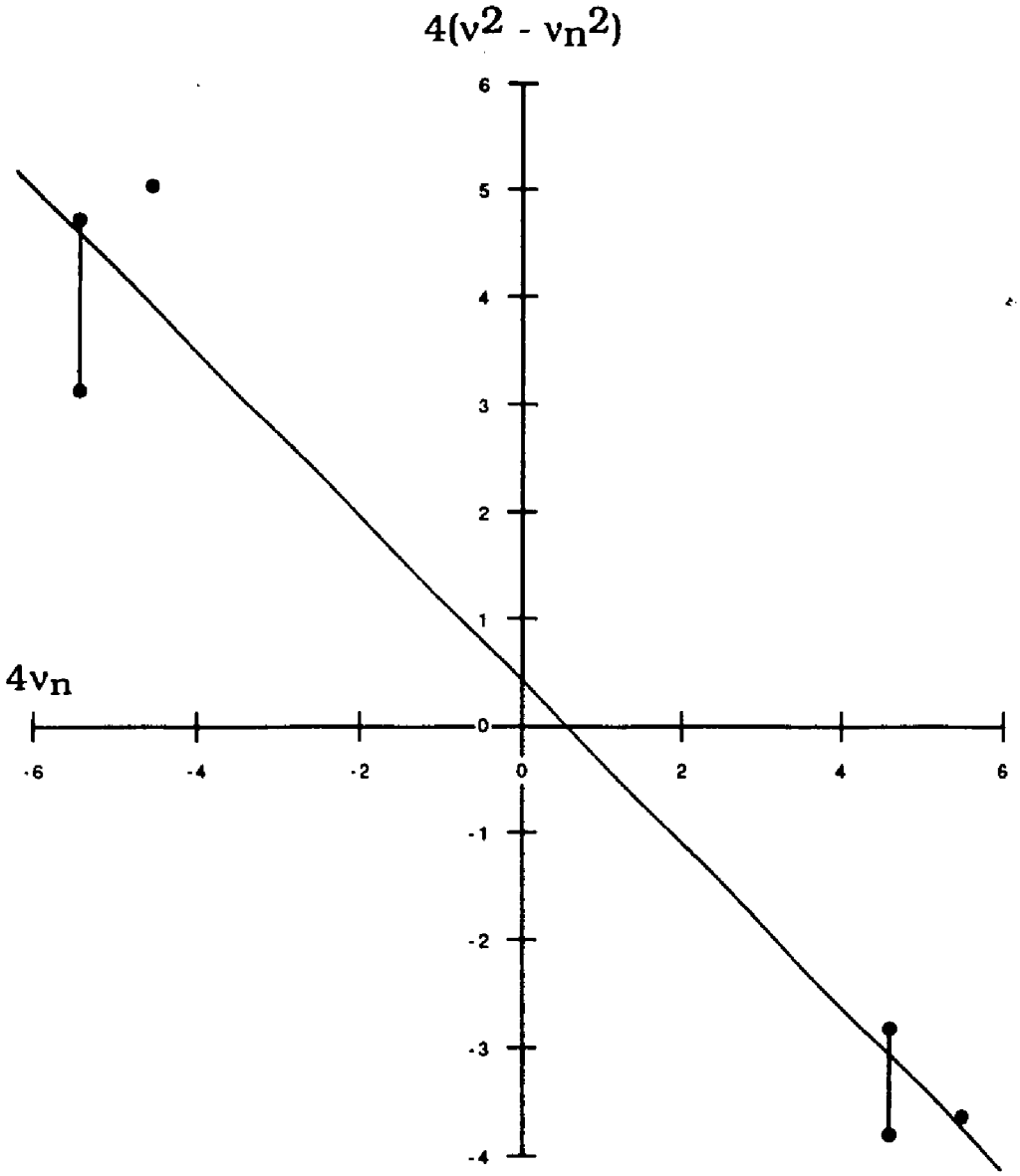

Figure 4.20 Graph of ESEEM data along g_{xx} as described by equations 4.1 and 4.2.

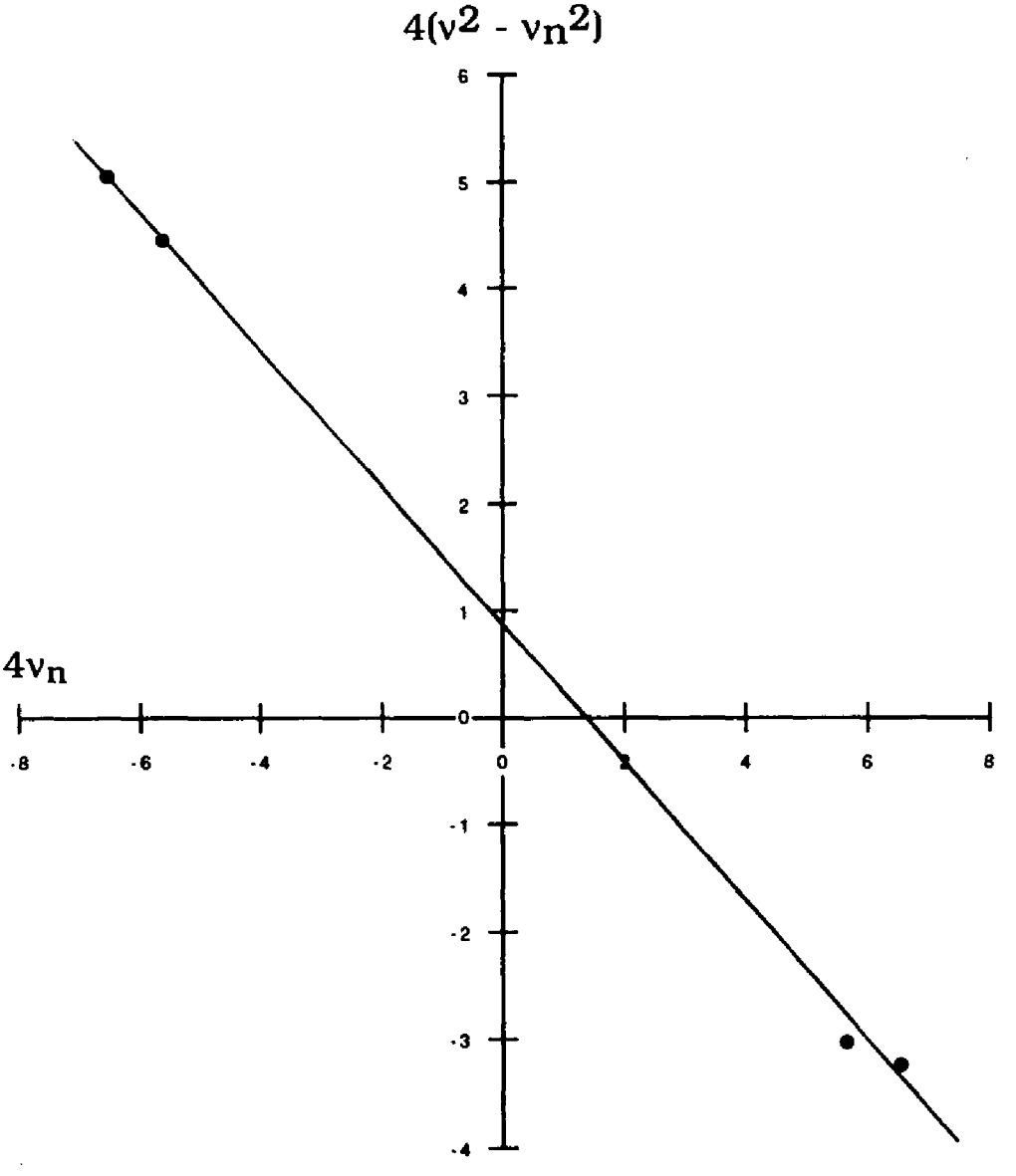

Figure 4.21 Graph of ESEEM data along g_{zz} as described by equations 4.1 and 4.2.

Frequency (GHz)	tau (μsec)	Peak Position (MHz)
		g_{xx}
8.78	175	.59 1.59 3.58
	263	.77 1.60
		g_{yy}
	162	1.36 2.75 4.09
	242	1.32 2.73 4.02
	323	1.35 2.73 4.06
		g_{zz}
	145	.48 1.09 1.75 2.5 3.60
	218	1.10 1.75 2.70 3.58
	290	1.11 1.76 2.70 3.53
		g_{xx}
10.34	207	.97 1.74 3.62
	415	.99 2.19 3.62
		g_{yy}
	191	1.53 3.19
	381	1.59 3.28
		g_{zz}
	257	1.36 1.98 2.78 3.90
	342	1.24 1.98 2.79 3.97

Table 4.1 ESEEM peak positions of $C^{15}N$ with various values for τ at spectrometer frequencies of 8.78 and 10.34 GHz.

frequency for ^{15}N may be the result of several factors including the magnitude of the coupling in combination with the many orientations which results in loss of resolution of the fine structure.

Additional analysis of the ^{15}N cyanide coupling could be approached in two ways. One possibility is tracking the ESEEM frequencies over the entire range of EPR absorption. This study has been limited to spectra taken at the three principal g-values, but spectra could be taken at many more fields which might allow resolved couplings to be observed close to g_{yy}. Alternatively, one could take spectra at additional spectrometer frequencies. The frequency range for the spectrometer used in these is experiments is limited to 8-11 GHz, but data at additional spectrometer frequencies would result in more points on the graphs of Figures 4.20 and 4.21 which would help reduce the uncertainty in the A and B values obtained.

ESEEM of ^{14}N

Quadrupole revisited. Nuclei with a nuclear spin, $I \geq 1$ possess a quadrupole moment, and therefore an ESEEM analysis of these nuclei must take into account the nuclear quadrupole interaction as well as electron-nuclear hyperfine coupling. The discussion of quadrupole in Chapter 1 was limited to cases of a weak axial quadrupole interaction. The requirement of a weak quadrupole interaction compared with the Zeeman coupling is well fulfilled for nuclei like deuterium, but violated for ^{14}N which also has a nuclear spin of I=1. In the X-band range which was used in these experiments, the Zeeman frequency of ^{14}N is about 1 MHz. Published data demonstrates that the quadrupole coupling constants for ^{14}N range from 1 to 5 MHz. Thus the

quadrupole coupling for ^{14}N is comparable with or exceeds the nuclear Zeeman frequency.

In disordered systems, ^{14}N nuclei induce various modulation frequencies differing essentially from the Zeeman frequency. There are many examples of deep modulation caused by ^{14}N with periods of several microseconds. Most often this modulation is caused by ^{14}N nuclei that are separated from the metal by several bonds. Since the general problem of analyzing ESEEM frequencies and amplitudes with strong quadrupole interaction has not been solved analytically for the ESE, magnetic coupling data are usually obtained from the Fourier transform of the ESE data.

The origins of the possible transitions can be understood by considering the energy diagram of an I=1 case.

The quadrupolar Hamiltonian is:

$$\hat{\mathcal{H}}_Q = e^2Qq/(4I(2I-1))\ [3\hat{I}^2_z - \hat{I}^2 - \eta/2(\hat{I}^2_+ + \hat{I}^2_-)] \qquad (4.3)$$

The quantity η is the asymmetry parameter and e^2Qq is the quadrupole coupling constant. The parameter K will be defined as $e^2Qq/4$. The complete Hamiltonian describing the system would include the term in Equation 4.3 as well as the terms in Equation 1.2. Figure 4.22 shows the resultant energy diagram. There are up to six "allowed" (normally forbidden $\Delta m_I=2$ transitions become allowed due to mixing of the states by the $\hat{I}^2_+$ and $\hat{I}^2_-$ operators) ESEEM transitions which are (to second order):

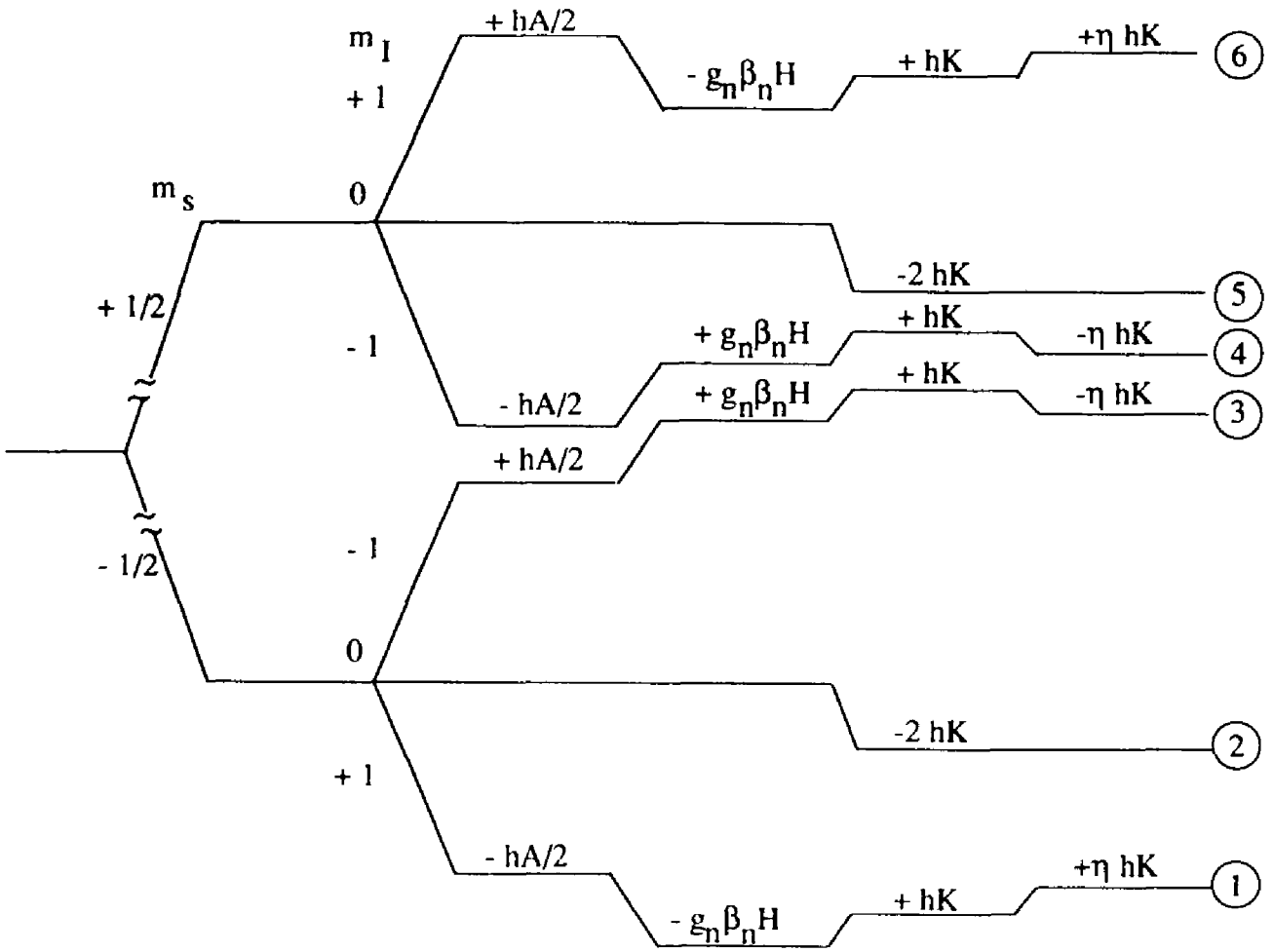

Figure 4.22 Energy diagram for an S=1/2, I=1 system as described by the Hamiltonian in equations 1.2 and 4.3.

$$6\leftrightarrow5 = hA/2 - g_N\beta_N H + 3hK + \eta hK \quad (4.5)$$

$$5\leftrightarrow4 = hA/2 - g_N\beta_N H - 3hK + \eta hK$$

$$6\leftrightarrow4 = hA - 2g_N\beta_N H + 2\eta hK \quad \text{from the upper spin manifold.}$$

$$3\leftrightarrow2 = hA/2 + g_N\beta_N H + 3hK - \eta hK \quad (4.6)$$

$$2\leftrightarrow1 = hA/2 + g_N\beta_N H - 3hK - \eta hK$$

$$3\leftrightarrow1 = hA + 2g_N\beta_N H - 2\eta hK \quad \text{from the lower spin manifold.}$$

Qualitative analysis [106,107] and subsequent numerical calculations [108] have shown that the ESEEM frequencies from ^{14}N which are actually observed in the ESE spectra of a disordered system depend on the ratio of ν_{eff}/K where $\nu_{eff} = g_N\beta_N H \pm A/2$.

Under conditions of exact cancellation when the nuclear Zeeman is equal to the hyperfine coupling, ν_{eff} equals zero for the upper spin manifold. The transition frequencies from the upper spin manifold given in equation 4.5 will then be equivalent to the zero-field NQR frequencies of :

$$\nu_+ = K(3 + \eta) \quad (4.7)$$

$$\nu_- = K(3 - \eta) \quad (4.8)$$

$$\nu_0 = 2K\eta \quad (4.9)$$

The inversion of energy levels 4 and 5 of Figure 4.22 occurs in the exact cancellation situation which causes the sign of equation 4.8 to be opposite that in equation 4.5. These frequencies display the characteristic of NQR frequencies where the sum of the two lower

frequencies is equal to the higher one. Equations 4.7, 4.8, and 4.9 are independent of the external magnetic field thus leading to narrow peaks in the modulation spectrum. The ESEEM spectrum remains dominated by these NQR frequencies if the ratio $\nu_{eff}/K < 1$.

The transitions from the lower electron spin manifold (Figure 4.22), where nuclear hyperfine and nuclear Zeeman terms are additive, are dependent on the external field and thus give rise to much broader spectral lines. Which of the lines are observed depends on the ratio of ν_{eff} to K. If K is small ($\nu_{eff}/K > 1$) then the Zeeman interaction will dominate and a sharp "double quantum" peak corresponding to the transition between levels 3 and 1 will be observed at approximately $4\nu_n$ ($hA + 2\nu_n = 4\nu_n$ at exact cancellation). A broader peak at half this frequency corresponding to the single quantum transitions from the lower spin manifold may also be observed.

In the other limit, as K becomes very large as compared to ν_{eff}, the transitions from the lower spin manifold (equation 4.6) approach the pure NQR frequencies. In the limit that K approaches infinity the same frequencies will be observed from both the upper and lower spin manifold. Typical experimental examples of ^{14}N modulation have Zeeman and quadrupole interactions which are similar in magnitude corresponding to a case between the two limits discussed above. In this intermediate case there is usually only a single peak from each manifold observed at

$$\nu_{dq} = 2 [\nu_{eff}^2 + K^2 (3 + \eta^2)]^{1/2} \qquad (4.10)$$

corresponding to the $\Delta m_I=2$ transition. The one-quantum transitions show a strong dependence on the magnetic field orientation and are consequently too broad to be detected. Thus the maximum number of lines from both manifolds (ignoring the combination peaks observed in the two-pulse ESE experiment) expected for a typical single ^{14}N nucleus is four. These are the frequencies described by equations 4.7-4.10. This number may increase with interactions of the electron with several nuclei.

The discussion above was limited to the situation of exact cancellation when the nuclear Zeeman and hyperfine terms are equal. At conditions deviating from exact cancellation, the pure quadrupole frequencies of the upper electron spin manifold become tainted by the Zeeman and hyperfine interaction. However, it has been shown that the simple spectral characteristics observed under exact cancellation conditions are also retained at small deviations from exact cancellation although there may be slight shifts in peak positions [109]. At large deviations from exact cancellation, where the Zeeman term exceeds the hyperfine interaction, the ESEEM powder patterns are comprised of two sharp double quantum resonances at the frequencies

$$\nu_{dq}= 2 [(g_N\beta_N H\pm A/2)^2 + K^2 (3 + \eta^2)]^{1/2} \qquad (4.11).$$

When the deviation from exact cancellation is intermediate, peaks corresponding to the $6\leftrightarrow5$ and $5\leftrightarrow4$ transitions broaden and overlap. The double quantum peak corresponding to the $6\leftrightarrow4$ transition remains sharp.

In contrast with the NQR frequencies, the frequency in Equation 4.10 must increase with magnetic field. When the EPR spectrum is sufficiently wide for selective excitement by ESE pulses this dependence is useful for assigning the lines in the spectrum to the correct transition. It is evident that the quadrupole and hyperfine coupling parameters are determined most accurately under the condition of exact cancellation when the nuclear Zeeman and hyperfine terms are equal. In this case the transitions from the upper spin manifold will be the pure NQR transitions in equations 4.7-4.9. If the double quantum peak from the lower spin manifold is observed, then the hyperfine coupling can be calculated in addition to the quadrupole parameters. If the double quantum peak is not present, the ^{14}N hyperfine coupling parameters are often obtained by substituting ^{15}N and scaling the values for the hyperfine by the ratio of the nuclear g-values for ^{15}N and ^{14}N. This makes it possible to determine the anisotropic hyperfine interactions for ^{14}N in disordered systems.

ESEEM spectra. Figures 4.23-4.28 show sample two and three pulse ESEEM data for the C^{14}N transferrin adduct. Table 4.2 summarizes the frequency results for each of the different tau values. As can be seen, there is considerable variation in peak location as tau is changed. In the spectrum of Figure 4.26 at g_{xx} there are peaks at 1.4, 2.56, and 3.03 MHz. The data for g_{yy} (Figure 4.27) has peaks at 2.23, 2.80, 3.48, and 4.30 MHz. The g_{zz} spectrum (Figure 4.28) has a very broad peak with multiple shoulders which reaches maximum intensity at 2.74 MHz, and has sharper peaks at 3.89 and 4.68 MHz

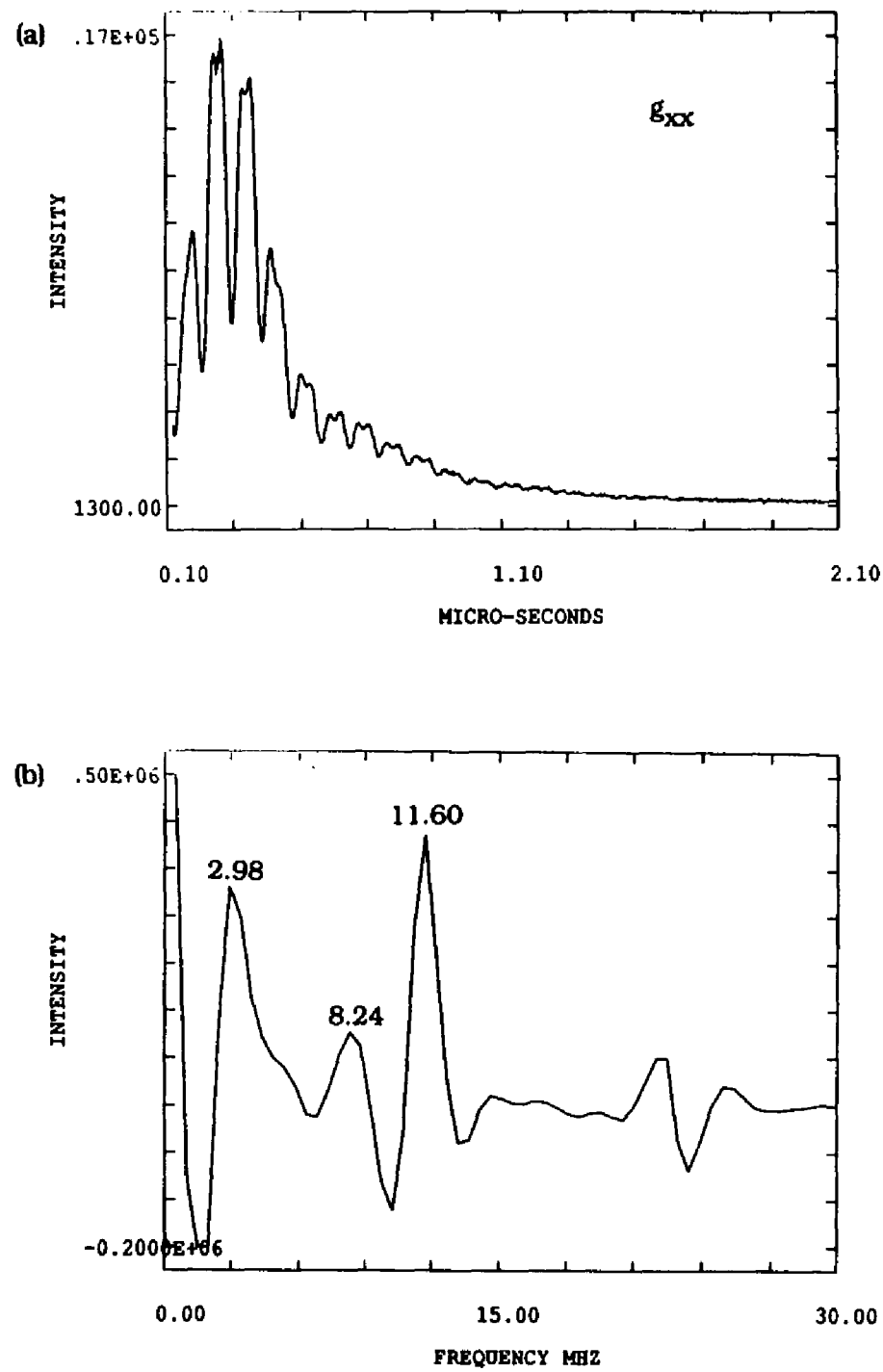

Figure 4.23 (a) Two pulse ESEEM spectrum of $C^{14}N$ adduct along g_{xx}. Data file TP0910.NIP. Frequency-8.78 GHz, Field-2677 G. (b) Fourier transform of (a).

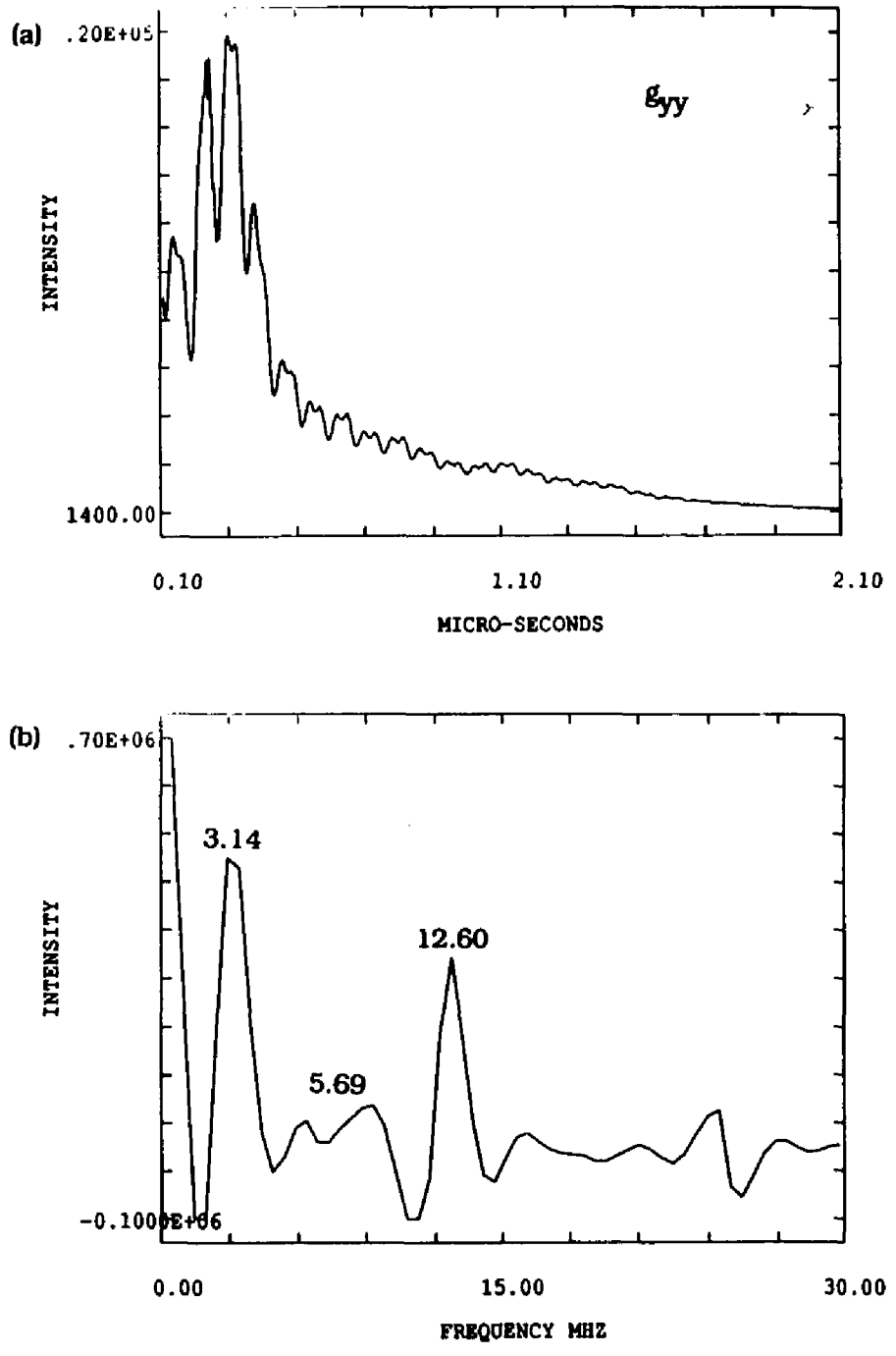

Figure 4.24 (a) Two pulse ESEEM spectrum of $C^{14}N$ adduct along g_{yy}. Data file TP0909.NIP. Frequency-8.78 GHz, Field-2906 G. (b) Fourier transform of (a).

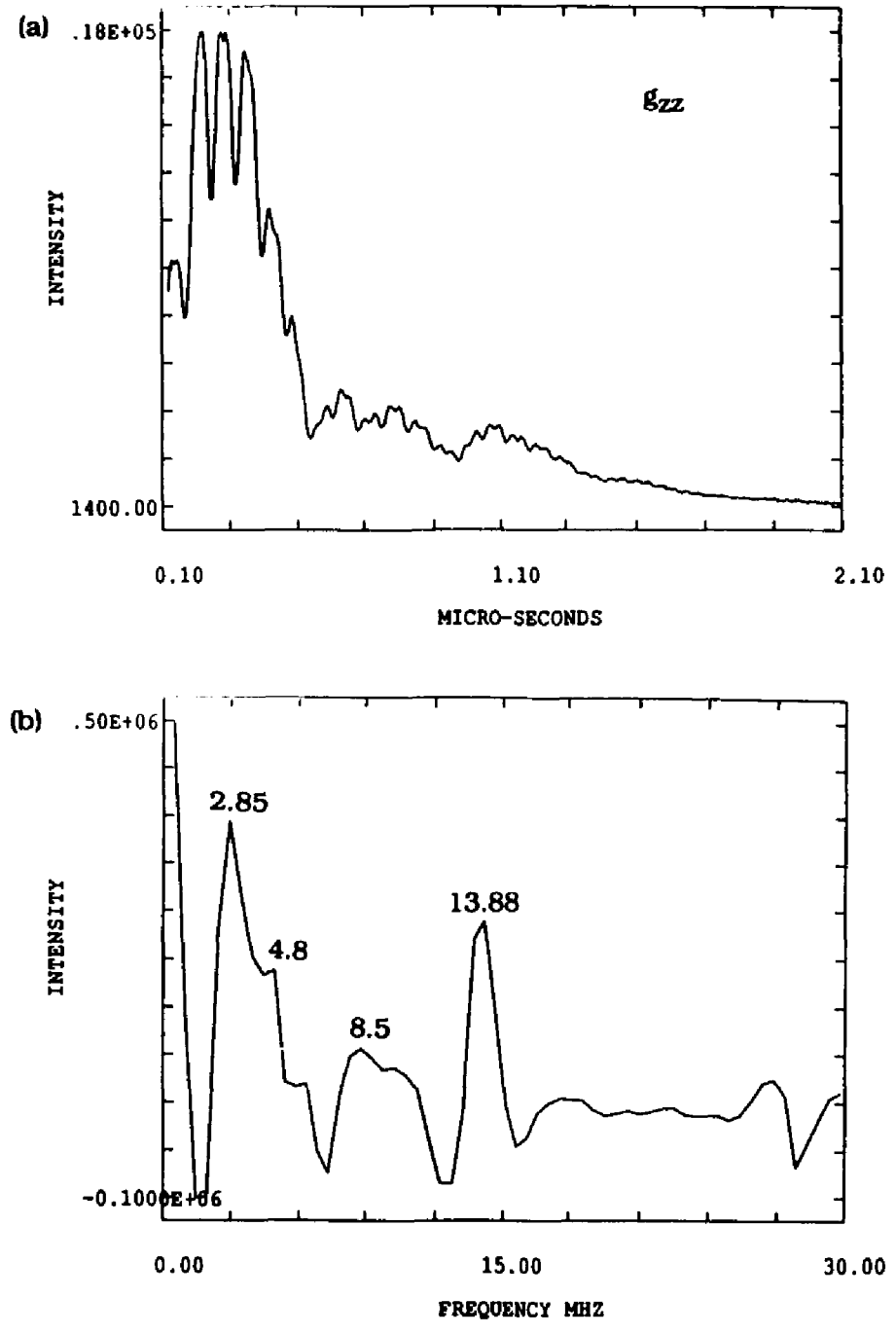

Figure 4.25 (a) Two pulse ESEEM spectrum of $C^{14}N$ adduct along g_{zz}. Data file TP0911.NIP. Frequency-8.78 GHz, Field-3226 G. (b) Fourier transform of (a).

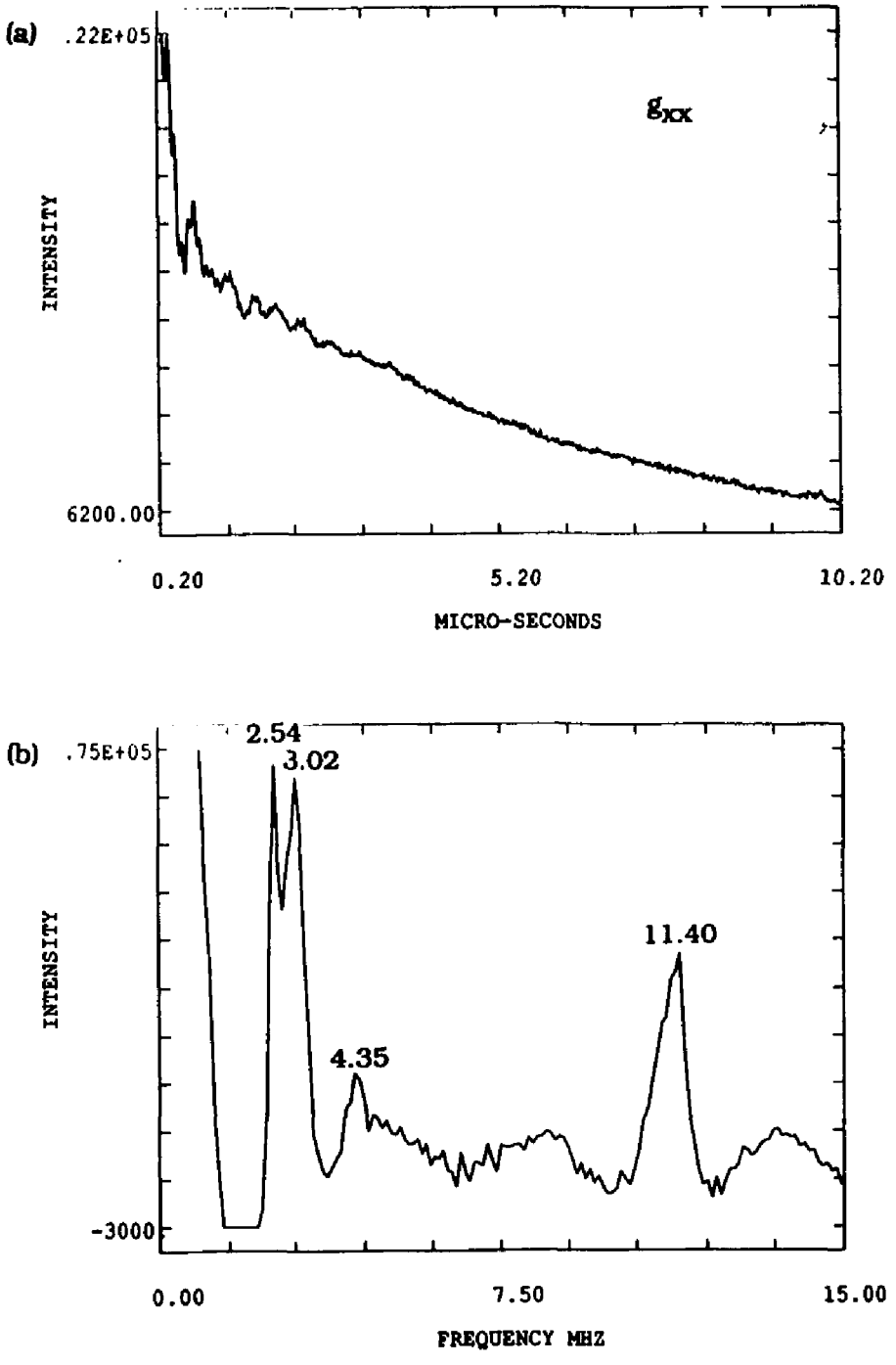

Figure 4.26 (a) Three pulse ESEEM spectrum of $C^{14}N$ adduct along g_{xx}. Data file SE2876.NIP. Frequency-8.78 GHz, Field-2677 G., tau-175 nsec. (b) Fourier transform of (a).

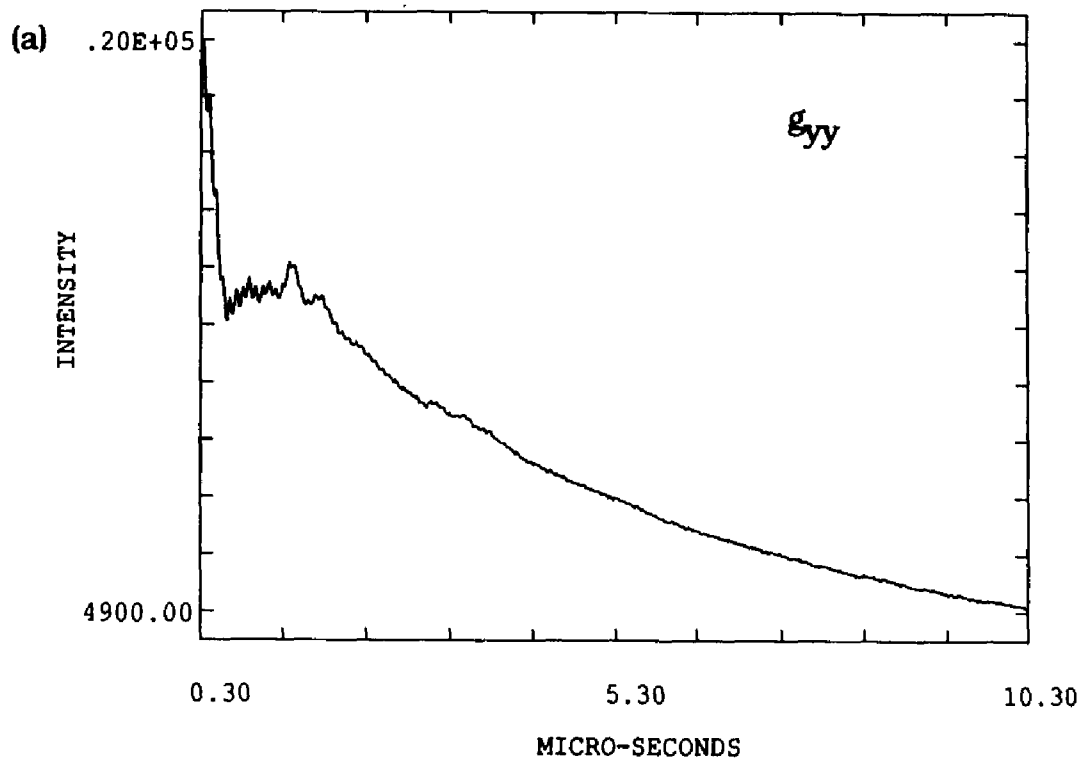

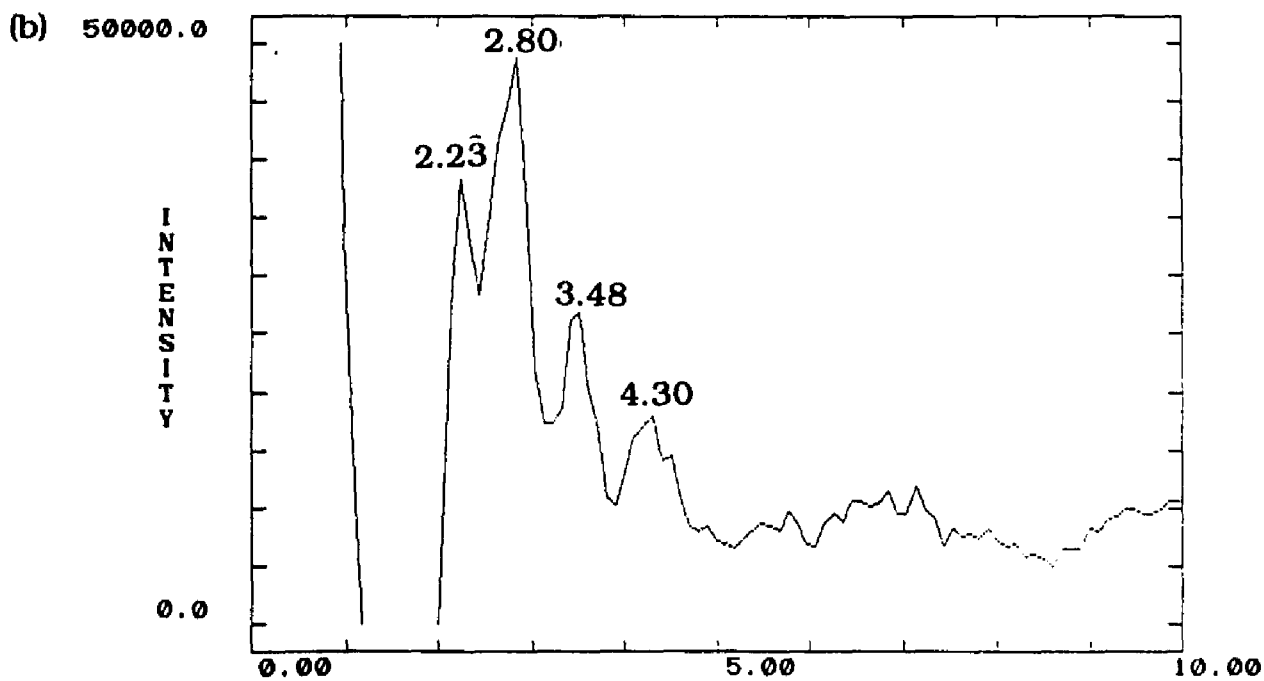

Figure 4.27 (a) Three pulse ESEEM spectrum of $C^{14}N$ adduct along g_{yy}. Data file SE2874.NIP. Frequency-8.78 GHz, Field-2906 G., tau-242 nsec. (b) Fourier transform of (a).

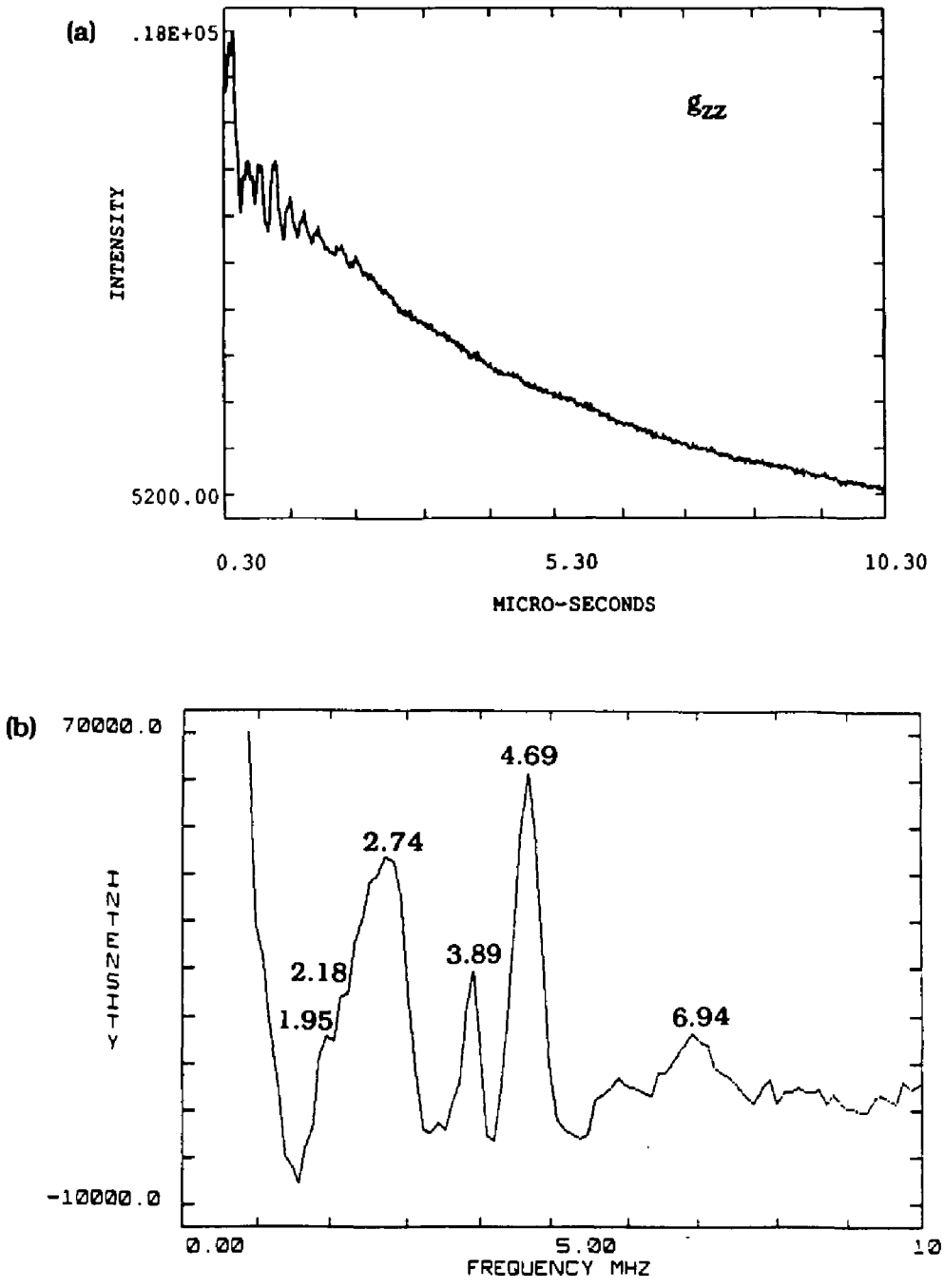

Figure 4.28 (a) Three pulse ESEEM spectrum of $C^{14}N$ adduct along g_{zz}. Data file SE2916.NIP. Frequency-8.87 GHz, Field-3256 G., tau-216 nsec. (b) Fourier transform of (a).

Frequency (GHz)	tau (μsec)	Peak Position (MHz)
		g_{xx}
8.78	175	2.54 3.02 4.35
	263	1.68 2.16 2.84
	350	2.54
		g_{yy}
	162	0.55 2.79 3.44 6.26
	242	2.23 2.80 3.48 4.30
	323	2.66 4.91 5.19
		g_{zz}
	145	2.54 3.88 4.67
	218	2.75 3.89 4.68 6.93
	290	2.52 4.68 1.02
		g_{xx}
10.52	242	0.27 0.74 1.14 2.98 3.30
	415	0.57 2.19 3.91
		g_{yy}
	191	0.76 2.82 3.68
	381	0.64 2.38 3.70
		g_{zz}
	257	0.66 2.46 4.90
	342	0.66 2.54

Table 4.2 ESEEM peak positions of $C^{14}N$ with various values for τ at spectrometer frequencies of 8.78 and 10.52 GHz.

and a very broad low amplitude peak at 6.94 MHz. These peaks are all in the frequency range expected for a nitrogen interaction.

The nitrogen nuclei possibly present in the adduct are the two nitrogens in histidine, and cyanide nitrogens. The directly bonded histidine nitrogen may or may not be detected in the ESEEM spectra. A coupling on the order of 30 MHz has been detected for the directly bonded nitrogen in ENDOR and EPR studies of copper-transferrin [110,76]. Such a coupling would be too large to give rise to modulation with the spectrometer frequencies used here, but weakly coupled directly bonded nitrogen has been detected in ESEEM studies of VO^{2+} substituted transferrin [111] and two-pulse studies of myoglobin[115]. The modulation due to nitrogen in Figures 4.23-4.25 is very deep compared to the nitrogen modulation in the VO^{2+} case and more closely resembles the remote nitrogen observed in copper substituted transferrin. The frequencies are higher than those observed in the copper case though which indicates a stronger interaction. Consequently, the possibility of modulation due to the coordinated nitrogen cannot be ruled out.

Presumably, any peaks due to the nitrogens in histidine would also be apparent in the $C^{15}N$ spectrum. There are some peaks which are present in both the $C^{15}N$ and $C^{14}N$ spectra. For instance, along g_{zz} there is a peak at 2.5-2.7 MHz (exact peak location is dependent on the tau value) in the spectra of both nitrogen isotopes. However, the 2.70 MHz peak in the ^{15}N spectrum also corresponds approximately to the combination frequency of the 1.1 and 1.7 MHz peaks. Based on the data at a single spectrometer frequency it cannot be stated

conclusively whether there is evidence of modulation due to the remote histidine nitrogen.

The ^{15}N spectra at the second spectrometer frequency, 10.5 GHz, were shown in Figures 4.13-4.18. The spectrum along g_{zz} is shown in Figure 4.15. The peak which corresponds to the 2.70 MHz peak at 8.8 GHz occurs at 2.78 MHz when a spectrometer frequency of 10.3 GHz is used. This is no longer a combination frequency of the peaks at 1.36 and 1.98 MHz. The 3.90 MHz peaks remains at twice the frequency of the second intense peak and so it can be assigned as a harmonic of the 1.98 peak.

The ^{14}N spectra at the 10.5 GHz spectrometer frequency are shown in Figures 4.29-4.34. Along g_{zz} (Figure 4.31) there is a broad peak in the range 2.5-2.9 MHz depending on tau value. Thus it is possible that this peak is due to a histidine nitrogen. However, data at the other g-values do not provide additional support of this assignment. There are other peaks which are present in both ^{14}N and ^{15}N spectra at one spectrometer frequency, such as the 2.6-2.8 MHz peak at 8.8 GHz at g_{yy}. But, this peak does not remain present for both the ^{14}N and ^{15}N spectra at the second spectrometer frequency. The modulation due to histidine nitrogen would be expected to be consistent for both the ^{14}N and ^{15}N cyanide spectra. The results are ambiguous since a peak may be present in both ^{14}N and ^{15}N cyanide spectra at one g-value, but not another or a peak may be present in both ^{14}N and ^{15}N cyanide spectra at one spectrometer frequency, but not the other. The possibility of modulation due to histidine nitrogen in the three-pulse experiments cannot be ruled out, but it is certainly

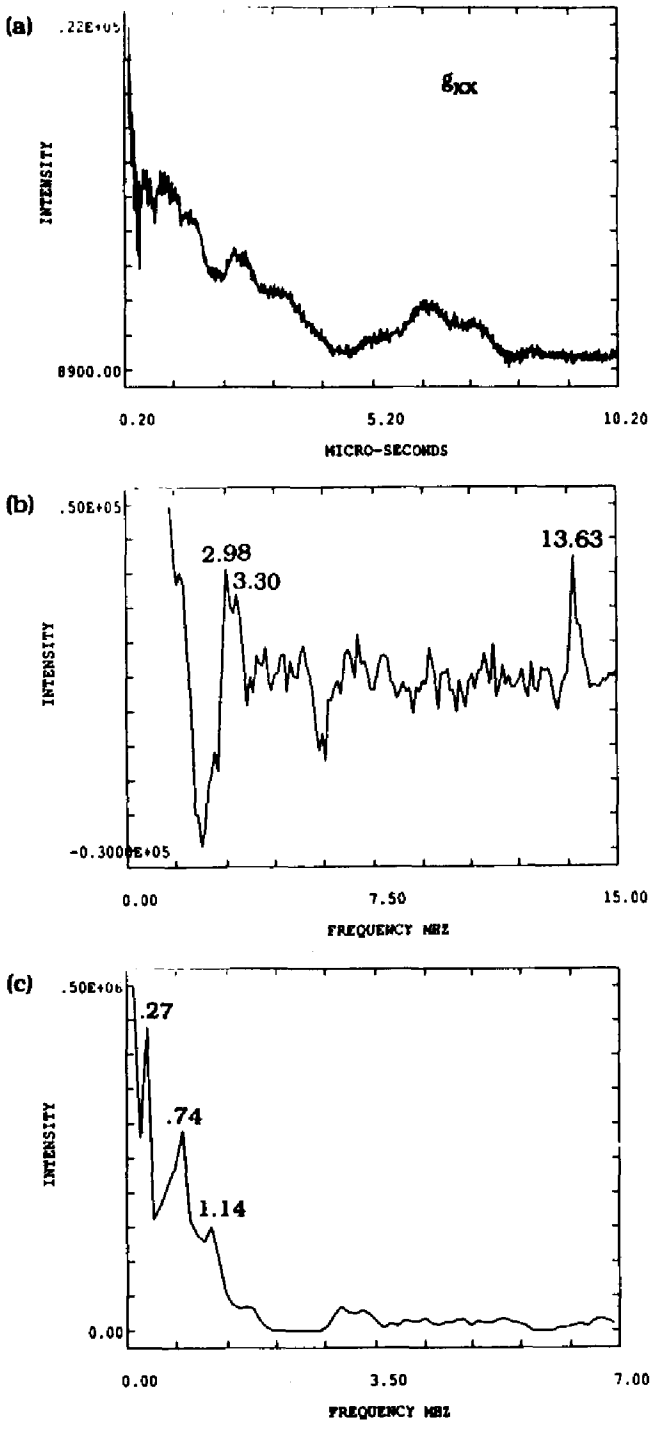

Figure 4.29 (a) Three pulse ESEEM spectrum of $C^{14}N$ adduct along g_{xx}. Data file SE4733.NIP. Frequency-10.51 GHz, Field-3214 G., tau-242 nsec. (b) Fourier transform of (a). (c) The very low frequency region of (b).

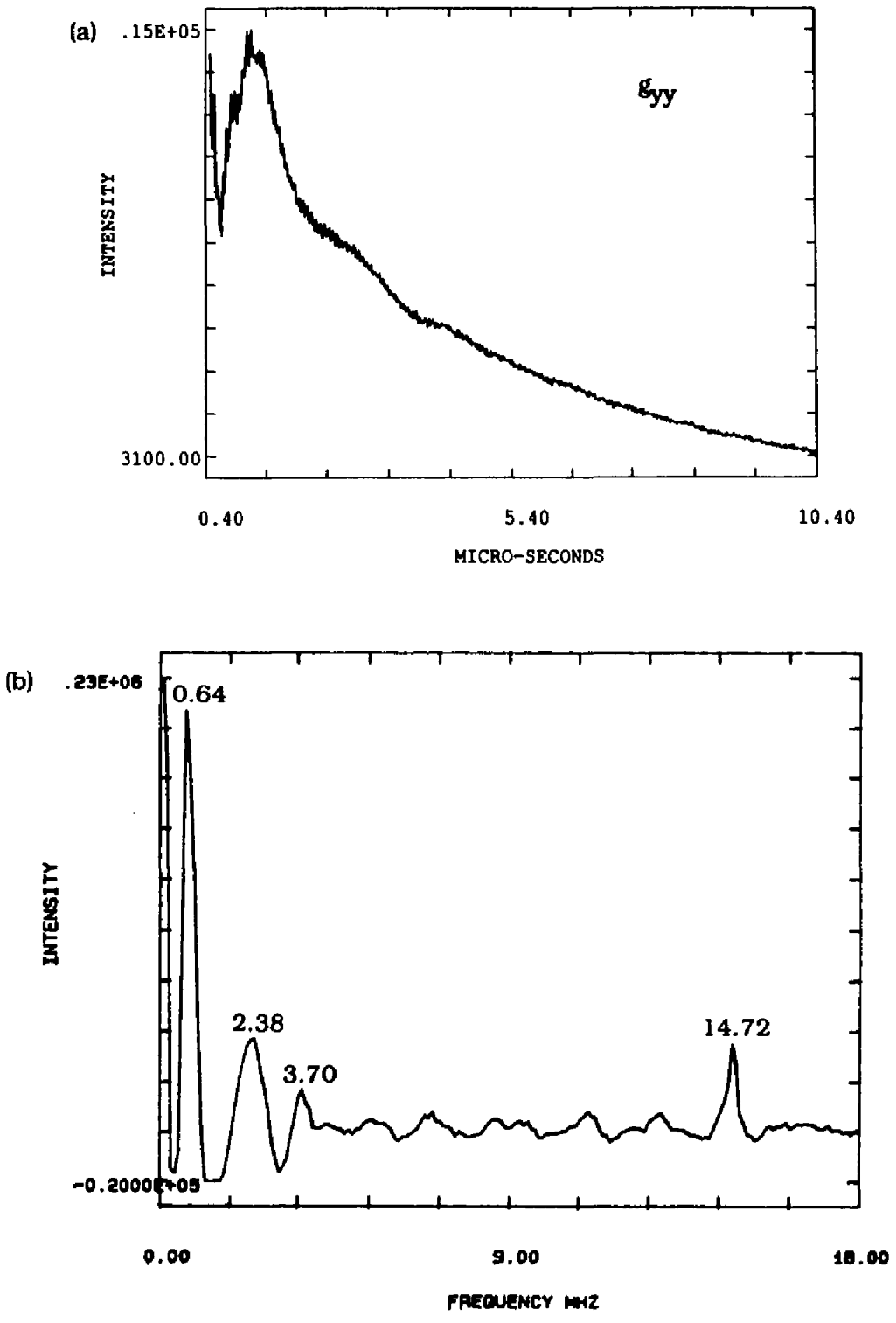

Figure 4.30 (a) Three pulse ESEEM spectrum of $C^{14}N$ adduct along g_{yy}. Data file SE4732.NIP. Frequency-10.51 GHz, Field-3481 G., tau-381 nsec. (b) Fourier transform of (a).

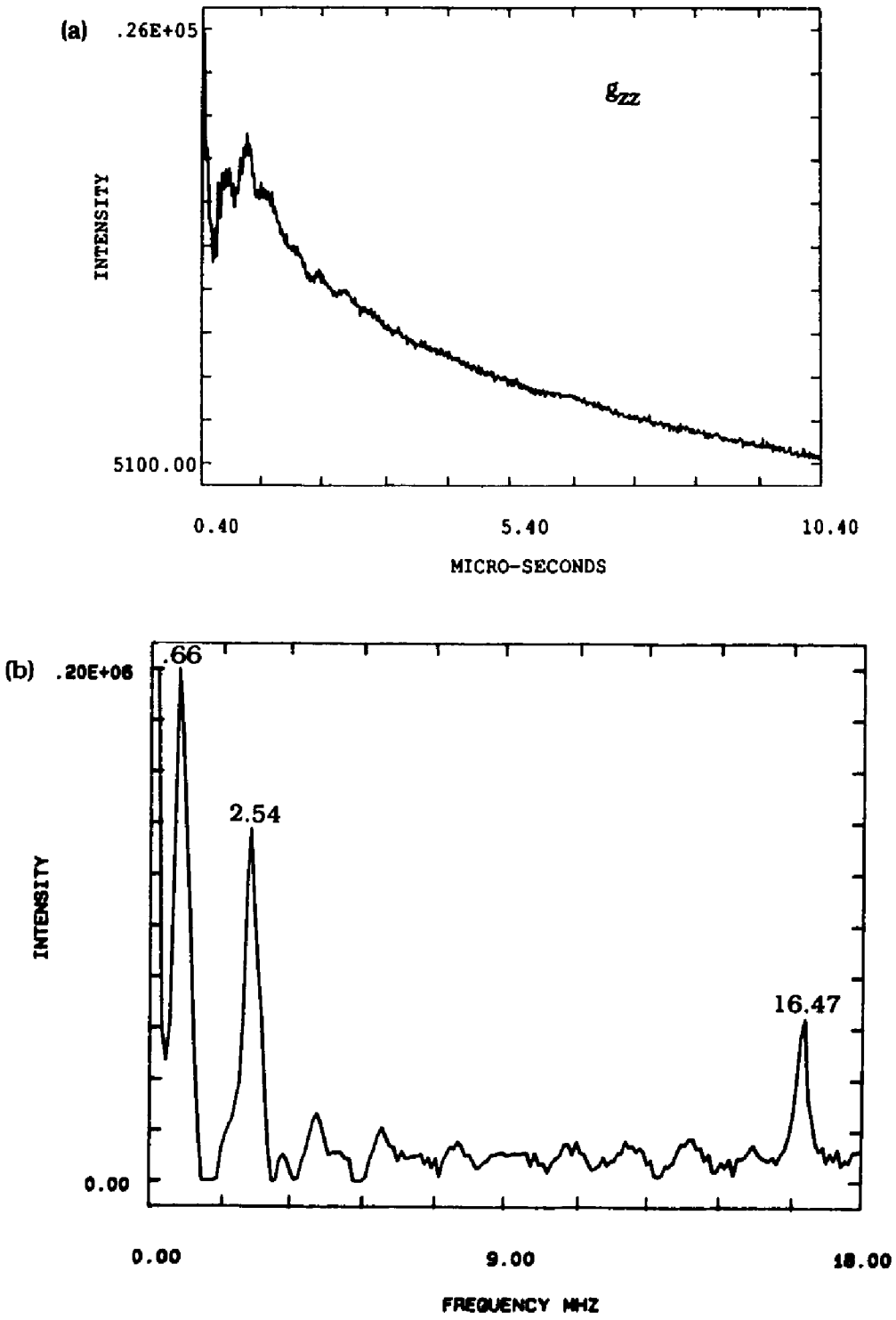

Figure 4.31 (a) Three pulse ESEEM spectrum of $C^{14}N$ adduct along g_{zz}. Data file SE4729.NIP. Frequency-10.52 GHz, Field-3875 G., tau-342 nsec. (b) Fourier transform of (a).

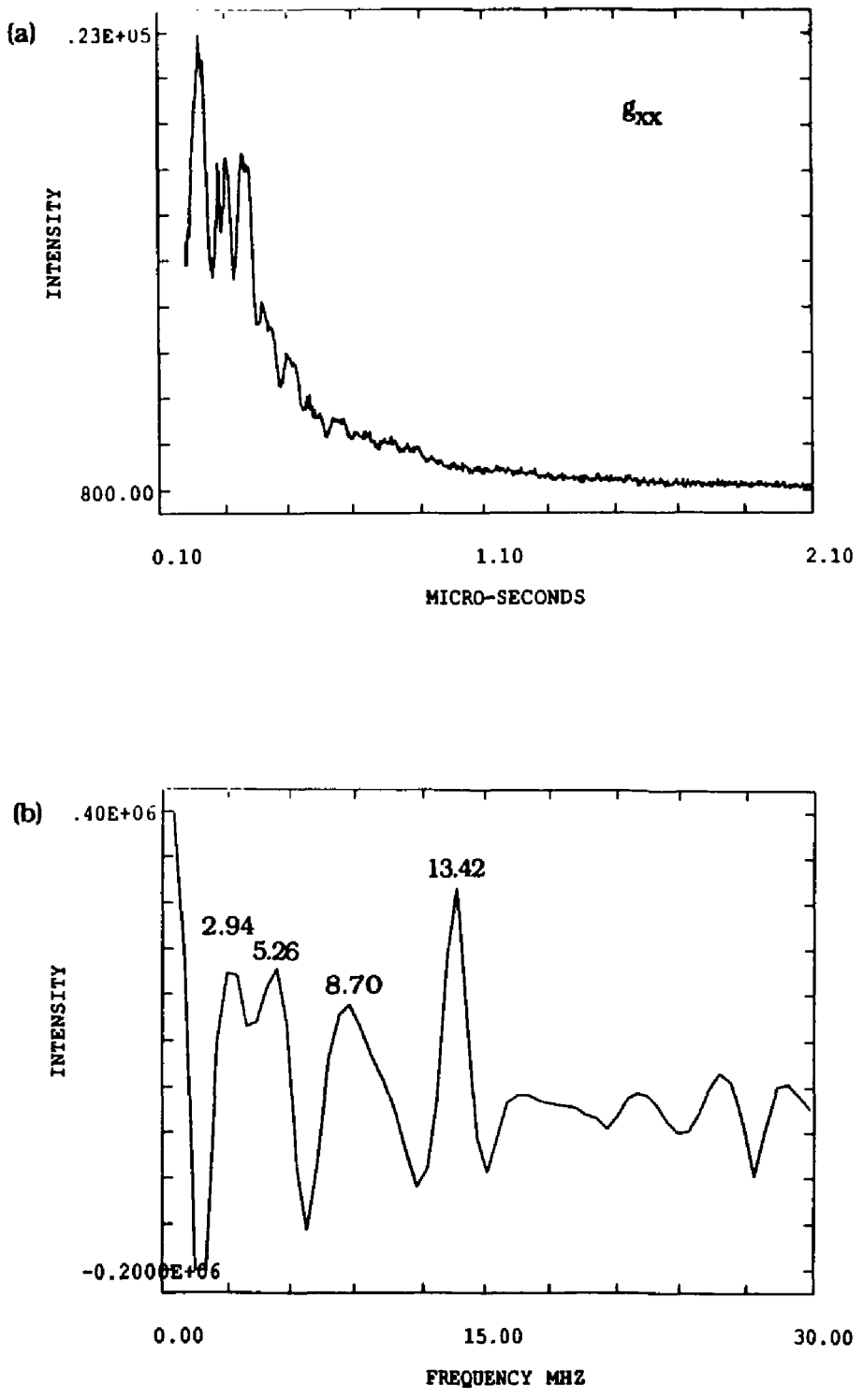

Figure 4.32 (a) Two pulse ESEEM spectrum of $C^{14}N$ adduct along g_{xx}. Data file TP1441.NIP. Frequency-10.52 GHz, Field-3214 G. (b) Fourier transform of (a).

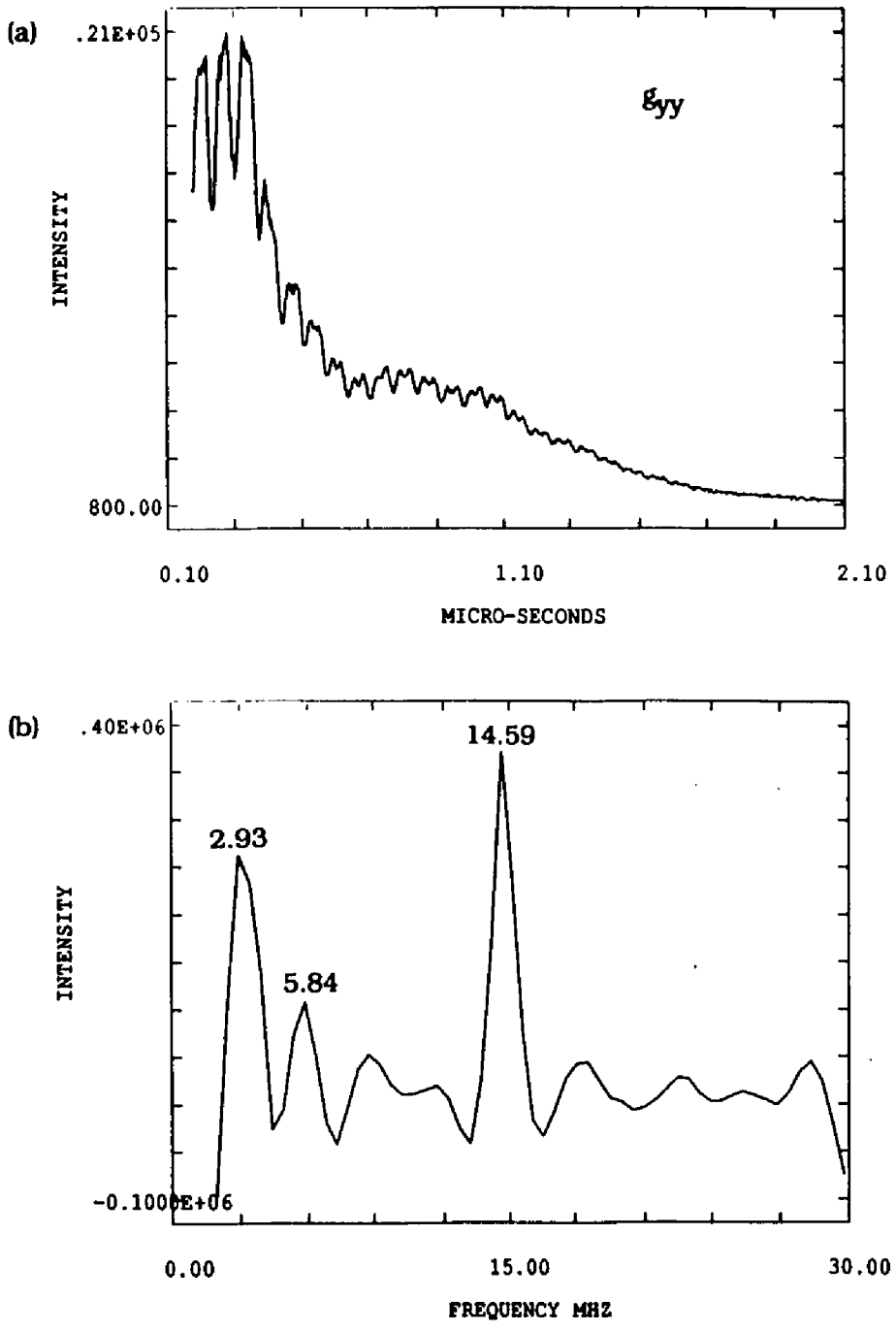

Figure 4.33 (a) Two pulse ESEEM spectrum of $C^{14}N$ adduct along g_{yy}. Data file TP1441.NIP. Frequency-10.52 GHz, Field-3481 G. (b) Fourier transform of (a).

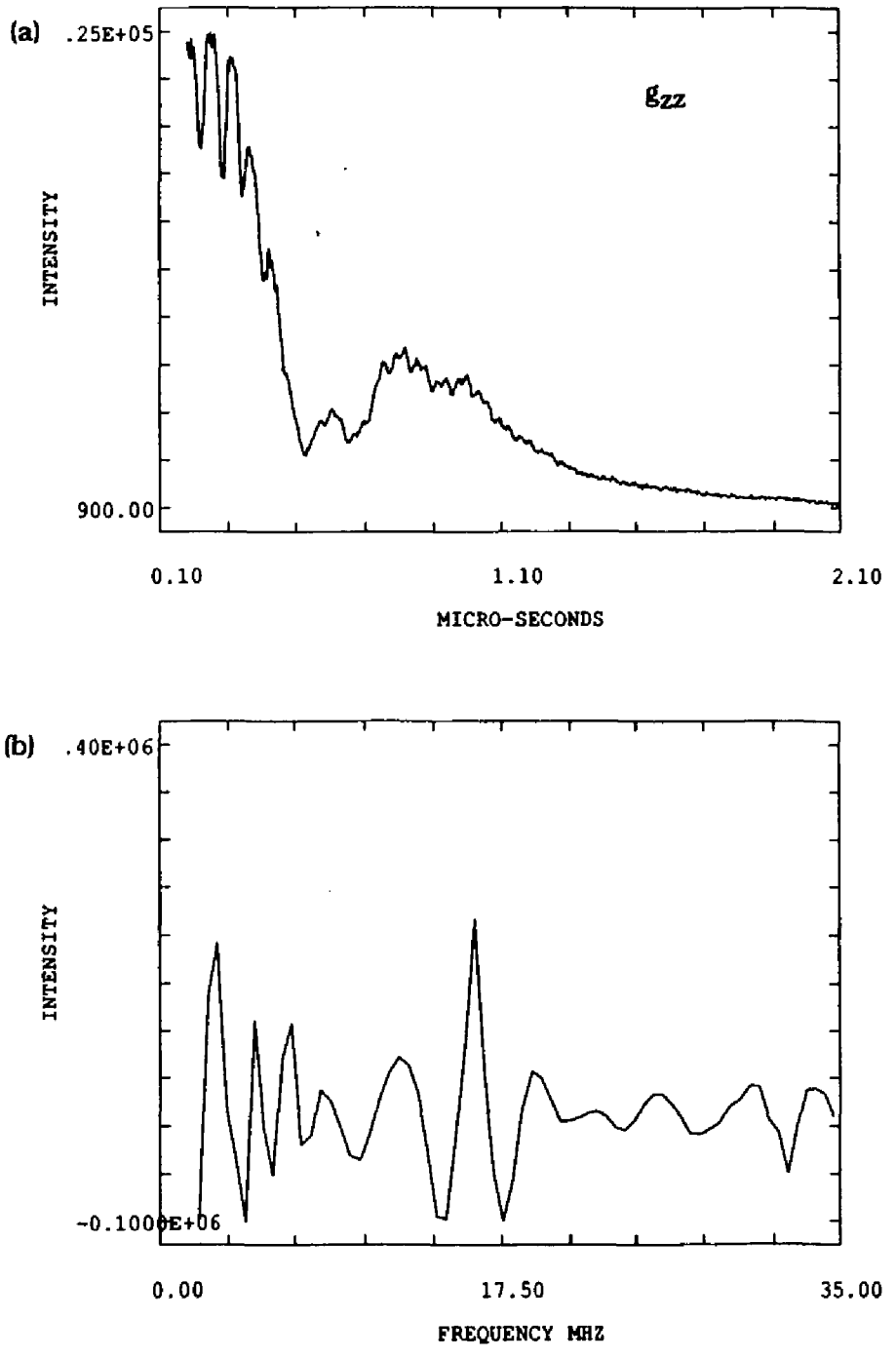

Figure 4.34 (a) Two pulse ESEEM spectrum of $C^{14}N$ adduct along g_{zz}. Data file TP1441.NIP. Frequency-10.52 GHz, Field-3807 G. (b) Fourier transform of (a).

not consistent at all g-values and spectrometer frequencies and, consequently, seems unlikely.

Ideally with ^{14}N data at two or more spectrometer frequencies one can perform a graphical analysis similar to that used for ^{15}N to obtain quadrupole interaction parameters. Unfortunately in this case, as can be seen by comparing the data at the two spectrometer frequencies, there is no clear correspondence between peaks at one frequency with the other. Normally with an ^{14}N nucleus one expects to observe a triplet of sharp peaks with these peaks corresponding to the NQR frequencies. As shown in equations 4.7-4.9 the sum of the lower two frequencies should then equal the third. Clearly this type of behavior is not seen in any of the transferrin ESEEM spectra.

The NQR of the cyanide nitrogens for a number of metal cyanides has been studied and values for K and η range from .87-1.05 MHz and 0-.03 respectively [112]. Assuming similar values for the transferrin case, one would expect to observe pure quadrupole peaks at approximately .05-.06 and 2.61-3.15 MHz. The extremely small value of η would make it difficult to completely resolve the NQR frequencies given by equations 4.7 and 4.8. As a result, it is probable that, at best, only two peaks would be observed. The peak at .05-.06 MHz is unlikely to be resolved even in an ESEEM spectrum. A frequency this low is often obscured and influenced by the decay of the background envelope. If this peak is not observed, then just a single peak in the 2.61-3.15 MHz range would be expected. There are certainly peaks within this range in the ^{14}N spectra and these may well be the expected quadrupole peaks, but the situation appears to be more complicated.

Some of the lines in the ESEEM spectra have a complex structure. For example, in Figure 4.28 the 2.74 MHz line has multiple shoulders at 1.95, 2.18, and 2.49 MHz. The entire peak covers a range of about 1.5 MHz. It is uncertain whether this is a single peak or several peaks superimposed. This observed complication of the line may be related to the contribution to the low-frequency region of lines arising from nuclei with hyperfine interaction constants for which exact cancellation does not hold. As a result, for these nuclei, the narrow NQR lines will be broadened, thus decreasing spectral resolution and complicating the spectra. Another possibility is that a small value for η is present. This would be expected for an axial system such as CN^- and would give rise to slightly different frequencies for ν_+ and ν_- as can be seen from Equations 4.7 and 4.8. These frequencies may not be completely resolved in the ESEEM spectrum thus giving rise to the complex lineshape observed.

The ^{15}N spectra (Figures 4.11 and 4.15) had less intense harmonic peaks at twice the frequency of some the fundamental peaks. The ^{15}N ESEEM spectra thus clearly indicate the presence of more than one cyanide group. It is unusual that equivalent harmonics are not seen in the ^{14}N spectra although it too must contain at least two cyanide groups. Such harmonics are commonly noted in a number of protein-^{14}N ligand systems [113,114].

A detailed analysis of the ^{14}N spectra was not possible. The major problem is that it is unclear whether the observed peaks are due to one or more cyanide nitrogens, the histidine nitrogens or a combination of the two. The modulation frequencies observed are inconsistent between the two and three pulse experiments. This may

be due to the inherent differences between the two experiments with the two-pulse spectra showing more strongly coupled nitrogen(s) than the three pulse spectra. The values of the hyperfine coupling obtained from the ^{15}N data and scaled for ^{14}N are between .46 and .62 MHz. The ^{14}N Zeeman frequency is .82-1.02 MHz for the 8.8 GHz spectra and 1.36-1.63 MHz for those at 10.5 GHz. It is apparent that "exact cancellation" of the Zeeman and hyperfine terms is not occurring at the spectrometer frequencies used here. Studies of the nitrogen interactions in DPPH which also has Zeeman and hyperfine coupling terms that do not cancel at X-band showed that analysis based on the X-band ESE alone was misleading [115,116]. The case here is more complicated since there are apparently several inequivalent nitrogens, but, as with DPPH, the solution to the problems in analysis may be in going to lower spectrometer frequency where exact compensation of the Zeeman frequency with hyperfine coupling can be achieved.

G=4.3 Signal

The EPR signal at g'=4.3 is characteristic of high spin Fe(III) and is due to a transition between levels of the middle Kramers doublet of the S=5/2 system. ESEEM in the g'=4.3 region from another high-spin iron protein, ferritin, had been observed [117] so ESEEM was performed at g'=4.3 for the transferrin-cyanide adduct. The signal at g'=4.3 is solely due to the N-terminal site in the cyanide adduct of transferrin. There is some indication from EPR that the N-terminal site is also perturbed by the presence of cyanide [40] although the iron is not converted to low-spin. Earlier work suggested that cyanide and bicarbonate may compete for binding at the N-terminal site. One thus

expects different ESEEM interactions than are observed for the g=2 region.

To see if a cyanide interaction could be observed, the CN isotopes were used. Comparison of the $C^{15}N$ and $C^{14}N$ time domain spectra in Figure 4.35 shows that they are virtually identical. The frequency domain of these spectra in Figure 4.36 reveals that there is no evidence in the ESEEM of even weakly interacting ^{15}N. This is in marked contrast with the g=2 region in which there were distinctive changes in the spectra when $C^{15}N$ was used. As with the g=2 region, there is no difference in the spectra recorded with the ^{13}CN isotope. Thus there is no evidence from ESEEM of an interaction at the N-terminal site due to cyanide.

The peaks that are observed in the spectrum are not due to cyanide nuclei. The x-ray structure shows that the ligands at both iron sites in transferrin are two tyrosines, one histidine, and one aspartate residue with the other coordination positions occupied by bidentate carbonate [26,27]. The resulting frequency spectrum with solvent exchange using D_2O is shown in Figure 4.37. This peak occurs at the deuterium Zeeman frequency of .98 MHz and no resolved deuterium splitting is apparent. Such a splitting should be visible if water coordinated directly to the iron center. Thus the ESEEM results are consistent with the x-ray structure. The number of ambient deuterium nuclei is large so the matrix peak is quite intense and, consequently, the peaks due to nitrogen are much smaller in comparison. Careful comparison of Figures 4.36 and 4.37 shows that the nitrogen frequencies are still present in the deuterium spectrum, but that the intensities are much smaller than that of the matrix peak.

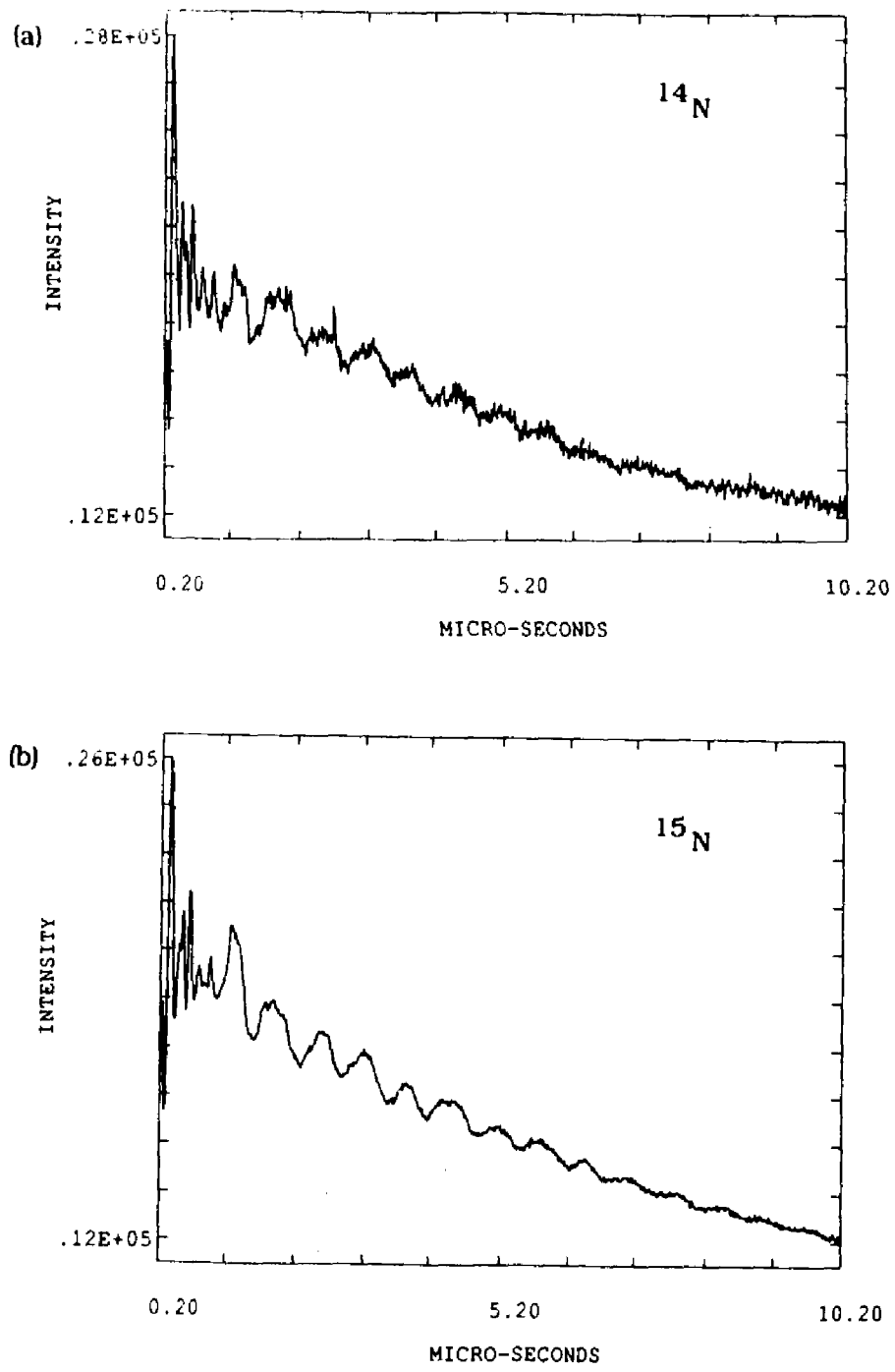

Figure 4.35 (a) Three pulse ESEEM spectrum of $C^{14}N$ at g'=4.3. Data file SE2882.NIP. Frequency-8.78 GHz, Field-1493 G., tau-156 nsec. (b) $C^{15}N$ spectrum. Data file SE2893.NIP. Frequency-8.79 GHz, Field-1493 G., tau-156 nsec.

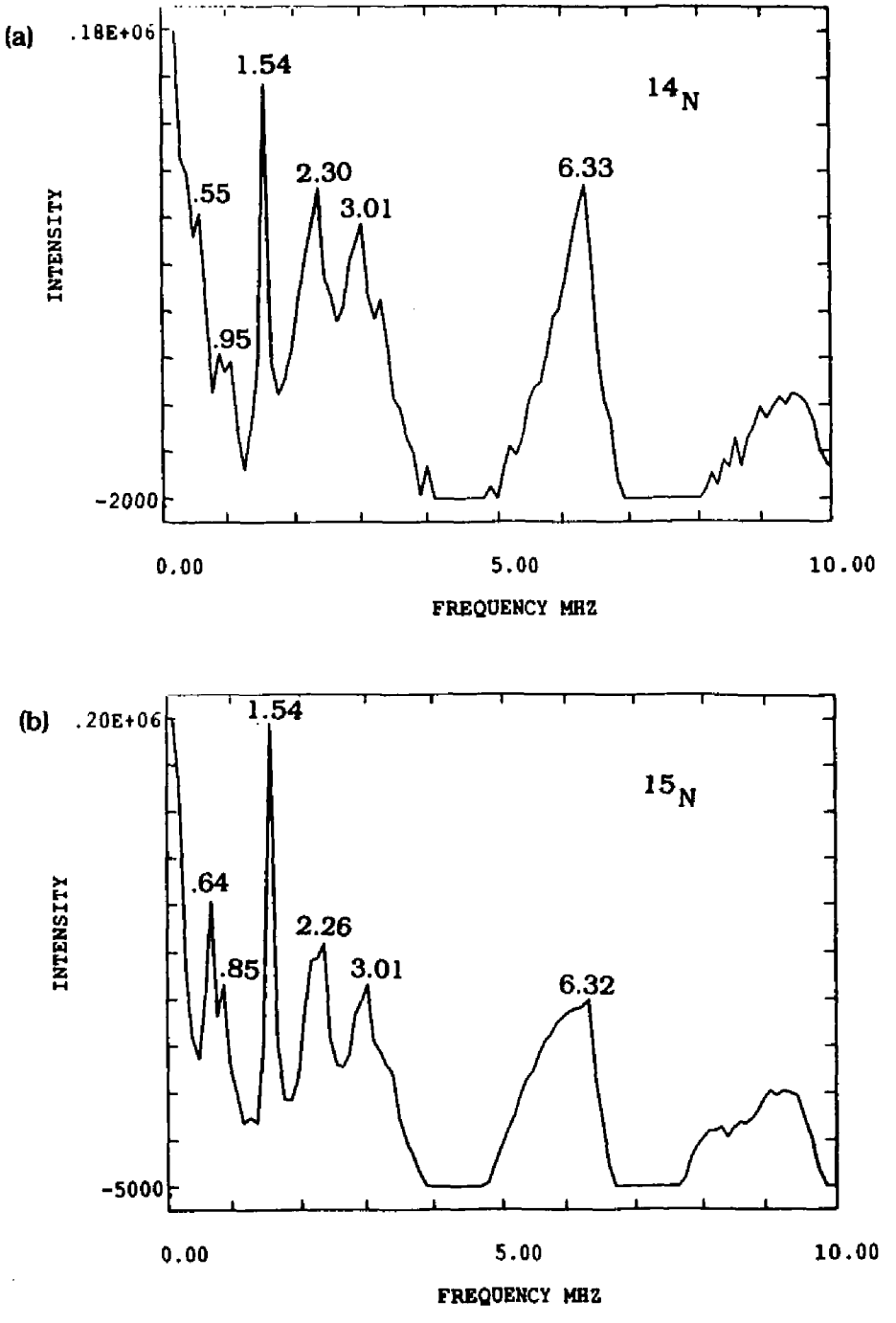

Figure 4.36 Frequency spectrum of Figure 4.35.

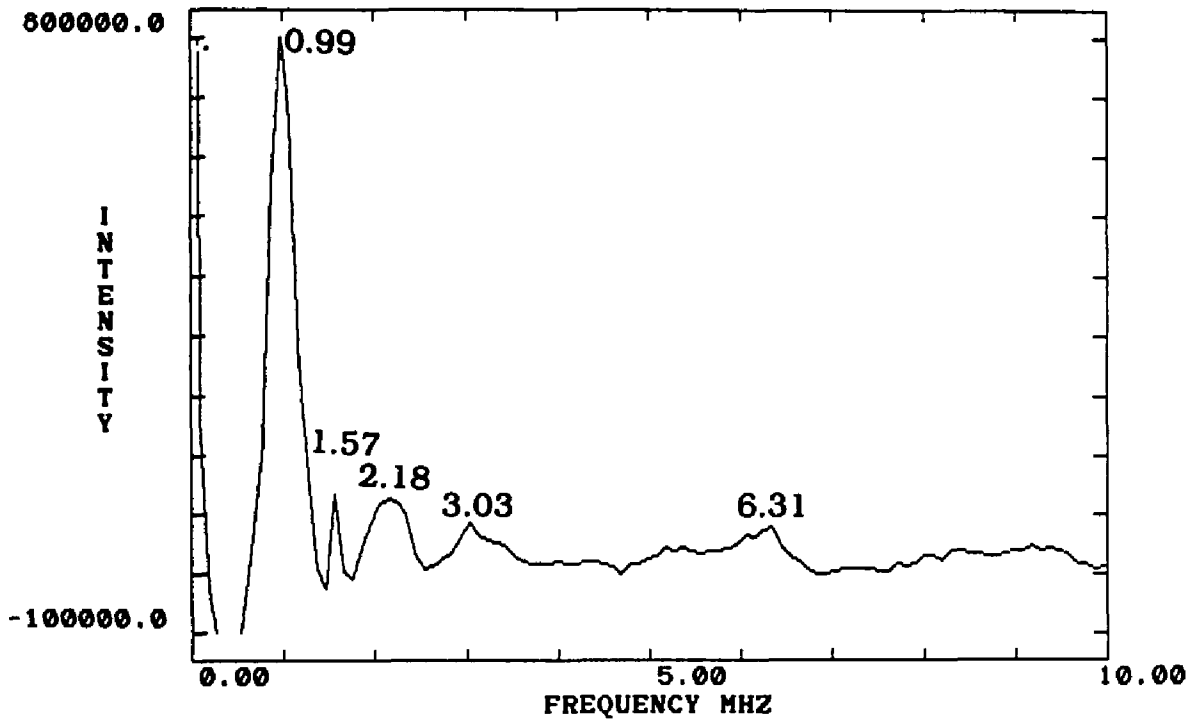

Figure 4.37 Frequency spectrum of three pulse D_2O sample at g'=4.3. Data file SE2906.NIP. Frequency-8.62 GHz, Field-1493 G., tau-156 nsec.

In contrast with the ESEEM of ferritin, the ESEEM signal in transferrin has clear modulation from nuclei other than protons. In the frequency spectra in Figure 4.36 there are sharp peaks at .55-.64, .85-.95, and 1.54 MHz. The peaks at 2.26-2.30 and 3.01 MHz are slightly broader and there is a very broad peak at 6.33 MHz. The Zeeman frequencies at this field are .46 MHz for ^{14}N and 6.36 MHz for protons. The frequency range of peaks would indicate that they are due to ^{14}N. One would not expect the directly coordinated ^{14}N of histidine to contribute to the modulation pattern since that nucleus would be strongly coupled. The NQR frequencies of L-histidine for the protonated nitrogen are 1.406, 0.749, and 0.657 MHz with K=.36 and η=.91 [118]. These frequencies are slightly different, but similar to the three lowest frequencies observed in the ESEEM. The differences are probably a result of a minor perturbation of the electron distribution about the remote nitrogen due to the protein structure. Such differences have been noted for a number of Cu(II)-imidazole proteins which have slightly different values for K and η than the powder NQR of protonated imidazole [119,120]. Assuming that these peaks are the NQR frequencies and using Equations 4.7-4.9, one obtains K= .40 and η=.86 (values for K and η are based on the average peak position for all values of tau). It is interesting that the histidine nitrogen interactions are so clear in the g'=4.3 region, but not in the g=2 region of the C-terminal site where histidine may also remain bound in the CN adduct.

The origins of the peaks at 2.30 and 3.01 MHz are not readily apparent. In an S=1/2 system, the maximum number of sharp peaks due to a single ^{14}N nucleus is four. This would seem to indicate the

presence of more than one ^{14}N at the N-terminal site. The peaks at 2.30 and 3.01 MHz could then be interpreted as the combination and harmonic peaks of the NQR frequencies as would be expected for two equivalent ^{14}N nuclei. However, the x-ray structure does not show two equivalent nitrogen nuclei. Thus it seems more likely that these peaks are a result of a single ^{14}N nucleus, the one that gives rise to the NQR frequencies, and are due to transitions of the S=5/2 system which are not normally observed in an S=1/2 system.

Although the peak at 6.33 MHz occurs near the proton Zeeman frequency of 6.36 MHz, the appearance of the line is unusual. The line due to bulk matrix proton interactions is usually quite sharp and narrow which is not the case here. It is possible that a broad "double quantum" type peak from nitrogen is superimposed upon the matrix hydrogen peak. Figure 4.38 shows the frequency spectrum at another tau value where the proton peak seems to be sharp and distinct from a lower amplitude broad peak. If this is a double quantum type peak due to nitrogen then it may be possible to determine the nitrogen hyperfine coupling from it by using an equation analogous to equation 4.10.

Conclusion

ESEEM spectroscopy was able to provide supplementary information to that obtained from the ENDOR studies. No resolved deuterium splittings were apparent in the ESEEM studies with D_2O. This indicates that water is not coordinated directly to the metal center at either the N-terminal or C-terminal sites which is consistent with the x-ray structure. The ESEEM spectra at g'=4.3, corresponding to the N-terminal site, has three peaks corresponding

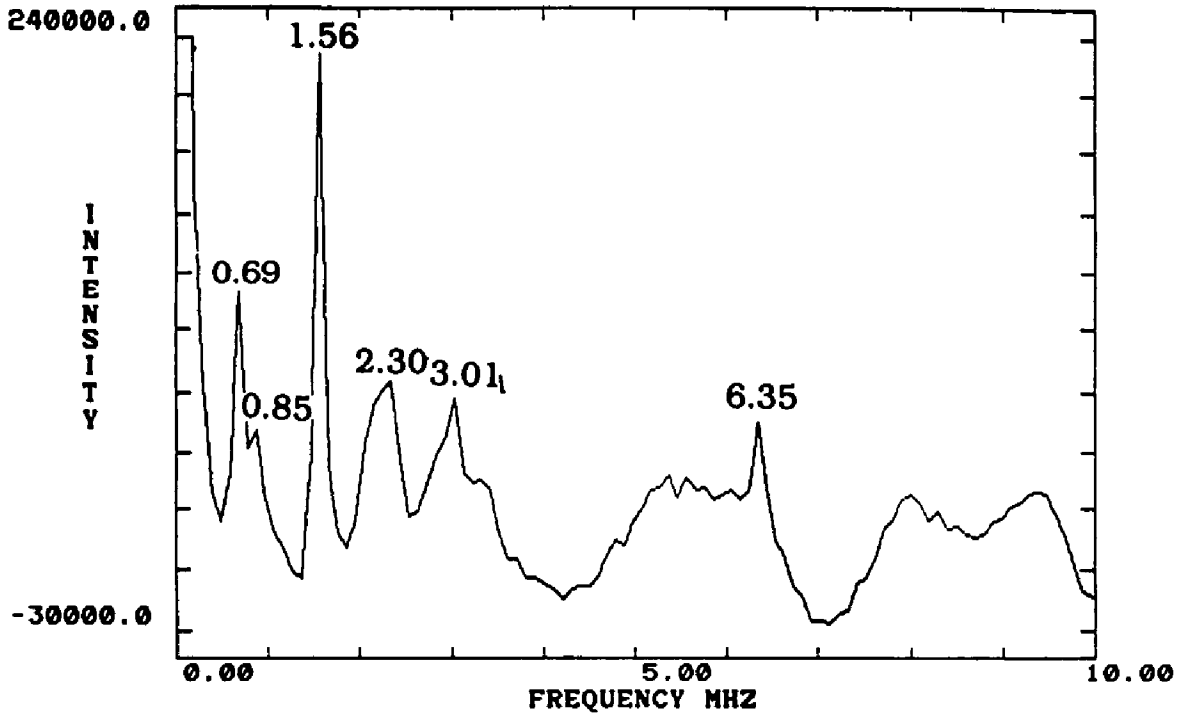

Figure 4.38 Frequency spectrum of adduct at g'=4.3. Data file SE2894.NIP. Frequency-8.70 GHz, Field-1493 G., tau-147 nsec.

to the NQR frequencies of histidine. Although the origins of all of the peaks in the g'=4.3 ESEEM spectrum could not be explained, there is no indication of cyanide interaction at the N-terminal site since isotopic substitution of CN^- does not substantially change the spectrum.

In the g=2 region it is apparent from ESEEM studies with $C^{15}N$ that there are at least two equivalent CN groups coordinated to the iron center. The maximum hyperfine coupling for nitrogen is observed near g_{xx} and is consistent with the ENDOR results which placed the carbon of the cyanide group along the g_{xx} axis. There is also a substantial hyperfine contribution observed along g_{zz}. This indicates that the nitrogen of the cyanide group is not directly on the g_{xx} axis and, consequently, that the CN bond is not aligned along the g_{xx} axis. However, the lack of resolved couplings along g_{yy} makes it impossible to pinpoint the nitrogen position exactly. Ideally, direct structural information can also be provided by the quadrupole coupling tensor. However, presumably because the Zeeman and hyperfine terms did not cancel at the spectrometer frequencies used, the pure quadrupole frequencies were not apparent in the complicated ^{14}N ESEEM spectra.

CHAPTER 5

SUMMARY OF ESEEM AND ENDOR RESULTS

ESEEM and ENDOR spectroscopy were used to study the interaction of the unpaired electron of the iron centers of transferrin with the magnetic nuclei of the cyanide(s) and other ligands. Using isotopic substitution of the the cyanide nitrogen with ^{15}N and the carbon with ^{13}C as well as exchanging water with D_2O provided additional information. Attempts to study the isotopically substituted ^{57}Fe nucleus were unsuccessful with both ENDOR and ESEEM.

Both the ENDOR and ESEEM results indicated that there is no water in the first coordination sphere of the N-terminal iron center. The ESEEM spectra of a sample exchanged with D_2O showed only a "matrix" peak at the free precessional frequency of deuterium. This peak is due to weakly interacting ambient water molecules and/or exchangeable protons on the ligands. Since resolved deuterium splittings due to coordinated D_2O have been observed with ESEEM in a number of protein systems it seems likely that if D_2O were bound in the transferrin adduct it should have been observed. The ENDOR results also showed no evidence of bound water. The ENDOR spectra have proton couplings only attributable to weakly interacting protons such as would be expected from remote ligand protons. D_2O exchange of the samples caused little change in the ENDOR spectra. ESEEM studies also indicated that there is no water directly coordinated at the C-terminal site which gives rise to the g'=4.3 signal. These results

are consistent with the x-ray structure of transferrin which also showed no water in the first coordination sphere at either iron-binding site.

The ENDOR spectra of the ^{13}CN adduct showed only one set of ^{13}C ENDOR resonances which probably corresponds to only one or two of the CN groups. Simulation of the spectra indicates a substantial isotropic coupling and smaller dipolar couplings. An analysis of the the orientation dependent dipolar term in the ENDOR studies with ^{13}CN clearly indicates that the carbon of the cyanide group is along the g_{xx} axis at a distance consistent with that of the x-ray studies of other metal cyanide complexes. The distance of 1.86 A, which best agreed with the x-ray studies of metal cyanide complexes, was calculated by attributing the anisotropic coupling to the combination of a pure dipole-dipole interaction and electron spin density on the carbon p-orbital due to the σ-bond. Since it was impossible to estimate the magnitude of additional contributions to the anisotropic coupling, this agreement may simply be due to the fortuitous cancellation of a number of these components. Although the ENDOR definitively located one CN group, the technique cannot be used quantitatively so the possibility of other cyanide groups bonded to the iron center is not ruled out. ^{13}C resonances in the ESEEM spectra were not observed presumably because of the large isotropic coupling.

ESEEM provided more information than ENDOR about the nitrogen interactions in the adduct. Some low frequency peaks, which were probably due to nitrogen, were observed in the ENDOR spectra. However, these peaks were very weak and could not be analyzed. On the other hand, the ESEEM spectra showed clearly resolved nitrogen

splittings. When $C^{15}N$ was used, resolved nitrogen interactions were observed along g_{xx} and g_{zz}. Because the nitrogen is bonded to the iron through carbon, this coupling should be primarily dipolar. Analysis of the splittings indicated only a small isotropic coupling as would be expected. The orientation dependence of the ^{15}N coupling indicates that the carbon-nitrogen bond is not aligned strictly along the g_{xx} axis, but is skewed toward g_{zz}. It is likely that the protein environment, particularly the arginine as pictured in Figure 1.9, causes this distortion. Due to variations in peak position with the time τ, there were considerable errors in the estimate of the anisotropic coupling for ^{15}N so a more quantitative analysis of the nitrogen position was not possible. This ambiguity may resolved by ESEEM studies at additional spectrometer frequencies.

The presence of harmonic peaks in the $C^{15}N$ ESEEM spectra clearly indicated that there is more that one equivalent nitrogen present in the adduct. It is unusual that these harmonics were not noted in the $C^{14}N$ spectra as well. The $C^{14}N$ ESEEM spectra were very complicated due to additional nitrogen interaction from the histidine ligand and a substantial quadrupole coupling of the cyanide nitrogen. Consequently, these spectra could not be analyzed successfully.

One plausible model of the adduct which is consistent with both the ENDOR and ESEEM results would be that of two cyanide groups *trans* to each other on the g_{xx} axis. This would presumably result in the displacement of the histidine ligand. The displacement of histidine is consistent with the ESEEM spectra which showed no signals attributable to the histidine ^{14}N nuclei. Since histidine

nitrogen interactions were quite clear in the ESEEM spectra at g'=4.3, it seems likely that they would also be observed in the g=2 region if histidine were present at the N-terminal site of the cyanide adduct However, the observation of ESEEM signals is dependent on complicated mechanisms and the lack of peaks due to a particular nucleus is not always indicative of the absence of that nucleus.

Although the ENDOR and ESEEM results of the cyanide adduct of trnasferrin did not conclusively determine the structure of the adduct, additional information about the nature of the adduct was obtained. This work illustrates the potential of the methods described for a wide variety of complexes involving nitrogen-containing ligands and paramagnetic metal centers.

APPENDIX A

CALCULATION OF DIPOLE-DIPOLE INTERACTION

To obtain a better estimate of the ^{13}C-iron distance, the dipolar interaction of a point nucleus located on the x-axis with an electron in a metal based d_{xy} orbital was calculated. This problem can be treated in a manner similar to the well-known case of an α proton with a carbon p orbital [121,122] although the integrals obtained in the present work are more complex. In order to simplify the calculation, the case of a d_{yz} orbital with the nucleus along the z axis is considered. The results for the x axis-d_{xy} orbital case follow simply from the z axis-d_{yz} case. Figure A.1 shows the coordinate system used in calculating the coupling tensor.

The tensor elements:

$$t^0_{xx} = \int \Psi\ (r, \theta, \phi) \left\{ \frac{3x^2 - r'^2}{r'^5} \right\} \Psi\ (r, \theta, \phi)\ d\tau$$

$$t^0_{yy} = \int \Psi\ (r, \theta, \phi) \left\{ \frac{3y^2 - r'^2}{r'^5} \right\} \Psi\ (r, \theta, \phi)\ d\tau$$

$$t^0_{zz} = \int \Psi\ (r, \theta, \phi) \left\{ \frac{3z^2 - r'^2}{r'^5} \right\} \Psi\ (r, \theta, \phi)\ d\tau$$

are calculated using the Slater $3d_{yz}$ orbital:

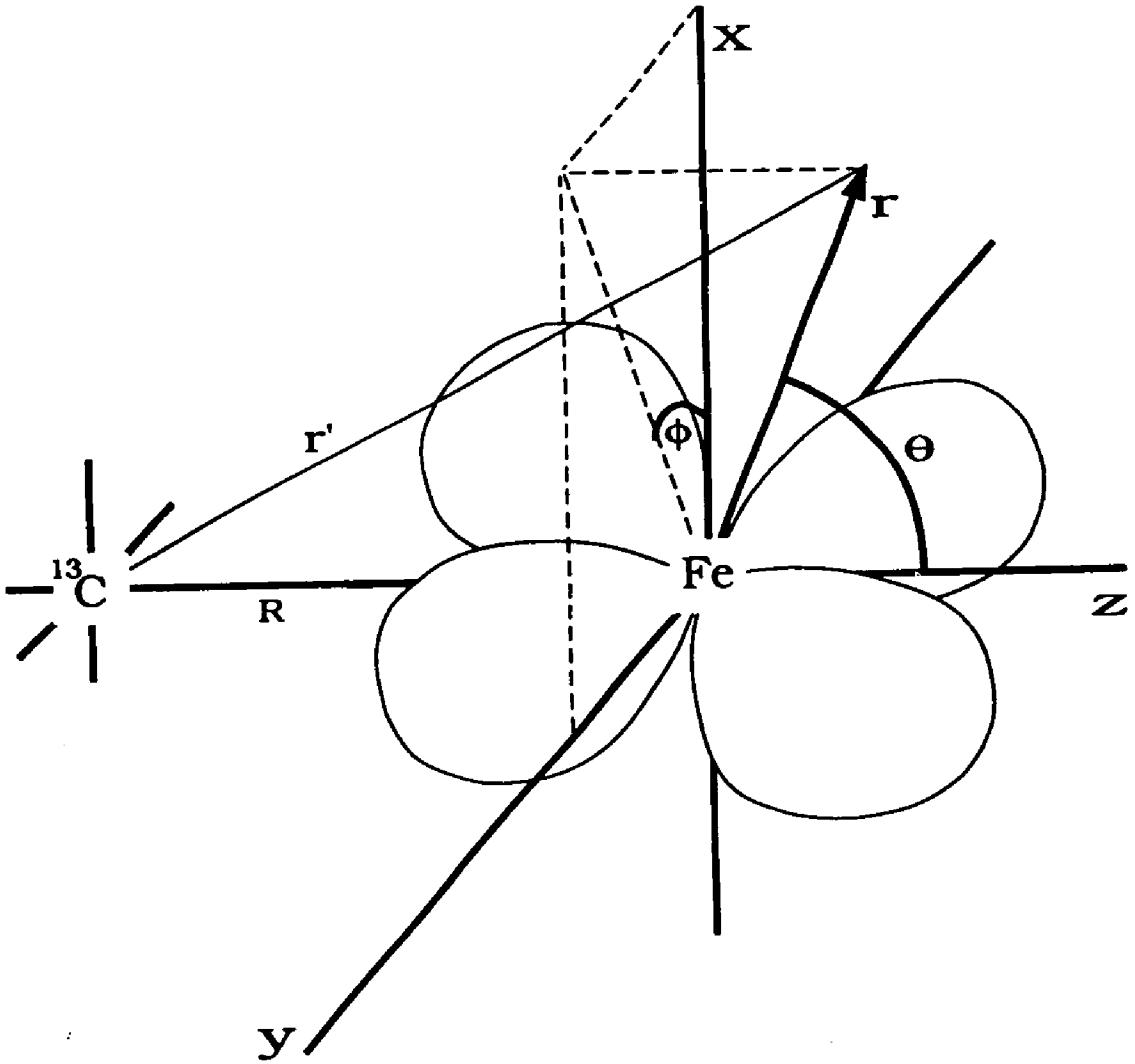

A.1 Definition of coordinates used in dipole-dipole calculation.

$$d_{yz} = \frac{2^{1/2}}{81\pi^{1/2}} \left(\frac{Z}{a_0}\right)^{7/2} r^2 e^{-Zr/3a_0} \sin\theta \cos\theta \sin\phi.$$

Let $K = \frac{Z}{a_0}$, $\rho = K r$, and $a = \frac{KR}{2}$.

The operators are expressed in terms of the polar coordinates r, θ, φ

$$x = r \sin\theta \cos\phi$$

$$= \frac{\rho \sin\theta \cos\phi}{K}$$

$$y = r \sin\theta \sin\phi$$

$$= \frac{\rho \sin\theta \sin\phi}{K}$$

$$z = r \cos\theta$$

$$= \frac{\rho \cos\theta}{K}$$

$$r'^2 = R^2 + r^2 - 2Rr \cos(180-\theta)$$

$$= R^2 + r^2 + 2Rr \cos\theta$$

$$(r')^5 = \left(\frac{4a^2}{K^2} + \frac{\rho^2}{K^2} + \frac{4a\rho \cos\theta}{K^2}\right)^{5/2}$$

$$\frac{3x^2 - r'^2}{(r')^5} = K^3 \frac{[3\rho^2 \sin^2\theta \cos^2\phi - 4a^2 - \rho^2 - 4a\rho \cos\theta]}{[4a^2 + \rho^2 + 4a\rho \cos\theta]^{5/2}}$$

$$d\tau = r^2 \sin\theta \, dr \, d\theta \, d\phi$$

$$d\tau = \frac{1}{K^3} \rho^2 \sin\theta \, d\rho \, d\theta \, d\phi$$

$$\Psi_{dyz}\Psi_{dyz} = \frac{2}{(81)^2\pi} K^7 \iiint \frac{\rho^4}{(K^4)} \exp(-2\rho/3) \sin^2\theta \cos^2\theta \sin^2\phi \, \frac{1}{K^3} \rho^2 \sin\theta \, d\rho \, d\theta \, d\phi$$

The elements to be calculated are of the form:

$$t^0_{xx} = \frac{2K^3}{(81)^2\pi} \iiint \rho^6 e^{-2\rho/3} \sin^3\theta \cos^2\theta \sin^2\phi \left[\frac{3\rho^2 \sin^2\theta \cos^2\phi - 4a^2 - \rho^2 - 4a\rho\cos\theta}{[4a^2+\rho^2+4a\rho\cos\theta]^{5/2}} \right] d\theta d\phi d\rho$$

$$t^0_{yy} = \frac{2K^3}{(81)^2\pi} \iiint \rho^6 e^{-2\rho/3} \sin^3\theta \cos^2\theta \sin^2\phi \left[\frac{3\rho^2 \sin^2\theta \sin^2\phi - 4a^2 - \rho^2 - 4a\rho\cos\theta}{[4a^2+\rho^2+4a\rho\cos\theta]^{5/2}} \right] d\theta d\phi d\rho$$

$$t^0_{zz} = \frac{2K^3}{(81)^2\pi} \iiint \rho^6 e^{-2\rho/3} \sin^3\theta \cos^2\theta \sin^2\phi \left[\frac{3\rho^2 \cos^4\theta - 4a^2 - \rho^2 - 4a\rho\cos\theta}{[4a^2+\rho^2+4a\rho\cos\theta]^{5/2}} \right] d\theta d\phi d\rho$$

where the limits of integration are $0 \le \theta \le \pi$, $0 \le \phi \le 2\pi$, and $0 \le \rho \le \infty$.

Consider first the detailed calculation for the element t^0_{xx}.

Let $G = [4a^2 + \rho^2 + 4a\rho\cos\theta]$.

$$t^0_{xx}=\frac{2K^3}{(81)^2\,\pi}\iiint\rho^6 e^{-2\rho/3}\sin^3\theta\cos^2\theta\sin^2\phi\left[\frac{3\rho^2\sin^2\theta\cos^2\phi-4a^2-\rho^2-4a\rho\cos\theta}{G^{5/2}}\right]d\theta d\phi d\rho$$

The integration over ϕ (limits 0 -> 2π) is straightforward and leads to two integrals:

I $\int \sin^2\phi\cos^2\phi$

II $\int \sin^2\phi$

$$\text{I}\quad \int \sin^2\phi\cos^2\phi = \frac{-1}{32}\sin 4\phi + \frac{\phi}{8}\Big] = \frac{\pi}{4}$$

$$\text{II}\quad \int \sin^2\phi = \frac{1}{2}\phi + \frac{1}{4}\sin^2\phi\Big] = \pi$$

$$t^0_{xx} = \frac{2K^3}{(81)^2}\iint \rho^6\, e^{-2\rho/3}\,\sin^3\theta\cos^2\theta\left[\frac{\frac{3}{4}\rho^2\sin^2\theta - 4a^2 - \rho^2 - 4a\rho\cos\theta}{G^{5/2}}\right] d\theta d\rho$$

The integrals over θ take on two values, one when $\rho < 2a$, the other when $\rho > 2a$ (these integrals are evaluated in Appendix B).

$$\int \sin^5\theta\cos^2\theta\, G^{-5/2} d\theta$$

$$\frac{1}{210a^5} + \frac{\rho^2}{252a^7} \quad \rho < 2a$$

$$\frac{16}{105\rho^5} + \frac{128a^2}{63\rho^7} \quad \rho > 2a$$

$\int \sin^3\theta \cos^2\theta \, G^{-5/2} d\theta$

$$\frac{a^2 + \rho^2}{30\, a^5 (4a^2 - \rho^2)} \qquad \rho < 2a$$

$$\frac{4\rho^2 + 64a^2}{15\rho^5 (\rho^2 - 4a^2)} \qquad \rho > 2a$$

$\int \sin^3\theta \cos^3\theta \, G^{-5/2} d\theta$

$$\frac{-3a^2\rho - \rho^3}{(21)(4)\, a^6 (4a^2 - \rho^2)} \qquad \rho < 2a$$

$$\frac{-128\, a^3 - 24a\rho^2}{21\rho^6 (\rho^2 - 4a^2)} \qquad \rho > 2a$$

so the ρ integral from 0 to 2a is:

$$\frac{2K^3}{(81)^2} \int \rho^6 e^{-2\rho/3} \left[\frac{3}{4} \rho^2 \left[\frac{1}{210a^5} + \frac{\rho^2}{252a^7} \right] - 2a^2 \frac{a^2 + \rho^2}{15a^5(4a^2 - \rho^2)} \right.$$

$$\left. - \rho^2 \frac{a^2 + \rho^2}{(30)a^5 (4a^2 - \rho^2)} - a\rho \frac{-3a^2\rho - \rho^3}{(21)a^6 (4a^2 - \rho^2)} \right] d\rho$$

$$= \frac{2K^3}{(81)^2} \int \rho^6 e^{-2\rho/3} \left[\frac{3\rho^2}{(4)(210)a^5} + \frac{3\rho^4}{(4)(252)a^7} \right.$$

$$- \frac{2a^4}{15a^5(4a^2-\rho^2)} - \frac{5a^2\rho^2}{30a^5(4a^2-\rho^2)} - \frac{\rho^4}{30a^5(4a^2-\rho^2)}$$

$$+ \frac{3a^2\rho^2}{(21)a^5(4a^2-\rho^2)} + \frac{\rho^4}{(21)a^5(4a^2-\rho^2)} \;]d\rho$$

$$= \frac{2K^3}{(81)^2} \int \rho^6 e^{-2\rho/3} \left[\frac{3\rho^2}{(4)(210)a^5} + \frac{3\rho^4}{(4)(252)a^7} - \frac{(7a^2-3\rho^2)(4a^2-\rho^2)}{(7)(3)(5)(2)a^5\,(4a^2-\rho^2)} \right] d\rho$$

$$= \frac{2K^3}{(81)^2} \int \rho^6 e^{-2\rho/3} \left[\frac{\rho^2}{(7)(2)(4)a^5} + \frac{\rho^4}{(4)(84)a^7} - \frac{1}{(3)(5)(2)a^3} \right] d\rho$$

Three integrals over ρ must then be evaluated. These are $\int \rho^8 e^{-2\rho/3} d\rho$, $\int \rho^{10} e^{-2\rho/3} d\rho$, and $\int \rho^6 e^{-2\rho/3} d\rho$.

$$\frac{1}{a^5(7)(2)(4)} \int \rho^8 e^{-2\rho/3} \, d\rho =$$

$$\left[\frac{-3(2)^4a^3}{(7)} - \frac{9(2)^5a^2}{(7)} - (3)^3(2)^3a - (3)^5(2)^2 - \frac{(5)(3)^6}{a} - \frac{(5)(3)^7}{a^2} - \frac{(5)(3)^9}{4a^3} - \frac{(5)(3)^{10}}{8a^4} - \frac{(5)(3)^{11}}{32a^5} \right] \exp(-4a/3) + \frac{(5)(3)^{11}}{32a^5}$$

$$\frac{1}{(4)(7)(3)(4)a^7} \int \rho^{10} e^{-2\rho/3} \, d\rho =$$

$$\left[-\frac{(2)^5}{(7)}a^3 - \frac{(2)^4(5)(3)}{(7)}a^2 - \frac{(5)(27)(3)(2)^2}{7}a - \frac{(3)^5(5)(2)^3}{(7)} - \frac{(3)^6(5)(2)}{a} \right.$$

$$- \frac{(3)^8(5)}{a^2} - \frac{(3)^9(5)^2}{4a^3} - \frac{(3)^{10}(5)^2}{4a^4} - \frac{(3)^{12}(5)^2}{16a^5} - \frac{(3)^{13}(5)^2}{32a^6}$$

$$\left. - \frac{(3)^{14}(5)^2}{(16)(8)a^7} \right] \exp(-4a/3) + \frac{(3)^{14}(5)^2}{(2)^7a^7}$$

$$\frac{-1}{(3)(5)(2)a^3} \int \rho^6 e^{-2\rho/3}\, d\rho =$$

$$\left[\frac{(2)^4}{5}a^3 + \frac{9(2)^3}{5}a^2 + (3)^3(2)a + (3)^4(2) + \frac{(3)^6}{(2)a} + \frac{(3)^7}{(4)a^2} \right.$$

$$\left. + \frac{(3)^6(9)}{(16)a^3} \right] \exp(-4a/3) + \frac{(3)^6(9)}{(16)a^3}$$

The θ integral from 2a to infinity is:

$$\frac{2K^3}{(81)^2} \int \rho^6 e^{-2\rho/3} \left[\frac{3\rho^2}{4} \left[\frac{16}{105\rho^5} + \frac{128a^2}{63\rho^7} \right] - 4a^2 \frac{4\rho^2+64a^2}{15\rho^2(\rho^2-4a^2)} \right.$$

$$\left. - \rho^2 \frac{4\rho^2+64a^2}{15\rho^2(\rho^2-4a^2)} - 4a\rho \frac{-128a^3-24a\rho^2}{21\rho^6(\rho^2-4a^2)} \right] d\rho$$

$$\frac{2K^3}{(81)^2} \int \rho^6 e^{-2\rho/3} \left[\frac{4}{(35)\rho^3} + \frac{96a^2}{(63)\rho^5} \right.$$

$$-\frac{(4)(64)a^4-80a^2\rho^2-4\rho^4}{(15)\rho^2(\rho^2-4a^2)}+\frac{(4)(128)a^4+(4)(24)a^2\rho^2}{21\rho^5(\rho^2-4a^2)}]d\rho$$

$$\frac{2K^3}{(81)^2}\int\rho^6e^{-2\rho/3}\left[\frac{4}{(35)\rho^3}+\frac{96a^2}{(63)\rho^5}+\frac{(\rho^2-4a^2)(-28\rho^2-192a^2)}{(7)15\rho^5(\rho^2-4a^2)}\right]d\rho$$

$$\frac{2K^3}{(81)^2}\int\rho^6e^{-2\rho/3}\left[\frac{-16}{(105)\rho^3}-\frac{(96)a^2}{(9)(7)(5)\rho^5}\right]d\rho$$

The integral over ρ must thus be evaluated for $\rho^3 e^{-2\rho/3}$ and $\rho e^{-2\rho/3}$.

$$\frac{-16}{(7)(15)}\int\rho^3e^{-2\rho/3}=\left[\frac{(-64)}{(7)(5)}a^3+\frac{(-144)}{(7)(5)}a^2+\frac{(-216)}{(7)(5)}a+\frac{(-162)}{(7)(5)}\right]\exp(-4a/3)$$

$$\frac{-96}{(9)(7)(5)}a^2\int\rho e^{-2\rho/3}=\left[\frac{-96}{(3)(7)(5)}a^3+\frac{-96}{(7)(5)(4)}a^2\right]\exp(-4a/3)$$

Adding all the terms for t^0_{xx} gives:

exponential terms (multiplied by exp(-4a/3)):

$$a^3:\left[\frac{-3(2)^4}{7}-\frac{(2)^5}{7}+\frac{(2)^4}{5}+\frac{-64}{35}-\frac{32}{(35)}\right]=\frac{-384}{(7)(5)}$$

$$a^2:\left[\frac{-9(32)}{7}-\frac{(16)(15)}{7}+\frac{(9)(8)}{5}+\frac{-144}{35}-\frac{24}{35}\right]=\frac{-2304}{35}$$

$$a: \left[-(27)(8) - \frac{(15)(27)(4)}{7} + (27)(2) + \frac{-216}{35} \right] = \frac{-13986}{35}$$

$$1: \left[-(3)^5(4) - \frac{(3)^5(5)(8)}{7} + (3)^4(2) + \frac{-162}{35} \right] = \frac{-11016}{5}$$

$$\frac{1}{a}: \left[-5(3)^6 - (3)^6(5)(2) + \frac{(3)^6}{(2)} \right] = \frac{-21141}{2}$$

$$\frac{1}{a^2}: \left[-5(3)^7 - 5(3)^8 + \frac{(3)^7}{4} \right] = \frac{-172773}{4}$$

$$\frac{1}{a^3}: \left[\frac{-5(3)^9}{4} - \frac{(3)^9(5)^2}{4} + \frac{(3)^8}{16} \right] = \frac{-2355399}{16}$$

$$\frac{1}{a^4}: \left[\frac{-5(3)^{10}}{8} - \frac{(3)^{10}(5)^2}{4} \right] = \frac{-3247695}{8}$$

$$\frac{1}{a^5}: \left[\frac{-5(3)^{11}}{32} - \frac{(3)^{12}(5)^2}{16} \right] = \frac{-27457785}{32}$$

$$\frac{1}{a^6}: \frac{-(3)^{13}(5)^2}{32}$$

$$\frac{1}{a^7}: \frac{-(3)^{14}(5)^2}{(8)(16)}$$

non-exponential terms: $\frac{5(3)^{11}}{32a^5}$

$$\frac{(3)^{14}(25)}{(2)^7 a^7}$$

$$\frac{(3)^6(9)}{(16)a^3}$$

$$t^0_{xx} = \frac{2K^3}{(81)^2}\left[\frac{-384}{(7)(5)}a^3 + \frac{-2304}{35}a^2 + \frac{-13986}{35}a - \frac{11016}{5} - \frac{21141}{2a} - \frac{172773}{4a^2}\right.$$
$$- \frac{2355399}{16a^3} - \frac{3247695}{8a^4} - \frac{27457785}{32a^5} - \frac{(3)^{12}(5)^2}{32a^6} - \frac{(3)^{13}(5)^2}{(8)(16)a^7}\Big] \exp(-4a/3)$$
$$+ \frac{5(3)^{11}}{(2)^5 a^5} + \frac{(3)^{14}(25)}{128a^7} - \frac{(3)^8}{16a^3}$$

to write this in terms of R:

$$\frac{2K^3}{(81)^2} = \frac{2(2a/R)^3}{(81)^2} = \frac{16a^3}{(3)^8 R^3}$$

$$t^0_{xx} = \frac{1}{R^3}\left[\left(-\frac{2048}{76545}a^6 - \frac{4096}{25515}a^5 - \frac{8288}{59049}a^4 - \frac{2176}{405}a^3\right.\right.$$
$$- \frac{232}{9}a^2 - \frac{316}{3}a - 359 - \frac{990}{a} - \frac{4185}{2a^2} -$$
$$\left.\left.\frac{6075}{2a^3} - \frac{18225}{8a^4}\right) \exp(-4a/3) + \frac{135}{2a^2} + \frac{18225}{8a^4} - 1\right] \qquad \text{(A.1)}$$

The integrals for t^0_{yy} are similar to those of t^0_{xx}.

$$t^0_{yy} = \frac{2K^3}{(81)^2\pi}\iiint \rho^6 e^{-2\rho/3}\sin^3\theta\cos^2\theta\sin^2\phi\left[\frac{3\rho^2\sin^2\theta\sin^2\phi - 4a^2-\rho^2-4a\rho\cos\theta}{G^{5/2}}\right]d\theta d\phi d\rho$$

The integrals over ϕ are the same as for t^0_{xx} except for:

$$\int \sin^4\phi d\phi = \frac{30}{8} - \frac{\sin^2\phi}{4} - \frac{\sin^4\phi}{32} \Big] = \frac{3\pi}{4}$$

$$t^0_{yy} = \frac{2K^3}{(81)^2}\int \rho^6 e^{-2\rho/3}\sin^3\theta\cos^2\theta\left[\frac{9/4\rho^2\sin^2\theta - -4a^2-\rho^2-4a\rho\cos\theta}{G^{5/2}}\right]d\theta d\rho$$

Integrals from 0 to 2a:

$$= \frac{2K^3}{(81)^2}\int \rho^6 e^{-2\rho/3}\left[\frac{9}{4}\rho^2\left(\frac{1}{210a^5} + \frac{\rho^2}{252a^7}\right) + \frac{-1}{(3)(5)(2)a^3} - \frac{\rho^2}{(7)(5)(2)a^5}\right]d\rho$$

$$= \frac{2K^3}{(81)^2}\int \rho^6 e^{-2\rho/3}\left[\frac{3\rho^2}{(4)(70)a^5} + \frac{\rho^4}{(4)(28)a^7} - \frac{1}{(3)(5)(2)a^3} - \frac{\rho^2}{(7)(10)a^5}\right]d\rho$$

$$= \frac{2K^3}{(81)^2}\int \rho^6 e^{-2\rho/3}\left[\frac{-\rho^2}{(4)(70)a^5} + \frac{\rho^4}{(4)(28)a^7} - \frac{1}{(3)(5)(2)a^3}\right]d\rho$$

The integrals in ρ were calculated for the t_{xx} case. For t_{yy}:

$\int \rho^8 e^{-2\rho/3}d\rho$ terms for $t_{yy} = (-1/5)\int \rho^8 e^{-2\rho/3}d\rho$ terms for t_{xx}

$\int \rho^{10} e^{-2\rho/3}d\rho$ terms for $t_{yy} = 3\int \rho^{10} e^{-2\rho/3}\,d\rho$ terms for t_{xx}

$\int \rho^6 e^{-2\rho/3}d\rho$ terms for $t_{yy} = \int \rho^6 e^{-2\rho/3}d\rho$ same as for t_{xx}

The θ integrals from 2a to infinity lead to terms:

$\int \rho^3 e^{-2\rho/3} d\rho$ terms for $t_{yy} = -\frac{1}{2} \times \int \rho^3 e^{-2\rho/3} d\rho$ terms for t_{xx}

$\int \rho\, e^{-2\rho/3} d\rho$ terms for $t_{yy} = -9 \times \int \rho e^{-2\rho/3} d\rho$ terms for t_{xx}

Combining all terms for t_{yy}:

exponential terms:

$$a^3: \left[\frac{3(2)^4}{35} - \frac{3(2)^5}{7} + \frac{(2)^4}{5} + \frac{32}{35} + \frac{288}{(35)}\right] = 0$$

$$a^2: \left[\frac{9(32)}{35} - \frac{3(16)(15)}{7} + \frac{(9)(8)}{5} + \frac{72}{35} + \frac{216}{35}\right] = -72$$

$$a: \left[\frac{216}{5} - \frac{3(15)(27)(12)}{7} + (27)(2) + \frac{216}{70}\right] = \frac{-69390}{35}$$

$$1: \left[(3)^5(4/5) - \frac{(3)^6(5)(8)}{7} + (3)^4(2) + \frac{162}{70}\right] = -3807$$

$$\frac{1}{a}: \left[(3)^6 - (3)^7(5)(2) + \frac{(3)^6}{(2)}\right] = \frac{-41553}{2}$$

$$\frac{1}{a^2}: \left[(3)^7 - 5(3)^9 + \frac{(3)^7}{4}\right] = \frac{-382725}{4}$$

$$\frac{1}{a^3}: \left[\frac{(3)^9}{4} - \frac{(3)^{10}(5)^2}{4} + \frac{(3)^8}{16}\right] = \frac{-5819607}{16}$$

$$\frac{1}{a^4}: \left[\frac{(3)^{10}}{8} - \frac{(3)^{11}(5)^2}{4} \right] = \frac{-8798301}{8}$$

$$\frac{1}{a^5}: \left[\frac{(3)^{11}}{32} - \frac{(3)^{13}(5)^2}{16} \right] = \frac{-79539003}{32}$$

$$\frac{1}{a^6}: \frac{-(3)^{14}(5)^2}{32}$$

$$\frac{1}{a^7}: \frac{-(3)^{15}(5)^2}{(8)(16)}$$

non-exponential terms: $\frac{-(3)^{11}}{32a^5}$

$$\frac{(3)^{15}(25)}{(2)^7 a^7}$$

$$\frac{(3)^6(9)}{(16)a^3}$$

$$t^0_{yy} = \frac{1}{R^3} \left[\left[\frac{-128}{729} a^5 - \frac{8224}{1701} a^4 - \frac{754}{81} a^3 - \frac{152}{3} a^2 - \frac{700}{3} a - 887 \right.\right.$$

$$\left. - \frac{2682}{a} - \frac{12123}{2a^2} - \frac{(3)^6(5)^2}{2a^3} - \frac{(3)^7(5)^2}{8a^4} \right] \exp(-4a/3) - \frac{(3)^3}{2a^2}$$

$$\left. + \frac{(3)^7(25)}{8a^4} - 1 \right] \qquad \text{(A.2)}$$

Using the fact that $t_{zz} = - t_{xx} - t_{yy}$ gives:

$$t^0_{zz} = \frac{1}{R^3}\Big[\Big[\frac{2048}{76545}a^6 + \frac{8576}{25515}a^5 + \frac{2056448}{(3)^{10}(7)}a^4 + \frac{5946}{(81)(5)}a^3$$

$$+ \frac{688}{9}a^2 + \frac{1016}{3}a + 1246 + \frac{3672}{a} + \frac{8154}{a^2} + \frac{12150}{a^3}$$

$$+ \frac{18225}{2a^4}\Big]\exp(-4a/3) - \frac{-54}{a^2} - \frac{18225}{2a^4} + 2\Big] \qquad \text{(A.3)}$$

Note that, as would be expected, these tensor elements reduce to the case of a point dipole-dipole interaction (i.e. $(3\cos^2\theta - 1)/R^3$) when a is large. Since a is proportional to R the electron-nuclear distance, a large value for a corresponds to a large distance between the electron and nucleus.

The above calculation was for a d_{yz} orbital with the nucleus along the z axis. For the case of the d_{xy} orbital with nucleus along x.

$$t'_{xx} = t^0_{zz}$$
$$t'_{yy} = t^0_{yy}$$
$$t'_{zz} = t^0_{xx}$$

where the ^{0} superscript represents the case calculated above and ' represents the d_{xy} - x axis problem.

The variable a is dependent on the effective nuclear charge, Z, and the distance, R. The Clementi rules [123] were used to obtain an approximate value for Z of 11.33. For large Z (as is the case for iron) the tensor elements calculated are relatively insensitive to small changes in Z. Changes in the value of Z by ± .3 only change the dipolar elements by a maximum of ± .02 MHz. Using R=2.09 Å which best matched the ^{13}C ENDOR data as discussed in Chapter 2, and multiplying by $gg_n\beta_n\beta_e$ gives the dipolar terms:

$A_{p,xx}$ = 4.73 MHz

$A_{p,yy}$ = -2.32 MHz

$A_{p,zz}$ = -1.78 MHz

Similar equations describing the dipolar interaction in the case of a d_{xy} orbital with the nucleus along the z axis were also calculated. Using the wavefunction for the d_{xy} orbital gives:

$$\Psi_{dxy}\Psi_{dxy} = \frac{1}{2(81)^2\pi} K^7 \iiint \frac{\rho^4}{(K^4)} \exp(-2\rho/3) \sin^4\theta \sin^2 2\phi \frac{1}{K^3} \rho^2 \sin\theta \, d\rho \, d\theta \, d\phi$$

The integrals to be evaluated are of the form:

$$t_{xx}=\frac{K^3}{2(81)^2\pi}\iiint\rho^6e^{-2\rho/3}\sin^5\theta\sin^2 2\phi\left[\frac{3\rho^2\sin^2\theta\cos^2\phi-4a^2-\rho^2-4a\rho\cos\theta}{[4a^2+\rho^2+4a\rho\cos\theta]^{5/2}}\right]d\theta d\phi d\rho$$

$$t_{yy}=\frac{K^3}{2(81)^2\pi}\iiint\rho^6e^{-2\rho/3}\sin^5\theta\sin^2 2\phi\left[\frac{3\rho^2\sin^2\theta\sin^2\phi-4a^2-\rho^2-4a\rho\cos\theta}{[4a^2+\rho^2+4a\rho\cos\theta]^{5/2}}\right]d\theta d\phi d\rho$$

$$t_{zz}=\frac{K^3}{2(81)^2\pi}\iiint\rho^6e^{-2\rho/3}\sin^5\theta\sin^2 2\phi\left[\frac{3\rho^2\cos^4\theta-4a^2-\rho^2-4a\rho\cos\theta}{[4a^2+\rho^2+4a\rho\cos\theta]^{5/2}}\right]d\theta\, d\phi\, d\rho$$

The integrals over ϕ are again straightforward. After integration over ϕ:

$$t_{xx}=\frac{K^3}{2(81)^2}\iint\rho^6e^{-2\rho/3}\sin^5\theta\left[\frac{\frac{3}{2}\rho^2\sin^2\theta-4a^2-\rho^2-4a\rho\cos\theta}{G^{5/2}}\right]d\theta d\rho$$

$$t_{yy}=\frac{K^3}{2(81)^2}\iint\rho^6e^{-2\rho/3}\sin^5\theta\left[\frac{\frac{3}{4}\rho^2\sin^2\theta-4a^2-\rho^2-4a\rho\cos\theta}{G^{5/2}}\right]d\theta d\rho$$

The integrals for θ take on two values, one for $\rho>2a$ and one for $\rho< 2a$. The necessary integrals are evaluated in Appendix B. The integrals over ρ are the same as those used in the detailed calculation shown above. The final equations are:

$$t_{xx}=\frac{1}{R^3}\left[\left(-\frac{256}{76545}a^5+\frac{(4)(116)}{(3)^4(5)}a^2+20a+103+\frac{(2)(189)}{a}-\frac{1917}{2a^2}\right.\right.$$

$$+\frac{(3)^5 25}{4a^3}+\frac{(3)^6(25)}{16a^4}\Big)\ \exp(-4a/3)+\frac{54}{a^2}+\frac{(3)^6 25}{16a^4}-1\Big]$$

$$t_{yy}=\frac{1}{R^3}\Big[\Big(+\frac{4}{81}a^3-\frac{8}{9}a^2+8a+48+\frac{180}{a}-\frac{945}{2a^2}+$$
$$\frac{(3)^5 25}{8a^3}+\frac{(3)^6(25)}{32a^4}\Big)\ \exp(-4a/3)+\frac{5\,(3)^3}{4a^2}-\frac{(3)^6\,25}{32a^4}-1\Big]$$

$$t_{zz}=\frac{1}{R^3}\Big[\Big(\frac{256}{76545}a^5+\frac{4}{81}a^3-\frac{104}{(3)^4(5)}a^2-4a-35-\frac{162}{a}-\frac{252}{a^2}-$$
$$\frac{(3)^5 25}{8a^3}-\frac{(3)^6(25)}{32a^4}\Big)\ \exp(-4a/3)-\frac{7(27)}{4a^2}+\frac{(3)^6 25}{32a^4}+2\Big]$$

APPENDIX B

INTEGRALS

1. $\int \sin\theta \, G^{-5/2} \, d\theta$
2. $\int \sin\theta \cos\theta \, G^{-5/2} \, d\theta$
3. $\int \cos^2\theta \sin\theta \, G^{-5/2} \, d\theta$
4. $\int \cos^3\theta \sin\theta \, G^{-5/2} \, d\theta$
5. $\int \sin^3\theta \, G^{-5/2} \, d\theta$
6. $\int \sin^3\theta \cos\theta \, G^{-5/2} \, d\theta$
7. $\int \sin^5\theta \, G^{-5/2} \, d\theta$
8. $\int \cos^4\theta \sin\theta \, G^{-5/2} \, d\theta$
9. $\int \sin^3\theta \cos^2\theta \, G^{-5/2} d\theta$
10. $\int \sin\theta \cos^5\theta \, G^{-5/2} \, d\theta$
11. $\int \sin^3\theta \cos^3\theta \, G^{-5/2} \, d\theta$
12. $\int \sin^5\theta \cos\theta \, G^{-5/2} \, d\theta$
13. $\int \sin\theta \cos^6\theta \, G^{-5/2} \, d\theta$
14. $\int \sin^5\theta \cos^2\theta \, G^{-5/2} \, d\theta$
15. $\int \sin^7\theta \, G^{-5/2} \, d\theta$

All these integrals are evaluated from $\theta = 0$ to π. The integrals take on two values:

I. when $\rho < 2a$

II. when $\rho > 2a$

These cases are indicated in the evaluation of the integral. The integrals are typically solved with integration by parts:

$$\int u \, dv = uv - \int v \, du .$$

Let $G = [\, 4a^2 + \rho^2 + 4a\rho\cos\theta \,]$.

1. $\int \sin\theta \, G^{-5/2} \, d\theta$

$$= \frac{2}{12a\rho} [\, 4a^2 + \rho^2 + 4a\rho\cos\theta \,]^{-3/2}$$

$$= \frac{1}{6a\rho} [\, 4a^2 + \rho^2 - 4a\rho \,]^{-3/2} - \frac{1}{6a\rho} [\, 4a^2 + \rho^2 + 4a\rho \,]^{-3/2}$$

I. $$= \frac{1}{6a\rho[2a-\rho]^3} - \frac{1}{6a\rho[2a+\rho]^3}$$

$$= \frac{[2a+\rho]^3 - [2a-\rho]^3}{6a\rho[2a-\rho]^3[2a+\rho]^3}$$

$$= \frac{24a^2+2\rho^3}{6a\rho[4a^2-\rho^2]^3}$$

$$= \frac{12a^2+\rho^2}{3a[4a^2-\rho^2]^3}$$

II. $$= \frac{1}{6a\rho[2a-\rho]^3} - \frac{1}{6a\rho[2a+\rho]^3}$$

$$= \frac{[2a+\rho]^3 - [2a-\rho]^3}{6a\rho[2a-\rho]^3[2a+\rho]^3}$$

$$= \frac{2}{3\rho} \frac{4a^2+3\rho^2}{[\rho^2-4a^2]^3}$$

2. $\int \sin\theta \cos\theta\, G^{-5/2} d\theta$

$u = \cos\theta \qquad du = -\sin\theta d\theta$

$dv = \sin\theta\, G^{-5/2} d\theta \qquad v = \frac{1}{6a\rho} G^{-3/2}$

$$= \frac{1}{6a\rho} \cos\theta G^{-3/2} + \frac{1}{6a\rho} \int \sin\theta G^{-3/2} d\theta$$

$$= \frac{1}{6a\rho} \cos\theta\, G^{-3/2} + \frac{1}{6a\rho} \frac{1}{2a\rho} G^{-1/2}$$

I. $$= -\frac{1}{6a\rho} \frac{1}{[2a-\rho]^3} + \frac{1}{12a^2\rho^2} \frac{1}{[2a-\rho]}$$

$$-\frac{1}{6a\rho} \frac{1}{[2a+\rho]^3} - \frac{1}{[12a^2\rho^2]} \frac{1}{[2a+\rho]}$$

$$= \frac{-2a\rho[2a+\rho]^3 + [2a-\rho]^2[2a+\rho]^3 - 2a\rho[2a-\rho]^3 - [2a+\rho]^2[2a-\rho]^3}{12a^2\rho^2\,[2a-\rho]^3\,[2a+\rho]^3}$$

$$= \frac{-2a\rho[16a^3+12a\rho^2] + 32a^4\rho - 16a^2\rho^3 + 2\rho^5}{12a^2\rho^2\,[2a-\rho]^3\,[2a+\rho]^3}$$

$$= \frac{-\rho}{6a^2} \frac{20a^2-\rho^2}{(4a^2-\rho^2)^3}$$

II. $$= -\frac{1}{6a\rho} \frac{1}{[\rho-2a]^3} + \frac{1}{12a^2\rho^2} \frac{1}{[\rho-2a]} - \frac{1}{6a\rho[2a+\rho]^3} - \frac{1}{12a^2\rho^2} \frac{1}{[2a+\rho]^3}$$

$$= \frac{-2a\rho\,[\,24a^2\rho+2\rho^3] + [64a^5-32a^3\rho^2+4a\rho^4]}{12a^2\rho^2[\rho^2-4a^2]^3}$$

$$= \frac{4a}{3\rho^2} \frac{[4a^2-5\rho^2]}{(\rho^2-4a^2)^3}$$

3. $\int \cos^2\theta \sin\theta \, G^{-5/2} \, d\theta$

$u = \cos\theta$ $\qquad du = -\sin\theta \, d\theta$

$dv = \cos\theta \sin\theta \, G^{-5/2} \, d\theta$ $\qquad v = \frac{1}{6a\rho} \cos\theta \, G^{-3/2} + \frac{1}{12a^2\rho^2} G^{-1/2}$

$$= \frac{1}{6a\rho} \cos^2\theta \, G^{-3/2} + \frac{1}{2a^2\rho^2} \cos\theta \, G^{-1/2} + \frac{1}{6a\rho} \int \sin\theta \cos\theta \, G^{-3/2} \, d\theta$$

$$+ \frac{1}{2a^2\rho^2} \int \sin\theta \, G^{-1/2} \, d\theta$$

A. $\int \sin\theta \cos\theta \, G^{-3/2} \, d\theta$

$$\frac{1}{2a\rho} \cos\theta \, G^{-1/2} + \frac{1}{2a\rho} \int \sin\theta \, G^{-1/2} \, d\theta$$

B. $\int \sin\theta \, G^{-1/2} \, d\theta = \frac{-1}{2a\rho} G^{+1/2}$

$$= \frac{1}{6a\rho} \cos^2\theta \, G^{-3/2} + \frac{1}{6a^2\rho^2} \cos\theta \, G^{-1/2} - \frac{1}{12a^3\rho^3} G^{1/2}$$

I. $$\frac{1}{6a\rho} \left[\frac{1}{[2a-\rho]^3} - \frac{1}{[2a+\rho]^3} \right] - \frac{1}{6a^2\rho^2} \left[\frac{1}{[2a-\rho]} + \frac{1}{[2a+\rho]} \right] + \frac{\rho}{6a^3\rho^3}$$

$$= \frac{1}{6a\rho} \left[\frac{24a^2\rho+2\rho^3}{(4a^2-\rho^2)^3} \right] - \frac{2}{3a\rho^2} \left[\frac{1}{(4a^2-\rho^2)} \right] + \frac{1}{6a^3\rho^2}$$

$$= \frac{1}{6a^3} \frac{8a^4 + 10a^2\rho^2 - \rho^4}{(4a^2 - \rho^2)^3}$$

II. $$\frac{1}{6a\rho}\left[\frac{1}{[\rho-2a]^3}-\frac{1}{[2a+\rho]^3}\right]-\frac{1}{6a^2\rho^2}\left[\frac{1}{[\rho-2a]}+\frac{1}{[2a+\rho]}\right]+\frac{1}{3a^2\rho^3}$$

$$=\frac{2}{3\rho}\frac{(4a^2+3\rho^2)}{(\rho^2-4a^2)^3}-\frac{1}{3a^2\rho}\frac{1}{(\rho^2-4a^2)}+\frac{1}{3a^2\rho^3}$$

$$=\frac{2}{3\rho^3}\left(\frac{\rho^4+20a^2\rho^2-32a^4}{(\rho^2-4a^2)^3}\right)$$

4. $\int \cos^3\theta \sin\theta\, G^{-5/2}\, d\theta$

$u = \cos\theta$ $\qquad du = -\sin\theta\, d\theta$

$dv = \cos^2\theta \sin\theta\, G^{-5/2}\, d\theta$

$$v = \frac{1}{6a\rho}\cos^2\theta\, G^{-3/2}+\frac{1}{6a^2\rho^2}\cos\theta\, G^{-1/2}-\frac{1}{12a^3\rho^3}G^{1/2}$$

$$=\frac{1}{6a\rho}\cos^3\theta\, G^{-3/2}+\frac{1}{6a^2\rho^2}\cos^2\theta\, G^{-1/2}-\frac{1}{12a^3\rho^3}\cos\theta\, G^{1/2}$$
$$+\frac{1}{6a\rho}\int \cos^2\theta \sin\theta\, G^{-3/2}\, d\theta+\frac{1}{6a^2\rho^2}\int \sin\theta\cos\theta\, G^{-1/2}\, d\theta$$
$$-\frac{1}{12a^3\rho^3}\int \sin\theta\, G^{1/2}\, d\theta$$

A. $$\int \cos^2\theta \sin\theta\, G^{-3/2}\, d\theta$$
$$=\frac{1}{2a\rho}\cos^2\theta\, G^{-1/2}-\frac{1}{2a^2\rho^2}\cos\theta\, G^{1/2}+\frac{1}{12a^3\rho^3}G^{3/2}$$

B. $$\int \sin\theta\cos\theta\, G^{-1/2}\, d\theta$$
$$=\frac{-1}{2a\rho}\cos\theta\, G^{1/2}+\frac{1}{12a^2\rho^2}G^{3/2}$$

C. $$\frac{-1}{6a\rho}G^{3/2}$$

$$= \frac{1}{6a\rho}\cos^3\theta\, G^{-3/2} + \frac{1}{4a^2\rho^2}\cos^2\theta\, G^{-1/2} - \frac{1}{4a^3\rho^3}\cos\theta\, G^{1/2} + \frac{1}{24a^4\rho^4} G^{3/2}$$

I. $$= \frac{-1}{6a\rho}\left[\frac{1}{[2a-\rho]^3} + \frac{1}{[2a+\rho]^3}\right] + \frac{1}{4a^2\rho^2}\left[\frac{1}{[2a-\rho]} - \frac{1}{[2a+\rho]}\right] + \frac{1}{a^2\rho^3} + \frac{1}{24a^4\rho^4}\left[(2a-\rho)^3 - (2a+\rho)^3\right]$$

$$= \frac{-1}{6a\rho}\left[\frac{16a^3 + 12a\rho^2}{[4a^2-\rho^2]^3}\right] + \frac{1}{4a^2\rho^2}\left[\frac{2\rho}{[4a^2-\rho^2]}\right] + \frac{1}{a^2\rho^3} - \frac{1}{a^2\rho^3} - \frac{1}{12a^4\rho}$$

$$= \frac{-24a^4\rho^2 - 6\rho^4a^2 + \rho^6}{12a^4\rho[4a^2-\rho^2]^3}$$

$$= \frac{-\rho}{12a^4}\,\frac{24a^2+6a^2\rho^2-\rho^4}{[4a^2-\rho^2]^3}$$

II. $$= \frac{-1}{6a\rho}\left[\frac{1}{[\rho-2a]^3} + \frac{1}{[2a+\rho]^3}\right] + \frac{1}{4a^2\rho^2}\left[\frac{1}{[\rho-2a]} - \frac{1}{[2a+\rho]}\right] + \frac{1}{2a^3\rho^2} + \frac{1}{24a^4\rho^4}\left[(\rho-2a)^3 - (2a+\rho)^3\right]$$

$$= \frac{4a}{3\rho^4}\,\frac{-3\rho^4-12\rho^2a^2+32a^4}{(\rho^2-4a^2)^3}$$

5. $$\int \sin^3\theta\, G^{-5/2}\, d\theta = \int \sin\theta\,(1-\cos^2\theta)\, G^{-5/2}\, d\theta$$

$$= \int \sin\theta\, G^{-5/2}\, d\theta - \int \sin\theta\cos^2\theta\, G^{-5/2}\, d\theta$$

I. $$= \frac{12a^2+\rho^2}{3a[4a^2-\rho^2]^3} - \frac{1}{6a^3}\,\frac{8a^4+10a^2\rho^2-\rho^4}{(4a^2-\rho^2)^3}$$

$$= \frac{1}{6a^3}\,\frac{1}{(4a^2-\rho^2)}$$

II. $$= \frac{2}{3\rho}\,\frac{4a^2+3\rho^2}{[\rho^2-4a^2]^3} - \frac{2}{3\rho^3}\,\frac{\rho^4+20a^2\rho^2-32a^4}{(\rho^2-4a^2)^3}$$

$$= \frac{4}{3\rho^3}\,\frac{1}{(\rho^2-4a^2)}$$

6. $\int \sin^3\theta \cos\theta\, G^{-5/2}\, d\theta$

$= \int (1-\cos^2\theta) \sin\theta \cos\theta\, G^{-5/2}\, d\theta$

$= \int \sin\theta \cos\theta\, G^{-5/2}\, d\theta - \int \cos^3\theta \sin\theta\, G^{-5/2}\, d\theta$

I. $$= \frac{-\rho}{6a^2}\,\frac{20a^2-\rho^2}{(4a^2-\rho^2)^3} + \frac{\rho}{12a^4}\,\frac{24a^4+6a^2\rho^2-\rho^4}{(4a^2-\rho^2)^3}$$

$$= \frac{-\rho}{12a^4}\,\frac{1}{(4a^2-\rho^2)}$$

II. $$= \frac{-4}{3}\,\frac{a}{\rho^2}\,\frac{5\rho^2-4a^2}{(\rho^2-4a^2)^3} + \frac{4}{3}\,\frac{a}{\rho^4}\,\frac{3\rho^4+12a^2\rho^2-32a^4}{(\rho^2-4a^2)^3}$$

$$= \frac{-8a}{3\rho^4}\,\frac{1}{(\rho^2-4a^2)}$$

7. $\int \sin^5\theta\, G^{-5/2}\, d\theta$

$\int (1-\cos^2\theta) \sin^3\theta\, G^{-5/2}\, d\theta = \int \sin^3\theta\, G^{-5/2}\, d\theta - \int \cos^2\theta \sin^3\theta\, G^{-5/2}\, d\theta$

I. $= \frac{1}{6a^3} \frac{1}{4a^2-\rho^2} - \frac{1}{30a^5} \frac{a^2+\rho^2}{4a^2-\rho^2}$

$= \frac{1}{30a^5}$

II. $= \frac{4}{3\rho^3} \frac{1}{\rho^2-4a^2} - \frac{4}{15\rho^5} \frac{\rho^2+16a^2}{\rho^2-4a^2}$

$= \frac{16}{15\rho^5}$

8. $\int \cos^4\theta \sin\theta \, G^{-5/2} \, d\theta$

$u = \cos^4\theta \qquad du = -4 \cos^3\theta \sin\theta \, d\theta$

$dv = \sin\theta \, G^{-5/2} \, d\theta \qquad v = \frac{1}{6a\rho} G^{-3/2}$

$\frac{1}{6a\rho} \cos^4\theta \, G^{-3/2} + \frac{2}{3a\rho} \int \cos^3\theta \sin\theta \, G^{-3/2} \, d\theta$

$u = \cos^3\theta \qquad du = -3 \cos^2\theta \sin\theta \, d\theta$

$dv = \sin\theta \, G^{-3/2} \, d\theta \qquad v = \frac{1}{2a\rho} G^{-1/2}$

$\frac{2}{3a\rho} [\frac{1}{2a\rho} \cos^3\theta \, G^{-1/2} + \frac{3}{2a\rho} \int \cos^2\theta \sin\theta \, G^{-1/2} \, d\theta]$

$\frac{1}{3a^2\rho^2} \cos^3\theta \, G^{-1/2} + \frac{1}{a^2\rho^2} \int \cos^2\theta \sin\theta \, G^{-1/2}$

$u = \cos^2\theta \qquad du = -2\cos\theta \sin\theta$

$dv = \sin\theta \, G^{-1/2} \qquad v = \frac{-1}{2a\rho} G^{+1/2}$

$$\frac{1}{a^2\rho^2}\left[\frac{-1}{2a\rho}\cos^2\theta\, G^{1/2} - \frac{1}{a\rho}\int \cos\theta\, \sin\theta\, G^{1/2}\right]$$

$$\frac{-1}{2a^3\rho^3}\cos^2\theta\, G^{1/2} - \frac{1}{a^3\rho^3}\int \cos\theta\, \sin\theta\, G^{1/2}$$

$u = \cos\theta \qquad du = -\sin\theta$

$dv = \sin\theta\, G^{1/2} \qquad v = \frac{-1}{6a\rho} G^{3/2}$

$$\frac{-1}{a^3\rho^3}\left[\frac{-1}{6a\rho}\cos\theta\, G^{3/2} - \frac{1}{6a\rho}\int \sin\theta\, G^{3/2}\right]$$

$$\frac{1}{6a^4\rho^4}\cos\theta\, G^{3/2} - \frac{1}{60a^5\rho^5} G^{5/2}$$

I. $$= \frac{1}{6a\rho}\frac{1}{(2a-\rho)^3} - \frac{1}{3a^2\rho^2}\frac{1}{(2a-\rho)} - \frac{1}{2a^3\rho^3}(2a-\rho) - \frac{1}{6a^4\rho^4}(2a-\rho)^3$$

$$- \frac{1}{60a^5\rho^5}(2a-\rho)^5 - \frac{1}{6a\rho}\frac{1}{(2a+\rho)^3} - \frac{1}{3a^2\rho^2}\frac{1}{(2a+\rho)}$$

$$+ \frac{1}{2a^3\rho^3}(2a+\rho) - \frac{1}{6a^4\rho^4}(2a+\rho)^3 + \frac{1}{60a^5\rho^5}(2a+\rho)^5$$

$$= \frac{1}{6a\rho}\left[\frac{1}{(2a-\rho)^3} - \frac{1}{(2a+\rho)^3}\right] - \frac{1}{3a^2\rho^2}\left[\frac{1}{(2a-\rho)} + \frac{1}{(2a+\rho)} + \frac{1(2\rho)}{2a^3\rho^3}\right]$$

$$- \frac{1}{6a^4\rho^4}\left[(2a-\rho)^3 + (2a+\rho)^3\right] + \frac{1}{60a^5\rho^5}\left[(2a+\rho)^5 - (2a-\rho)^5\right]$$

$$= \frac{1}{6a\rho}\left[\frac{24a^2\rho+2\rho^3}{(4a^2-\rho^2)^3}\right] - \frac{1}{3a^2\rho^2}\left[\frac{4a}{(4a^2-\rho^2)}\right] - \frac{1}{a^3\rho^2}$$

$$- \frac{1(2)}{6a^4\rho^4} [\, 8a^3+6a\rho^2 \,] + \frac{1(2)}{60a^5\rho^5} [\, 80a^4\rho + 40a^2\rho^3 + \rho^5 \,]$$

$$= \frac{1}{3a\rho} [\, \frac{12a^2\rho + \rho^3}{(4a^2-\rho^2)^3} \,] - \frac{1}{3a^2\rho^2} [\, \frac{4a}{4a^2-\rho^2} \,] + \frac{1}{a^3\rho^2}$$

$$- \frac{8}{3a\rho^4} - \frac{2}{a^3\rho^2} + \frac{8}{3a\rho^4} + \frac{4}{3a^3\rho^2} + \frac{1}{30a^5}$$

$$= \frac{1}{3a\rho} [\, \frac{12a^2\rho+\rho^3}{(4a^2-\rho^2)^3} \,] - \frac{4}{3a\rho^2(4a^2-\rho^2)} + \frac{1}{3a^3\rho^2} + \frac{1}{30a^5}$$

II. $$= \frac{1}{6a\rho} [\, \frac{1}{(\rho-2a)^3} - \frac{1}{(2a+\rho)^3} \,] - \frac{1}{3a^2\rho^2} [\, \frac{1}{(\rho-2a)} + \frac{1}{(2a+\rho)} \,]$$

$$- \frac{1}{2a^3\rho^3} [\, (\rho-2a) - (2a+\rho) \,] - \frac{1}{6a^4\rho^4} [\, (\rho-2a)^3 + (2a+\rho)^3 \,]$$
$$+ \frac{1}{60a^5\rho^5} [\, (2a+\rho)^5 - (\rho-2a)^5 \,]$$

$$= \frac{2}{3\rho} \frac{4a^2+3\rho^2}{(\rho^2-4a^2)^3} - \frac{1}{3a^2\rho^2} [\, \frac{2\rho}{(\rho^2-4a^2)} \,] + \frac{2a}{a^3\rho^3} - \frac{1}{6a^4\rho^4} [\, 2\rho^3 + 24a^2\rho \,]$$

$$+ \frac{1}{60a^5\rho^5} [\, 32a^5 + 80a^3\rho^2 + 10a\rho^4 \,]$$

$$= \frac{2}{3\rho} \frac{4a^2+3\rho^2}{(\rho^2-4a^2)^3} - \frac{2}{3a^2\rho} \frac{1}{(\rho^2-4a^2)} + \frac{2}{a^2\rho^3} - \frac{1}{3a^4\rho} - \frac{4}{a^2\rho^3}$$

$$+ \frac{16}{15\rho^5} + \frac{8}{3a^2\rho^3} + \frac{1}{3a^4\rho}$$

$$= \frac{2}{3\rho}\frac{(4a^2+3\rho^2)}{(\rho^2-4a^2)^3} - \frac{2}{3a^2\rho}\frac{1}{(\rho^2-4a^2)} + \frac{2}{3a^2\rho^3} + \frac{16}{15\rho^5}$$

9. $\int \sin^3\theta \cos^2\theta\, G^{-5/2}\, d\theta$

$= \int \sin\theta \cos^2\theta\, G^{-5/2}\, d\theta - \int \cos^4\theta \sin\theta\, G^{-5/2}\, d\theta$

I. $$= \frac{12a^2\rho+\rho^3}{3a\rho(4a^2-\rho^2)^3} - \frac{2}{3a\rho^2(4a^2-\rho^2)} + \frac{1}{6a^3\rho^2}$$

$$- \frac{12a^2\rho+\rho^3}{3a\rho(4a^2-\rho^2)^3} + \frac{4}{3a\rho^2(4a^2-\rho^2)} - \frac{1}{3a^3\rho^2} - \frac{1}{30a^5}$$

$$= \frac{2}{3a\rho^2(4a^2-\rho^2)} - \frac{1}{6a^3\rho^2} - \frac{1}{30a^5}$$

$$= \frac{1}{3a}\left[\frac{20a^4-a^2(4a^2-\rho^2)-\rho^2(4a^2-\rho^2)}{10a^4\rho^2(4a^2-\rho^2)}\right]$$

$$= \frac{1}{3a}\left[\frac{a^2\rho^2+\rho^4}{10a^4\rho^2(4a^2-\rho^2)}\right]$$

$$= \frac{1}{30a^5}\frac{a^2+\rho^2}{(4a^2-\rho^2)}$$

II. $$= \frac{1}{6a\rho}\left[\frac{12a\rho^2+16a^3}{(\rho^2-4a^2)^3}\right] - \frac{1}{3a^2\rho}\frac{1}{(\rho^2-4a^2)} + \frac{1}{3a^2\rho^3}$$

$$- \frac{2}{3\rho}\frac{4a^2+3\rho^2}{(\rho^2-4a^2)^3} + \frac{2}{3a^2\rho}\frac{1}{(\rho^2-4a^2)} - \frac{2}{3a^2\rho^3} - \frac{16}{15\rho^5}$$

$$= \frac{1}{3a^2}\frac{1}{(\rho^2-4a^2)} - \frac{1}{3a^2\rho^3} - \frac{16}{15\rho^5}$$

$$= \frac{1}{3\rho}\left[\frac{1}{a^2(\rho^2-4a^2)} - \frac{1}{a^2\rho^2} - \frac{16}{5\rho^4}\right]$$

$$= \frac{1}{3\rho}\left[\frac{5\rho^4-5\rho^2(\rho^2-4a^2) - 16(\rho^2-4a^2)}{5\rho^4a^2(\rho^2-4a^2)}\right]$$

$$= \frac{1}{3\rho}\left[\frac{a^2\rho^2 + 64a^4}{5\rho^4a^2(\rho^2-4a^2)}\right.$$

$$= \frac{4\rho^2+64a^2}{15\rho^5(\rho^2-4a^2)}$$

10. $\int \sin\theta \cos^5\theta\, G^{-5/2}\, d\theta$

$u = \cos^5\theta \qquad du = -5\cos^4\theta \sin\theta\, d\theta$

$dv = \sin\theta\, G^{-5/2}\, d\theta \qquad v = \frac{1}{6a\rho} G^{-3/2}$

$$= \frac{1}{6a\rho}\cos^5\theta\, G^{-3/2} + \frac{5}{6a\rho}\int \cos^4\theta \sin\theta\, G^{-3/2}\, d\theta$$

$u = \cos^4\theta \qquad du = -4\cos^3\theta \sin\theta\, d\theta$

$dv = \sin\theta\, G^{-3/2}\, d\theta \qquad v = \frac{1}{2a\rho} G^{-1/2}$

$$\frac{5}{6a\rho}\left[\frac{1}{2a\rho}\cos^4\theta\, G^{-1/2} + \frac{2}{a\rho}\int \cos^3\theta \sin\theta\, G^{-1/2}\, d\theta\right]$$

$$\frac{5}{12a^2\rho^2}\cos^4\theta\, G^{-1/2} + \frac{5}{3a^2\rho^2}\int \cos^3\theta \sin\theta\, G^{-1/2}\, d\theta$$

$u = \cos^3\theta \qquad du = -3\cos^2\theta \sin\theta\, d\theta$

$$dv = \sin\theta\, G^{-1/2}\, d\theta \qquad v = \frac{-1}{2a\rho} G^{+1/2}$$

$$\frac{5}{3a^2\rho^2}\left[\frac{-1}{2a\rho}\cos^3\theta\, G^{+1/2} - \frac{3}{2a\rho}\int \cos^2\theta \sin\theta\, G^{+1/2}\, d\theta\right]$$

$$\frac{-5}{6a^3\rho^3}\cos^3\theta\, G^{+1/2} - \frac{5}{2a^3\rho^3}\int \cos^2\theta \sin\theta\, G^{1/2}\, d\theta$$

$$u = \cos^2\theta \qquad du = -2\cos\theta \sin\theta\, d\theta$$
$$dv = \sin\theta\, G^{1/2}\, d\theta \quad v = \frac{-1}{6a\rho} G^{3/2}$$

$$\frac{-5}{2a^3\rho^3}\left[\frac{-1}{6a\rho}\cos^2\theta\, G^{3/2} - \frac{1}{3a\rho}\int \cos\theta \sin\theta\, G^{3/2}\, d\theta\right]$$

$$\frac{5}{12a^4\rho^4}\cos^2\theta\, G^{3/2} + \frac{5}{6a^4\rho^4}\int \cos\theta \sin\theta\, G^{3/2}\, d\theta$$

$$u = \cos\theta \qquad du = -\sin\theta\, d\theta$$
$$dv = \sin\theta\, G^{3/2}\, d\theta \quad v = \frac{-1}{10a\rho} G^{5/2}$$

$$\frac{5}{6a^4\rho^4}\left[\frac{-1}{10a\rho}\cos\theta\, G^{5/2} - \frac{1}{10a\rho}\int \sin\theta\, G^{5/2}\, d\theta\right]$$

$$\frac{-1}{12a^5\rho^5}\cos\theta\, G^{5/2} - \frac{1}{12a^5\rho^5}\int \sin\theta\, G^{5/2}\, d\theta$$

$$\frac{1}{(12)(14)a^6\rho^6} G^{7/2}$$

$$= \frac{1}{6a\rho}\cos^5\theta\, G^{-3/2} + \frac{5}{12a^2\rho^2}\cos^4\theta\, G^{-1/2} - \frac{5}{6a^3\rho^3}\cos^3\theta\, G^{1/2}$$

$$+ \frac{5}{12a^4\rho^4}\cos^2\theta\, G^{3/2} - \frac{1}{12a^5\rho^5}\cos\theta\, G^{5/2} + \frac{1}{(12)(14)a^6\rho^6} G^{7/2}$$

I. $$= \frac{-1}{6a\rho}\frac{1}{[2a-\rho]^3} + \frac{5}{12a^2\rho^2}\frac{1}{[2a-\rho]} + \frac{5}{6a^3\rho^3}[2a-\rho] + \frac{5}{12a^4\rho^4}[2a-\rho]^3$$

$$+ \frac{1}{12a^5\rho^5}[2a-\rho]^5 + \frac{1}{(12)(14)a^6\rho^6}[2a-\rho]^7 - \frac{1}{6a\rho}\frac{1}{[2a+\rho]^3}$$

$$- \frac{5}{12a^2\rho^2}\frac{1}{[2a+\rho]} + \frac{5}{6a^3\rho^3}[2a+\rho] - \frac{5}{12a^4\rho^4}[2a+\rho]^3$$

$$+ \frac{1}{12a^5\rho^5}[2a+\rho]^5 + \frac{1}{(12)(14)a^6\rho^6}[2a+\rho]^7$$

$$= \frac{-1}{6a\rho}\left[\frac{1}{[2a-\rho]^3} + \frac{1}{[2a+\rho]^3}\right] + \frac{5}{12a^2\rho^2}\left[\frac{1}{[2a-\rho]} - \frac{1}{[2a+\rho]}\right]$$

$$+ \frac{5}{6a^3\rho^3}\left[(2a-\rho) + (2a+\rho)\right] + \frac{5}{12a^4\rho^4}\left[(2a-\rho)^3 - (2a+\rho)^3\right]$$

$$+ \frac{1}{12a^5\rho^5}\left[(2a-\rho)^5 + (2a+\rho)^5\right]$$

$$+ \frac{1}{(12)(14)a^6\rho^6}\left[(2a-\rho)^7 + (2a-\rho)^7\right]$$

$$= -\frac{1}{6a\rho}\left[\frac{16a^3+12a^2\rho^2}{(4a^2-\rho^2)^3}\right] + \frac{5}{12a^2\rho^2}\left[\frac{2\rho}{(4a^2-\rho^2)}\right] + \frac{20a}{6a^3\rho^3}$$

$$- \frac{5}{6a^4\rho^4}(12a^2\rho+\rho^3) + \frac{1}{6a^5\rho^5}\left[10a\rho^4 + 10(2)^3a^3\rho^2 + (2)^5a^5\right]$$

$$- \frac{1}{(6)(14)a^6\rho^6} [\, 7(2)^6a^6\rho + 35(2)^4\rho^3 + 21(2)^2a^2\rho^5 + \rho^7 \,]$$

$$= \frac{-1}{3a\rho} \frac{(8a^3+6a\rho^2)}{(4a^2-\rho^2)^3} + \frac{5}{6a^2\rho(4a^2-\rho^2)} - \frac{1}{6a^4\rho} - \frac{1\rho}{(6)(14)a^6}$$

II. $$= \frac{-1}{6a\rho} \frac{1}{[\rho-2a]^3} + \frac{5}{12a^2\rho^2} \frac{1}{[\rho-2a]} + \frac{5}{6a^3\rho^3} [\rho-2a] + \frac{5}{12a^4\rho^4} [\rho-2a]^3$$

$$+ \frac{1}{12a^5\rho^5} [\rho-2a]^5 + \frac{1}{(12)(14)a^6\rho^6} [\rho-2a]^7$$

$$- \frac{1}{6a\rho} \frac{1}{[2a+\rho]^3} - \frac{5}{12a^2\rho^2} \frac{1}{[2a+\rho]} + \frac{5}{6a^3\rho^3} [2a+\rho] - \frac{5}{12a^4\rho^4} [2a+\rho]^3$$

$$+ \frac{1}{12a^5\rho^5} [2a+\rho]^5 - \frac{1}{(12)(14)a^6\rho^6} [2a+\rho]^7$$

$$= \frac{-1}{6a\rho} [\, \frac{1}{[\rho-2a]^3} + \frac{1}{[2a+\rho]^3} \,] + \frac{5}{12a^2\rho^2} [\, \frac{1}{[\rho-2a]} - \frac{1}{[2a+\rho]} \,]$$

$$+ \frac{5}{6a^3\rho^3} [\, (\rho-2a) + (2a+\rho) \,] + \frac{5}{12a^4\rho^4} [\, (\rho-2a)^3 - (2a+\rho)^3 \,]$$

$$+ \frac{1}{12a^5\rho^5} [\, (\rho-2a)^5 + (2a+\rho)^5 \,] + \frac{1}{(12)(14)a^6\rho^6} [(\rho-2a)^7 - (2a+\rho)^7 \,]$$

$$= \frac{-1}{6a\rho} [\, \frac{(2)(12a^2\rho+\rho^3)}{(-4a^2+\rho^2)^3} \,] + \frac{5}{12a^2\rho^2} [\, \frac{4a}{(-4a^2+\rho^2)} \,] + \frac{5\rho}{3a^3\rho^3}$$

$$+ \frac{5}{12a^4\rho^4} [\, -2(8a^3+6a\rho^2) \,] + \frac{1}{12a^5\rho^5} [\, 2(\rho^5+40a^2\rho^3+80a^4\rho) \,]$$

$$+ \frac{1}{(12)(14)a^6\rho^6} [\, -2(2)^7a^7 + 21(2)^5a^5\rho^2 + 35(2)^3a^3\rho^4 + 14a\rho^6]$$

$$= \frac{-1}{3a\rho} [\, \frac{(12a^2\rho+\rho^3)}{(\rho^2-4a^2)^3} \,] + \frac{5}{3a\rho^2(\rho^2-4a^2)} - \frac{4}{3a\rho^4} - \frac{(2)^5a}{21\rho^6}$$

11. $\int \sin^3\theta \cos^3\theta\, G^{-5/2}\, d\theta$

$\int \sin\theta\, (1-\cos^2\theta) \cos^3\theta\, G^{-5/2}\, d\theta$

$\int \sin\theta \cos^3\theta\, G^{-5/2}\, d\theta - \int \sin\theta \cos^5\theta\, G^{-5/2}\, d\theta$

I. $$= \frac{-8a^3-6a\rho^2}{3a\rho[4a^2-\rho^2]^3} + \frac{1}{2a^2\rho[4a^2-\rho^2]} - \frac{1}{12a^4\rho} + \frac{1}{3a\rho} \frac{8a^3+6a\rho^2}{[4a^2-\rho^2]^3}$$

$$- \frac{5}{6a^2\rho(4a^2-\rho^2)} + \frac{1}{6a^4\rho} + \frac{\rho}{(6)(14)a^6}$$

$$= \frac{-1}{3a^2\rho(4a^2-\rho^2)} + \frac{1}{12a^4\rho} + \frac{\rho}{(6)(14)a^6}$$

$$= \frac{1}{3a^2} [\, \frac{-1}{\rho(4a^2-\rho^2)} + \frac{1}{4a^2\rho} + \frac{\rho}{28a^4} \,]$$

$$= \frac{\rho}{3a^6} \frac{(-3a^2-\rho^2)}{(28)(4a^2-\rho^2)}$$

II. $$= \frac{-1}{3a} \frac{[\rho^2+12a^2]}{[\rho^2-4a^2]^3} + \frac{1}{a\rho^2[\rho^2-4a^2]} - \frac{2}{3a\rho^4} + \frac{1}{3a\rho} \frac{[12a^2\rho+\rho^3]}{(\rho^2-4a^2)^3}$$

$$- \frac{5}{3a\rho^2(\rho^2-4a^2)} + \frac{4}{3a\rho^4} + \frac{(2)^5a}{21\rho^6}$$

$$= \frac{-2}{3a\rho^2(\rho^2-4a^2)} + \frac{2}{3a\rho^4} + \frac{32}{21\rho^6}$$

$$= \frac{2}{3\rho^2}\left[\frac{-1}{a(\rho^2-4a^2)} + \frac{1}{a\rho^2} + \frac{16a}{7\rho^4}\right]$$

$$= \frac{2}{3\rho^2}\left[\frac{-7\rho^4+7\rho^2(\rho^2-4a^2)+16a^2(\rho^2-4a^2)}{7a\rho^4(\rho^2-4a^2)}\right]$$

$$= \frac{2(-12a\rho^2-64a^3)}{21\rho^6(\rho^2-4a^2)}$$

$$= \frac{24a\rho^2-128a^3}{21\rho^6(\rho^2-4a^2)}$$

12. $\int \sin^5\theta \cos\theta\, G^{-5/2}\, d\theta$

$= \int \sin\theta \cos\theta\, (1-\cos^2\theta)^2\, d\theta$

$= \int \sin\theta \cos\theta\, d\theta - 2\int \sin\theta \cos^3\theta\, d\theta + \int \sin\theta \cos^5\theta\, d\theta$

I. $= \frac{-\rho}{6a^2}\,\frac{20a^2-\rho^2}{(4a^2-\rho^2)3}$

$$- 2\left[\frac{-1}{6a\rho}\,\frac{16a^3+12a\rho^2}{[4a^2-\rho^2]3} + \frac{1}{4a^2\rho^2}\left[\frac{2\rho}{[4a^2-\rho^2]}\right] - \frac{1}{12a^4\rho}\right]$$

$$\frac{-1}{3a\rho}\,\frac{(8a^3+6a\rho^2)}{(4a^2-\rho^2)^3} + \frac{5}{6a^2\rho(4a^2-\rho^2)} - \frac{1}{6a^4\rho} - \frac{1\rho}{(6)(14)a^6}$$

$$= -\frac{1\rho}{(6)(14)a^6}$$

II. $= \frac{4a}{3\rho^2}\frac{[4a^2-5\rho^2]}{(\rho^2-4a^2)^3} - 2[\frac{4a}{3\rho^4}\frac{-3\rho^4-12\rho^2a^2+32a^4}{(\rho^2-4a^2)^3}]$

$\frac{-1}{3a\rho}[\frac{(12a^2\rho+\rho^3)}{(\rho^2-4a^2)^3}] + \frac{5}{3a\rho^2(\rho^2-4a^2)} - \frac{4}{3a\rho^4} - \frac{(2)^5a}{21\rho^6}$

$= -\frac{(2)^5a}{21\rho^6}$

13. $\int \sin\theta \cos^6\theta\, G^{-5/2}\, d\theta$

$u = \cos^6\theta \qquad du = -6\cos^5\theta \sin\theta\, d\theta$

$dv = \sin\theta\, G^{-5/2}\, d\theta \qquad v = \frac{1}{6a\rho} G^{-3/2}$

$= \frac{1}{6a\rho}\cos^6\theta\, G^{-3/2} + \frac{1}{a\rho}\int \cos^5\theta \sin\theta\, G^{-3/2}\, d\theta$

$u = \cos^5\theta \qquad du = -5\cos^4\theta \sin\theta\, d\theta$

$dv = \sin\theta\, G^{-3/2}\, d\theta \qquad v = \frac{1}{2a\rho} G^{-1/2}$

$\frac{1}{a\rho}[\frac{1}{2a\rho}\cos^5\theta\, G^{-1/2} + \frac{5}{2a\rho}\int \cos^4\theta \sin\theta\, G^{-1/2}\, d\theta]$

$\frac{1}{2a^2\rho^2}\cos^5\theta\, G^{-1/2} + \frac{5}{2a^2\rho^2}\int \cos^4\theta \sin\theta\, G^{-1/2}\, d\theta$

$u = \cos^4\theta \qquad du = -4\cos^3\theta \sin\theta\, d\theta$

$dv = \sin\theta\, G^{-1/2}\, d\theta \qquad v = \frac{-1}{2a\rho} G^{+1/2}$

$\frac{5}{2a^2\rho^2}[\frac{-1}{2a\rho}\cos^4\theta\, G^{+1/2} - \frac{2}{a\rho}\int \cos^3\theta \sin\theta\, G^{+1/2}\, d\theta]$

$$\frac{-5}{4a^3\rho^3}\cos^4\theta\, G^{+1/2} - \frac{5}{a^3\rho^3}\int \cos^3\theta \sin\theta\, G^{1/2}\, d\theta$$

$u = \cos^3\theta \qquad du = -3\cos\theta \sin\theta\, d\theta$

$dv = \sin\theta\, G^{1/2}\, d\theta \quad v = \frac{-1}{6a\rho} G^{3/2}$

$$\frac{-5}{a^3\rho^3}\left[\frac{-1}{6a\rho}\cos^3\theta\, G^{3/2} - \frac{1}{2a\rho}\int \cos^2\theta \sin\theta\, G^{3/2}\, d\theta\right]$$

$$\frac{5}{6a^4\rho^4}\cos^3\theta\, G^{3/2} + \frac{5}{2a^4\rho^4}\int \cos^2\theta \sin\theta\, G^{3/2}\, d\theta$$

$u = \cos^2\theta \qquad du = -2\cos\theta \sin\theta\, d\theta$

$dv = \sin\theta\, G^{3/2}\, d\theta \quad v = \frac{-1}{10a\rho} G^{5/2}$

$$\frac{5}{2a^4\rho^4}\left[\frac{-1}{10a\rho}\cos^2\theta\, G^{5/2} - \frac{1}{5a\rho}\int \cos\theta \sin\theta\, G^{5/2}\, d\theta\right]$$

$$\frac{-1}{4a^5\rho^5}\cos^2\theta\, G^{5/2} - \frac{1}{2a^5\rho^5}\int \cos\theta \sin\theta\, G^{5/2}\, d\theta$$

$u = \cos\theta \qquad du = -\sin\theta\, d\theta$

$dv = \sin\theta\, G^{5/2}\, d\theta \quad v = \frac{-1}{14a\rho} G^{7/2}$

$$-\frac{1}{2a^5\rho^5}\left[\frac{-1}{14a\rho}\cos\theta\, G^{7/2} - \frac{1}{14a\rho}\int \sin\theta\, G^{7/2}\, d\theta\right]$$

$$\frac{1}{28a^6\rho^6}\cos\theta\, G^{7/2} + \frac{1}{28a^6\rho^6}\int \sin\theta\, G^{7/2}\, d\theta$$

$$\frac{1}{28a^6\rho^6}\left[-\frac{1}{18a\rho}G^{9/2}\right.$$

$$-\frac{1}{(28)(18)a^7\rho^7}G^{9/2}$$

$$=\frac{1}{6a\rho}\cos^6\theta\,G^{-3/2}+\frac{1}{2a^2\rho^2}\cos^5\theta\,G^{-1/2}-\frac{5}{4a^3\rho^3}\cos^4\theta\,G^{1/2}$$

$$+\frac{5}{6a^4\rho^4}\cos^3\theta\,G^{3/2}-\frac{1}{4a^5\rho^5}\cos^2\theta\,G^{5/2}+\frac{1}{28a^6\rho^6}\cos\theta\,G^{7/2}$$

$$-\frac{1}{(28)(18)a^7\rho^7}G^{9/2}$$

I.
$$=\frac{1}{6a\rho}\left[\frac{1}{[2a-\rho]^3}-\frac{1}{[2a+\rho]^3}\right]-\frac{1}{2a^2\rho^2}\left[\frac{1}{[2a-\rho]}+\frac{1}{[2a+\rho]}\right]$$

$$+\frac{5}{4a^3\rho^3}\left[(2a+\rho)-(2a-\rho)\right]-\frac{5}{6a^4\rho^4}\left[(2a-\rho)^3+(2a+\rho)^3\right]$$
$$+\frac{1}{4a^5\rho^5}\left[(2a+\rho)^5-(2a-\rho)^5\right]-\frac{1}{(28)a^6\rho^6}\left[(2a-\rho)^7+(2a+\rho)^7\right]$$

$$-\frac{1}{(28)(18)a^7\rho^7}\left[(2a-\rho)^9-(2a+\rho)^9\right]$$

$$=\frac{1}{6a\rho}\left[\frac{24a^2\rho+2\rho^3}{(4a^2-\rho^2)^3}\right]-\frac{1}{2a^2\rho^2}\left[\frac{4a}{(4a^2-\rho^2)}\right]+\frac{5}{2a^3\rho^2}$$

$$-\frac{5(2)}{6a^4\rho^4}\left[8a^3+6a\rho^2\right]+\frac{1(2)}{4a^5\rho^5}\left[80a^4\rho+40a^2\rho^3+\rho^5\right]$$

$$-\frac{1(2)}{28a^6\rho^6}\left[128a^7+672a^5\rho^2+280a^3\rho^4+14a\rho^6\right]$$

$$- \frac{1(2)}{(28)(18)a^7\rho^7} [\, -\rho^9 - 144a^2\rho^7 - 2016a^4\rho^5 - 5376a^6\rho^3 - 2304a^8\rho]$$

$$= \frac{1}{6a\rho} [\, \frac{24a^2\rho+2\rho^3}{(4a^2-\rho^2)^3}] \; - \frac{2}{a\rho^2} [\, \frac{1}{(4a^2-\rho^2)}] + \frac{5}{2a^3\rho^2} - \frac{40}{3a\rho^4} - \frac{10}{a^3\rho^2}$$

$$+ \frac{40}{a\rho^4} + \frac{20}{a^3\rho^2} + \frac{1}{2a^5} - \frac{64a}{7\rho^6} - \frac{48}{a\rho^4} - \frac{20}{a^3\rho^2} - \frac{1}{a^5} + \frac{\rho^2}{252a^7}$$

$$+ \frac{4}{7a^5} + \frac{8}{a^3\rho^2} + \frac{64}{3a\rho^4} + \frac{64a}{7\rho^6}$$

$$= \frac{1}{6a\rho} [\, \frac{24a^2\rho+2\rho^3}{(4a^2-\rho^2)^3}] \; - \frac{2}{a\rho^2} [\, \frac{1}{(4a^2-\rho^2)}] + \frac{1}{2a^3\rho^2} + \frac{1}{14a^5} + \frac{\rho^2}{252a^7}$$

II. $$= \frac{1}{6a\rho} [\, \frac{1}{[\rho-2a]^3} - \frac{1}{[2a+\rho]^3}] - \frac{1}{2a^2\rho^2} [\, \frac{1}{[\rho-2a]} + \frac{1}{[2a+\rho]}]$$

$$+ \frac{5}{4a^3\rho^3} [\, (2a+\rho) - (\rho-2a)] - \frac{5}{6a^4\rho^4} [\, (\rho-2a)^3 + (2a+\rho)^3]$$

$$+ \frac{1}{4a^5\rho^5} [\, (2a+\rho)^5 - (\rho-2a)^5] - \frac{1}{(28)a^6\rho^6} [\, (\rho-2a)^7 + (2a+\rho)^7]$$

$$- \frac{1}{(28)(18)a^7\rho^7} [\, (\rho-2a)^9 - (2a+\rho)^9]$$

$$= \frac{2}{3\rho} \frac{4a^2+3\rho^2}{(\rho^2-4a^2)^3} - \frac{1}{2a^2\rho^2} [\, \frac{2\rho}{(\rho^2-4a^2)}] + \frac{5}{a^2\rho^3} - \frac{5}{6a^4\rho^4} [\, 2\rho^3 + 24a^2\rho]$$

$$+ \frac{2}{4a^5\rho^5} [\, 32a^5 + 80a^3\rho^2 + 10a\rho^4]$$

$$- \frac{2}{28a^6\rho^6}[\rho^7 + 84a^2\rho^5 + 560a^4\rho^3 + 448a^6\rho]$$

$$- \frac{2}{(28)(18)a^7\rho^7}[-512a^9 - 4608a^7\rho^2 - 4032a^5\rho^4 - 672a^3\rho^6 - 18a\rho^8]$$

$$= \frac{2}{3\rho}\frac{4a^2+3\rho^2}{(\rho^2-4a^2)^3} - \frac{1}{a^2\rho}\frac{1}{(\rho^2-4a^2)} + \frac{5}{a^2\rho^3} - \frac{5}{3a^4\rho} - \frac{20}{a^2\rho^3} + \frac{16}{\rho^5} + \frac{40}{a^2\rho^3}$$

$$+ \frac{5}{a^4\rho} - \frac{\rho}{14a^6} - \frac{6}{a^4\rho} - \frac{40}{a^2\rho^3} - \frac{32}{\rho^5} + \frac{128a^2}{63\rho^7} + \frac{128}{7\rho^5} + \frac{16}{a^2\rho^3} + \frac{24}{9a^4\rho} + \frac{\rho}{14a^6}$$

$$= \frac{2}{3\rho}\frac{4a^2+3\rho^2}{(\rho^2-4a^2)^3} - \frac{1}{a^2\rho}\frac{1}{(\rho^2-4a^2)} + \frac{1}{a^2\rho^3} + \frac{16}{7\rho^5} + \frac{128a^2}{63\rho^7}$$

14. $\int \sin^5\theta \cos^2\theta\, G^{-5/2}\, d\theta$

$= \int \sin^5\theta \cos^2\theta\, G^{-5/2}\, d\theta = \int \sin\theta \cos^2\theta\, (1-\cos^2\theta)^2\, G^{-5/2}\, d\theta$

$= \int \sin\theta \cos^2\theta\, G^{-5/2}\, d\theta - 2\int \sin\theta \cos^4\theta\, G^{-5/2}\, d\theta + \int \sin\theta \cos^6\theta\, G^{-5/2} d\theta$

I. $$= \frac{1}{6a\rho}\left[\frac{24a^2\rho+2\rho^3}{(4a^2-\rho^2)^3}\right] - \frac{2}{3a\rho^2}\left[\frac{1}{(4a^2-\rho^2)}\right] + \frac{1}{6a^3\rho^2}$$

$$- \frac{1}{3a\rho}\left[\frac{24a^2\rho+2\rho^3}{(4a^2-\rho^2)^3}\right] + \frac{8}{3a\rho^2}\left[\frac{1}{(4a^2-\rho^2)}\right] - \frac{2}{3a^3\rho^2} + \frac{1}{15a^5}$$

$$+ \frac{1}{6a\rho}\left[\frac{24a^2\rho+2\rho^3}{(4a^2-\rho^2)^3}\right] - \frac{2}{a\rho^2}\left[\frac{1}{(4a^2-\rho^2)}\right] + \frac{1}{2a^3\rho^2} + \frac{1}{14a^5} + \frac{\rho^2}{252a^7}$$

$$= \frac{1}{210a^5} + \frac{\rho^2}{252a^7}$$

II. $= \frac{2}{3\rho}\frac{(4a^2+3\rho^2)}{(\rho^2-4a^2)^3} - \frac{1}{3a^2\rho}\frac{1}{(\rho^2-4a^2)} + \frac{1}{3a^2\rho^3}$

$- \frac{4}{3\rho}\frac{(4a^2+3\rho^2)}{(\rho^2-4a^2)^3} + \frac{4}{3a^2\rho}\frac{1}{(\rho^2-4a^2)} - \frac{4}{3a^2\rho^3} - \frac{32}{15\rho^5}$

$+ \frac{2}{3\rho}\frac{4a^2+3\rho^2}{(\rho^2-4a^2)^3} - \frac{1}{a^2\rho}\frac{1}{(\rho^2-4a^2)} + \frac{1}{a^2\rho^3} + \frac{16}{7\rho^5} + \frac{128a^2}{63\rho^7}$

$= \frac{16}{105\rho^5} + \frac{128a^2}{63\rho^7}$

15. $\int \sin^7\theta\, G^{-5/2}\, d\theta$

$= \int \sin^5\theta\,(1-\cos^2\theta)\, G^{-5/2}\, d\theta = \int \sin^5\theta\, G^{-5/2}\, d\theta - \int \sin^5\theta\cos^2\theta\, G^{-5/2}\, d\theta$

I. $= \frac{1}{30a^5} - \frac{1}{210a^5} - \frac{\rho^2}{252a^7}$

$= \frac{1}{35a^5} - \frac{\rho^2}{252a^7}$

II. $= \frac{16}{15\rho^5} - \frac{16}{105\rho^5} - \frac{128a^2}{63\rho^7}$

$= \frac{32}{35\rho^5} - \frac{128a^2}{63\rho^7}$

REFERENCES

[1] Scholes, C.P. in *Multiple Electron Resonance Spectroscopy* ; M.M. Dorio and J.H. Freed, Eds.; Plenum Press: New York, 1979.

[2] Sands, R.H. in *Multiple Electron Resonance Spectroscopy*; Dorio, M.M., Freed, J.H., Eds.; Plenum Press: New York, 1979.

[3] Hahn, E. L. *Phys. Rev.*, **1950**, *80*, 580.

[4] Rowan, L. G.; Hahn, E. L.; Mims, W. B. *Phys. Rev.*, **1965**, *A61*, 137.

[5] Kevan, L. in *Time Domain Electron Spin Resonance*; L. Kevan and R. N. Schwartz, Eds.; Wiley: New York, 1979.

[6] Schweiger, A.; Gemperle, C.; Ernst, R.R. *J. Magn. Reson.* **1990**, *86*, 70.

[7] Schweiger, A. ACC-Workshop on Electron Spin Echo Spectroscopy, Amsterdam, 1988.

[8] Mims, W.B.; Peisach, J. in *Biological Magnetic Resonance*, Vol. 3, L.J. Berliner and J.R. Reuben, Eds. Plenum: New York, 1981.

[9] Mims, W. B., *Phys. Rev.*, **1972**, *B5*, 2409.

[10] Mims, W. B., *Phys. Rev.*, **1972**, *B6*, 3543.

[11] Mims, W.B. in *Electron Paramagnetic Resonance* S. Geschwindt, ed. Plenum Press: New York, 1972, pp. 263-351.

[12] Mims, W.B.; Peisach, J. in *Biological Magnetic Resonance* ; Vol. 3, L.J. Berliner and J. Reuben, Eds. Plenum Press: New York, 1981; pp. 213-263.

[13] Kevan, L; Bowman, M.K.; Narayana, P.A.; Boekman, R.K.; Yudanov, V.F.; Tsvetkov, Yu.D. *J. Chem. Phys.* **1975**, *63*, 409.

[14] Mims, W.B.; Peisach, J. *J. Biol. Chem.* **1979**, *254*, 4321.

[15] Cornelius, J.B.; McCracken, J.; Clarkson, R.; Belford, R.L.; Peisach, J. submitted for publication.

[16] L. Kevan and L.D. Kispert, *Electron Spin Double Resonance Spectrosocpy* ; John Wiley and Sons: New York, 1976.

[17] M.M. Dorio and J.H. Freed Eds., *Multiple Electron Resonance Spectroscopy* ; Plenum Press: New York, 1979.

[18] Feher, G.; Isaacson, R. A.; Scholes, C. P.; Nagel, R. L. *Ann. N.Y. Acad. Sci.* **1973**, *222*, 86.

[19] Scholes, C.P., Isaacson, R. A., Feher, G. *Biochim. Biophys. Acta* **1972**, *263*, 448.

[20] Hyde, J.S. in *Magnetic Resonance in Biological Systems.*; A. Ehrenberg, B.G. Malmstrom, T.Vanngard, Eds.; Pergamon: London, 1967; p. 63.

[21] Hutterman, J. ; Kappl, R. in *Metal Ions in Biological Systems*; Vol. 22. H. Sigel, Ed.; M. Dekker: New York, 1986; p. 3.

[22] Kevan, L. and Kispert, L.D. *Electron Spin Double Resonance Spectroscopy.* John Wiley and Sons: New York, 1976; p. 28.

[23] Schweiger,A. *Structure and Bonding. Vol. 51*; Springer Verlag: Berlin, 1982; p. 3.

[24] Flanagan, H.L.; Singel, D.J. *Chem. Phys. Lett.* **1987**, *137*, 391-397.

[25] Chasteen, N.D. in *Iron Binding Proteins without Cofactors or Sulfur Clusters*; Advances in Inorganic Biochemistry Vol. 5, E.C. Theil, G.L. Eichorn and L.G. Marzilli, Eds.; Elsevier: New York, 1983; pp 201-233.

[26] J.M.; Baker, E.N. *Proc. Natl. Acad. Sci. USA* **1987**, *84*, 1769.

[27] Anderson, B.F.; Baker, H.M.; Haridas, M.; Norris, G.E.; Rumball, S.V.; Smith, C.A.; Baker, E.N. Abstracts, XXVII Interl. Conf. Coord. Chem., Australia, **1989**, S20.

[28] Schlabach, M.R.; Bates, G.W. *J. Biol. Chem.* **1975**, *250*, 2182-2188.

[29] Williams, J.; Chasteen, N.D.; Moreton, K. *Biochem. J.* **1982**, *201*, 537-532.

[30] Chasteen, N.D.; Williams, J. *Biochem. J.* **1981**, *193*, 717-727.

[31] Baldwin, D. *Biochim. Biophys. Acta.* **1980**, *623*, 183-188.

[32] Baldwin, D.A.; de Sousa, D.M.R. *Biochem. Biophys. Res. Commun.* **1981**,*99*, 1101-1107.

[33] Scholes, C.P.; Van Camp, H.L. *Biochim. Biophys. Acta* **1976**, *434*, 290- 296.

[34] LoBrutto, R.L.; Wei, Y.H.; Mascarenhas, R.; Scholes, C.P.; King, T.E. *J. Biol. Chem.* **1983**, *258*, 7437-7448.

[35] Wittaker, J.W.; Lipscomb, J.D. *J. Biol. Chem.* **1984**, *259*, 4487-4495.

[36] Orville, A.M.; Lipscomb, J.D. *J. Biol. Chem.* **1989**, *264*, 8791-8801.

[37] Spartalian, K.; Carrano, C.J. *Inorg. Chem.* **1989**, *28*, 19-24.

[38] Carrano, C.J.; Carrano, M.W.; Sharma, K.; Backes, G; Sanders-Loehr, submitted for publication.

[39] McDevitt, M.R.; Addison, A.W.; Sinn, E.; Thompson, L.K. submitted for publication.

[40] Swope, S.K.; Chasteen, N.D.; Weber, K.E.; Harris, D.C. *J. Am. Chem. Soc.* **1988**, *110*, 3835-3840.

[41] Kevan, L. in *Time Domain Electron Spin Resonance*, Kevan, L. and Schwartz, R. N. Eds.; Wiley: New York, 1979.

[42] Salikov, K. M. and Tsvetkov, Y. D. in *Time Domain Electron Spin Resonance*, Kevan, L. and Schwartz, R. N. Eds.; Wiley: New York, 1979.

[43] Tang, J.; Lin, C. P.; Norris, J. R. *J. Chem. Phys.* **1985**, *83*, 4917.

[44] Kevan, L.; Bowman, M.K.; Narayana, P. A.; Boeckman, R. K.; Yudanov, V. F.; Tsvetkov, Yu. D. *J. Chem. Phys.* **1975**, *63*, 409.

[45] The programs ANDYI, ANDYI1, and TPANDYI were written and modified at the University of Illinois in collaboration with Jeff Cornelius.

[46] Kevan, L.; Bowman, M.K.; Narayana, P.A.; Boekman, R.K.; Yudanov, V.F.; Tsvetkov, Yu.D. *J. Chem. Phys.* **1975**, *63*, 409.

[47] Narayana, P.A.; Bowman, M.K., Kevan, L. Yudanov, V.F.; Tsvetkov, Yu. D. *J. Chem. Phys.*. **1975**, *63*, 3365.

[48] Narayana, P.A.; Kevan, L. *J. Chem. Phys.* **1976**, *65*, 3379.

[49] Mims, W.B.; Davis, J.L. *J. Chem. Phys.* **1976**, *64*, 4836.

[50] Mims, W.B.; Peisach, J.; Davis, J.L. *J. Chem. Phys.* **1977**, *66*, 5536.

[51] Iwasaki, M.; Toriyama, K. *J. Chem. Phys.* **1985**, *82*, 5415-5423.

[52] Mims, W.B. in Fourier, Hadamard, and Hilbert Transforms in Chemistry, Marshall, A.G Ed. Plenum Press. New York. p.316.

[53] Mims, W. B. *J. Magn. Reson.* **1984**, *59*, 291.

[54] The program FTBILL was written at the University of Illinois by Jeff Cornelius. The program is specifically designed to handle ESE data in formats from Albert Einstein College of Medicine and Argonne National Lab.

[55] Kumaresan, R.; Tufts, D. W. *IEEE Trans.* **1982**, *ASSP-30*, 833.

[56] Barkhuijsen, H.; deBeer, R.; Bovee, W. M. M. J.; vanOrmondt, D. *J. Magn. Reson.* **1985**, *61*, 465.

[57] Barkhuijsen, H.; deBeer, R.; vanOrmondt, D. *J. Magn. Reson.* **1985**, *64*, 343.

[58] Tang, J.; Lin, C. P.; Bowman, M. K.; Norris, J. R. *J. Magn. Reson.* **1985**, *62*, 167.

[59] Tang, J.; Norris, J. R. *J. Chem. Phys.* **1986**, *84*, 5210.

[60] Barkhuijsen, H.; de Beer, R.; Duijvestijn, C.; van der Lugt, D.; van Ormondt, D.; Wind, R.A. *J. Magn. Reson.* **1985**, *62*, 253.

[61] Barkhuijsen, H.; de Beer, R.; Pronk, B.J.; van Ormondt, D. *J. Magn. Reson.* **1985**, *61*, 284.

[62] Iwasaki, M; Toriyama, K.; Nunome, K. *J. Chem. Phys.* **1985**, *82*, 5415-5423.

[63] Rist, G.H.; Hyde, J.S. *J. Chem. Phys.* **1970**, *52*, 4633-4643.

[64] Rist, G.H.; Hyde, J.S. *J. Chem. Phys.* **1968**, *49*, 2449-2451.

[65] Jorin, E.; Rudin, M.; Schweiger, A.; Gunthard, Hs. H. *Chem. Phys. Letters* **1980**, *69*, 193.

[66] Hurst, G.C.; Henderson, T.A.; Kreilick, R.W. *J. Am. Chem. Soc.* **1985**, *107*, 7294-7299.

[67] Iwasaki, M. *J. Magn. Reson.* **1974**, *16*, 417.

[68] The program ANGSEL which calculates the orientations contributing to the ENDOR spectrum and the ENDOR frequencies was a modified version of the program described in [66] and was obtained from Dr. J. B. Cornelius of the Biotechnology Resource in Pulsed EPR Spectroscopy at the Albert Einstein College of Medicine.

[69] Reijerse, E.J.; Keijzers, C.P. *J. Magn. Reson.* **1987**, *71*, 83-96.

[70] Reijerse, E.J.; van Aerle, N.A.J.M.; Keijzers, C.P. *J. Magn. Reson.* **1986**, *67*, 114-124.

[71] Gurbiel, R.J.; Hoffman, B.M. *J. Magn. Res.* **1989**, *82*, 309-317.

[72] Gurbiel, R.J.; Batie, C.J.; Sivaraja, M.; True, A.E.; Fee, J.A.; Hoffman, B.M.; Ballou, D.P. *Biochemistry* **1989**, *28*, 4861-4879.

[73] vanWilligen, H. *J. Magn. Res.* **1980**, *39*, 37-46.

[74] Mulks, C.F.; vanWilligen, H. *J. Phys. Chem.* **1981**, *85*, 1220-1224.

[75] Mulks, C.F.; Scholes, C.P.; Dickinson, L.C.; Lapidot, A. *J. Am. Chem. Soc.* **1979**, *101*, 1645-1654.

[76] Aasa, R; Aisen, P. *J. Biol. Chem.* **1968**, *243*, 2399-2404.

[77] Hoffman, B.M.; Venters, R.A.; Roberts, J.E. *J. Am. Chem. Soc.* **1982**, *104*, 4711-4712.

[78] True, A.E.; Nelson, M.J.; Venters, R.A.; Orme-Johnson, W.H.; Hoffman, B.M. *J. Am. Chem. Soc.* **1988**, *110*, 1943-1950.

[79] Scholes, C.P.; Isaacson, R.A.; Yonetani, T.; Feher, G. *Biochim. Biophys. Acta* **1973**, *322*, 457-462.

[80] Wertz,J.E. and Bolton,J.R. *Electron Spin Resonance*; New York: McGraw Hill: New York, 1972; Table C.

[81] Kuska, H.A.; Rogers, M.T. *J. Chem. Phys.* **1964**, *41*, 3802-3805.

[82] Lowenstein, A.; Shporer, M.; Navon, G. *J. Am. Chem. Soc.* **1963**, *85*, 2855-2856.

[83] Davis, D.G.; Kurland, R.G. *J. Chem. Phys.* **1967**, *46*, 388-390.

[84] Schweiger, A.; Wolf, R.; Gunthard, Hs.H.; Ammeter, J.H.; Deiss, E. *Chem. Phys. Letters* **1980**, *71*, 117-122.

[85] Schweiger,A. *Structure and Bonding. Vol. 51*; Springer Verlag: Berlin, 1982; p. 50.

[86] Curry, N.A.; Runciman, W.A. *Acta. Cryst.* **1959**, *12*, 674-678.

[87] Maer, K.; Beasley, M.L.; Collins, R.L.; Milligan, W.O. *J. Am. Chem. Soc.* **1968**, *90*, 3201-3208.

[88] Gupta, M.P.; Milledge, H.J.; McCarthy, A.E. *Acta. Cryst.* **1974**, *B30*, 656-661.

[89] The limit that the anisotropic component of approximately 2.2 MHz is due completely to electron spin density in a carbon 2p orbital (where unit spin density gives a coupling of 90.8 MHz) corresponds to a p orbital spin density of 2.42% (2.2/90.8 X 100). In this limit no structural information could be obtained.

[90] Williams, J.; Chasteen, N.D.; Moreton, K. *Biochem. J.* **1982**, *201*, 537-532.

[91] Chasteen, N.D.; Williams, J. *Biochem. J.* **1981**, *193*, 717-727.

[92] Nishida, Y.; Oshio, S.; Kida, S. *Inorg. Chim. Acta* **1977**, *23*, 59.

[93] Bailey, S.; Evans, R.W.; Garratt, R.C.; Gorinsky, B.; Hasnain, S.; Horsburgh, C.; Jhoti, H.; Lindley, P.F.; Mydin, A.; Sarra, R.; Watson, J.L. *Biochemistry* **1988**, *27*, 5804-5812.

[94] Anderson, B.F.; Baker, H.M.; Dodson, E.J.; Norris, G.E.; Rumball, S.V.; Waters, J.M.; Baker, E.N. *Proc. Natl. Acad. Sci. USA* **1987**, *84*, 1769.

[95] Anderson, B.F.; Baker, H.M.; Haridas, M.; Norris, G.E.; Rumball, S.V.; Smith, C.A.; Baker, E.N. Abstracts, XXVII Interl. Conf. Coord. Chem., Australia, **1989**, S20.

[96] Zweier, J.; Aisen, P.; Peisach, J.; Mims, W.B. *J. Biol. Chem.* **1979**, *254*, 3512-3515.

[97] Roberts, J.E.; Brown, T.G.; Hoffman, B.M.; Aisen, P. *Biochim. Biophys. Acta* **1983**, *747*, 49-54.

[98] McCracken, J.; Peisach, J.; Dooley, D.M. *J. Am. Chem. Soc.* **1987**, *109*, 4054-4072.

[99] Peisach, J.; Mims, W.B. *J. Biol. Chem.* **1984**, *259*, 2704.

[100] Doi, K.; McCracken, J.; Peisach, J.; Aisen, P. *J. Biol. Chem.* **1988**, *263*, 5757-5763.

[101] Crookham, H.; Brown, D.; Belford, R.L.; Clarkson, R.B. International Electron Paramagnetic Resonance Symposium, 31st Rocky Mountain Conference, Denver, 1989.

[102] Schmidt, J. *Chem. Phys. Lett.*, **1972**, *14*, 411.

[103] Mims, W.B.; Nassau, K.; McGee, J.D. *Phys. Rev.* **1961**, *123*, 2059.

[104] Liao, P.F.; Hartman, S.R. *Phys. Rev.* **1973**, *B8*, 69.

[105] Singel, D.J. submitted for publication.

[106] Dikanov, S.A.; Tsvetkov, Yu. D.; Bowman, M.K.; Astashkin, A.V. *Chem. Phys. Lett.* **1982**, *90*, 149.

[107] Astashkin, A.V.; Dikanov, S.A.; Tsvetkov, Yu.D. *J. Struct. Chem.* **1984**, *25*, 200.

[108] Flanagan, H.L.; Singel, D.J. *J. Chem. Phys.* **1987**, *87*, 5606-5616.

[109] Flanagan, H.L.; Singel, D.J. *Chem. Phys. Lett.* **1987**, *137*, 391-397.

[110] Roberts, J.E.; Brown, T.G.; Hoffman, B.M.; Aisen, P. *Biochim. Biophys. Acta* **1983**, *747*, 49-54.

[111] Eaton, S.S.; Dubach, J.; Kundalika, M.M.; Eaton, G.R., Thurman, G.; Ambruso, D.R. *J. Biol. Chem.* **1989**, *264*, 4776-4781.

[112] Ikeda, R.; Nakamura, D.; Kubo, M. *Proceedings Xth International Conf. on Coordination Chem.*, Japan **1967**, p. 110.

[113] Kosman, D.J.; Peisach, J.; Mims, W.B. *Biochemistry* **1980**, *19*, 1304.

[114] McCracken, J.; Pember, S.O.; Benkovic, S.J.; Villafranca, J.J.; Miller, R.J.; Peisach, J. *J. Am. Chem. Soc.* **1988**, *110*, 1069-1074.

[115] Flanagan, H.L.; Gerfen, G.J.; Singel, D.J. *J. Chem. Phys.* **1988**, *88*, 20-24.

[116] Flanagan, H.L.; Singel, D.J. *Chem. Phys. Lett.* **1987**, *137*, 391-397.

[117] Chasteen, N.D; McCracken, J.; Peisach, J. unpublished results.

[118] Hunt, M.J.; Mackay, A.L.; Edmonds, D.T. *Chem. Phys. Lett.* **1975**, *34*, 473.

[119] Kosman, D.J.; Peisach, J.; Mims, W.B. *Biochemistry* **1980**, *19*, 1304.

[120] Fee, J.A.; Peisach, J.; Mims, W.B. *J. Biol. Chem.* **1981**, *256*, 1910.

[121] McConnell, H.M.; Strathdee, J. *Mol. Phys.* **1959**, *2*, 127-138.

[122] Atherton, N.M. *Electron Spin Resonance*; Wiley: New York, 1973; pp 130-131.

[123] Clementi, E.; Raimondi, D.L. *J. Chem. Phys.* **1963**, *38*, 2686-2689.